Quantum Confined Noble Metal Monolayer Protected Clusters Investigated Using Linear and Nonlinear Microscopy

by

Neranga Abeyasinghe

A dissertation submitted in partial fulfillment
of the requirements for the degree of
Doctor of Philosophy
(Chemistry)
in the University of Michigan
2017

Doctoral Committee:

Professor Theodore G. Goodson III, Chair
Professor Eitan Geva
Professor Raoul Kopelman
Professor John C. Schotland
Professor Nils G. Walter

DEDICATION

To my parents, to my family and to all my teachers.

ACKNOWLEDGEMENTS

As a human being born on this planet, it is impossible to achieve anything without the assistance and guidance from one's fellow human beings. For example, the food that we eat and many consumables that we consume are all products of the labor of many others. This dissertation work and a journey that took place several decades around the sun taught me how grateful I should be for everything I have got so far. First and foremost, I would like to thank my parents, my two sisters and my brother-in-law for everything they have provided to see this day. Their encouragement and understanding helped me to pay my debts back. This dissertation work in particular would not have taken place in a vacuum. I would like to extend my heartfelt gratitude to Prof. Theodore Goodson III, who had mentored me through my journey of the graduate school. His guidance and support had been instrumental in accomplishing what I am presenting now at the culmination of my tenure at the University of Michigan. Prof. Nils Walter, Prof. Eitan Geva, Prof. Raoul Kopelman and Prof. John Schotland are gratefully acknowledged for serving in my committee whose guidance was immensely helpful. Also, Prof. Kenichi Kuroda is acknowledged for agreeing in such short notice to serve as a substitute member at my oral defense. I would like to thank Dr. Oleg Varnavski for being the master of many things. His help and guidance was instrumental in successfully completing the cutting edge work this dissertation presents. All members at the Goodson group are also acknowledged. Especially, Dr. Sung Hei Yau, Dr. Jeffery Raymond, Dr. Joseph Furgal, Dr. Leslie Upton, Dr. Oluwasegun Adegoke, Dr. Phi Doan, Rosina

Ho Wu, Bradly Keller, and Ricardo Vasquez are all acknowledged for their discussions and feedback. Linda van Blaircum at the Goodson group must be thanked million times for being the glue that keeps everything together in the Goodson group. Also, I would like to thank and wish best of luck for the current and newly joined scientists at the Goodson lab!

I would also like to extend my gratitude to my collaborators at the Carnegie Mellon University, University of Malaga, Spain and here at the University of Michigan. Prof. Rongchao Jin, Prof. Juan Casado, Prof. Paul Zimmerman, Dr. Santosh Kumar, Dr. John F. Mansfield, Dr. Kai Sun, and Alan Chien (Zimmerman group) are gratefully acknowledged. With their collaborations, I was able to learn and accomplish many things and grow as a scientist. Being at the Chemistry Department of the University of Michigan helped me to establish many connections spanning the entire world that I would otherwise not have been able to do. Everyone at the U of M Chemistry is thanked for their friendship, discussions, curiosity and the mere presence. Especially, graduate coordinator Liz Oxford, and the previous graduate coordinators at the Department of Chemistry, Margarita Bekiares and Anna Stryker and everyone at CHEM 1500 are gratefully acknowledged. All of the teachers that I took classes from in my first two years at U of M are acknowledged for their teaching. Prof. Eitan Geva, Prof. Roseanne Sension, Prof. Julie Biteen, Prof. Kevin Kubarych, Prof. Robert Robertson at MSE and Prof. Ari Gafni are gratefully acknowledged for their teaching. Also, Stilliana, Carson, Chris, Brenda and all instructors at ELI and CRLT are gratefully acknowledged for the training on teaching techniques and American English. All of my international colleagues I met during this time are gratefully acknowledged for their friendship. International center at the University of Michigan deserves much appreciation for their great service to international students. Their guidance was really helpful throughout my time in Michigan. Also, I must thank Prof. Marina von Neumann Whitman for letting me ask some important questions about her, her father and his thoughts on certain aspects of science. I must thank many such individuals whom I was able to meet during my time in Ann Arbor. Overall, the University of Michigan is a place that gave me many opportunities to grow as an intellectual, a scientist and a global citizen.

I would also like to thank all of my teachers and mentors I had since my kindergarten until the undergraduate studies at the University of Colombo. If not for their initial guidance, nurturing, kind encouragement and mentoring this would not have been possible. Also, I would like to thank all of my friends who encouraged me to come to the US and to U of M to do my PhD. As a matter of fact, I know there are many who are thanking them for encouraging me to come here. Also, I would like to thank Dr. Mohottala and Mrs. Mohottala for their caring and help during my first trip to the US which is quite a memorable time. Dr. Dushy Mendis is also acknowledged for letting me know about Ann Arbor several months before I set foot in the US. Mr. Udana, Mrs. Gayani and Lahiru are gratefully acknowledged for their help in many ways in the times of settling in.

Ann Arbor is a great college town with many peace-loving human beings and a lot of trees. I would like to thank all of my friends in Ann Arbor for their great discussions and friendship. I would also like to specially thank my Sri Lankan friends in Ann Arbor and elsewhere in the US for their help, company, discussions and questions. These are some of the greatest and peaceful people I have ever met in my life and I wish all of them the perfect, unabated contentment as soon as they can! Finally, I would like to thank anyone whom I couldn’t mention by name and all of the human beings that I met. May all beings be happy, peaceful and content!

TABLE OF CONTENTS

LIST OF FIGURES

Abstract

Elemental quantum confined nanocluster systems were previously demonstrated to have unusual optical, electronic, catalytic and magnetic properties suggesting to classify them as a new form of matter. Optical investigations in solution phase ensembles using monolayer protected nanoclusters (MPCs) allowed the community to experimentally confirm that the metal-to-insulator transition in gold occurs at ~300 gold atoms. However, investigations of single nanoclusters using optical microscopy and spectroscopy to determine effects of quantum confinement in MPCs were not reported until now. In my dissertation work, I interrogated isolated single quantum confined Au_{25} MPCs on a solid substrate. My observations made on isolated and aggregated MPCs on solid using two-photon excited fluorescence (TPEF) near-field scanning optical microcopy (NSOM) revealed that their native quantum confinement effects manifest primarily when they are isolated from aggregates and solution ensembles. This is consistent with the picture of narrowing of the density of states (DOS) when the quantum clusters are removed from aggregates and studied in isolation on solid. Also, it agrees with the enhancement expected for volume-normalized oscillator strengths (f_{12}/V) of electronic transitions in the presence of quantum size effects. In order to obtain isolated single nanoclusters on solid, I devised a procedure where I synthesized MPCs, isolated them in solution phase and then deposited isolated single nanoclusters on solid substrate with ~160 nm average inter-nanocluster distances. Scanning transmission electron microscopy (STEM) confirmed the isolation of single nanoclusters on solid. The investigations of isolated MPCs on

solid using aperture-based TPEF NSOM elicit ~30 nm point resolution which is ~5-fold better than the typical confocal point resolution. Also, my findings on possible local field enhancement for MPCs suggest the potential to use isolated MPCs, MPC arrays, meshes or lattices to obtain significantly enhanced TPEF properties that can be used in molecular computing, bioimaging, sensing, and data storage applications.

On a separate investigation, I explored materials that can increase the theoretical efficiency limit of organic photovoltaics (OPV) via intramolecular singlet exciton fission (iSEF). I interrogated a quinoidal bithiophene molecule in solution that revealed highly efficient ultrafast iSEF with ~180% singlet-to-triplet conversion efficiency. Our finding of iSEF in a small molecule invigorates theoretical and experimental investigations of small molecule iSEF materials to make highly efficient solar cells.

Chapter 1

Introduction

1.1 Quantum Confined Elemental Clusters: A new form of matter

As many of us are aware of, when arranging chemical elements in the periodic table we follow a set of fundamental quantum mechanical rules; namely, the filling up of electrons in space and time according to their principle (n), angular momentum (l), magnetic (m_l) and electronic spin (m_s) quantum numbers. [1-3] Such arrangement of elements allowed chemists, physicists and engineers to classify certain elements as metals, non-metals or metalloids, facilitating their use in

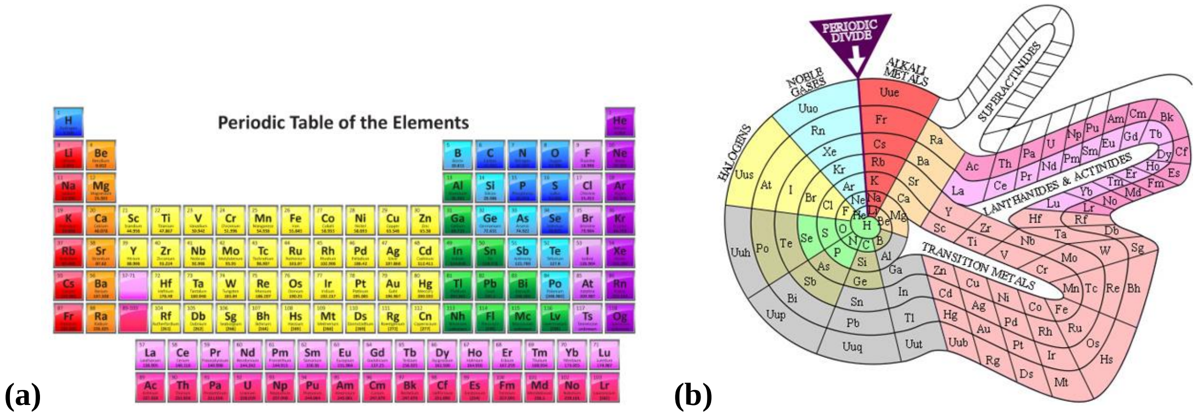

Figure 1-1[4] (a) Typical representation of the periodic table of elements (b) alternative form of the periodic table that relies on the building up (Aufbau) principle to form an *elemental* real estate. This elemental landscape would be where one can potentially introduce an additional (3rd) dimension along which new elemental nanoclusters with unique size dependent properties are introduced. http://sciencenotes.org/printable-periodic-table/,

countless applications in the last two centuries. As a case in point, metals tend to demonstrate a unique set of properties that distinguish them from non-metals (and metalloids). For instance, the superior thermal and electrical conductivity of metals and their metallic lustre are typical hallmarks of the physical nature of metals. However, during the previous 4 decades, scientists have been trying to make and explore novel nanomaterials from the basic elements found in the periodic table that fundamentally deviate their physical behavior from their elemental counterparts. [5-18] The field of nanoclusters thus emerged may potentially present a new form of matter that may perhaps be able to add a new dimension to the periodic table of elements. [10, 18] These materials demonstrate unique size-dependent physical behavior and possess previously unanticipated optical, electronic, magnetic, and catalytic properties. [19-27] Therefore, this rapidly growing field of elemental cluster materials present us with a unique opportunity to study fundamental physical laws abound at the nanoscale materials that may culminate in the addition of a novel dimension to materials chemistry.

In order to understand the properties of nanoclusters in the context of atomic elements and their bulk counterparts, we can begin with comparing the density of states picture for different sizes of an elemental material. [9] As can be observed in Figure 1-2, the 3-dimensional object has continuous distribution of electronic densities of states (DOS), which, for example, may resemble a bulk metal such as gold or silver. When a single dimension is reduced to dimensions approaching the Fermi wavelength of an electron the material is said to be quantum confined in 1-dimension. These are termed quantum wells (2-D). Graphene is a material that can be considered as a 2-D material [28] whose finding and characterization resulted in the 2010 Nobel prize in physics. In graphene one dimension is quantum confined as it is only atomically thick. For quantum wells the density of states become step-like along the energy axis indicating sharp changes in the densities of electronic states at certain energies while retaining uniform density at other energies. As one reduces another dimension of the material below the Fermi wavelength of an electron of the material one can obtain a quantum wire (1-D) which is now quantum confined in two-dimensions

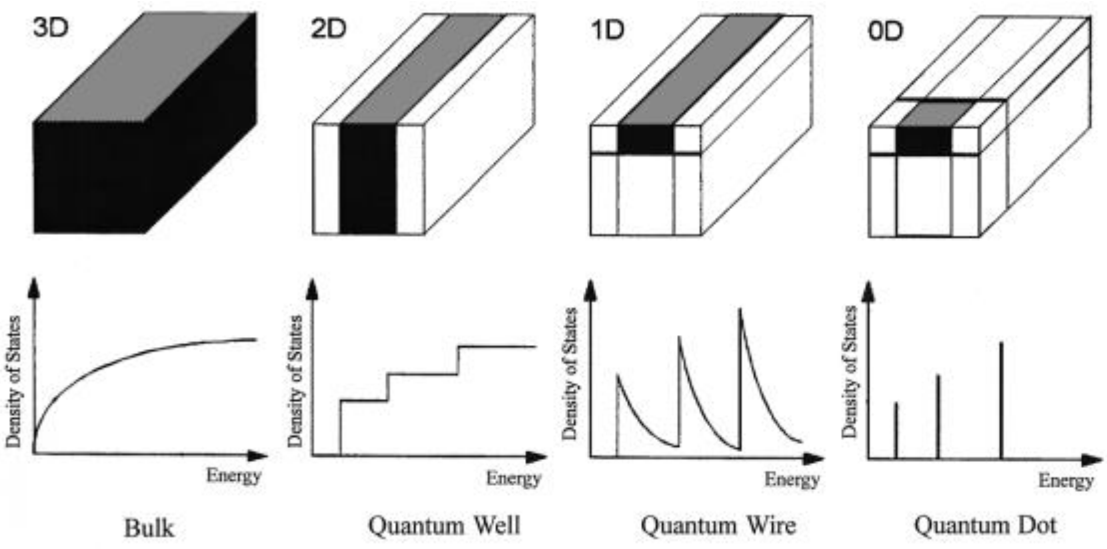

Figure 1-2 Formation of a zero (0D) dimensional quantum confined system by reducing the dimensions of a bulk material

(e.g. carbon nanotubes). As is depicted in the figure 1-2, the DOS becomes narrower as certain energies are becoming significantly more probable than the others while retaining a continuous distribution of energies. Finally, if you make the particle size (in all 3-dimensions) smaller than the Fermi wavelength of the electron the (0D) quantum “dots” results. The DOS picture produces sharp lines as opposed to broad distributions of energy. In principle, if these nanoclusters can be studied in isolation, the presence of these sharp lines indicates an unusually strong per-cluster absorption cross sections at specific allowed excitation energies/wavelengths. As can be understood, this enhancement arises from the quantum confinement effects for a monodisperse nanocluster sample that causes the formation of discrete energy levels. [29, 30] However, if one has quantum confined clusters with different cluster diameters one may have different transition energies. [29] This observation highlights another critical aspect in quantum clusters, namely the Quantum size effect which indicates changing of properties of a nanocluster by changing its size (number of atoms).

Quantum confinement effects were initially predicted by Frohlich [29] in 1937 where he described his theoretical findings as follows "*……… large differences occur at low temperatures between the specific heat of the electrons of an infinitely large metal and those of small metal particles*." Several decades later, in 1962, Ryogo Kubo elaborated on these observations to give a more thorough theoretical description of quantum confinement effects. [30] In order to better understand quantum size effects one can refer to the Figure 1-3. First, we can define an average energy level spacing δ for an elemental material which is typically referred to as the Kubo gap. [31] At room temperature (~ 293 K) the thermal energy is $k_BT = 25.2$ meV; where k_B is the Boltzmann constant (1.38×10^{-23} JK^{-1}) and T is the absolute temperature. Therefore, as can be observed in Figure 1-3, when the $\delta > k_BT$, one should be able to observe quantum confinement effects in nanoclusters due to discrete band gap separation. However, another interesting fact of Quantum size effects appear when we consider the following equation which is known as the Kubo criterion.[31]

Equation 1-1 $$\delta = \frac{4E_f}{3N}$$

In the above expression the E_f is the Fermi Energy for the given element which indicates the highest energy for a ground state electron in a metal at absolute zero (which is ~5.5 eV for gold). N indicates the number of electrons present in the material. Since average energy level spacing (δ) is inversely proportional to the number of valence electrons, it is clear that the average band gap in a nanocluster must vary with the size of an elemental nanocluster. These varying band gaps for different number of atoms of a nanocluster can introduce a diverse range of physical properties even for nanoclusters made out of the same element. This is indeed the potential of this new form of matter that can have a gamut of physical properties which in turn may be able to

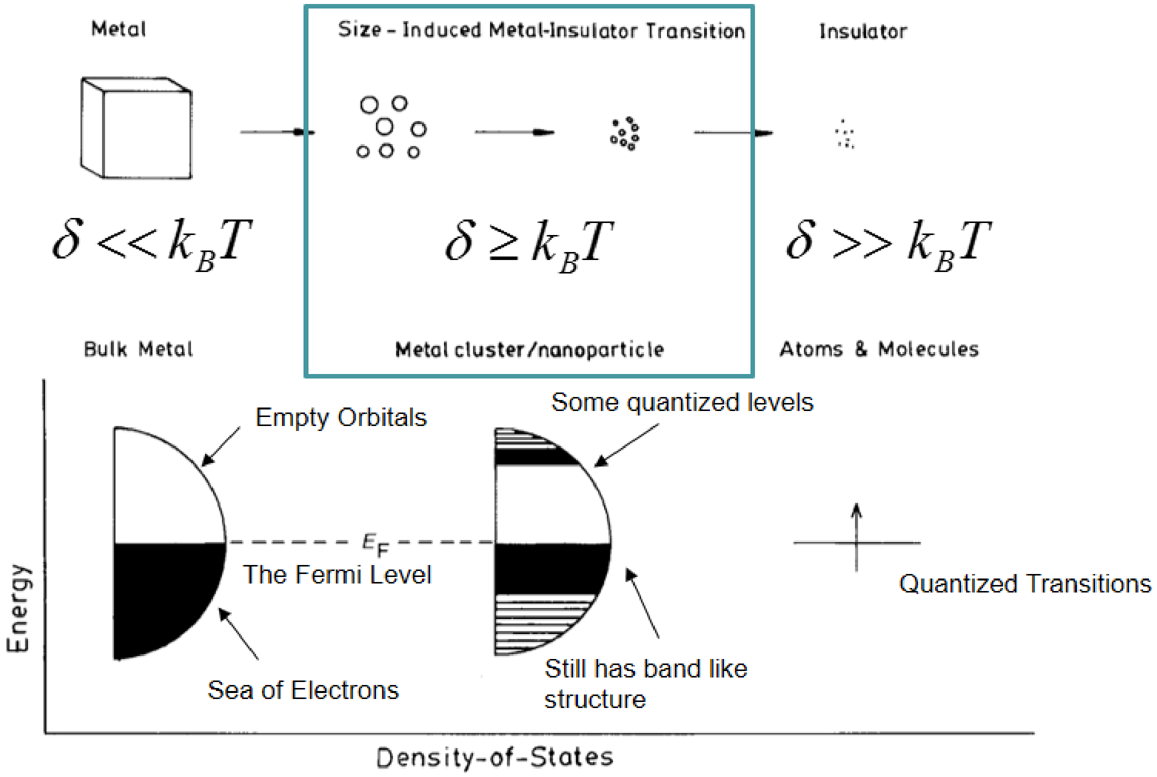

Figure 1-3 Formation of a zero (0D) dimensional quantum confined system by reducing the dimensions of a bulk material. White spaces are unoccupied states while the black spaces indicate occupied states (The blue square includes the size range of quantum confined nanoclusters and the size regime larger than quantum confined clusters)

incorporate another dimension to the periodic table of elements. In other words, quantum confined nanoclusters are "embryonic" portions of the bulk metal possessing properties that are dramatically different from that of the parent metal (in terms of structure and function). Also, their physical behavior may not be strictly categorized as that of molecules (or atoms for that matter) due to the presence of energy bands with many filled valence electrons even though there is a band gap. Another important caveat (figure 1-3) is that when the δ approaches thermal energy, the metallic properties begin to dominate and the nanomaterial appears to lose quantum confinement effects. From the equation 1-1, we can determine the approximate size range where the metal-to-insulator transition (quantum confinement) occurs. If we take a noble metal gold as an example, N= 291.

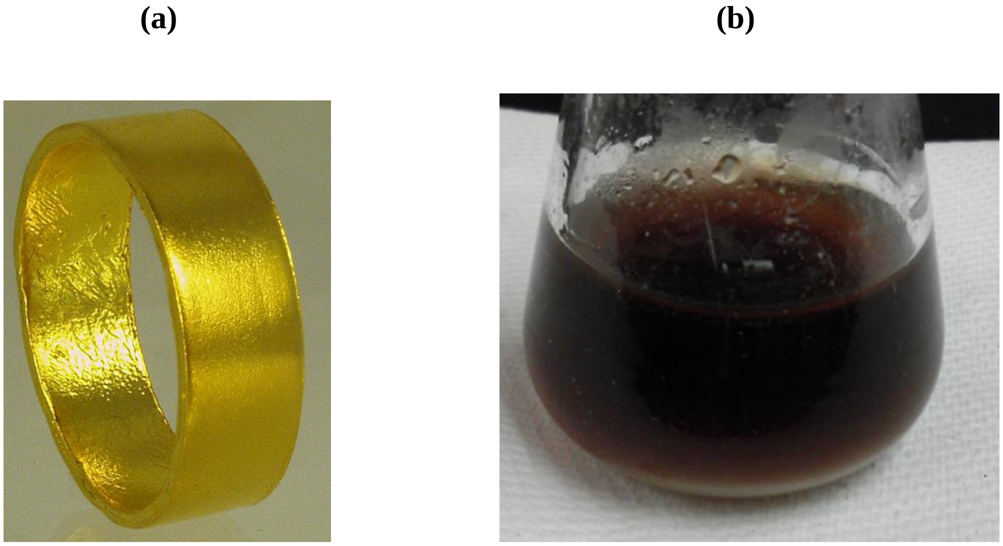

Figure 1-4 Difference in the physical appearance of bulk gold and gold nanoclusters (a) Bulk gold (24 carat gold ring) (b) Quantum confined gold nanocluster solution

From previous published work on nanoclusters, this indicates Au nanoclusters with diameters > 2.0 nm would lose quantum confinement effects. [20-24] From figure 1-3, when the $\delta << k_BT$, it is clear that positively charged metal cations are arranged in a periodic infinite lattice forming the band structure and are immersed in a sea of electrons which is well known as the metallic phase of matter due to the infinite periodicity of atoms forming the band structure. [19] The electrons fill up energy bands up to the Fermi energy with a continuous DOS. On the contrary, when one considers a Au atom, the HOMO-LUMO separation is the highest and demonstrates strictly atomic properties. In summary, it is clear that quantum confined nanocluster materials serve as a new form of matter that holds great promise as they have fundamentally different physical properties from the bulk elements and their atomic counterparts. [19-27]

1.2 Gas phase nanocluster investigations and the modeling of “magic clusters”

Since the earliest studies of alkali metal and inert gas clusters in the gas phase vapor beams [5-7], a general theme appeared. That is, the nanoclusters formed in the gas phase followed a pattern where certain “magic numbers” of atoms in a cluster seemed to produce unusual stability over other sizes of clusters which resulted in the term “magic clusters”.[32] Theoretical treatments of such clusters was carried out starting from the first principles of quantum mechanics. Using the free electron model for valence electrons of a cluster we can consider the nanocluster according to particle in a box model. The general Schrodinger equation can be written as in equation 1-2.

Equation 1-2 $$\left(\frac{-\hbar^2}{2m}+V\right)\phi = E\phi$$

If one considers 3-dimensional Cartesian coordinates, the quantum numbers in each direction are related as follows, $n^2 = n_x^2 + n_y^2 + n_z^2$. If one assumes a spherical potential well, the energy of the nanoclusters can be given according to the following equation.

Equation 1-3 $$E_n = \frac{\hbar^2\pi^2n^2}{2m\,a^2}$$

If we consider a sphere with radius n, the energy levels are distributed on the surface of a sphere. This resembles the Jellium model that was introduced to describe the stability of gas phase sodium clusters. [33-35] The primary approximation of the Jellium model is that the conduction electrons of the elements are moving in a uniform positively charged spherical potential background (spherical potential well) where the nuclear charges are somewhat shielded by the core electrons and the structure of the lattice is replaced by this average positive background. The spherical potential used in such calculations are as follows.[36]

Equation 1-4 $$\mathrm{U(r)} = -\left[\frac{\mathrm{Uo}}{\exp\left[\frac{\mathrm{r-ro}}{\varepsilon}\right]+1}\right]$$

Where r_o (the effective radius) is defined as,

Equation 1-5 $$\boldsymbol{r_0 = r_S N^{\frac{1}{3}} = \left(\frac{3}{4\pi}\right)[\rho N]^{\frac{1}{3}}}$$

N is the number of atoms, U is the Fermi energy (work function of the metal at 0 K), ε is the permittivity in vacuum, and the $\boldsymbol{\rho}$ is the electron density. Electron filling in this spherical potential naturally gave rise to the shell closing for specific number of valence electrons (thus atoms) resulting in stable "magic clusters" (figure 1-5).[36] While the Jellium model was able to predict the stability of N=2, 20, 40, 58 nanocluster sizes for gas phase Na clusters, the spherical potential assumed was unable to explain certain other nanocluster sizes observed (N=12, 14, 26, 30, 34,…). Therefore, a different potential model that is able to fit in all observed nanocluster sizes was required.

In 1985 Clemenger[37] started applying the ellipsoidal Nilsson potential (known as Nilsson-Clemenger potential) for nanocluster modeling which was borrowed from the ellipsoidal potential

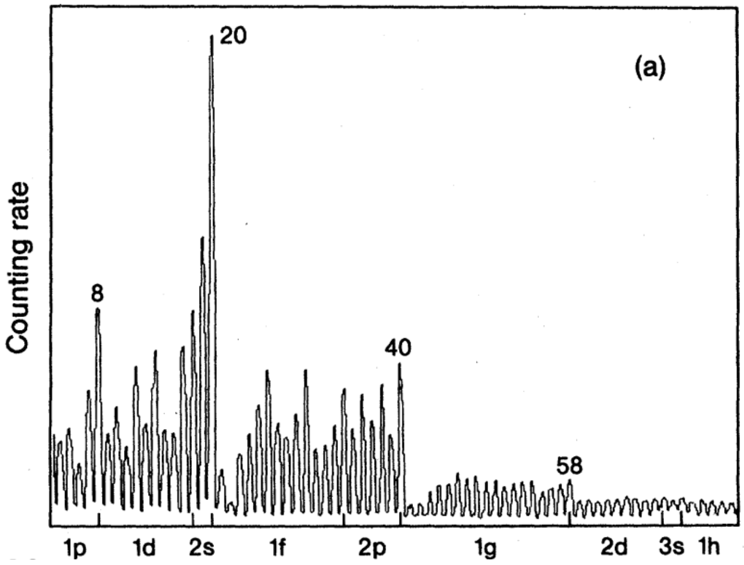

Figure 1-5 Mass spectra for Na clusters showing magic stability of certain nanocluster sizes [36]

well model used to describe nuclear stability. In this model, the modified Nilsson Hamiltonian used for valence free-electrons of the nanoclusters was assumed to take ellipsoidal shapes (rather than spherical) adding up to form a spherical shell.

Equation 1-6 $$\boldsymbol{\hat{H} = \frac{p^2}{2m} + \frac{1}{2} m\omega_0^2\left(\Omega_\perp^2\rho^2 + \Omega_z^2 z^2\right) - \mathrm{U}\hbar\omega_3\left(l^2 - \langle l^2 \rangle\right)}$$

Here the term involving Ω denotes the ellipsoidal correction for the otherwise spherical harmonic oscillator potential well. The term ω is the angular frequency of the harmonic oscillator, *p* is the momentum of the electron, *m* is the mass of the electron etc. The strong correlation between the energy level sequencing with these ellipsoidal subshells and the sequence of alkali metal mass spectra indicated that the metal clusters are in fact adopting approximately ellipsoidal shapes. [37]

The remarkable agreement with the experimental observations and the potential well models for nanoclusters indicated that these materials may be behaving similar to elemental "superatoms"[10, 19, 25] which will have distinct physical properties compared to their atomic building blocks. However, the fact that these nanocluster studies were carried out in the gas phase (under ultra-high vacuum) indicated that their practical use and the techniques to study their physics could become limited. Therefore, in order to understand the fundamental physical properties of this new form of matter, cluster systems that are stable in the condensed/solution phase under ambient conditions was preferred. Hence, the ability to synthesize monodisperse stable metal nanoclusters in solution phase was an exciting major step forward in the field of nanocluster studies. [38- 43]

1.3 Solution phase metal nanoclusters and metal nanoparticles

In section 1.1, using Kubo criterion, I have indicated a size limit (> 2 nm) for gold clusters that show quantum confinement effects. But, since nanoparticles of an element can have diameters larger than their quantum confined sizes, it seems imperative to define the following terminology so that the two types of nanomaterials can be distinguished. From this point on ward quantum confined clusters of any element will be identified as "*nanoclusters*" while the larger particles will be referred to as "*nanoparticles*". For example, *gold nanoclusters* will have diameters *below 2 nm* while gold nanoparticles will be larger than 2 nm. As will be discussed in detail in this and the sections that follow, I think that a clear physical difference between the two types of matter are experimentally established and justifies our terminology.

Nanoparticle synthesis in the condensed phase had been predominantly focused on gold nanoparticles due to their high stability and potential use in a wide variety of applications involving catalysis, photodynamic therapy etc.[19, 44- 49] Synthesis of gold colloids in the modern era have been reported about a century and a half ago. In 1857 Michael Faraday had reported the observation of ruby colored solutions for gold under reduction with Phosphorous. [50] This is the first documented observation found of gold nanoparticle synthesis. Faraday surmised that the colloidal solution thus produced should contain particles that are much smaller than the wavelength of visible radiation.

In 1951, using electron microscopy for characterization, Turkevich and coworkers have used a citrate reduction method to obtain a wide range of sizes (polydisperse) for spherical gold nanoparticles (ranging from about 10 nm to 25 nm diameters). [51] Two decades later, in 1973 Frens reported the synthesis of monodisperse spherical gold nanoparticles (as small as 16 nm in diameter) by controlling the concentration of the citrate solution. [52] As can be understood all of the condensed phase nanoparticle studies before 1990s were primarily focused on synthesizing gold nanoparticles (as opposed to nanoclusters) due to the presence of properties such as surface plasmon resonance (SPR) which is now a field of its own right with many applications. [44-46, 48, 53,54]

To understand optical absorption and scattering by nanoparticles, Gustav Mie[55] had introduced his theory which utilized the classical electromagnetic solutions for light-particle interactions. He treated the electromagnetic field from the first principles and the particle by its dielectric function. When the external field is applied the charges tend to separate within the boundaries of the particle. And when the field was removed the charges will return to their original positions. When applied this model with an electromagnetic excitation field, the excitation of the particle by light leads to a resonance which is denoted by Mie resonance frequency (ω_M^2).

Equation 1-7 $$\boldsymbol{\omega_M^2 = \frac{Q^2}{M_n \alpha}}$$

Here, the Q is the total charge, the M_n is the mass of the valence electrons and α stands for polarizability. The frequency of the collective oscillations of the valence electrons of the particle under an oscillating electromagnetic field corresponds to the surface plasmon (or plasmon polariton)[19] resonance frequency (SPR). [44-46, 48] However, this SPR signal for steady state absorption becomes dampened for particle sizes below the mean free path of an electron and disappear for quantum confined noble metal nanoclusters leading to a significant contrast between the steady state absorption spectra of nanoparticles and nanoclusters. [19- 21]

Most of the previous research of colloids until the 1990s was strictly focused on these nanoparticles that do not demonstrate quantum confinement effects. However, the nanoparticle synthesis in the condensed phase created a solid synthetic foundation for the "magic" nanocluster field to grow rapidly. Monolayer protected gold nanocluster synthesis by Schmid and coworkers and Brust *et al* paved the way to synthesize atomically precise gold nanoclusters in the solution phase. [38-43, 56-66] This is a significant advancement in the field of quantum clusters since solution phase optical investigations were made possible. Also, since noble metal nanoclusters (especially gold) proved to be relatively stable and due to their unusual optical, electronic, magnetic and catalytic properties, the field of noble metal nanocluster research in the condensed phase grew into a hot field of research during the last two decades. [11- 17, 20- 27, 38- 43, 56- 67]

Initial Brust synthesis was subsequently modified and optimized to obtain stable monodisperse gold nanoclusters in the solution phase. [43, 57- 66] Also, the ability to synthesize them in large quantities is helpful since that can allow one to use them in future applications. In Brust synthesis (sometimes referred to as Brust-Schiffrin synthesis), a thiolate ligand reacts with the Au(III) ions in solution under strongly reducing conditions. $NaBH_4$ is used as the reducing agent. Due to the use of a monolayer of thiolate ligands, the synthesis can be directed to obtain specific sizes of gold nanoclusters under controlled reaction conditions (concentrations, temperature and stirring speeds). [43] Due to the high stability of the Au-S bond, thiolate protected gold nanoclusters produce extremely stable quantum confined clusters. Therefore, thiolate protected gold nanoclusters are ideal candidates to study the quantum confinement of elemental nanoclusters in the condensed phase.

1.4 Structure of nanocluster super atoms

Since the first reported synthesis of gold nanoclusters by Schmid and Brust, [38-43, 66] it was highly desired to find the correct atomic composition and the 3-dimensional structure of nanoclusters. This is particularly important to understand the fundamental rules that govern the quantum confinement and the stability of atomically precise nanoclusters. [68] After 2007, many crystal structures and exact atomic compositions of nanoclusters were solved for many sizes of gold and silver nanoclusters (Au_{102}, Au_{25}, Au_{309}, Ag_{44} etc). [11- 17, 65]

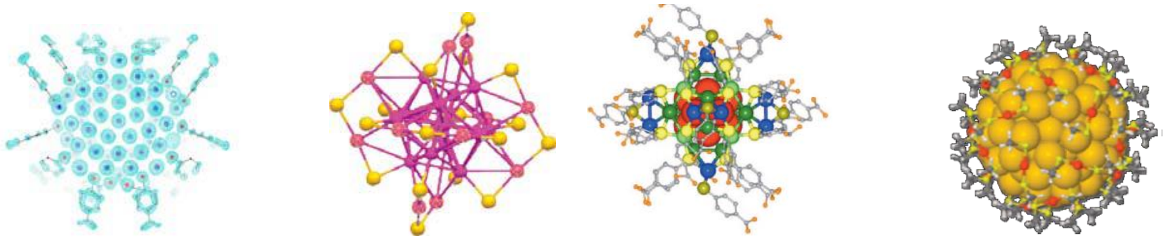

(a) **(b)** **(c)** **(d)**

Figure 1-6 Structures and atomic arrangement of Au and Ag nanoclusters [11, 13, 15, 65] (a) Au_{102} (b) Au_{25} (c) Ag_{44} (d) Au_{144}

As shown in the figure 1-6, using X-Ray crystallography or high resolution aberration corrected scanning transmission electron microscopy (Ac-TEM), certain stable nanocluster compositions were determined with atomic precision. The question one may ask is do they follow any stability rules? And can they predict physical properties (e.g. absorption spectra)? One approach of stabilization was proposed by Schmid for his Au_{55} clusters. [69] In his approach, the atomic packing to form shell closing was considered as the major stabilization force. These clusters are known as “closed-shell clusters” to imply the clusters that obey the following rule. For any stable nanocluster the ‘n’ stands for the number of shells where the clusters are formed when the shells are completely closed by the given number of atoms.

Equation 1-8 **Number of atoms in the Cluster Core = $10*n^2 + 2$**

If we consider a central Au atom surrounded by subsequent shells of atoms, Au_{13} (1 shell), Au_{55} (2 shells) etc results. As is evident, this was specifically useful for describing the stability of Au_{55} nanoclusters and the presence of Au_{13} cores. However, there appeared many other stable nanoclusters in the condensed phase whose stability cannot be explained just by the equation 1-8. Also, the packing rules introduced do not predict the electronic energy level arrangement or many physical/optical properties of the nanoclusters. Therefore, a model/understanding beyond atomic packing was required to describe the stability of other highly stable nanoclusters (e.g. Au_{25})

After solving the crystal structure of Au_{102} and Au_{25} monolayer protected nanoclusters, the field of nanocluster had a more comprehensive understanding of the stability and electronic/optical properties of “non-closed-shell nanoclusters”. [11, 13, 14] Jin and coworkers and Schatz and coworkers determined the optical properties of Au_{25} nanoclusters using TDDFT calculations based on the crystal structure of the nanocluster. [13] As depicted in figure 1-6(b), the crystal structure of Au_{25} possess the Au_{13} icosahedral core structure surrounded by 12 gold atoms that are bound to S atoms of the thiolate ligand in such a manner that they form S-Au-S-Au-S “staple” motifs. This idea, which is also referred to as “divide and protect” approach, seems to stabilize these nanocluster structures, although the exact mechanism of their formation is not clear yet. [70] In all of the nanocluster structures, the metal core appears to be intact and behave like a “super atom”. The main difference between the gas phase nanoclusters and the solution phase nanoclusters is the presence of a monolayer for solution phase ligand protected nanoclusters. However, the metal core of a monolayer protected nanocluster seems to follow the same electronic shell closing expected for gas phase nanoclusters. This presented a great opportunity for spectroscopists to study the optical properties of these “super atoms” or “magic clusters” in the condensed phase. During the last decade, using ultrafast linear and nonlinear spectroscopy, our group was able to elucidate the unique effects that occur at the metal-to-insulator transition for gold and silver monolayer protected clusters in the condensed phase. [20, 21, 23, 24, 71- 79]

1.5 Optical investigations of quantum confinement in condensed phase using noble metal nanoclusters

Due to the high chemical stability of gold and silver monolayer protected clusters, they are good candidates for interrogation of quantum confinement using optical spectroscopy that can also be used in subsequent applications. [43, 68, 79] Linear and nonlinear optical spectroscopy of quantum confined materials can reveal many intricate properties unique to quantum confinement. For example, gold nanoparticles (with diameters greater than 2 nm) show a surface plasmon resonance (SPR) absorption peak at ~520 nm which may redshift as one increases the particle diameter. The SPR peak in the optical absorption spectrum is absent in quantum confined nanoclusters. [19, 77] This is due to the molecule-like band gap separation and formation of discrete energy levels for quantum clusters (as depicted in section 1.1) that prevents/dampens the collective oscillation of plasmon polaritons. In this section, I discuss various optical techniques that have been used and that can be utilized for investigation of quantum confinement. For detailed descriptions of the spectroscopic and microscopic techniques the reader is referred to the Chapter 5 of this dissertation.

Steady state emission of monolayer protected gold nanoclusters demonstrates a clear contrast to their bulk counterparts. For example, the fluorescence quantum yield of quantum confined gold nanoclusters [80] is 6 orders of magnitude higher than bulk gold, [81] and about 2 orders of magnitude higher than plasmonic nanoparticles. [82, 83] This enhancement in emission can also be attributed to the presence of discrete energy levels reducing the possible nonradiative pathways available to lose excitation energy of a nanocluster compared to their larger counterparts (nanoparticles and bulk gold). In chapter 3 of this dissertation, I discuss the effects of disassembly of Au_{25} nanoclusters in solution causing the emissive densities of states to reduce resulting in a narrowing of the emission spectrum. Interestingly, the steady state absorption of the 13-atom icosahedral core remains unaltered upon disassembly indicating quantum confinement of the super atom core from the surrounding environment.

Similarly, one can use the two-photon absorption cross section of a material as a measure the speed of excitation delocalization and the symmetry of the excited state. [84- 87] Two-photon absorption is a third-order nonlinear optical process which involves the simultaneous absorption of two photons. Therefore, two-photon absorption and its subsequent emission intensity is proportional to the square of the incident intensity of light. From the previous studies conducted in our group we observed that the per-atom two-photon cross section is much higher for quantum nanoclusters compared to gold nanoparticles. And the highest per-atom cross section was observed for Au_{25} nanoclusters, the smallest nanocluster studied in that investigation. [24] In chapter 3 of this dissertation, I discuss the interrogation of the two-photon absorption properties of isolated single Au_{25} nanoclusters on a solid substrate that reveal interesting quantum confinement effects when studied in the absence of ensemble effects and aggregation using high resolution near-field scanning optical microscopy (NSOM). [88- 95] Also, in chapter 2, I discuss a study on the bright two-photon emission from DNA templated Ag nanoclusters indicating enhancement in emission upon quantum confinement of the cluster.

Time resolved fluorescence emission can also reveal many details of an emissive excited state. Using a fluorescence up conversion technique, Yau *et al* had demonstrated a clear distinction between gold nanoparticles and nanoclusters. [77] Due to fast electron-phonon scattering events in gold nanoparticles, the emissive excited states appear to be significantly shorter lived compared to those of gold nanoclusters. On the contrary, gold quantum confined nanoclusters tend to have longer emission lifetimes. In chapter 2, I discuss the effects of DNA capping on the ultrafast relaxation of Ag nanocluster excited states, revealing quantum confinement effects when the ligand protection is introduced.

Ultrafast transient absorption can also reveal interesting properties of quantum confined systems. [23, 77] In a transient absorption experiment an initial pulse excites the chromophore to an excited state, then a second pulse probes the excited state. Depending on the probe wavelength used, one may be able to observe the dynamics of the excited state at a wide range of transient absorption wavelengths or an intensity change of a single probe wavelength. In chapter 2, I describe the transient absorption studies that were carried out on DNA templated Ag nanoclusters revealing the behavior of “molecule-like” state formation upon enclosing/confinement of a Ag nanocluster.

Single chromophore investigations eliminate the ensemble averaging and inter-nanocluster coupling effects that could otherwise hide the effects of quantum confinement. [96] Therefore, in order to learn more fundamental details of electronic states and quantum confinement of super atom clusters, I carried out ultrafast nonlinear microscopy of single nanoclusters. The interrogations reveal quantum confinements effects for isolated elemental nanoclusters that were not reported until now. Chapter 3 discusses the synthesis, isolation and spectroscopy/microscopy of monolayer protected Au_{25} nanoclusters.

In summary, linear and nonlinear spectroscopy of nanoclusters can reveal many details of their electronic states and their ultrafast dynamics that can unveil unique effects present in elemental super atom clusters. Therefore, the optical investigations and single nanocluster microscopy can reveal new nanocluster physics and properties that can be used in exciting potential applications such as biological imaging/sensing, molecular computers and optoelectronics. [26, 97- 108]

1.6 Dissertation outline

In this dissertation work I aimed to find answers to the following questions. Do DNA-templated Ag nanoclusters show effects of quantum confinement when studied in solution phase ensembles? How do the optical properties of quantum confined nanoclusters change when single nanoclusters are removed from the solution ensembles and studied on solid substrate? How does the isolation of nanoclusters from their aggregates and the ensuing removal of inter-nanocluster interactions affect their two-photon absorption cross sections? On a different set of experiments, I studied small organic molecules for potential photovoltaic applications. The main goal of that interrogation was to explore if it is possible to find a small organic chromophore (as opposed to a polymer) that give high yields for ultrafast *intramolecular* singlet exciton fission. If such molecules can be found, their triplet exciton extraction at a single molecular scale could eliminate the requirement of inter-chromophore coupling that is required for high efficiency *intermolecular* singlet exciton fission. In effect, this could potentially result in molecular scale tuning of solar cell efficiency to obtain high efficiency organic photovoltaic (OPV) devices.

The remainder of this dissertation is organized as follows. In chapter 2, I discuss investigations that were carried out on DNA templated Ag nanoclusters. Their quantum confined properties investigated through steady state absorption and emission, two-photon absorption, time-resolved fluorescence and ultrafast transient absorption are discussed. The work discussed were published in the journal *Nanoscale.* In chapter 3, I discuss linear and nonlinear optical interrogation of stable monodisperse Au_{25} nanoclusters. The synthesis of monodisperse Au_{25} nanoclusters using a well refined technique for atomically precise nanocluster synthesis is used. Following their synthesis, Au_{25} nanoclusters are disassembled in solution phase which reveals quantum confined properties of elemental super atom clusters. Then, their subsequent deposition on solid substrate and confirmation of single nanoclusters using STEM are discussed. At much lower concentrations (~85 times) than that was used for STEM, Au_{25} nanoclusters are deposited on the substrates and investigated using two-photon excited near-field scanning optical microscopy (TPEF NSOM). Subsequently, an enhancement in two-photon absorption cross section of Au_{25} single nanoclusters when removed from solid state aggregates are discussed. This serves as the first report of optical investigations of quantum confinement in single elemental nanoclusters on solid substrates. The work discussed is published in the *Journal of the American Chemical Society* as a full article. In Chapter 4, I switch gears to discuss the linear and nonlinear spectroscopy of a quinoidal bithiophene molecule that revealed highly efficient intramolecular singlet exciton fission with singlet to triplet conversion efficiency of ~180%. Two-color nonlinear transmission experiments, triplet sensitization time resolved experiments, time correlated single photon counting experiments revealing delayed fluorescence, concentration dependent steady state absorption, solvent polarity dependent nonlinear transmission experiments, time resolved fluorescence up conversion and degenerate and two-color pump-probe experiments all reveal the ultrafast formation of a triplets via an intramolecular singlet fission process. This work is published in the *Journal of Physical Chemistry Letters*. In Chapter 5, I summarize the insights gained from the investigations of quantum confined metal nanoclusters and the quinoidal bithiophene molecule for intramolecular singlet exciton fission. Also, the future directions of the research projects outlined above will be discussed. Chapter 5 includes detailed experimental techniques utilized in TPEF NSOM, linear and nonlinear spectroscopic techniques used for the investigations of noble metal monolayer protected nanoclusters and quinoidal bithiophenes. Synthesis procedure of monodisperse Au_{25} elemental clusters are also discussed.

Since the observations of Faraday in 1847, gold nanoparticle investigations had captured many researchers' attention. However, Frohlich's and Kubo's work has clearly shown that there will be a new dimension for elemental materials that will possess quantum confinement properties with unique behavior compared to the metal nanoparticles Faraday had observed, bulk metals or molecules. However, until the optimization of atomically precise nanocluster synthesis, these elemental nanocluster materials could not be studied with confidence. During the last two decades, investigations of quantum confined materials received ever increasing attention from the scientific community due to the ability to synthesize stable quantum clusters with exactly known composition and structure. From our optical investigations it is clear that quantum confined nanoclusters made from elements possess properties that deviate from their bulk metal counterparts, metal nanoparticles and elemental atoms/molecules, revealing a new form of matter. Therefore, the quantum confined nanocluster studies reveal a new dimension that could be added to the periodic table introducing a new degree of freedom to material sciences.

1.7 References

1. Pauling, L. Nature of the chemical bond. 1st ed., Cornell University Press, Ithaca, N. Y., (1939).
2. Hazlehurst, T. H. Quantum numbers and the periodic table. *J. Chem. Educ.* 580-581 (1941).
3. Mendeleev, D. I. *J. Russ. Chem. Soc.*, **1** (2-3), 35, 60 (1869).
4. "Classifying: Calm The Chaos Quiz". *Chemistryland.com*. N.p., 2016. Web. 19 Dec. 2016.
5. Foster, P. J., Leckenby, R. E., Robbins, E. J. The ionization potentials of clustered alkali metal atoms. *J. Phys. B At. Molec. Phys.* **2,** 478-483 (1969).
6. Sattler, K., Muhlbach, J. and Recknagel, E. Generation of metal clusters from 2 to 500 atoms. *Phys. Rev. Lett.* **45,** 821-824 (1980).
7. Harris, I. A., Kidwell, R. S. and Northby, J. A. Structure of charged Argon clusters formed in a free jet expansion. *Phys. Rev. Lett.* **53,** 2390-2393 (1984).
8. Brennan, J. G., Siegrist, T., Stuczynski, S. M., and Steigerwald, M. L. The transition from molecules to solids: Molecular syntheses of $Ni_9Te_6(PEt_3)_8$, $Ni_{20}Te_{18}(Pet_3)_{12}$, and NiTe. *J. Am. Chem. Soc.* **111,** 9240-9241 (1989).
9. Klabunde, K. J. Nanoscale materials in chemistry. 1st ed., John Wiley & Sons, Inc., New York, N. Y. (2001).
10. Roy, X., *et al* Nanoscale atoms in solid-state chemistry. *Science* **341,** 157-160 (2013).
11. Jadzinsky, P. D. *et al*. Structure of a thiol monolayer-protected gold nanoparticle at 1.1 Å resolution. *Science* **318,** 430-433 (2007).
12. Li, Z. Y. *et al*. Three-dimensional atomic-scale structure of size-selected gold nanoclusters. *Nature.* **451,** 46-48 (2008).
13. Zhu, M. *et al*. Correlating the crystal structure of a thiol-protected Au_{25} cluster and optical properties. *J. Am. Chem. Soc.* **130,** 5883-5885 (2008).
14. Heaven, M. W. *et al*. Crystal structure of the gold nanoparticle $N(C_8H_{17})_4][Au_{25}(SCH_2CH_2Ph)_{18}]$. *J. Am. Chem. Soc.* **130,** 3754-3755 (2008).
15. Desireddy, A. *et al*. Ultrastable silver nanoparticles. *Nature.* **501,** 399-402 (2013).
16. Yang, H. *et al*. All-thiol-stabilized Ag_{44} and $Au_{12}Ag_{32}$ nanoparticles with single crystal structures. *Nat. Commun.* **4,** 2422 (2013).

17. Azubel, M. *et al*. Electron microscopy of gold nanoparticles at atomic resolution. *Science* **345,** 909-912 (2014).
18. Khanna, S. N. and Castleman, A. W., Jr. Clusters, superatoms, and building blocks of new materials. *J. Phys. Chem. C* **113,** 2664-2675 (2009).
19. Kreibig, U. and Vollmer, M. Optical Properties of metal clusters. Springer-Verlag, Berlin, Germany (1995).
20. Yau, S. H., Varnavski, O. and Goodson III, T. An ultrafast look at Au nanoclusters. *Acc. Chem. Res.* **46,** 1506-1516 (2013).
21. Varnavski, O. *et al*. Critical size for the quantum confinement in optically excited gold clusters. *J. Am. Chem. Soc.* **132,** 16-17 (2010).
22. Yuan, X. *et al*. Highly luminescent silver nanoclusters with tunable emissions: cyclic reduction-decomposition synthesis and antimicrobial properties. *NPG Asia Materials* **5,** e39 (2013).
23. Yau, S. H., *et al*. Bright two-photon emission and ultrafast relaxation dynamics in a DNA-templated nanocluster investigated by ultrafast spectroscopy. *Nanoscale* **4,** 4247-4254 (2012).
24. Ramakrishna, G. *et al*. Quantum-sized gold nanoclusters as efficient two-photon absorbers. *J. Am. Chem. Soc.* **130,** 5032-5033 (2008).
25. Zhu, M. *et al*. Reversible switching of magnetism in thiolate-protected Au_{25} superatoms. *J. Am. Chem. Soc.* **131,** 2490-2492 (2009).
26. Chen, S. *et al*. Gold nanoelectrodes of varied size: Transition to molecule-like charging. *Science* **280,** 2098-2101 (1998).
27. Lopez-Acevedo, O., Kacprzak, K. A., Akola, J. & Hakkinen, H., Quantum size effects in ambient CO oxidation catalyzed by ligand-protected gold clusters, *Nature Chem.* **2,** 329-334 (2010).
28. Novoselov, K. S. *et al.* Two dimensional atomic crystals. *Proc. Natl. Acad. Sci.* **102,** 10451-10453 (2005).
29. Frohlich, H. The specific heat of the electrons of small metal particles at low temperatures. *Physica IV.* **5,** 406-412 (1937).
30. Kubo, R. Electronic properties of metallic fine particles. *J. Phys. Soc. Japan* **17,** 975-986 (1962).

31. Rao, C. N. R., Kulkarni, G. U, Thomas, P. J. and Edwards, P. P. Size-dependent chemistry: Properties of nanocrystals. *Chem. Eur. J.* **8,** 28-35 (2002).

32. De Heer, W. A., Knight, W. D., Chou, M. Y. and Cohen, M. L. Electronic shell structure and metal clusters. *Solid State Physics* **40,** 93-181 (1987).

33. Ekardt, W. Collective multipole excitations in small metal particles: Critical angular momentum l^{cr} for the existences of collective surface modes. *Phys. Rev. B* **32,**1961-1970 (1985).

34. Beck, D. E. Self-consistent calculations of eigenfrequencies for the electronic excitations in small jellium spheres. *Phys. Rev. B* **35,**7325-7333 (1987).

35. Bonacic-Koutecky, V., Fantucci, J. P. and Koutecky, J. Quantum chemistry of small clusters of elements of group Ia, Ib, and IIa: Fundamental concepts, predictions, and interpretation of experiments. *Chem. Rev. B* **91,**1035-1108 (1991).

36. Knight, W. D. *et al* Electronic shell structure and abundances of sodium clusters. *Phys. Rev. Lett.* **52,** 2141-2143 (1984).

37. Clemenger, K. Ellipsoidal shell structure in free-electron metal clusters. *Phys. Rev. B* **32,** 2141-2143 (1985).

38. Brust, M., Walker, M., Bethell, D., Schiffrin, D. J., Whyman, R. Synthesis of thiol-derivatized gold nanoparticles in two-phase liquid-liquid system. *J. Chem. Soc.* 801- 802 (1994).

39. Brust, M., Fink, J., Bethell, D., Schiffrin, D., Kiely, C. Synthesis and functionalization of gold nanoparticles. *J. Chem. Soc.* 1655-1656 (1995).

40. Dubois, L. H., Nuzzo, R. G. Synthesis, structure and properties of model organic surfaces *Annu. Rev. Phys. Chem.* **43,** 437-463 (1992).

41. Bain, C. D., Evall, J., Whitesides, G. M. Formation of monolayers by coadsportion of thiols on gold: Variation in the head group, tail group and solvent. *J. Am. Chem. Soc.* **111,** 7155-7164 (1989).

42. Wu, Z., Shuhan, J. & Jin, R. One-pot synthesis of atomically monodisperse, thiol-functionalized Au_{25} nanoclusters. *J. Mater. Chem.* **130,** 622-626 (2009).

43. Qian, H., Zhu, M., Wu, Z. & Jin, R. Quantum sized gold nanoclusters with atomic precision. *Acc. Chem. Res.* **45,** 1470-1479 (2012).

44. Kreibig, U. and Zacharias, P. Surface plasma resonances in small spherical silver and gold particles. *Zeitschrift fur Physik* **231,** 128–143 (1970).

45. Zsigmondy, R. *Colloids and the Ultramicroscope: A Manual of Colloid Chemistry and Ultramicroscopy*; Wiley: New York, 1909.

46. Murphy, C. J., Gole, A. M., Hunyadi, S. E. and Orendorff, C. J. One-dimensional colloidal gold and silver nanostructures. *Inorganic Chemistry* **45,** 7544–7554 (2006).

47. Lang, H. F., May, R. A., Iversen, B. L. and Chandler, B. D. Dendrimer-encapsulated nanoparticle precursors to supported platinum catalysts. *J. Am.Chem. Soc* **125,** 14832–14836 (2003).

48. Burda, C., Chen, X., Narayanan, R. and El-Sayed, M. A. Chemistry and properties of nanocrystals of different shapes. *Chem. Rev.* **105,** 1025–102 (2005).

49. Lucky, S. S., Soo, K. C. and Zhang, Y. Nanoparticles in photodynamic therapy. *Chem. Rev.* **115,** 1990–2042 (2015).

50. Faraday, M. Experimental relations of gold to light. *Phil. Trans. R. Soc. Lond.* **147,** 145-181 (1847).

51. Turkevich, J., Stevenson, P. C., Hillier, J. A study of the nucleation and growth process in the synthesis of colloidal gold. *Discussions of the Faraday Society.* 55-75 (1951).

52. Frens, G. Controlled nucleation for regulation of particle size in monodisperse gold suspension. *Nature Physical Science.* **241,** 20-22 (1973).

53. Lal, S, Clare, S. E. and Halas, N. J. Nanoshell-enabled photothermal cancer therapy: Impending clinical impact. *Acc. Chem. Res.* **41,** 1842-1851 (2008).

54. Catchpole, K. R. and Polman, A. Design principles for particle plasmon enahcned selar cells. *Appl. Phys. Lett.* **93,** 191113 (2008).

55. Mie, G. Beiträge zur Optik trüber Medien, speziell kolloidaler Metallösungen. *Annalen der Physik* **330,** 377–445 (1908).

56. Schmid, G., Pfeil, R., Boese, R., Bandermann, F., Meyer, S., Calis, G. H. M. and Vandervelden, W. A. Au_{55} $[P(C_6H_5)_3]_{12}Cl_6$ - A gold cluster of an exceptional size. *Chemische Berichte-Recueil* **114,** 3634–3642 (1981).

57. Brust, M., Fink, J., Bethell, D., Schiffrin, D. J., and Kiely, C. Synthesis and reactions of functionalized gold nanoparticles. *J. Chem. Soc. Chem. Commun.* 1655-1656 (1995).

58. Negishi, Y., Takasugi, Y., Sato, S., Yao, H., Kimura, K., and Tsukuda, T. Magic numbered Au(n) clusters protected by glutathione monolayers (n = 18, 21, 25, 28, 32, 39): Isolation and spectroscopic characterization. *J. Am. Chem. Soc.* **126,** 6518–6519 (2004).

59. Lopez-Acevedo, O., Tsunoyama, H., Tsukuda, T., Häkkinen, H. and Aikens, C. M. Chirality and electronic structure of the thiolate-protected Au_{38} nanocluster. *J. Am. Chem. Soc.* **132,** 8210–8218 (2010).

60. Shichibu, Y., Negishi, Y., Tsukuda, T. and Teranishi, T. Large-scale synthesis of thiolated Au_{25} clusters via ligand exchange reactions of phosphine-stabilized Au_{11} clusters. *J. Am. Chem. Soc.* **127,** 13464–13465 (2005).

61. Ackerson, C. J., Jadzinsky, P. D. and Kornberg, R. D. Thiolate ligands for synthesis of water-soluble gold clusters. *J. Am. Chem. Soc.* **127,** 6550–6551 (2005).

62. Wu, Z., Suhan, J. and Jin, R. One-pot synthesis of atomically monodisperse, thiol functionalized Au_{25} nanoclusters. *J. Mater. Chem.* **19,** 622 (2009).

63. Kumar, S., Bolan, M. D. and Bigioni, T. P. Glutathione-stabilized magic-number silver cluster compounds. *J. Am. Chem. Soc.* **132,** 13141–13143 (2010).

64. Schaaff, T. G., Knight, G., Shafigullin, M. N., Borkman, R. F. and Whetten, R. L. Isolation and selected properties of a 10.4 kDa Gold: Glutathione cluster compound. *J. Phys. Chem. B* **102,** 10643–10646 (1998).

65. Lopez-Acevedo, O., Akola, J., Whetten, R. L., Gronbeck, H. and Hakkinen, H. Structure and Bonding in the Ubiquitous Icosahedral Metallic Gold Cluster $Au\text{-}_{144}(SR)_{60}$. *J. Phys. Chem. C* **113,** 5035–5038 (2009).

66. Templeton, A. C., Wuelfing, W. P. and Murray, R. W. Monolayer-Protected Cluster Molecules. *Acc. Chem. Res.* **33,** 27-36 (2000).

67. Hicks, J. F.; Miles, D. T.; Murray, R. W. Quantized Double-Layer Charging of Highly Monodisperse Metal Nanoparticles. *J. Am. Chem. Soc.* **124,** 13322–13328 (2002).

68. Jin, R. Super robust nanoparticles for biology and biomedicine. *Angew. Chem. Int. Ed.* **47,** 6750–6753 (2008).

69. Schmid, G. The relevance of shape and size of Au_{55} clusters. *Chem. Soc. Rev.* **37,** 1909–1930 (2008).

70. Hakkinen, H., Walter, M. and Gronbeck, H. Divide and protect: Capping gold nanoclusters with molecular gold-thiolate rings. *J. Phys. Chem. B* **110,** 9927–9931 (2006).

71. Varnavski, O., Ispasoiu, R. G., Balogh, L., Tomalia, D. and Goodson, T. Ultrafast time resolved photoluminescence from novel metal–dendrimer nanocomposites. *J. Chem. Phys.* **114,** 1962 (2001).

72. Ispasoiu, R. G., Balogh, L., Varnavski, O. P., Tomalia, D. A. and Goodson, T. Large optical limiting from novel metal-dendrimer nanocomposite materials. *J. Am. Chem. Soc.* **122,** 11005–11006 (2000).

73. Goodson, T., Varnavski, O. and Wang, Y. Optical properties and applications of dendrimer-metal nanocomposites. *Int. Rev. Phys. Chem.* **23,** 109–150 (2004).

74. Ramakrishna, G., Dai, Q., Zou, J., Huo, Q. and Goodson III, T. Interparticle electromagnetic coupling in assembled gold-necklace nanoparticles. *J. Am. Chem. Soc.* **129,** 1848–1849 (2007).

75. Varnavski, O., Ramakrishna, G., Kim, J., Lee, D. and Goodson, T. Optically excited acoustic vibrations in quantum-sized monolayer-protected gold clusters. *ACS Nano* **4,** 3406–3412 (2010).

76. Devadas, M. S., Kim, J., Sinn, E., Lee, D., Goodson, T. and Ramakrishna, G. Unique Ultrafast Visible Luminescence in Monolayer-Protected Au_{25} Clusters. *J. Phys. Chem. C* **114,** 22417–22423 (2010).

77. Yau, S. H., Varnavski, O., Gilbertson, J. D., Chandler, B., Ramakrishna, G. and Goodson, T. Ultrafast Optical Study of Small Gold Monolayer Protected Clusters: A Closer Look at Emission. *J. Phys. Chem. C* **114,** 15979–15985 (2010).

78. Ho Wu, R., Yau, S. H. and Goodson III, T. Linear and nonlinear optical properties of monolayer protected gold nanocluster films. *ACS Nano* **10,** 562-572 (2016).

79. Negishi, Y. *et al*. Origin of magic stability of thiolated gold clusters: A case study on $Au_{25}(SC_6H_{13})_{18}$. *J. Am. Chem. Soc.* **129,** 11322-11323 (2008).

80. Wu, Z. & Jin, R. On the ligand's role in the fluorescence of gold nanoclusters. *Nano Lett.* **10,** 2568-2573 (2010).

81. Mooradian, A., Photoluminescence of metals. *Phys. Rev. Lett.* **22,** 185 (1969).

82. Dulkeith, E. *et al*. Plasmon emission in photoexcited gold nanoparticles. *Phys. Rev. B* **70,** 205424 (2004).

83. Goodson III, T., Varnavski, O. & Wang, Y. Optical properties and applications of dendrimer-metal nanocomposites. *Int. Rev. Phys. Chem.* **23,** 109-150 (2004).

84. Goeppert-Mayer, M. Elementary processes with two quantum transitions. *Ann. Phys. (Berlin)* **9,** 273-294 (1931).

85. Mahan, G. D. Theory of two-photon spectroscopy in solids. *Phys. Rev.* **170,** 825-838 (1978).

86. Bonin, K. D. and McIlrath, T. J. Two-photon electric dipole selection rules. *J. Opt. Soc. Am. B* **1,** 52-55 (1984).

87. Wang, C-K., Mecak, Y. L. and Agren, H. Effects of pi centers and symmetry on two-photon absorption cross sections of organic chromophores. *J. Chem. Phys.* **114,** 9813-9820 (2001).

88. Betzig, E. & Chichester, R. J. Single molecules observed by near-field scanning optical microscopy. *Science*. **262,** 1422-1425. (1993).

89. Betzig, E. & Trautman, J. K. Near-field optics: Microscopy, spectroscopy, and surface modification beyond the diffraction limit. *Science*. **257,** 189-195 (1992).

90. Xie, X. S. & Dunn, R. C. Probing single molecule dynamics. *Science* **265,** 361-364 (1994).

91. Trautman, J. K., Macklin, J. J., Brus, L. E. & Betzig, E. Near-field spectroscopy of single molecules at room temperature. *Nature* **369,** 40-42. (1994).

92. Betzig, E., Trautman, J. K., Harris, T. D., Weiner, J. S. & Kostelak, R. L. Breaking the diffraction barrier: Optical microscopy on a nanometric scale. *Science* **251,** 1468-1470 (1991).

93. Betzig, E., Lewsi, A., Harootunian, A., Isaacson, M & Kratschmer, E. Near-field scanning optical microscopy (NSOM): Development and biophysical applications. *Biophys. J.* **49,** 269-279 (1986).

94. Sanchez, E. J., Novotny, L. & Xie, X. S. Near-field fluorescence microscopy based on two-photon excitation with metal tips. *Phys. Rev. Lett.* **82,** 4014-4017 (1999).

95. Lewis, M. K., Wolanin, P., Gafni, A. & Steel, D. G. Near-field scanning optical microscopy of single molecules by femtosecond two-photon excitation. *Opt. Lett.* **23,** 1111-1113 (1998).

96. Moerner, W. E. & Fromm, D. P. Methods of single molecule fluorescence spectroscopy and microscopy. *Review of Scientific Instruments* **74,** 3597-3619 (2003).

97. Drobizhev, M., Makarov, N. S., Hughes, T. & Rebane, A. Resonance enhancement of two-photon absorption in fluorescent proteins. *J. Phys. Chem. B* **111,** 14501-14504 (2007).

98. Drobizhev, M., Makarov, N. S., Tillo, S. E., Hughes, T. & Rebane, A. Two-photon absorption properties of fluorescent proteins. *Nature Methods* **8,** 393-399 (2011).
99. Ponder, M. & Mathies, R. Excited-state polarizabilities and dipole moments of Diphenylpolyenes and Retinal. *J. Phys. Chem.* **87,** 5090-5098 (1983).
100. Drobizhev, M., Scott, J. N., Callis, P. R. & Rebane, A. All-optical sensing of the components of the internal local electric field in proteins. *IEEE Photonics J.* **4,** 1996-2001 (2012).
101. Kaplan, A. E. and Volkov, S. N. Nanoscale stratification of local optical fields in low dimensional atomic lattices. *Phys. Rev. Lett.* **101,** 133902 (2008).
102. Bedeaux, D. and Bloembergen, N. On the relation between macroscopic and microscopic nonlinearities. *Opt. J. Eur. Opt. Soc. Part B* **69,** 57-66 (1973).
103. Dolgaleva, K., Boyd, R. W. and Sipe, J. E. Cascaded nonlinearity caused by local field effects in the two-level atom. *Phys. Rev. A* **76,** 063806 (2007).
104. Baev, A., Autschbach, J., Boyd, R. W. Prasad, P. N. Microscopic cascading of second order molecular nonlinearity: new design principles for enhancing third order nonlinearity. *Opt. Express* **18,** 8713-8721 (2010).
105. Dolgaleva, K. and Boyd, R. W. Local field effects in nanostructured photonic materials. *Advances in Optics and Photonics* **4,** 1-77 (2012).
106. Huang, X., Atwood, C. S., Moir, R. D., Hartshorn, M. A., Vonsattel, J.-P., Tanzi, R. E., & Bush, A. I. Zinc-induced Alzhemier's A-*beta*-140 Aggregation is Mediated by Conformational factors. *J. Biol. Chem.* **272,** 26464-26470 (1997).
107. Atwood, C. S., Moir, R. D., Huang, X., Scarpa, R. C., Bacarra, N. M., Romano, D. M., Hartshorn, M. A., J.-P., Tanzi, R. E., & Bush, A. I. Dramatic Aggregation of Alzheimer A-*beta* by Cu(II) is Induced by Conditions Representing Physiological Acidosis. *J. Biol. Chem.* **273,** 12817-12826 (1998).
108. Curtain, C. C., Ali, F., Volitakis, I., Cherny, R. A., Norton, R. S., Beyreuther, K., Barrow, C, J., Masters, C. L., Bush, A. I., & Barnham, K. J. Alzheimer's disease Amyloid-*beta* Binds Copper and Zinc to generate an Allosterically Ordered Membrane Penetrating Structure Containing Superoxide Dismutase-like Subunits. *J. Biol. Chem.* **276,** 20466-20473 (2001).

Chapter 2

Investigating Quantum Confined DNA-templated Ag Nanoclusters in Solution Phase using Linear and Nonlinear Spectroscopy

2.1 Original Publication Information

This chapter primarily contains material that was originally published as the following document.

“Bright two-photon emission and ultra-fast relaxation dynamics in a DNA-templated nanocluster investigated by ultra-fast spectroscopy”

Sung Hei Yau, Neranga Abeyasinghe, Meghan Orr, Leslie Upton, Oleg Varnavski, James H. Werner, Hsin-Chih Yeh, Jaswinder Sharma, Andrew P. Shreve, Jennifer S. Martinez & Theodore Goodson III

Nanoscale **2012**, 4, 4247-4254.

In this chapter, I describe the experimental outcomes and the scientific insights we have been able to gain through the investigations of DNA templated Ag elemental quantum clusters.

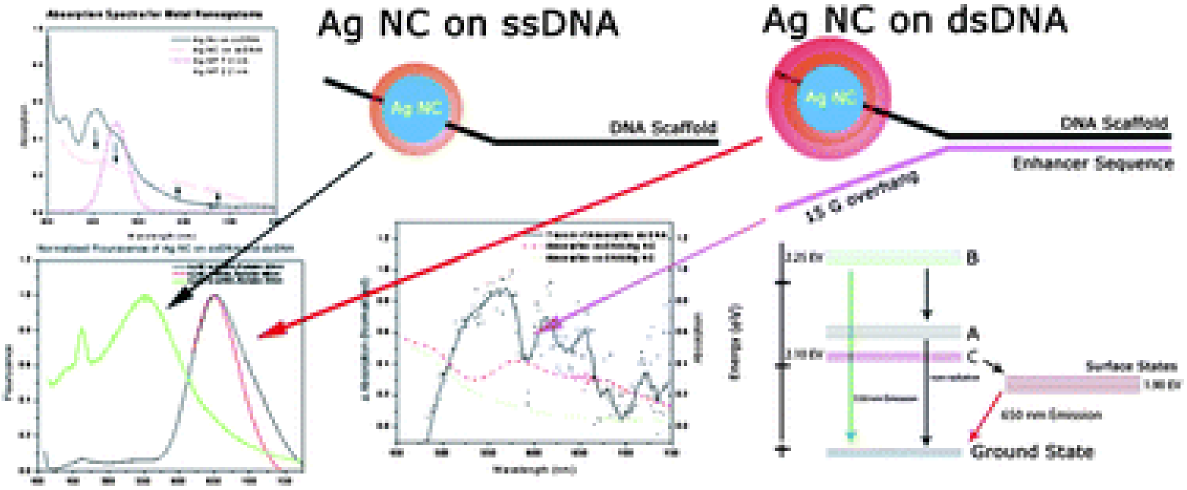

Figure 2-1 Table of contents image as published for DNA-templated Ag NCs.

2.2 Introduction

Previous spectroscopic investigations of Au nanoclusters in the solution phase revealed unique quantum confinement effects. [1-12] The spectroscopic distinction observed between the nanoparticles (> 2 nm) and quantum clusters (< 2 nm) is significant. [1, 2, 4, 9, 11] Steady state absorption for Au nanoparticles show the surface plasmon resonance (SPR) band at ~520 nm which is absent in the absorption spectra of Au nanoclusters. [1, 11] Quantum confined Au nanoclusters in solution phase revealed extremely large per-atom two photon absorption cross sections for the smallest nanoclusters studied (~17000 GM for Au_{25}). [4, 12] Additionally, time resolved fluorescence up conversion studies revealed that the Au nanoclusters tend to show relatively longer fluorescence emission lifetimes compared to Au nanoparticles. [1, 11] As a result of these long lived emissive excited states the quantum confined nanoclusters tend to have about 6 orders of magnitude larger fluorescence quantum yields [13] compared to the bulk gold [14] and about 2 orders of magnitude larger quantum yields compared to gold nanoparticles. [7, 15] All of the above observations are consistent with the energy band separation for quantum confined nanoclusters (as shown in section 1.1) resulting in discrete densities of electronic states (DOS). [16-23] Additionally, degenerate pump probe experiments for Au nanoclusters in the solution phase have shown an oscillating transient absorption features indicating quantum confinement effects. [2, 9] For 3 nm diameter Au nanoparticles, the oscillatory transient profile was absent indicating a clear distinction between the nanoparticles and nanoclusters. The spectroscopic signatures observed in solution-phase Au nanocluster investigations proves the strength of linear and nonlinear spectroscopic characterization of quantum confinement of super atom clusters to reveal their "molecular-like" behavior. Therefore, Au NCs can be considered to obey the "superatom" model where the quantum confined stable metal nanoclusters are formed. [24] Also, their relatively high emission quantum yields and large two-photon absorption cross sections can imply their potential future use in bioimaging/sensing, optoelectronics and molecular computing. [25-33]

An important question one may have is, do all metal nanoclusters show the same spectroscopic signatures under quantum confinement? To answer this question, we turn to silver nanoclusters which are composed of noble metal atoms similar to gold. The ability to contribute one valence electron for each atom of a silver nanocluster and similar Fermi energies as that of gold should ensure that magic number clusters of silver resemble the properties and geometries observed for gold. [16-19] In order to test this hypothesis, stable Ag nanocluster synthesis in the solution should be materialized. Recent advancements in silver nanocluster synthesis indicates that their spectroscopic investigations in high yield is possible. [34, 35]

In this work, we investigated Ag nanoclusters (NCs) that are stabilized by DNA and are also referred to as NanoCluster Beacons. [36-38] They have Ag NCs nested in single stranded DNA (ssDNA). While they are present in single strands they tend to be less emissive. When a complementary DNA strand form an enclosing around Ag NCs with the correct stabilizing sequence they tend to enhance the fluorescence emission. These double stranded DNA (dsDNA) templated Ag nanoclusters are good candidates to test the effects of nanocluster ligand stabilization effects on quantum confinement. They were reported to have a quantum yield of ~30% when stabilized with the correct DNA sequence. Therefore, DNA-templated nanoclusters serve as strong candidates for fundamental spectroscopic investigations as well as biological imaging applications.

Typical characterization of nanoclusters involves mass spectrometry and electron microscopy. [39- 41] For DNA-templated Ag nanoclusters, mass spectrometric characterization measures an average number of Ag atoms present in the nanocluster system. However, it does not reveal how many Ag atoms are present per Ag nanocluster. Therefore, Ag K-edge Extended X-ray Absorption Fine Structure (EXAFS) has been used to identify the Ag nanocluster sizes present and reveals how many metal-metal and metal-ligand bonds are present. [38] The bond distances observed were consistent with the bond distance found in Ag nanoclusters. While the exact composition is not clear, we can state that each nanocluster contained 8 to 20 Ag atoms. Therefore, our goal in these investigations are to investigate the quantum confinement from a qualitative standpoint to examine if Ag nanoclusters show the same general behavior that was shown by quantum confined Au nanoclusters in the condensed phase.

In the remainder of this chapter, I will be discussing experiments carried out in solution ensembles of DNA-templated Ag nanocluster systems and the ensuing insights of their quantum confinement. The steady state absorption and emission experiments were carried out on these DNA-templated Ag NCs. After demonstrating the clear difference between steady state spectra of ssDNA-Ag NCs and dsDNA-Ag NCs, I will move to two-photon absorption experiments that were carried out on dsDNA-Ag nanocluster systems indicating bright two-photon fluorescence. Femtosecond time-resolved transient absorption experiments also reveal the formation of a new bleach state for the dsDNA-Ag NCs indicating a clear effect of quantum confinement upon stabilization of the nanoclusters. Finally, I will discuss the long lived fluorescence up conversion results that are also indicative of the quantum confinement for dsDNA-Ag NCs.

2.3 Results and Discussion

For all of the experiments described below, the detailed experimental procedures are included in the Chapter 5.

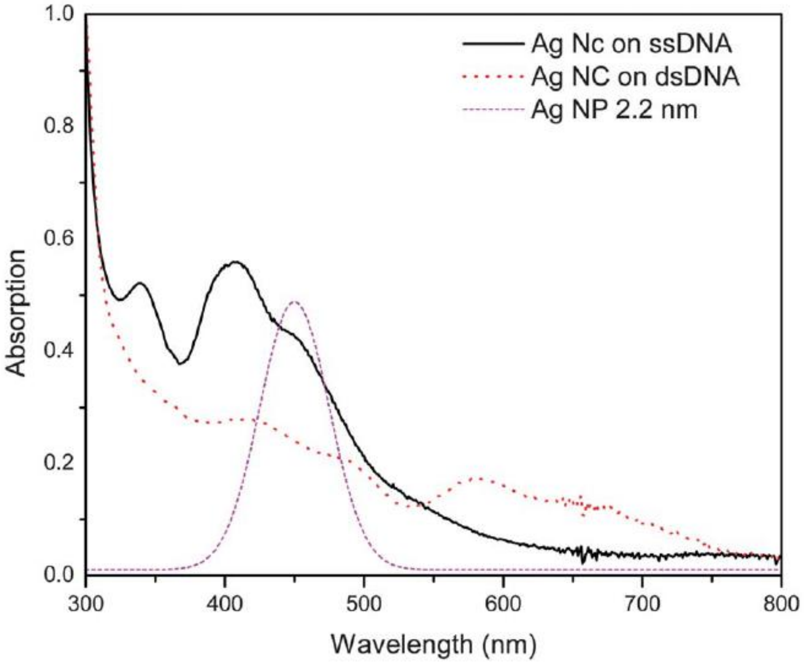

Figure 2-2 Steady state absorption spectra of DNA-templated Ag NCs and comparison with Ag nanoparticle steady state absorption

2.3.1 Steady state absorption

Steady state absorption spectra are shown in figure 2-2. As can be observed, the Ag nanoparticle (NP) surface plasmon resonance (SPR) at ~455 nm was modeled in order to compare it with the NC results. The ssDNA Ag NC seems to show a shoulder in the absorption spectrum that corresponds to the SPR peak for Ag NPs. [42] Since pure DNA would not absorb above 300 nm, an absorption at 455 nm by DNA is highly unlikely. Also, when dsDNA is added, the Ag NCs no longer show any sign of SPR (which may rule out the presence of Ag NPs in the solution). Rather, the steady state absorption spectrum changes to give several distinct absorption peaks at 580 nm and 670 nm that were absent before. This is an indication of quantum confinement effects in Ag NCs due to the presence of discrete transitions indicating that the dsDNA-Ag NCs show molecular-like behavior.

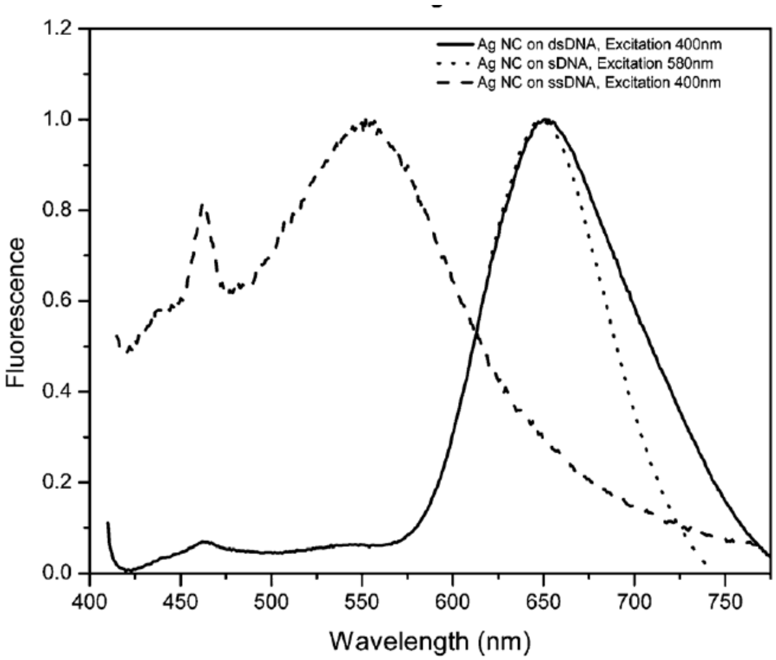

Figure 2-3 Steady state emission spectra of DNA-templated Ag NCs

2.3.2 Steady state emission and excitation spectra

Normalized steady state emission spectra for Ag NCs on dsDNA and ssDNA are compared. As depicted in figure 2-3, when excited at 400 nm, ssDNA-Ag NCs show an emission peak at 550 nm whereas for dsDNA-Ag NCs the ~550 nm peak is relatively weakened compared to a new emission peak that appears at 650 nm. The peak observed at 470 nm under 580 nm excitation is the Raman signal from the solvent. The quantum efficiency of 650 nm emission for dsDNA templated Ag NCs were previously reported to be ~30%. Also, the 650 nm emission observed for dsDNA-Ag NCs are 8 times stronger than the 550 nm emission observed for ssDNA-Ag NCs. As depicted in figure 2-4, when an excitation spectrum was taken for 650 nm emission, one can easily see that the excitation maximum occurs at 580 nm. This is consistent with the formation of a new state for dsDNA-Ag NCs steady state absorption at 580 nm.

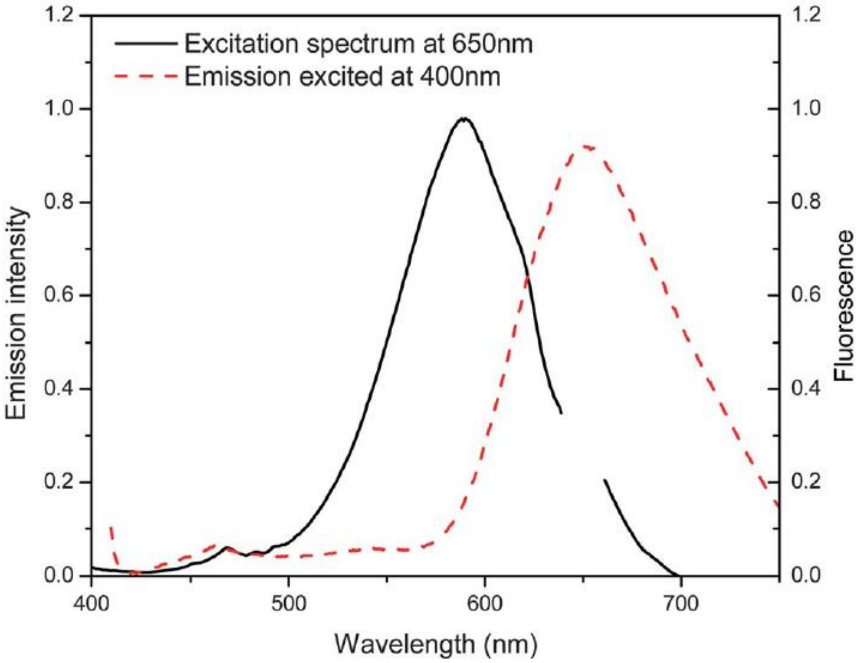

Figure 2-4 Steady state excitation and emission spectra of dsDNA-templated Ag NCs

2.3.3 Two-photon absorption

We conducted two-photon absorption (TPA) at 800 nm excitation for DNA template Ag NCs in the solution phase. For the excitation, an 80 MHz laser with ~ 110 fs pulses were used (see

Chapter 5 for more details of the experiments). The two-photon excited fluorescence was observed at 630 nm. The two-photon fluorescence spectra and power dependent two-photon plot for dsDNA-Ag NCs are shown in figure 2-5. As can be seen, a slope of 2 for log-log plot indicates two-photon absorption at 800 nm excitation. The calculated two-photon absorption cross section

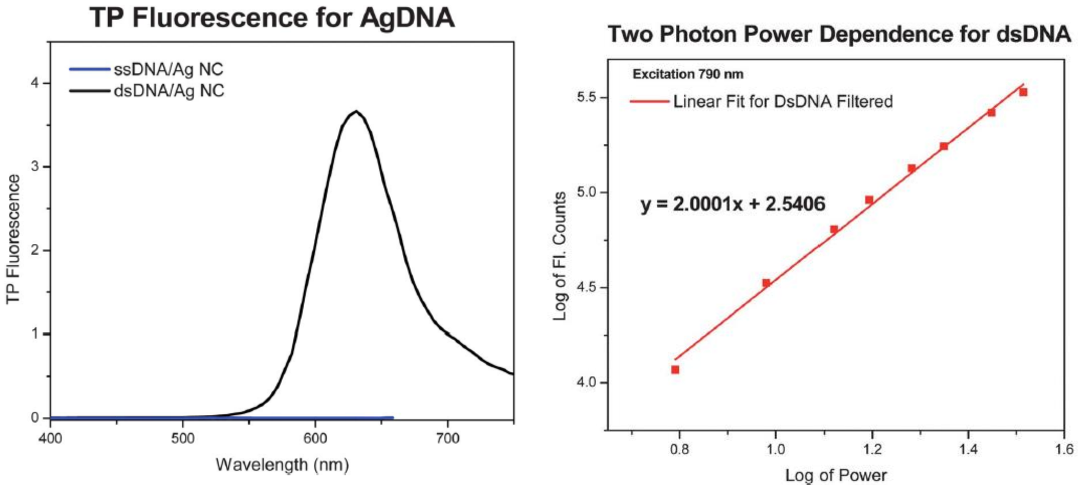

Figure 2-5 Two photon fluorescence spectra of ssDNA and dsDNA Ag NCs and the log-log power dependent fluorescence for dsDNA-Ag NCs.

for dsDNA-Ag NCs is ~3000 GM. The action cross section of 900 GM (3000*0.3 GM) for these chromophores indicate their extremely bright emission under two-photon excitation. Therefore, DNA-templated Ag NCs are strong candidates for multiphoton imaging in biological systems. It must be noted that ssDNA-Ag NCs do not seem to show any two photon absorption. However, one photon absorption of ssDNA-Ag NCs at 400 nm are much stronger than at any other wavelength. The weak to zero two-photon emission for ssDNA-Ag NCs indicates that the presence of 580 nm state of dsDNA may be serving as a point of transition of TPA excitation energy through

580 nm to 650 nm. Due to absence of this state, ssDNA-Ag NCs seem to be less emissive. The strong excitation spectrum at 580 nm of dsDNA-Ag NCs is consistent with this argument.

2.3.4 Wavelength resolved femtosecond transient absorption

Transient absorption was used to investigate the excited state dynamics of DNA-templated Ag nano-systems under study. Transient absorption measures the difference between the steady state absorption and the excited state absorption using pump-probe spectroscopy. In our experiments, the change in absorption is measured starting from the first 100 fs following excitation up to 1.6 ns, producing excited state absorption snap-shots from 450 nm to 750 nm range of wavelengths. When excited using the pump beam at 470 nm, the transient absorption spectrum shown in figure 2-6 results. As can be observed, a bleach signal at ~590 nm can be seen for dsDNA-

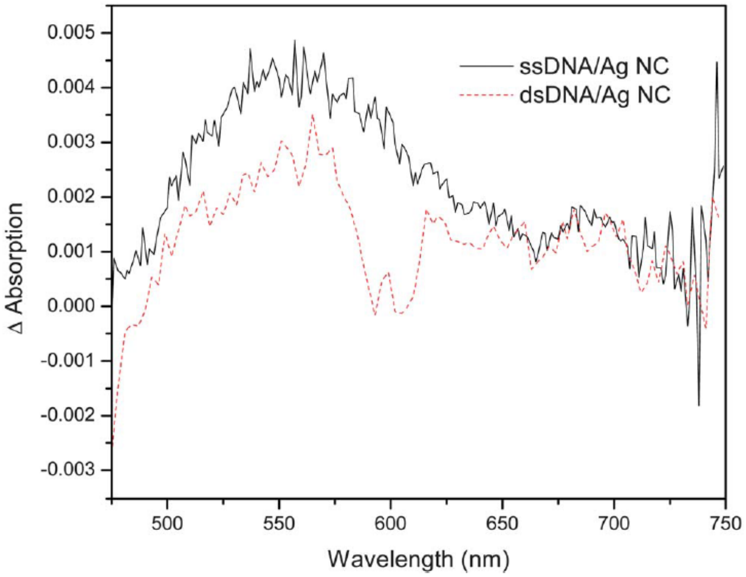

Figure 2-6 Transient absorption of DNA-templated Ag NCs under 470 nm excitation. The transient absorption spectra at 20 ps are shown.

Ag NCs. This bleach can be directly related to the steady state absorption at 580 nm for dsDNA-

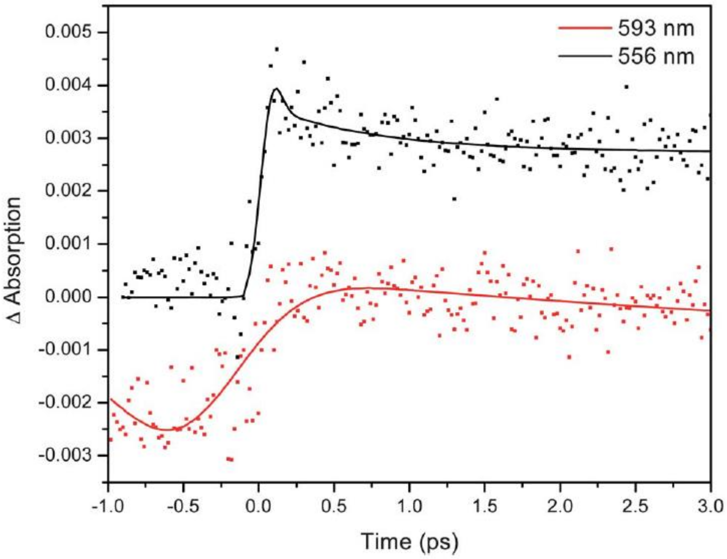

Figure 2-7 Transient absorption kinetic fit for dsDNA-Ag NCs for 470 nm excitation and 692 nm and 556 nm transient data.

Ag NCs. If we take a look at the kinetic trace for that bleach state (figure 2-7), it is clear that it has a non-zero component even before zero time. This observation indicates the presence of a long lived bleach state beyond the repetition rate of the laser (1 kHz) which is 1 ms or longer. Also, since the bleach state at 590 nm corresponds to the 580 nm excitation maximum for 650 nm emission, this 590 nm bleach should be directly related to the 650 nm emission. Therefore, the unusually large quantum yield at 650 nm emission could also be explained by this long-lived bleach state. The presence of such long lived excitations in nanoclusters indicate their discrete electronic energy level formation resulting due to quantum confinement effects. Therefore, it is clear that dsDNA-Ag NCs shows many signs of quantum confinement effects in the condensed phase.

2.3.5 Femtosecond-resolved fluorescence up conversion

Using time-resolved up conversion, we have studied the dsDNA-Ag NCs. From the steady state emission data, we decided to conduct fluorescence up conversion experiments for 550 nm, 600 nm and 650 nm emission. However, detectable signals were obtained for 550 nm and 600 nm emission. From previous experiments by others using time-correlated single photon counting experiments, the 650 nm emission was shown to have a 3.48 ns life time. [35] Since the 650 nm emission was not observed for the time window between 60 fs to 4 ps, we can state that the 650 nm emission occurs from a later transition (consistent with the 580 nm bleach state observed previously). The emission at 550 nm and 600 nm shows similar dynamics with rise times of 3.85 ps and 2.49 s for 550 nm and 600 nm emission wavelengths respectively. This alludes to the possibility that both emissive states seem to be originating from the same initial state. Since this

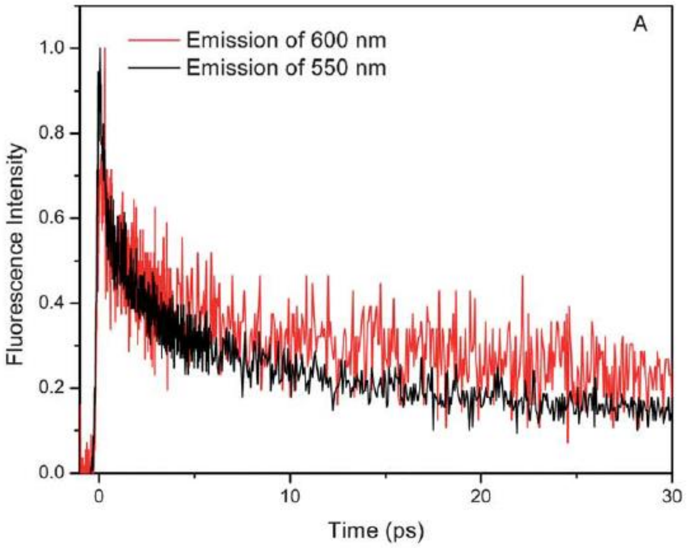

Figure 2-8 Fluorescence up conversion data for 550 nm and 600 nm emission.

weak emission is present in both ssDNA and ds DNA Ag NCs, this emission could be attributed to the metal core emission.

The emission from the 650 nm, on the other hand, could be a result of a triplet state, a charge transfer state or a surface state. Based on our previous experiments on Au monolayer protected nanoclusters, the emission observed is more likely to be from the surface states of the dsDNA-Ag NCs. And it is highly probable that the energy transfer to 650 nm state occurs at a much later time than interrogated in this experiment. However, one important difference between Au NCs and dsDNA-Ag NCs is that the quantum yield observed for the surface states (i.e. near IR emission) for Au NCs was on the order of 10^{-4} which is about 3 orders of magnitude weaker than observed for dsDNA-Ag NCs. [13]

2.4 Summary and Conclusions

As was observed in the aforementioned linear and nonlinear optical investigations of ssDNA-Ag NCs and dsDNA-Ag NCs, we were able to find quantum confinement effects for Ag NCs. The most prominent quantum confinement effects were observed for dsDNA-Ag NCs upon capping using the stabilizing DNA sequences/ligand. dsDNA-Ag NCs showed discrete absorption peaks that arise from discrete electronic transitions which is a signature of quantum confined nanoclusters. Quantum yield reported for these Ag NCs indicate that they are about 9 orders of magnitude stronger than typical bulk metal emissions and about 5 orders of magnitude stronger than noble metal nanoparticles. The unusually strong two-photon absorption for dsDNA-Ag NCs follow a similar trend observed by Au nanocluster materials while the action cross section for Ag NCs are much larger than that of gold. This is another indication of quantum confinement of these condensed phase Ag NC systems. When investigated using ultrafast time-resolved spectroscopy, we were able to observe a long lived emissive excited state for dsDNA-Ag NCs at 650 nm which was attributed to a bleach state at 580 nm of the transient absorption. This bleach state directly corresponds to the 580 nm steady state absorption feature and the excitation maximum for 650 nm emission. Interestingly, the 580 nm emission appears to last longer than the laser repetition rate (1 kHz) which indicates a >1 ms lived bleach state. The presence of long lived emission for 650 nm is consistent with the fluorescence quantum yields observed for dsDNA-Ag NCs. Also, the fact that 550 nm and 600 nm can be observed for both ssDNA and dsDNA Ag NCs mean that the emission at 500 nm should be taking place from the quantum confined metal core states. Whereas the 650 nm emission which is absent in ssDNA-Ag NCs comes from the surface emissive state present in the nanoclusters upon stabilization by the ligand. Similar observations were made with solution phase investigations of Au quantum confined clusters.

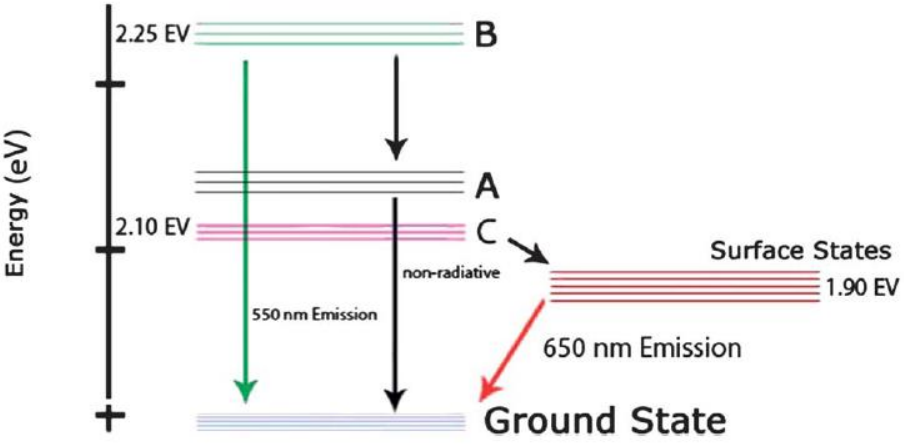

Figure 2-9 Energy level diagram proposed for dsDNA-Ag nanoclusters.

Based on the steady state absorption, emission, wavelength resolved transient absorption and time-resolved fluorescence up conversion and nonlinear spectroscopic data, we can present the energy level diagram for dsDNA-Ag NCs (figure 2-9). According to our model, the singlet emission at 540 nm occurs from the state “B” associated with the Ag metal core while the emission at 650 nm originates from the surface emissive states. We attribute the high yield singlet emission at 650 nm to the efficient energy transfer between 590 nm absorption and surface emissive states. It must be noted that the state “C” of the dsDNA-Ag NCs is formed upon binding of the stabilizer sequence of the second DNA strand. This implies that the state “C” is not present in ssDNA-Ag NCs.

In conclusion, our linear and nonlinear spectroscopic investigations of DNA-templated Ag NCs in solution phase ensembles indicates the presence of quantum confinement effects in ligand stabilized Ag NCs. Their potential use in multiphoton imaging in biological systems is highly favored due to the unusually large two-photon absorption cross sections observed. This study indicates that similar to the previous investigations of Au NCs in solution phase, the Ag NCs also tend to follow the “superatom” picture. [20- 24, 43- 48] However, the current studies (as well as many previous studies reported for quantum confined nanoclusters) provide us with average optical responses of quantum confined Ag NC ensembles. Typically, this effect hides the effects of heterogeneity among nanoclusters. [49] Also, when nanoclusters are studied in the condensed phase the inter-nanocluster interactions may come into play affecting the optical responses due to dipole coupling, fluorescence quenching or energy transfer between nanoclusters. [12, 50] Therefore, in order to get a more detailed understanding of the optical responses of quantum confined systems, it is desired to study them as single nanoclusters that will reveal the effects of heterogeneity and eliminate possible inter-nanocluster interactions that may be present.

2.5 References

1. Yau, S. H., Varnavski, O. & Goodson III, T. An ultrafast look at Au nanoclusters. *Acc. Chem. Res.* **46,** 1506-1516 (2013).
2. Varnavski, O. *et al*. Critical size for the quantum confinement in optically excited gold clusters. *J. Am. Chem. Soc.* **132,** 16-17 (2010).
3. Yuan, X. *et al*. Highly luminescent silver nanoclusters with tunable emissions: cyclic reduction-decomposition synthesis and antimicrobial properties. *NPG Asia Materials* **5,** e39 (2013).
4. Ramakrishna, G. *et al*. Quantum-sized gold nanoclusters as efficient two-photon absorbers. *J. Am. Chem. Soc.* **130,** 5032-5033 (2008).
5. Varnavski, O.; Ispasoiu, R. G.; Balogh, L.; Tomalia, D.; Goodson, T. Ultrafast time resolved photoluminescence from novel metal–dendrimer nanocomposites. *J. Chem. Phys.* **114,** 1962 (2001).
6. Ispasoiu, R. G.; Balogh, L.; Varnavski, O. P.; Tomalia, D. A.; Goodson, T. Large optical limiting from novel metal-dendrimer nanocomposite materials. *J. Am.Chem. Soc* **122,** 11005–11006 (2000).
7. Goodson III, T., Varnavski, O. & Wang, Y. Optical properties and applications of dendrimer-metal nanocomposites. *Int. Rev. Phys. Chem.* **23,** 109-150 (2004).
8. Ramakrishna, G., Dai, Q., Zou, J., Huo, Q. and Goodson III, T. Interparticle electromagnetic coupling in assembled gold-necklace nanoparticles. *J. Am.Chem. Soc* **129,** 1848–1849 (2007).
9. Varnavski, O.; Ramakrishna, G.; Kim, J.; Lee, D.; Goodson, T. Optically excited acoustic vibrations in quantum-sized monolayer-protected gold clusters. *ACS Nano* **4,** 3406–3412 (2010).
10. Devadas, M. S.; Kim, J.; Sinn, E.; Lee, D.; Goodson, T.; Ramakrishna, G. Unique Ultrafast Visible Luminescence in Monolayer-Protected Au_{25} Clusters. *The Journal of Physical Chemistry C* **2010**, *114*, 22417–22423.
11. Yau, S. H.; Varnavski, O.; Gilbertson, J. D.; Chandler, B.; Ramakrishna, G.; Goodson, T. Ultrafast Optical Study of Small Gold Monolayer Protected Clusters: A Closer Look at Emission †. *The Journal of Physical Chemistry C* **2010**, *114*, 15979–15985.

12. Ho Wu, R., Yau, S. H. & Goodson III, T. Linear and nonlinear optical properties of monolayer protected gold nanocluster films. *ACS Nano* **10,** 562-572 (2016).

13. Wu, Z. & Jin, R. On the ligand's role in the fluorescence of gold nanoclusters. *Nano Lett.* **10,** 2568-2573 (2010).

14. Mooradian, A., Photoluminescence of metals. *Phys. Rev. Lett.* **22,** 185 (1969).

15. Dulkeith, E. *et al*. Plasmon emission in photoexcited gold nanoparticles. *Phys. Rev. B* **70,** 205424 (2004).

16. Frohlich, H. The specific heat of the electrons of small metal particles at low temperatures. *Physica IV.* **5,** 406-412 (1937).

17. Kubo, R. Electronic properties of metallic fine particles. *J. Phys. Soc. Japan* **17,** 975-986 (1962).

18. Rao, C. N. R., Kulkarni, G. U, Thomas, P. J. and Edwards, P. P. Size-dependent chemistry: Properties of nanocrystals. *Chem. Eur. J.* **8,** 28-35 (2002).

19. Kreibig, U. and Vollmer, M. Optical Properties of metal clusters. Springer-Verlag, Berlin, Germany (1995).

20. De Heer, W. A., Knight, W. D., Chou, M. Y. and Cohen, M. L. Electronic shell structure and metal clusters. *Solid State Physics* **40,** 93-181 (1987).

21. Ekardt, W. Collective multipole excitations in small metal particles: Critical angular momentum l^{cr} for the existences of collective surface modes. *Phys. Rev. B* **32,**1961-1970 (1985).

22. Beck, D. E. Self-consistent calculations of eigenfrequencies for the electronic excitations in small jellium spheres. *Phys. Rev. B* **35,**7325-7333 (1987).

23. Bonacic-Koutecky, V., Fantucci, J. P. and Koutecky, J. Quantum chemistry of small clusters of elements of group Ia, Ib, and IIa: Fundamental concepts, predictions, and interpretation of experiments. *Chem. Rev. B* **91,**1035-1108 (1991).

24. Walter, M., Akola, J., Lopez-Acevedo, O., Jadzinsky, P. D., Calero, G., Ackerson, C. J., Whetten, R. L., Gronbeck, H. and Hakkinen, H. A Unified View of ligand-protected gold clusters as superatom complexes. *Proc. Natl. Acad. Sci.* **105,** 9157-9162 (2008).

25. Drobizhev, M., Makarov, N. S., Hughes, T. and Rebane, A. Resonance enhancement of two-photon absorption in fluorescent proteins. *J. Phys. Chem. B* **111,** 14501-14504 (2007).

26. Drobizhev, M., Makarov, N. S., Tillo, S. E., Hughes, T. and Rebane, A. Two-photon absorption properties of fluorescent proteins. *Nature Methods* **8,** 393-399 (2011).
27. Ponder, M. & Mathies, R. Excited-state polarizabilities and dipole moments of Diphenylpolyenes and Retinal. *J. Phys. Chem.* **87,** 5090-5098 (1983).
28. Drobizhev, M., Scott, J. N., Callis, P. R. & Rebane, A. All-optical sensing of the components of the internal local electric field in proteins. *IEEE Photonics J.* **4,** 1996-2001 (2012).
29. Kaplan, A. E. & Volkov, S. N. Nanoscale stratification of local optical fields in low dimensional atomic lattices. *Phys. Rev. Lett.* **101,** 133902 (2008).
30. Bedeaux, D. & Bloembergen, N. On the relation between macroscopic and microscopic nonlinearities. *Opt. J. Eur. Opt. Soc. Part B* **69,** 57-66 (1973).
31. Dolgaleva, K., Boyd, R. W. & Sipe, J. E. Cascaded nonlinearity caused by local field effects in the two-level atom. *Phys. Rev. A* **76,** 063806 (2007).
32. Baev, A., Autschbach, J., Boyd, R. W. Prasad, P. N. Microscopic cascading of second order molecular nonlinearity: new design principles for enhancing third order nonlinearity. *Opt. Express* **18,** 8713-8721 (2010).
33. Dolgaleva, K. & Boyd, R. W. Local field effects in nanostructured photonic materials. *Advances in Optics and Photonics* **4,** 1-77 (2012).
34. Kumar, S., Bolan, M. D. and Bigioni, T. P. Gltathione-stabilized magic-number silver cluster compounds. *J. Am. Chem. Soc.* **133,** 13141–13143 (2010).
35. Dance, I. G., Fisher, K. J., Herath Banda, R. M. and Scudder, M. L. Layered structure of crystalline compunds AgSR. *Inorg. Chem.* **30,** 183–187 (1991).
36. Yeh, H. C., Sharma, J., Han, J., Martinez, J. and Werner, J. A DNA-silver nanocluster probe that fluoresces upon hybridization. *Nano. Lett.* **10,** 3106–3110 (2010).
37. Sharma, H. C. Yeh, H. Yoo, J. H. Werner and J. Martinez, *Chem. Commun.* **46,** 3280–3282 (2010).
38. Neidig, M., Sharma, J., Yeh, H. C., Martinez, J., Conradson, S. and Shreve, A. Ag K-edge EXAFS analysis of DNA-Templated fluorescent silver nanoclusters: Insight into the structural origins of emission tuning by DNA sequence variations. *J. Am. Chem. Soc.* **133,** 11837– 11839 (2011).

39. Azubel, M. *et al*. Electron microscopy of gold nanoparticles at atomic resolution. *Science* **345,** 909-912 (2014).
40. Negishi, Y., Nobusada, K. & Tsukuda, T. Glutathione-protected gold clusters revisited: Bridging the gap between gold (I)-thiolate complexes and thiolate-protected gold nanocrystals. *J. Am. Chem. Soc.* **127,** 5261-5270 (2005).
41. Li, Z. Y. *et al*. Three-dimensional atomic-scale structure of size-selected gold nanoclusters. *Nature.* **451,** 46-48 (2008).
42. Peng., S., McMahon, J. M., Schatz, G. C., Gray, S. K. and Sun, Y. Reversing the size-dependence of surface plasmon resonances. *Proc. Natl. Acad. Sci.* **107,** 14530-14534 (2010).
43. Schmid, G. The relevance of shape and size of Au_{55} clusters. *Chem. Soc. Rev.* **37,** 1909–1930 (2008).
44. Qian, H., Zhu, M., Wu, Z. & Jin, R. Quantum sized gold nanoclusters with atomic precision. *Acc. Chem. Res.* **45,** 1470-1479 (2012).
45. Jin, R., Zeng, C., Zhou, M. and Chen, Y. Atomically precise colloidal metal nanoclusters and nanoparticles: Fundamentals and opportunities. *Chem. Rev.* **116,** 10346–10413 (2016).
46. Wang, Y. and Herron, N. Nanometer-sized semiconductor clusters: Materials synthesis, quantum size effects, and photophysical properties. *J. Phys. Chem.* **95,** 525-532 (1991).
47. Khanna, S. N. and Castleman, A. W., Jr. Clusters, superatoms, and building blocks of new materials. *J. Phys. Chem. C* **113,** 2664-2675 (2009).
48. Aikens, C. M. Electronic structure of ligand-passivated gold and silver nanoclusters. *J. Phys. Chem. Lett.* **2,** 99-104 (2011).
49. Moerner, W. E. and Fromm, D. P. Methods of single molecule fluorescence spectroscopy and microscopy. *Review of Scientific Instruments* **74,** 3597-3619 (2003).
50. Yip, W-T., Hu, D., Yu, J., Bout, D. A. V. and Barbara, P. F. Classifying the photophysical dynamics of single- and multi-chromophoric molecules by single molecule spectroscopy. *J. Phys. Chem. A* **102,** 7564-7575 (1998).

Chapter 3

Solid State Quantum Confined Gold Quantum Dots Investigated using Two-photon Excited Fluorescence Near-field Scanning Optical Microscopy

3.1 Original Publication Information

This chapter primarily contains material that was originally published as the following document.

"Enhanced Emission from Single Isolated Gold Quantum Dots Investigated using Two-Photon Excited Fluorescence Near-field Scanning Optical Microscopy"

Neranga Abeyasinghe, Santosh Kumar, Kai Sun, John F. Mansfield, Rongchao Jin & Theodore Goodson III

Published in *the Journal of American Chemical Society* as a full article **(DOI: 10.1021/jacs.6b07737).**

The modifications to the original document is cosmetic and are used only to conform to the format of this dissertation or to provide uniformity of enumeration. I contributed to this paper by synthesizing water soluble Au_{25} nanolusters, preparing pH controlled samples, conducting steady state absorption and emission experiments, preparing samples for scanning transmission electron microscopic (STEM) and near-field microscopic experiments, conducting TPEF NSOM experiments, analyzing and fitting TPEF NSOM data and doing relevant calculations. Following the complete description of the aforementioned paper, I elaborate more on the large aggregate (~150 nm wide) two-photon excited fluorescence near-field scanning optical microscopy that preceded single nanocluster work (which was not included in the paper).

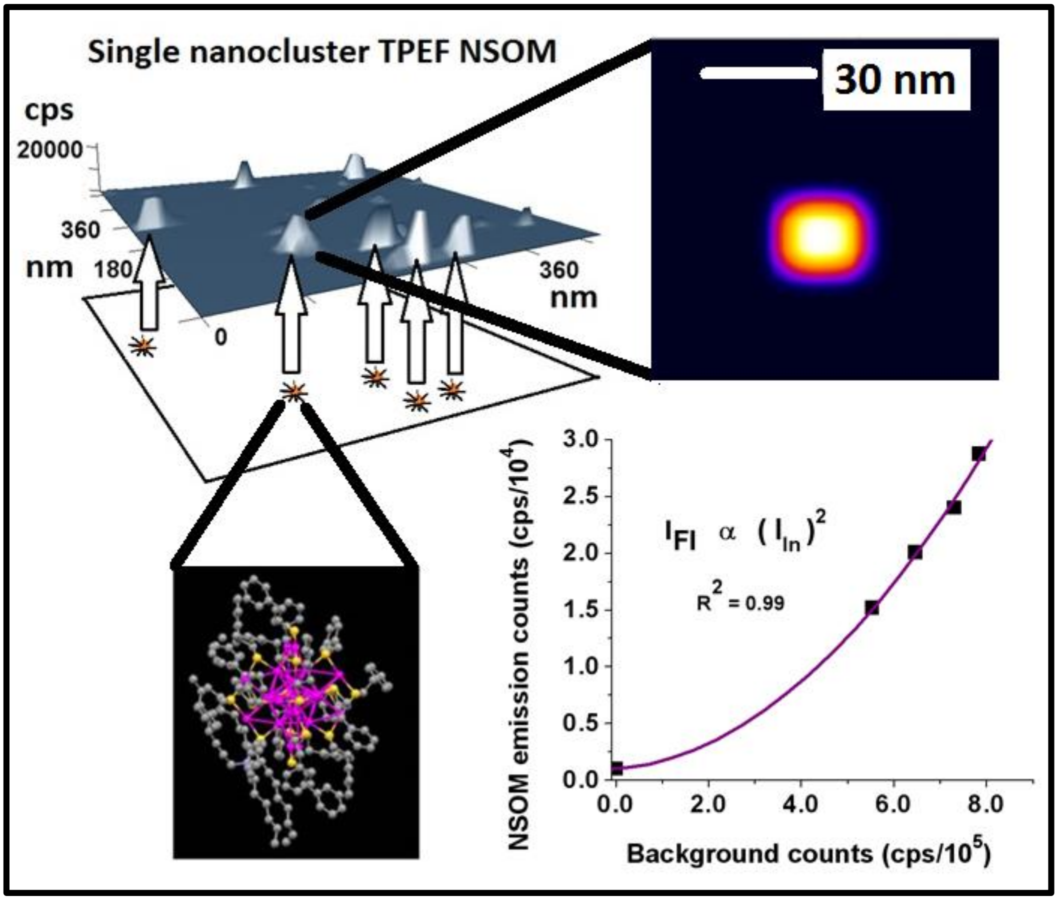

Figure 3-1 Table of contents image as published.

3.2 Abstract

New approaches in molecular nanoscopy are greatly desired for interrogation of biological, organic, and inorganic objects with sizes below the diffraction limit. Our current work investigates emergent monolayer protected gold quantum dots (nanoclusters) composed of 25-gold by utilizing two-photon excited fluorescence (TPEF) near-field scanning optical microscopy (NSOM) at single nanocluster concentrations. Here, we demonstrate an approach to synthesize and to obtain isolated single nanoclusters on solid glass substrates. Their subsequent investigation using TPEF NSOM reveals that even when they are separated by several tens-of-nanometer distances we can excite and interrogate single nanoclusters individually. Interestingly, we observe an enhanced two-photon absorption cross section for single Au_{25} NCs that can be attributed to few-atom local field effects and to *local-field induced microscopic cascading (LFIMC)*, indicating their potential to be used in ultrasensitive sensing, disease diagnostics, cancer cell therapy, and molecular computers. Finally, we report room temperature aperture-based TPEF NSOM imaging of these nanoclusters (NCs) for the first time at 30 nm point resolution which is a *~5-fold* improvement compared to the previous best result for the same technique. This report unveils the employment of the unique combination of unusually large two-photon absorption cross section and high photo stability of the gold-nanoclusters to (non-destructively) investigate *stable* isolated single nanoclusters using TPEF NSOM, which is the *first* ever reported optical study of monolayer protected single quantum clusters which also unveils a very promising direction in spectroscopy of nano-sized objects, bioimaging, ultrasensitive sensing, molecular computers and high density data storage.

3.3 Introduction

Quantum-confined monolayer protected noble metal nanoclusters (NCs; with metal core diameters < 2.5 nm) have recently emerged as a novel class of nanomaterials following the first determination of their crystal/atomic structure,[1-7] and the demonstration of their remarkable catalytic,[8] electronic,[9] magnetic,[10] and optical properties.[11-15] These unique properties in NCs are due to the band-gap opening as their metal core diameters approach the Fermi wavelength of free valence electrons; an effect termed *quantum confinement*. Even though their optical properties were studied extensively for nanocluster ensembles, [11-15] evidence of *single NC optical properties* were not reported until the current work. The advantage of single NC (single molecule) investigations is that they manage to draw out many intricate and fundamental details of individual nanoclusters/molecules and effects of heterogeneity that are lost due to ensemble averaging; and their unique individual behaviors can serve as reporters of their immediate nano-environments. [16] Therefore, probing of single nanoclusters is desired to further appreciate the unique optical, electronic and catalytic properties of these nanomaterials. However, previously reported single nanocluster investigations were conducted using electron microscopic techniques (e.g. High angle annular dark field [HAADF] STEM imaging or combined with EELS, aberration-corrected [AC] TEM) that tend to perturb and alter the structure of the nanocluster while it is being investigated.[2, 7, 17,18] If one is to use the NCs in bio-imaging and sensing applications, electron microscopy becomes incompatible due to the high likelihood of damaging or altering the metal-core structure.[7] For this reason, so far, room temperature TEM investigations of isolated monolayer protected clusters were not reported for stable clusters smaller than Au_{55}.[19] Additionally, since single NCs can be utilized in many potential applications (e.g. sensing, bio-imaging and electronics), it is desired to study them using an approach that can likely be utilized in such endeavors. Therefore, in order to learn potentially promising properties of *single nanoclusters*, optical spectroscopy and microscopy is an ideal avenue owing to the non-destructive nature of optical excitation. More importantly, since quantum confined nanoclusters can have exceptional optical properties due to their unique electronic structures [11-15] one may be able to exploit such properties to conduct single NC spectroscopy. Thus, with the aim of interrogating and eliciting the unique properties of single NCs in a non-invasive and non-destructive manner, novel approaches of employing unique optical properties of the quantum confined nanoclusters are desired.

Many advances in optical imaging and spectroscopy of nanoscale objects were reported during the past few decades.[20-31] The ability to obtain point resolutions that are below the diffraction limit (~λ/2; >200 nm for optical microscopy) was considered as major progress as they allowed closely-spaced nano-sized objects to be probed when they are separated by tens of nanometers apart. Point resolution of a microscope can be defined as the full width at half maximum (FWHM) of the representative point spread function (PSF) obtained from a single point-like object. For far-field optical microscopy, improvement of *point resolution* below 200 nm required the modification of the excitation or detection mechanism.[20-23] It was generally considered that if a molecule has a nonlinear optical response, diffraction-unlimited point resolutions can be attained readily. [21] Nonetheless, with far-field two-photon excited fluorescence imaging, the excitation spot in the x-y plane (lateral) will be twice as large compared to its one-photon counterpart. [21] Consequently, typical *far-field* multiphoton fluorescence microscopy [32] has not been able to enhance the lateral point resolution below 200 nm (It must be noted that recent reports on nonlinear microscopy of metals were able to obtain *localization accuracy* on the nanometer dimensions. Localization accuracy derives from a numerical determination of the precision of the maximum of PSF).[33, 34] However, it must be noted that due to the use of longer wavelengths for excitation, multiphoton fluorescence microscopy has the advantages of lower background fluorescence; and due to quadratic dependence of fluorescence on excitation intensity, improved contrast of the optical image is observed.[30]

Contrary to far-field techniques, near-field optical imaging eliminates the diffraction barrier altogether by using evanescent fields near (<<λ) a sharp metal tip or an aperture (by reducing the effective excitation volume).[24 -30] Betzig *et al*[24] have demonstrated room-temperature one-photon excited fluorescence (1PEF) NSOM with point resolutions below 100 nm. Compared to 1PEF NSOM, multi-photon fluorescence (e.g. TPEF) NSOM is also able to realize an enhanced point resolution due to its independence of diffraction by lateral confinement of light and strong intensity dependence inherent to two-photon excitation. In other words, TPEF NSOM carries all of the advantages of typical TPEF microscopy *and* the ability to (unlike far-field TPEF) obtain sub-diffraction *point resolutions*. Along these lines, TPEF NSOM of Rhodamine B single molecules were reported by Steel and coworkers[35]. However, point resolutions better than ~175 nm were not materialized for aperture based TPEF NSOM. It was inferred that with smaller diameters of the apertures, insufficient intensities of the electric field component at the optical near-field may have caused this difficulty. [35] Also, rapid photo-damage of *typical* organic TPEF chromophores under high TPEF excitation intensities clearly limits the success of this approach. However, since noble-metal nanoclusters have demonstrated high stability under optical excitation, we explored the possibility of employing (while revealing) exceptional TPEF properties of NCs[15] for the interrogation of single isolated nanoclusters with TPEF NSOM technique that will also afford lateral resolutions an order of magnitude below the diffraction barrier. This could allow the individual nanoclusters to be placed on a substrate several tens of nanometers apart and investigate their nonlinear optical properties with exciting one nanocluster at a time.

Previous investigations on 25-gold atom nanoclusters (Au_{25} NCs) have revealed exceptionally large two-photon absorption cross sections in the solution phase NCs ($\delta = 4.27 \times 10^5$ GM [GM= 10^{-50}cm^{4}s/photon])[15] and in NC films ($\delta \sim 10^6$ GM)[36], highlighting their potential to be used in multiphoton single nanocluster spectroscopy. Also, gold NCs have shown enhanced emission quantum yields in the solution phase ($\eta \geq 1 \times 10^{-4}$)[37] orders of magnitude higher than their larger (> 2.5 nm core diameter) counterparts such as gold nanoparticles (NPs) ($\eta \sim 10^{-6}$)[38, 39] and smooth gold films[37] ($\eta \sim 10^{-10}$). Since water soluble $Au_{25}SG_{18}$ (glutathione protected Au_{25}) can be easily synthesized with high monodispersity, [41-43] they can potentially be used in biological imaging applications. Moreover, compared to Ag NCs, Au NCs are well studied and possess greater chemical stability [44] and Cu NCs were not reported to possess unusually high TPA cross sections. Out of all of the Au NCs that have been studied so far Au_{25} are the most stable. Nonetheless, as mentioned earlier, no monolayer protected single nanocluster study (room temperature TEM or Optical) was reported for a *stable* monolayer protected nanoclusters smaller than Au_{55}.[19] Therefore, given the extraordinarily high stability reported for Au_{25} NCs, [44] their relatively smaller size (~1.2 nm) and low bio-toxicity compared to semiconductor quantum dots, [45] Au_{25} NCs are strong candidates for being adopted in high-resolution optical imaging, high density data storage and ultrasensitive sensing of nano-environments.

In this article, using aperture-based TPEF NSOM imaging, we report the first observations of single $Au_{25}SG_{18}$ NCs by demonstrating exceptional TPEF properties of the material. We investigate their dissolution into *single* NCs in solution, and confirm the presence of isolated single NCs on solid substrates by utilizing scanning transmission electron microscopy (STEM/TEM). We probe their optical properties at ~***30 nm*** **(~λ/27)** point resolution using aperture-based TPEF NSOM while exciting one nanocluster at a time. Therefore, in the current work we report the utilization of unusual nonlinear optical properties of nanoclusters for their interrogation at single NC concentrations which is a unique and non-destructive approach to obtain, confirm and conduct single NC nonlinear spectroscopy and imaging.

3.4 Results and Discussion

3.4.1 Steady-state spectroscopy

$Au_{25}SG_{18}$ dissolved in water produces a steady state UV-Visible absorption spectrum (Figure 3-2 a) with the characteristic absorption features observed for 400 nm (3.10 eV), 450 nm (2.76 eV), and 690 nm (1.80 eV). These absorption features indicate the strong monodisperse nature and the characteristics of quantum-confinement in Au_{25} nanoclusters. If the nanocluster sample contained many different sizes of nanoclusters, they cause a smoothening and disappearance of the specific absorption features observed due to slightly different absorption energies for different sizes. The synthetic procedure has been optimized previously to obtain monodisperse nanoclusters with atomic precision (through size focusing), [41-43] (see chapter 5 for more details). Also, when excited at 400 nm, water soluble $Au_{25}SG_{18}$ NCs show an emission feature at ~700 nm (Figure 3-2 b). This is consistent with the previous steady state emission observed for $Au_{25}SG_{18}$ NC solutions and can be attributed to the lowest lying transition that was observed within the visible wavelengths.

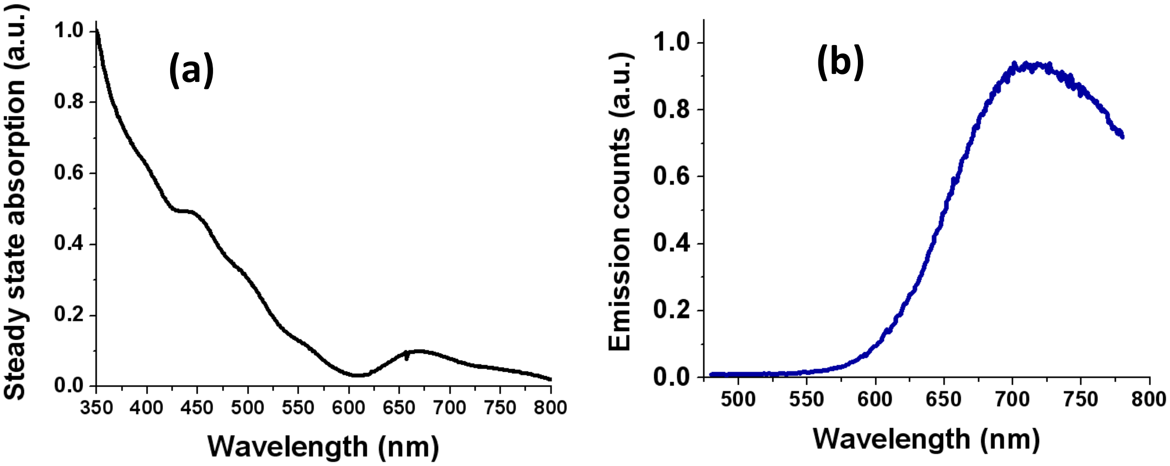

Figure 3-2 Steady state absorption and emission spectra of $Au_{25}SG_{18}$ nanoclusters in solution

3.4.2 Preparing isolated single nanoclusters on substrate

Even though one can assume that $Au_{25}SG_{18}$ NCs are not aggregated due to dissolution in water, there is no confirmation as to whether they are actually isolated from one another. This issue becomes critical when it comes to single nanocluster spectroscopy and microscopy as aggregate responses could be different from the isolated NCs. Therefore, pH=7.2 solutions and a total of 2-minute sonication time (in two one-minute sonication steps) were used for dissolving $Au_{25}SG_{18}$ NCs. Since 18 glutathione ligands each have two ionizable carboxylic groups (pK1 = 2.12, pK2 = 3.53), at pH=7.2, we hypothesized that the nanoclusters will form complete negatively charged ions on the distant carboxylic ends of the ligands causing coulombic repulsion between single nanoclusters to occur (Figure 3-3a). [46] This approach should not only facilitate the complete

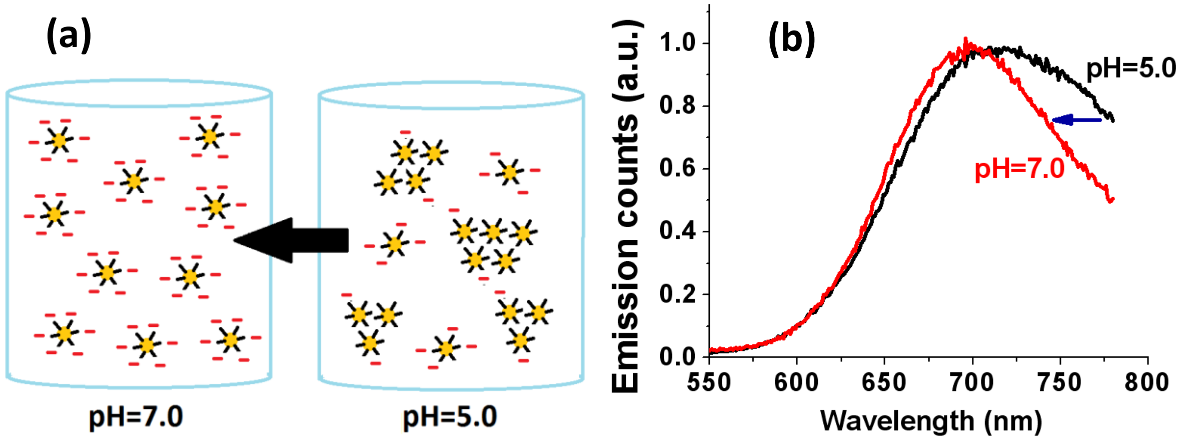

Figure 3-3: Isolation of $Au_{25}SG_{18}$ single nanoclusters in solution and corresponding steady state emission spectra at elevated pH values

(a) Schematic of pH control: When moving from pH=5.0 to pH=7.0 solutions, $Au_{25}SG_{18}$ NCs get complete negatively charged spherical environment causing strong inter-nanocluster repulsion which should render the isolation of single NCs in solution. Orange color corresponds to Au_{25} NC metal atom cluster, black color – glutathione ligands, red color – representative negative charges due to ionization of carboxylic end groups of the glutathione (monolayer) ligands. (b) The steady state emission of $Au_{25}SG_{18}$ gets narrower (shown by blue arrow) when moving from pH=5.0 to pH=7.0 solutions consistent with the single nanocluster isolation in solution phase.

dissolution of $Au_{25}SG_{18}$ NCs in water but it also should ensure that the isolated single nanoclusters are prevented from aggregation while they are in solution.

Interestingly, as depicted in the Figure 3-3b, when the pH of the solution was changed from pH=5.0 to pH= 7.0 the steady state emission spectrum narrows significantly (approximately by 100 nm). On the contrary, the two steady state absorption spectra for the two solutions with different pH values appear almost the same with about < 10 nm blue shift for the pH=7.0 $Au_{25}SG_{18}$ NC solution (see Figure 3-15 in section 3.9). This clearly agrees with our aforementioned hypothesis where the Au_{25} NC aggregation occurring at pH=5.0 causes an increase in the emissive densities of states that results in a broader emission spectrum compared to pH=7.0 solution. Since the nanocluster steady state absorption is largely affected by its 13-gold atom icosahedral core structures, [3] the effect of aggregation in pH=5.0 on absorption appears to be minimal since most of the effects of aggregation or close proximity are likely felt only by the surface emissive states (except through symmetry).

3.4.3 Confirming isolated single nanoclusters using STEM/TEM

In order to confirm that the TPEF NSOM samples would contain isolated single nanoclusters on the substrate, we have conducted scanning transmission electron microscopy (STEM/TEM) imaging experiment for Au_{25} NC solutions (pH=7.2) *drop cast* on holey-carbon copper grids and air-dried for >10 minutes. These solutions were *~85-fold* more concentrated than the solutions used for *spin coating* of the samples prepared for the TPEF NSOM experiment which will be discussed later (figure 3-6). As can be observed in figure 3-4a and 3-4b, we were able to observe isolated single $Au_{25}SG_{18}$ NCs on the substrate even with very slow evaporation of the solvent and at 120 nM concentrations. From the size histogram analysis (figure 3-11) >80% of the STEM image features show a diameter of 1.21 ±0.15 nm confirming single Au_{25} isolated NCs while ~17% features had diameters and shapes consistent with the sizes and shapes of Au$_{25}$ NC

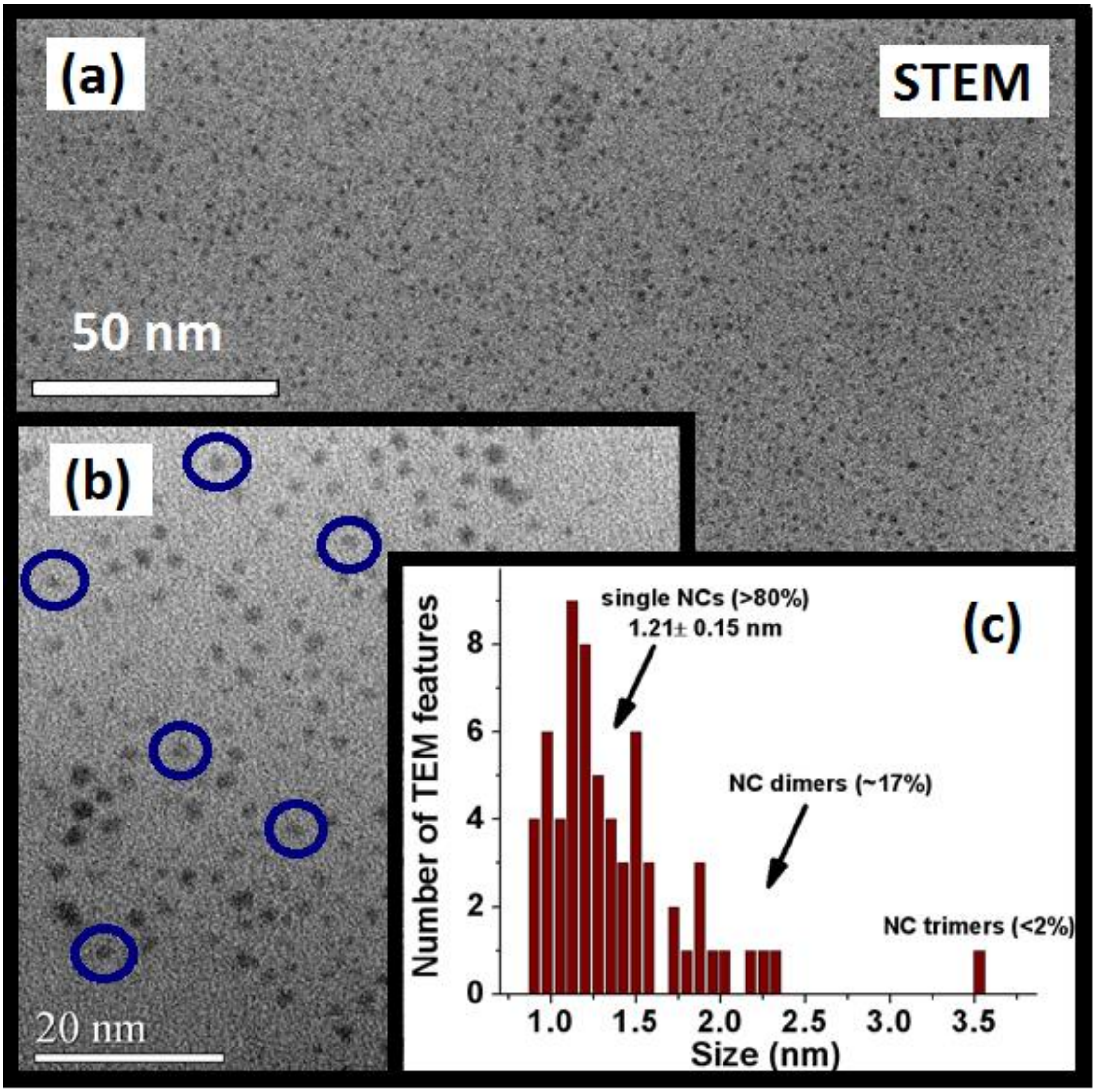

Figure 3-4: Au$_{25}$ single nanocluster STEM bright-field (BF) images; drop cast film for ~85-fold higher concentration

(a) STEM (BF) image of Au$_{25}$ SG$_{18}$ nanoclusters *drop cast* on holey-carbon copper grid for 120 nM Au$_{25}$ SG$_{18}$ solution dissolved in pH=7.2 solution. STEM (BF) field of view is 225 nm x 225 nm. Slow drying of the sample took >10 minutes. (b) STEM image of the same area with higher resolution. Few single nanocluster images are encircled in blue. (c) From the STEM (BF) image size distribution analysis we observed >80% of single Au$_{25}$ nanocluster densities with 1.21 ± 0.15 nm mean diameter; ~17% of the TEM features observed were from Au$_{25}$ nanocluster dimers. <2% of the features correspond to Au$_{25}$ nanocluster trimers. Au$_{25}$ SG$_{18}$ nanocluster density ~16,300 nanoclusters/µm^2. Since the solutions used for TPEF NSOM sample preparation had ~85 times lower nanocluster concentrations, the likelihood of dimer formation can be estimated to be <0.1%. Therefore, it is clear that our samples used for TPEF NSOM investigations contained *isolated single Au$_{25}$ nanocluster* densities on plasma cleaned glass substrate (see supporting information for details).

dimers. Only <2% of nanoclusters were forming Au_{25} NC trimers. This further proves that the technique of using pH=7.2 indeed had rendered strong inter-nanocluster repulsion. For the TPEF NSOM scans (figure 3-6a) discussed later, we have used 1.4 nM solutions of Au_{25} NC (pH=7.2) which are 85-fold diluted compared to the solutions used for STEM. Therefore, the inter-nanocluster collision frequency of 1.4 nM solutions should be reduced by 85 times. This implies that for the 1.4 nM concentrations used for spin coating of single nanoclusters on solid substrates (figure 3-6a), we should expect <0.1% likelihood for any form of Au_{25} NC aggregation (see supporting information for more details). Also, from our observation of average inter-nanocluster distances of ~*7.8 nm* for 120 nM solutions drop cast on solid substrate, we estimated the average inter-nanocluster distances for 1.4 nM solution spin-coated on glass substrate to be around *160 nm*. This infers that the surface density of nanoclusters is 39 nanoclusters/μm^2 which agrees well with the ~23 nanoclusters/μm^2 observed for TPEF NSOM (see figure 3-6 and the supporting information in section 3.9).

The spectroscopic evidence reported in sections 3.4.1, 3.4.2 and the STEM characterization indicated above clearly indicate that single $Au_{25}SG_{18}$ NCs can be isolated in solution through pH control. Using these pH=7.2 solutions, we have prepared 1.4 nM solutions of $Au_{25}SG_{18}$ NCs and 4 µL volumes were spin-coated using 1400 rpm speeds on plasma cleaned glass cover slips (see Section 3.6 for experimental details). Then the samples were oven-dried under vacuum that were subsequently used to conduct TPEF NSOM experiments.

Also, as indicated in the supporting figure 3-16, we have carried out concentration dependent AFM studies on Au_{25} NCs in the absence of pH increase to pH=7.0 which clearly indicates evidence of aggregation as the concentration was increased. The feature diameters tend to slightly increase while the feature density (i.e. number of AFM features/area) drops dramatically for concentrations above 1.5 nM (see figure 3-17). Therefore, it is clear that in the absence of pH-induced disassembly we indeed do see Au_{25} NC aggregation (while the STEM scans for pH-induced disassembly demonstrates the isolation of Au_{25} NCs in to single nanoclusters).

3.4.4 TPEF NSOM experiments on isolated Au_{25} nanoclusters

As depicted in Figure 3-5a and 3-5b, we used a femtosecond pulsed laser with 810 nm excitation wavelength coupled to a single mode optical fiber for TPEF NSOM. The aperture diameter of the probe used for the current NSOM study is ~40 nm (See supporting information for SEM). Average near-field excitation powers used were ~600 μW. Highest TPEF NSOM counts observed were on the order of 30,000 cps. TPEF NSOM scans were conducted with 10 nm pixel

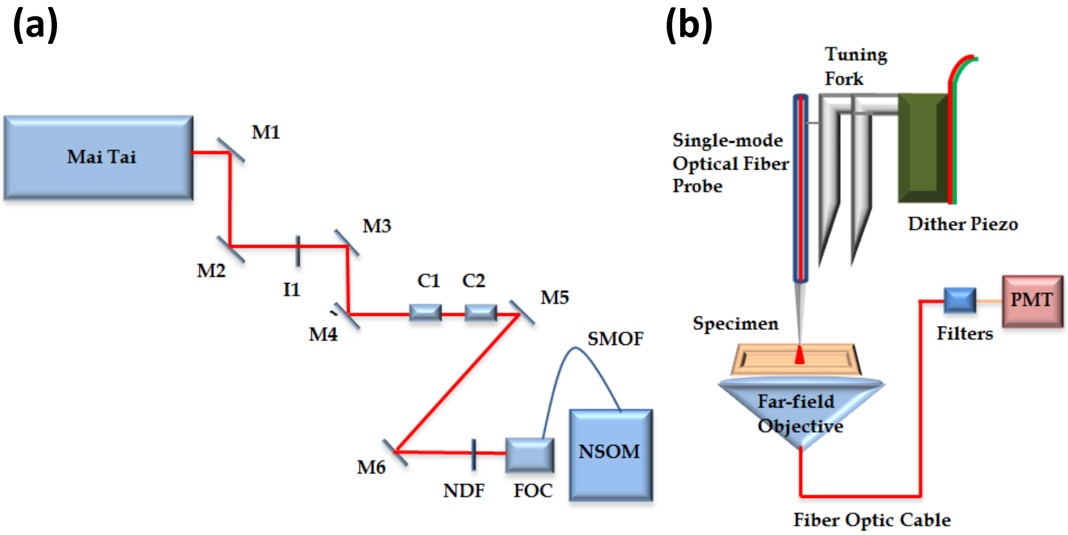

Figure 3-5: TPEF NSOM of Au_{25} single nanoclusters and the experimental set up

(a) 810 nm femtosecond output from the Mai Tai is coupled to a single mode optical fiber. (M1 through M6 are reflective mirrors, I1: iris, C1 and C2: collimating lenses, NDF: neutral density filter, FOC: fiber optic coupler, SMOF: Single mode optical fiber) (b) near-filed illumination geometry inside the NSOM (Tip-sample distance <<<λ).

sizes and 36 ms bin times. From the intensity dependent TPEF NSOM scans we confirmed the quadratic dependence of NSOM fluorescence intensity on incident background counts (figure 3-

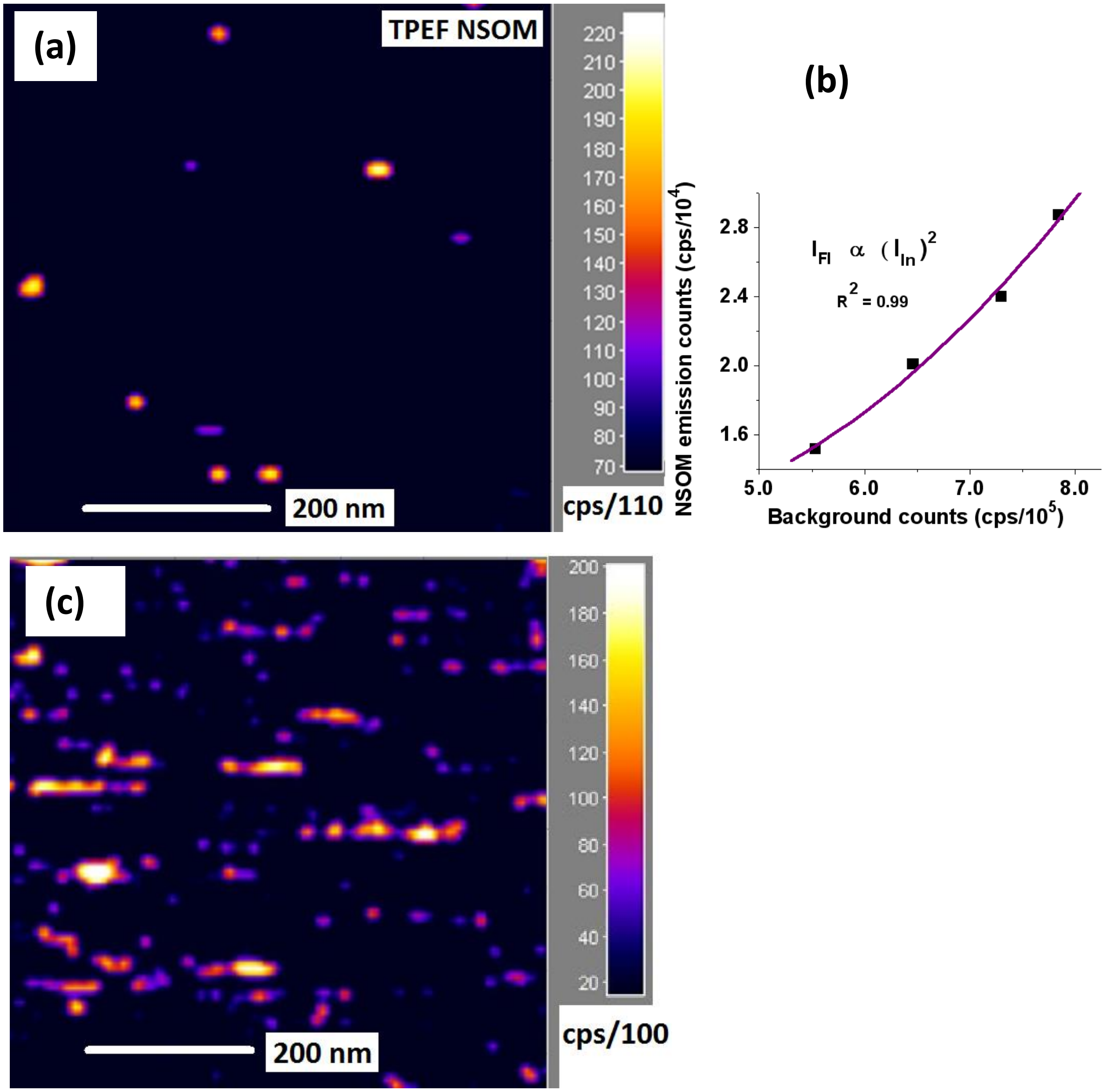

Figure 3-6: TPEF NSOM of Au$_{25}$ single nanoclusters for samples prepared using 1.4 nM and 12.0 nM solutions

(a) TPEF NSOM image of Au$_{25}$SG$_{18}$ single nanocluster concentrations (by spin-coating 1.4 nM solution on plasma cleaned glass). TPEF NSOM feature density is ~23 features/µm^2. TPEF counts observed for the highest intensity feature was ~25,000 cps for ~625 µW near-field excitation. (b) Plot of fluorescence intensity versus incident background intensity. The quadratic dependence proves TPEF response from the NSOM fluorescence. (c) TPEF NSOM image for a sample prepared by spin-coating 12.0 nM Au$_{25}$ solutions.

6b): A corresponding slope for the log-log plot was ~1.77 which is nearly quadratic (The TPEF NSOM response was reproduced for three different $Au_{25}SG_{18}$ NCs samples using the same sample preparation procedure). The TPEF NSOM feature density was ~23 nanoclusters/μm^2 which agrees well with the estimated isolated single nanocluster densities (39 nanoclusters/μm^2) derived from STEM/TEM data shown earlier. From the calculations in section 3.4.3, it can be concluded that the samples used for TPEF NSOM investigations indicated in figure 3-6 had isolated single Au_{25} NCs on plasma cleaned glass substrates separated by ~160 nm distances, which is much larger than the NSOM tip diameter ~40 nm. This indicates that with our sample preparation conditions we can be confident that, on average, near-field two-photon excitation was localized on single isolated nanoclusters. To our knowledge this is the *first report of isolated single nanocluster* TPEF NSOM. Additionally, our report of Au_{25} single nanocluster investigations serve as the first report of *any* room temperature monolayer protected *stable* single nanocluster smaller than Au_{55} investigated in detail using *any* technique. [19] As mentioned earlier, Ag NCs show relatively low chemical stability while Cu NCs were not reported to show significantly high TPA cross sections. Therefore, it is clear that according to our current work, monolayer protected Au_{25} NCs demonstrate their high optical stability and unusual optical properties when they are isolated from the ensemble. This puts protected Au_{25} NCs in a unique position for their unusual material and optical properties that are not collectively present in other noble metal nanoclusters (i.e. in Ag NCs and Au NCs).

Also, the approach of isolating single nanoclusters right at the beginning of dissolution allows one not to rely too much on other single molecule confirmatory techniques such as fluorescence blinking which could occur from more than a single nanocluster due to inter-chromophore energy transfer processes.[47] Additionally, as can be observed in figure 3-6a, certain

TPEF NSOM features are separated by <50 nm distances (as expected for a population of inter-nanocluster distances). This confirms that our TPEF NSOM excitation was able to excite individual nanoclusters even when they are separated by several tens-of-nanometer distances.

In order to understand the effect of concentration on TPEF NSOM feature density, we can compare the current data with the TPEF NSOM data obtained for a single nanocluster sample (figure 3-6c) prepared using 12.0 nM $Au_{25}(PET)_{18}$ solutions (PET= SCH_2CH_2Ph). The solution was sonicated for 1 and a half minutes prior to spin coating using the same conditions as before. As depicted in figure 3-6c, most of the TPEF NSOM features observed seem to be larger (in the x-y plane) than the NSOM tip diameter (~40 nm). This is due to the individual nanoclusters being in close proximity to one another on the substrate due to *inter-nanocluster spacing that are smaller than the NSOM tip diameter* and having many such single nanoclusters in one field of view (hence elongated TPEF NSOM features). Using the STEM data depicted above, we calculated the expected nanocluster density of the 12.0 nM sample to be ~ 334 nanoclusters/μm^2 and the average inter-nanocluster distance to be ~55 nm. This indicates that in a field of view of concern, some of the nanoclusters could have inter-nanocluster distances that are smaller than the NSOM tip diameter causing the TPEF NSOM features to overlap and form larger or elongated features (as can be predicted from figure 3-6a where inter-nanocluster distances <50 nm were observed when the *average* inter-nanocluster distance is ~160 nm). Therefore, our experimental evidence is consistent with the picture that for 1.4 nM samples depicted in figure 3-6a, the TPEF NSOM features observed were indeed originated from isolated single nanoclusters excited individually by TPEF NSOM.

3.4.5 Enhanced two-photon absorption (TPA) cross section

Since it is clear that we have isolated single Au_{25} NC TPEF NSOM, two-photon absorption (TPA) cross section can be estimated for single Au_{25} NCs from the NSOM fluorescence intensity observed. As can be seen in figure 3-7a, the TPA cross section histogram for the 23 features indicated a somewhat non-Gaussian distribution. The average TPA cross section calculated (δ_{solid} = 6.99 x 10^5 GM) appears to be enhanced by ~64% compared to the solution phase counterpart. This completely unexpected enhancement in TPA cross section deserves further understanding.

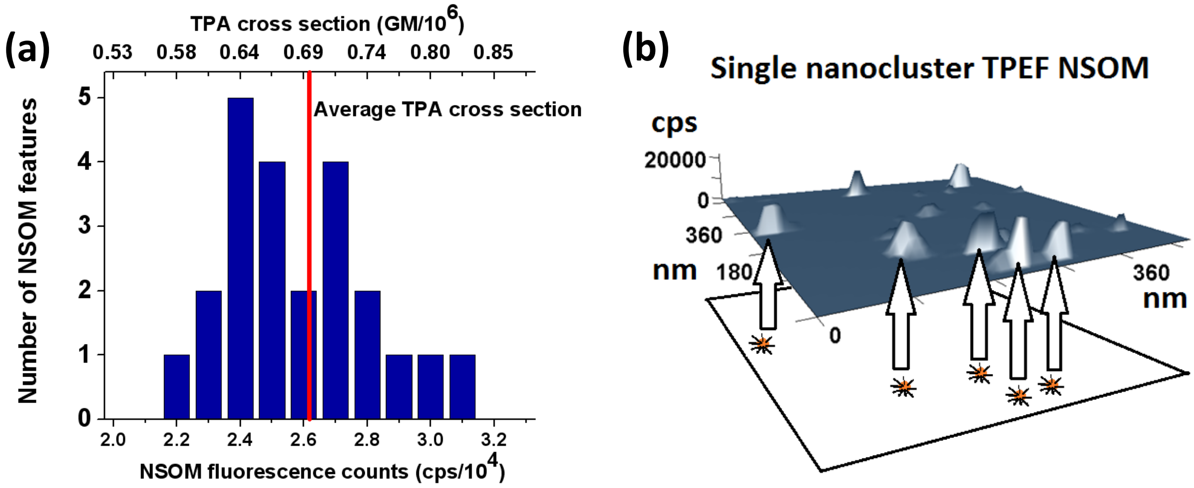

Figure 3-7: TPA cross section enhanced for Au_{25} single nanoclusters on plasma-cleaned glass substrate (a)Intensity histogram for 23 TPEF NSOM features and corresponding TPA cross sections. The average TPA cross section is enhanced on solid phase compared to solution phase counterpart.

(b) A 3-dimensional presentation of a TPEF NSOM image for quantum-confined single $Au_{25}SG_{18}$ nanoclusters.

Since the two-photon absorption cross section is a *third-order nonlinear optical property* (imaginary part of χ^3) the enhanced δ_{solid} value observed can be attributed to a *local field enhancement* due to changes in the refractive indices. On solid glass cover slips, it can be assumed that Au_{25} NCs are surrounded mainly by air (n~1.00). The solvent dielectric environment reported by Ramakrishna *et al*[15] (for hexane n=1.375), has a higher refractive index. It can be inferred that a local field enhancement in χ^3 caused an enhanced δ_{solid} value. Interestingly, a similar enhancement of χ^3 (real component) was reported by Wang *et al* [48] for nanometer-sized CdS clusters.

To interpret the enhancement observed, the two-photon absorption process with respect to a two-level approximation can be considered. [49] It is clear that there is an enhancement in the difference between the dipole moments of the excited state with respect to the ground state $\Delta\mu_{10}$ (~33%) when the nanoclusters were placed on the solid substrate (see supporting information). This additional enhancement (that can not be explained by changes in the refractive indices) can be attributed to *a local-field induced dipole moment change* due to a change in polarizability of the excited state with respect to the ground state. [50, 51] A similar enhancement of $\Delta\mu_{10}$ in the electric-field-sensitive protein *mCherry* was previously reported by Rebane and coworkers. [52] This implies that local field effects on single Au_{25} NCs are enhancing the TPA cross sections improving their sensitivity to the environment.

In order to further understand this effect, we have utilized models related to the *few-atom* local-field enhancement predicted for "magic" number systems [53] and l*ocal field induced microscopic cascading* (LFIMC) effects[54-57] on the third order nonlinear response. Interestingly, from our calculations we obtain enhancement factors ranging from 1.5 to 10 for Au_{25} NC systems! From previous theoretical and experimental work by Bloembergen and coworkers, [54] and Boyd and coworkers, [55, 56] it has been demonstrated that the local-field effects can create cascaded contributions of the second order polarization to the third order susceptibility. Interestingly, Kaplan and Volkov have theoretically predicted that nanoscale (near-field) local-field enhancement effects may be possible for certain "magic" numbered 1D or 2D systems such as quantum clusters.[53] We think our observation of enhanced TPA cross section for Au_{25} NCs serves as the *first such experimental evidence* of a material that shows few-atom local-field enhancement induced nonlinear cascading predicted for quantum cluster systems. Further investigations on Au_{25} NC nonlinear optical properties may reveal a more detailed picture of this effect. Therefore, as indicated by Boyd [56] and Volkov, [53] our results suggest that Au_{25} NCs can potentially be used as chromophores in ultrasensitive biosensing, molecular computers and molecular logic.

3.4.6 Superior point resolution for aperture-based TPEF NSOM

As shown in figure 3-8, the lateral point resolution is significantly better than the typical resolution for confocal fluorescence microscopy (~200 nm)[58] and previously reported TPEF NSOM resolution of 175 nm for Rhodamine B single molecules. [35] For TPEF NSOM feature with S/N ~ 7, the point resolution observed was ~***30 nm*** **(~λ/27)** which is a *5-fold improvement* in point resolution for the same technique (see supporting information for the Gaussian fitting of data without smoothening). Moreover, it could be argued that the TPEF NSOM point resolution observed is better than the probe diameter (~40 nm) which can be attributed to the intensity dependence of TPEF NSOM that reduces the size of the excitation point spread function compared to its one-photon counterpart. Therefore, with the point resolution around several tens of nanometers obtained from the current approach, we were able to excite and interrogate isolated nanoclusters one at a time (on the solid substrate). Also, the fact that we were able to observe a point resolution (30 nm) *5-fold* better than the previous resolution (~175 nm) for the same aperture-based TPEF NSOM technique can be attributed to the unusually large TPA cross section of these isolated single nanoclusters and their high photostability compared to many organic chromophores.

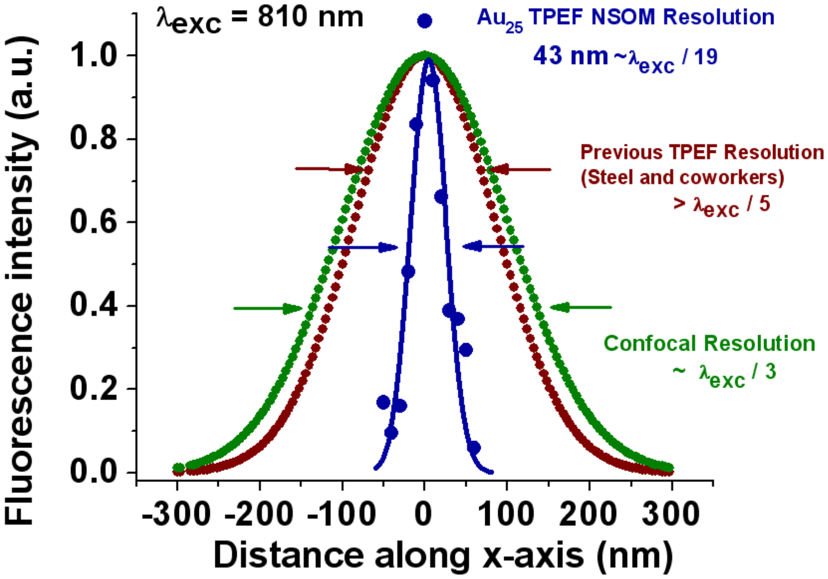

Figure 3-8: TPEF NSOM point resolution reaches 30 nm with Au_{25} clusters

Comparison between transverse point resolution attainable with confocal fluorescence microscopy, previous aperture-based TPEF NSOM, and with the current approach. The point resolution ***43±7 nm* (~λ/19)** FWHM for TPEF NSOM of $Au_{25}SG_{18}$ single nanoclusters (blue) in the current work (from a feature with S/N ~ 7) evidently surpasses the previously observed value. Also, the point resolution without averaging adjacent points (without smoothening) produce ***30±5 nm* (~λ/27)** resolution for the same image which is *greater than 5-fold* improvement for the aperture-based TPEF NSOM technique.

3.5 Conclusion of single nanocluster TPEF NSOM investigations

It is clear that an enhanced TPA cross section of Au_{25} NCs due to local field effects and their high photostability under two-photon near-field excitation were revealed while interrogating them using aperture-based TPEF NSOM. We attribute the unusually enhanced TPA cross section of isolated single nanoclusters to *few-atom* local-field enhancement predicted for "magic" number systems that may possess enhancement factors up to 10 for Au_{25}! The superior resolution observed was otherwise not possible with typical organic chromophores. Therefore, we can state that we have employed (and unveiled) the unique properties of these quantum confined nanocluster materials while optically detecting and investigating them (or *any* nanocluster) for the first time at single nanocluster concentrations.

In summary, with the adoption of unique optical properties of an emergent nanomaterial (Gold NCs) and using high-resolution non-linear near-field microscopy (TPEF NSOM), we have optically interrogated single isolated gold nanoclusters of ~1.2 nm diameter. According to our knowledge, the point resolution reported (~30 nm) in this study is the best observed for the aperture-based TPEF NSOM imaging (*5-fold improvement*) that have rendered two-photon excitation of individual nanoclusters that are separated by <50 nm distances. Furthermore, as confirmed in this work, the ability to obtain isolated NCs in solution and on solid substrate introduces a method to unambiguously control and confirm the single-molecule-nature of the experiment which can also be utilized in many similar glutathione capped single nanoparticle/nanocluster studies. The observed enhancement (64%) in the average two-photon absorption cross section (when the NCs were moved from solution ensemble to isolated single NCs) can be attributed to the few-atom local-field enhancement effects. Also, the heterogeneity and the asymmetry of the observed distribution in two-photon cross section indicates possible heterogeneous distribution of local field strengths.

Current approach of employing the unusually large TPA cross sections and photo stability of single 25-gold atom nanoclusters in TPEF NSOM can be used for future single nanocluster investigations. Additionally, TPEF of these nanoclusters can potentially be used in ultrasensitive sensing of local fields to probe their local nano-environments. Therefore, this study indicates that Au_{25} single nanoclusters may be used in sensing of biological systems (e.g. proteins) that can render nano-environments with varying local fields. For example, in Alzheimer’s disease, the formation of certain Amyloid beta aggregates are induced by the presence of increased metal ion concentrations. [59- 62] Since local accumulation of metal ions can cause enhanced local electric fields, TPEF imaging using Au_{25} NCs can be a promising approach to diagnose early onset of diseases such as Alzheimer's. Therefore, Au_{25} nanoclusters, along with their local field sensitive two-photon response (and the use of more biologically transparent two photon excitation wavelengths) are promising candidates for imaging and diagnostics of biological tissues. Our recent studies clearly suggest that the Au_{25} NCs can be inserted into biological cells without any apparent toxicity and can be used subsequently in cellular imaging applications. [62] Also we were able to observe accelerated damage of cells when cell-inserted Au_{25} NCs were excited using laser irradiation indicating the potential to use them in cancer cell therapy.

3.6 Experimental section

3.6.1 Synthesis of $Au_{25}SG_{18}$

The Au_{25} capped with glutathione (SG) was synthesized in two steps as follows.

3.6.1 (a) Synthesis of Au_nSG_m Clusters:

A 0.1698 g portion of $HAuCl_4$ was dissolved in 100 ml of Methanol and stirred at 0 °C (ice bath) for 15 minutes. Following the dissolution (and cooling) step, 0.614 g of GSH (glutathione) was added to the mixture and the reaction was left to proceed (while stirring) for another 30 minutes. Subsequently, 0.1891 g $NaBH_4$ was dissolved in 25 ml water and added drop wise in to the reaction mixture. The reaction was further run for another 1 hr. All of the aforementioned steps were condcuted in a 0 °C ice bath. After the reaction with $NaBH_4$ was complete (i.e. after 1 hr), the resulting reaction mixture was centrifuged and the precipitate was washed 3 times with Methanol (vortex, sonicate and then centrifuge) followed by drying in the vacuum at room temperature.

3.6.1 (b) Etching of Au_nSG_m clusters to obtain monodisperse $Au_{25}SG_{18}$ nanoclusters:

The resulting Au_nSG_m clusters (82 mg) were dissolved in 7 ml water and heated in a water bath at 55 °C followed by the addition of a 132 mg portion of GSH. (Water bath was set at least an hour prior to the beginning of the experiment and the temperature was set at 55 °C which was maintained throughout the experiment). The reaction was stirred slowly (~300-400 rpm; not faster than that) for 4 hr. Then the reaction mixture was centrifuged followed by discarding of the precipitate. The resulting supernatant was transferred to a new centrifuge tube followed by the addition of 2-3 ml of Ethanol to precipitate $Au_{25}SG_{18}$ nanoclusters. This preciptate was further purified 3 times by dissolution (by water) and precipitation (by Ethanol) cycles to obtain monodisperse $Au_{25}SG_{18}$ nanoclusters. Then the solid nanocluster sample was dried in vacuum at room temperature which was subsequently stored in the freezer. We used milipore grade water for all of our synthesis and purification steps. Also all of the solvents used were of spectroscopic grade (or better). All of our glassware were cleaned in a base bath for 24 hours followed by rinsing with milipore water and oven drying for 12 hours before being used.

3.6.2 Sample preparation for TPEF NSOM

$Au_{25}SG_{18}$ nanoclusters were dissolved in pH=7.2 water and filtered using 220 nm-pore PTFE filters to remove undissolved large aggregates. Then, the solutions were sonicated for 1 minute to dissolve any aggregated clusters. Then the solutions were diluted (in a series of dilutions) to obtain 1.4 nM concentrations of $Au_{25}SG_{18}$ nanoclusters. Subsequently, following another 1-minute sonication time, and a filtering step (using 220 nm-pore PTFE filters), a 4 µL volume of the solution (using a calibrated micropipette) was spin-coated on a plasma cleaned glass substrate at 1400 rpm for 40 seconds. Then the resulting glass substrates were vacuum dried under ~10 inHg at 40 ^{0}C for 2.5 hours. The dried and cooled (to room temperature under vacuum) samples were then used for TPEF NSOM imaging and spectroscopy.

3.6.3 TPEF NSOM experiment

A Mai Tai femtosecond laser source with a repetition rate of 80 MHz was used for the excitation (see figure 3). Pulses of ~ 110 fs (FWHM) at 810 nm were coupled to a single mode optical fiber (maximum throughput at ~ 780 nm) and the tapered end of the optical fiber serves as the local excitation source for the NSOM set-up (Mo Scan NSOM set up by CDP systems, see ref 63 for previous work with the set up). Near-field illumination of the sample generates the two-photon excited fluorescence (TPEF) from single gold nanoclusters. Raster scanning of the 1 um x 1 um areas with 10 nm pixels at 36 milliseconds bin times generated TPEF NSOM images. The fluorescence emission of the single gold nanoclusters and transmitted 810 nm photons were collected using a far-field inverted objective and transferred through a fiber optic cable to a photomultiplier tube (PMT). As shown in figure 3(d), the transmitted 810 nm light is sent through a filter housing and attenuated using a two 808 nm notch filters and a short-pass filter. Thus, the anti-stokes shifted TPEF can be detected (in the visible region) with sufficient intensities for single molecule imaging. The TPEF NSOM intensities were analyzed using FemtoScan Online software and the Gaussian fits for TPEF NSOM point resolution were obtained using Origin 7 fitting software. The final TPEF NSOM scans were displayed using ImageJ software.

3.6.4 STEM characterization

$Au_{25}SG_{18}$ nanoclusters were dissolved in pH=7.2 water and filtered using 220 nm-pore PTFE filters to remove undissolved large aggregates. Then, the solutions were sonicated for 1 minute to dissolve any aggregated clusters. Then the solutions were diluted to obtain 120 nM concentrations of $Au_{25}SG_{18}$ nanoclusters. Subsequently, following another filtering step (using 220 nm-pore PTFE filters) a 1 uL volume of the solution (using a calibrated micropipette) was *drop-cast* on 200 mesh Holey Carbon copper grid and dried in air for > 10 minutes. The copper grids were purchased from SPI supplies and were used as it is. Subsequently, the samples were characterized using STEM with JEM-2100F electron microscope with a CEOS probe corrector. The size distribution histograms were analyzed using ImageJ software.

3.7 TPEF NSOM imaging of monolayer protected Au_{25} nanocluster *aggregates* on a solid substrate

As discussed in the introduction of the paper, monolayer protected Au_{25} nanoclusters were shown to possess unusual chemical stability [44] and remarkable optical properties [11-15] in solution phase. In the preceding decade Goodson group [11-15, 39] pioneered in the investigation of solution phase nonlinear optical properties of noble metal nanocluster ensembles. The observation of unusually large two-photon absorption cross sections in solution phase for Au nanoclusters and the highest per atom cross section for Au_{25} (~17000 GM)[15] were reported by our group in 2008. However, no reports were made on how the TPEF properties of these Au_{25} nanoclusters vary when they are removed from solution ensembles. In the previous part of my dissertation work, my goal was to remove these nanoclusters from the solution phase ensemble and deposit them as individual nanoclusters on solid substrates to study their two-photon excited fluorescence (TPEF) using a sub-diffraction imaging technique, namely, near-field scanning optical microscopy (NSOM). By doing so I hoped to uncover hitherto unobserved fundamental physical/optical properties of these materials which were discussed earlier. In this section I would like to describe the TPEF NSOM observations that were made for small (~100 nm diameter) and large (~1000 nm diameter) aggregates preceding single nanocluster investigations and the physical insights that followed.

In order to be able to ensure that TPEF NSOM is possible for solid phase Au_{25} nanoclusters, the first step was to study them as aggregates. Therefore, I have drop caste 20 μL volumes of 5 μM Au_{25} nanoclusters on to freshly cleaved mica cover slides. Due to high surface energies of the substrates, the solution (dissolved in water) spreads rapidly on the substrate surface and formed various sizes of aggregates. As shown in figure 3-9, I was able to obtain TPEF NSOM images for nanocluster aggregates that are about ~1 μm wide and less than 100 nm thick. It is clear that the TPEF NSOM signal from these nanoclusters were significant. As can be observed in the figure 3-9, the TPEF intensity was not necessarily correlating with the size/thickness of the aggregate as some of the features of the same thickness tend not to be as brightly fluorescent as others upon two-photon near field excitation. This inhomogeneity in TPEF NSOM response became more significant as smaller aggregates were investigated.

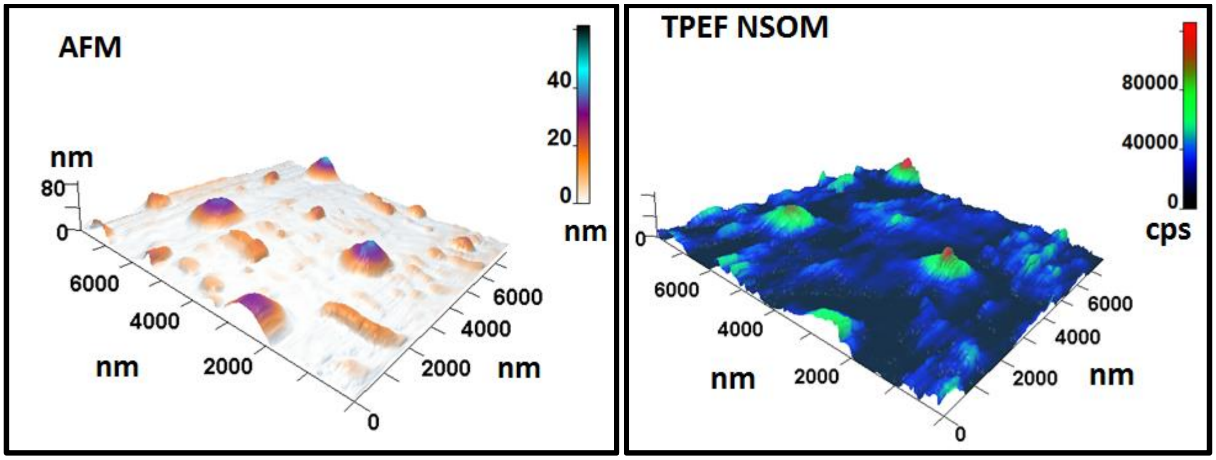

Figure 3-9 TPEF NSOM of large Au_{25} aggregates (~1000 nm diameter)

When the solutions were diluted to obtain ~500 nM solutions of Au_{25} nanoclusters and drop caste on freshly cleaved mica (20 µL), smaller aggregates formed. As depicted in figure 3-10, it is clear that the smallest nanocluster aggregate was about ~100 nm in diameter and ~20 nm in thickness (A) displayed TPEF NSOM while a relatively thicker (C) aggregate (~ 30 nm thickness) did not show any TPEF. This clearly indicates that the inter-nanocluster distances or packing were playing a major role in either enhancing or quenching of the nanocluster two-photon excited fluorescence. In a recent paper on nanocluster ensemble films, our group was able to conclude that for average inter-nanocluster distance < 8 nm there is an inter-nanocluster *dipole coupling* which gave rise to an enhancement in two-photon absorption cross section. [36] Also, for average distances < 8 nm inter-nanocluster energy transfer causes an increase in emission, while a lowering of emission was observed for average distances > 8 nm. Interestingly, the observed TPEF NSOM for smaller aggregates indicate that the inter-nanocluster effects are not invariably observed for all aggregates and can differ from aggregate to aggregate (i.e. while some aggregates are TPEF active the others of similar external dimensions were not). The per-cluster two-photon absorption cross section observed for the aggregate A is *4.4 times weaker than that of isolated single nanoclusters* on solid. This observation clearly indicates that the proximity of nanoclusters to one another is possibly causing coupling of their excitation dipoles veiling the quantum confinement effects of the nanoclusters. This is likely due to the broadening of the density of states (DOS) in the film/aggregate causing a reduction in the volume normalized oscillator strength (f_{12}/V). Also, our current observation could be explained by the few-cluster local field enhancement effects for Au_{25} nanocluster aggregates. [53-57]

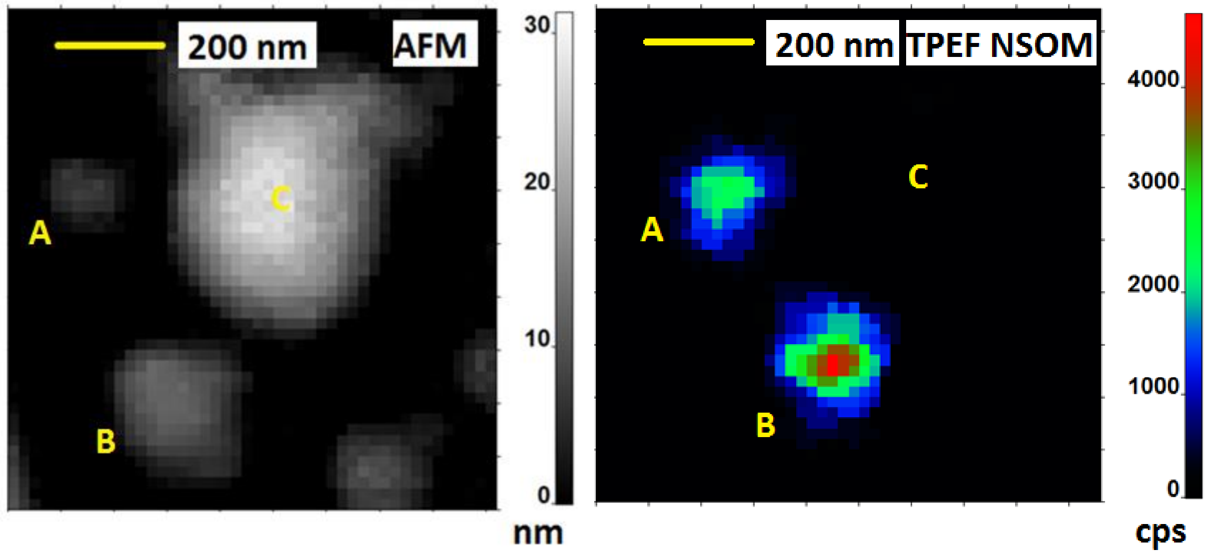

Figure 3-10 TPEF NSOM of small Au_{25} aggregates (~150 nm diameter)

As theoretically predicted by Kaplan and Volkov, since the inter-nanocluster arrangement in an aggregate can also cause either enhancement or quenching of local field effects, certain aggregates that were formed seem to possess such disruptions of “magic number arrangements” of Au_{25} nanoclusters (at a much longer distance than discussed before). [53] This should result in reduced two-photon absorption which in turn causes a quenching/reduction of TPEF NSOM response. In an ensemble study of films one may not be able to gain this insight as the optical response is averaged over millions of nanoclusters shrouding the localized effects of nanocluster arrangement in the film. Therefore, our current observation of aggregate TPEF NSOM also warrants the use of NSOM as a very powerful technique for learning finer details of quantum cluster arrangement and their optical properties in the nanoscale.

It must also be noted that the near-fields generated by nanocluster excitations can be mutually enhanced or quenched depending on the relative arrangement of the nanoclusters in space, their inter-nanocluster distances and the actual number of nanoclusters involved in a nanocluster lattice. This observation can be understood as having a standing wave involving all nanocluster excitations of the lattice/structure (e.g. 1D, 2D or 3D array of nanoclusters) where all/most of the antinodes of the localized excitation spatially overlap with all/most of the nanoclusters, enhancing the two-photon absorption cross section of each nanocluster. This idea can be further extended to covalently linked cluster arrays to produce fine-tuned inter-nanocluster distances and specific number of nanoclusters in an array to produce orders of magnitude stronger two photon absorption cross sections via enhanced local field effects!

The TPEF NSOM observed for Au_{25} nanocluster aggregates further justifies the need to study the isolated Au_{25} nanoclusters to gain a more fundamental physical understanding of their quantum confinement effects on solid substrate. Once the nanoclusters are removed from ensemble/aggregates and placed at average distances > 50 nm, their nonlinear optical properties *should not be affected by neighboring nanoclusters*. Compared to aggregate studies, isolated nanocluster investigations eliminate the inter-nanocluster events (dipole coupling, energy transfer) and reveal the behavior of just 25-gold atom clusters under two-photon excitation allowing for a much clearer and quantitative understanding of the photo-physics of these quantum confined systems.

With that in mind I started to use much lower nanocluster concentrations (0.75 nM) for sample preparation of nanoclusters with a pH adjustment to ensure that isolated single 25-gold clusters are obtained in solution. Then, the isolated single nanoclusters were deposited on the substrate and investigated using TPEF NSOM. As indicated in the previous sections, I was able to gain some unexpected and fascinating insights as to how the two-photon properties of isolated Au_{25} quantum clusters vary from solution phase and aggregate level ensembles revealing some unique and fundamental physics of these systems.

3.8 Overall conclusion

We reported the *first optical interrogation* of the *quantum confined* monolayer protected single nanoclusters on solid revealing enhanced two-photon absorption cross sections for isolated single nanoclusters. This clearly differs from the TPEF NSOM of Au_{25} NCs aggregates studied in section 3.7 where inter-nanocluster interactions significantly alter the optical response of quantum confined nanoclusters. Therefore, our single nanocluster TPEF NSOM results are the first optical confirmation observed of quantum confinement in monolayer protected single gold nanoclusters on solid substrate. When studied as isolated single nanoclusters that are separated by average distances ~160 nm, Au_{25} NCs demonstrated unexpectedly enhanced two-photon absorption (TPA) cross sections. This indicates when the Au_{25} NCs were removed from solution ensemble and placed on solid substrates and studied using near-field two-photon excitation, local field enhancement had caused an enhancement in TPA cross section. According to our knowledge, this is the first observation of a few-atom local field enhancement observed, which was theoretically predicted for "magic" numbered clusters/dots.[53] Also, the enhancement in two-photon absorption cross section can be attributed to *local-filed induced microscopic cascading* (LFIMC) of the second order polarizability on to the third order susceptibility.[54-57] However, it must be noted that further investigations on LFIMC of Au_{25} will be able to add more details and understanding of the physical mechanism of this effect. Interestingly, due to the presence of LFIMC, Au_{25} NCs can be potentially utilized in biosensing and molecular computing applications.[53-57]

Alternatively, by using a model where two-photon absorption occurs via a two-level system, I was able to determine the possibility of electric field sensing of these isolated single nanoclusters when TPEF excitation is used. Since some two-photon fluorescent proteins were reported for such electric field sensing ability, the actual mechanism of enhancement may also be explained using possible local electric fields.[49-52] However, the reasons for the presence of such electric fields on a plasma cleaned substrate are not clear. It is possible that the electric *field-gradient* arising from the optical near-field excitation may be causing the enhancement in this instance. [64]

When compared to isolated Au_{25} single nanocluster two-photon absorption cross section (0.69 x 10^6 GM), the per-cluster TPEF response for Au_{25} aggregate was weaker at least by a *factor of 4.4*. This decrease in two-photon absorption cross section can be attributed to inter-nanocluster interactions that could be veiling the quantum confinement effects present in these systems. The local field effects exerted by neighboring nanoclusters may be reducing the two-photon absorption cross section of these materials. Since the TPEF response for certain other aggregates did not give observable TPEF NSOM responses, I think that the inter-nanocluster distance and the geometry of the nanocluster packing in an aggregate should be playing a crucial role in either enhancing or quenching the two-photon absorption effects. This phenomenon was predicted by Kaplan and Volkov [53] from a different perspective indicating that certain magic number arrangements of systems can give either enhanced or reduced local electric fields. Since these quantum cluster systems possess relatively large number of valence electrons, and their atomic arrangement and arrangement in aggregates can form "magic number systems", I think that their local field effects could be able to explain the observations described above. This in turn opens up another possibility to be tested in the field of nanocluster arrays. If ideal inter-nanocluster distances for local field enhancements of adjacent nanoclusters can be found (e.g. nanoclusters connected via covalent bonds), one may be able to enhance the two-photon absorption cross section by at least an order of magnitude (or more)! Therefore, through the investigations of Au_{25} aggregate TPEF NSOM response, I was able to unveil the possible roles played by inter-nanocluster interactions in nanocluster ensembles and their ability to hide the native effects of isolated single elemental nanoclusters. Therefore, it is clear that when I was able to remove the nanoclusters from the nanocluster aggregates, a significant enhancement in two-photon absorption cross section is observed likely due to the removal of inter-nanocluster interactions while giving rise to the local field enhancement from the magic cluster itself resulting in an enhanced two-photon absorption cross section.

The local field enhanced two-photon absorption observed for TPEF NSOM of isolated single Au_{25} NCs clearly indicates the possibility of using these materials in exciting applications such as biosensing, molecular computing and molecular logic. Also, due to the very small size of these nanoclusters (~1.2 nm diameter) they are strong candidates for use in < 10 nm semiconductors/transistors. Author feels that as metal oxide based semiconductors suffer heat related problems with current flow below 10 nm dimensions, if the local field induced excitons (a form of standing wave called *locsitons* occurring due to spatial arrangement of atoms/nanoclusters) can be adopted, next generation molecular transistors or literally *nano-sized computers* may come from these quantum-confined noble metal nanoclusters or nanocluster arrays aligned/connected with specific geometries!

3.9 Supporting information

3.9.1: Two-photon excited fluorescence (TPEF) near-field scanning optical microscopy (NSOM)

As indicated in figure 3-6 of the main text we were able to obtain TPEF NSOM for 1.4 nM solutions spin-coated on plasma cleaned glass substrates. The quadratic dependence of NSOM counts on background counts proves a nonlinear photoexcitation that is giving rise to the NSOM fluorescence signal. Another TPEF NSOM image and its corresponding quadratic dependence on

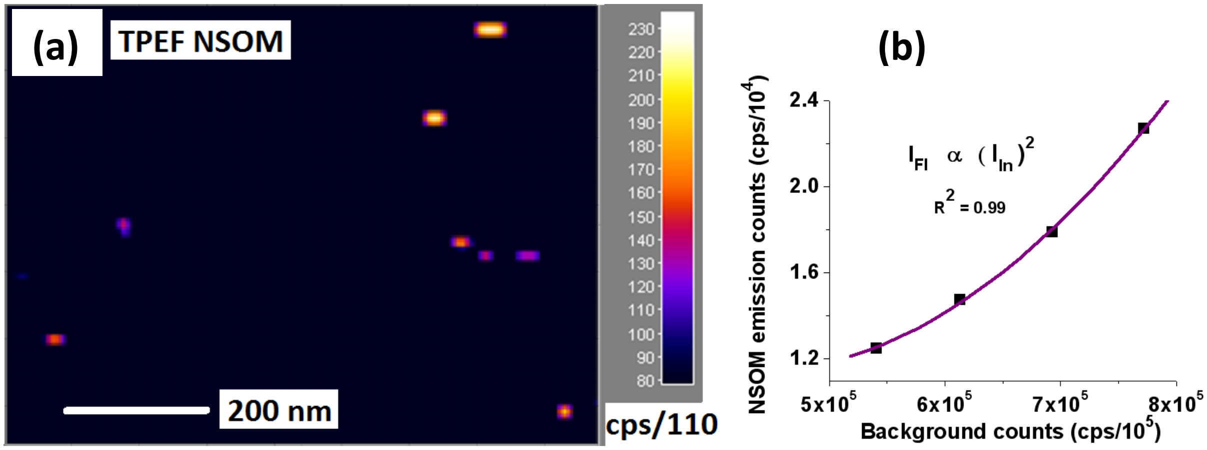

Figure 3-11: TPEF NSOM of Au_{25} single nanoclusters and quadratic dependence

(a) TPEF NSOM image of $Au_{25}SG_{18}$ single nanocluster concentrations (by spin-coating 1.4 nM solution on plasma cleaned glass). This was another sample prepared using the same conditions (volume, plasma cleaned glass and) as the sample presented in figure 3 of the main text. TPEF NSOM feature density was again ~20 features/µm^2 consistent with other TPEF NSOM images observed. TPEF counts observed for the highest intensity feature was ~25,000 cps for ~600 µW near-field excitation. (b) Plot of fluorescence intensity versus incident background intensity. The quadratic dependence proves TPEF response from the NSOM fluorescence.

fluorescence is shown in figure 3-11. The sample preparation conditions were the same as that was used for the TPEF NSOM samples mentioned in the main text indicating that for $Au_{25}SG_{18}$ the TPEF NSOM signal is obtained reproducibly. The log-log plot for the image in the figure 3-11 shows a slope of ~1.65.

3.9.2 STEM image size distribution analysis and the estimation of nanocluster density for the samples used for single nanocluster TPEF NSOM

As indicated in the experimental section, STEM imaging was conducted on 120 nM solutions (pH=7.2) of $Au_{25}SG_{18}$ drop cast (1 µL) on Holey carbon copper grids. The sample was left in air for >10 minutes for drying. Subsequently, the STEM imaging was conducted using a JEM-2100F electron microscope with a CEOS probe corrector. As was depicted in figure 3-4 of the main text,

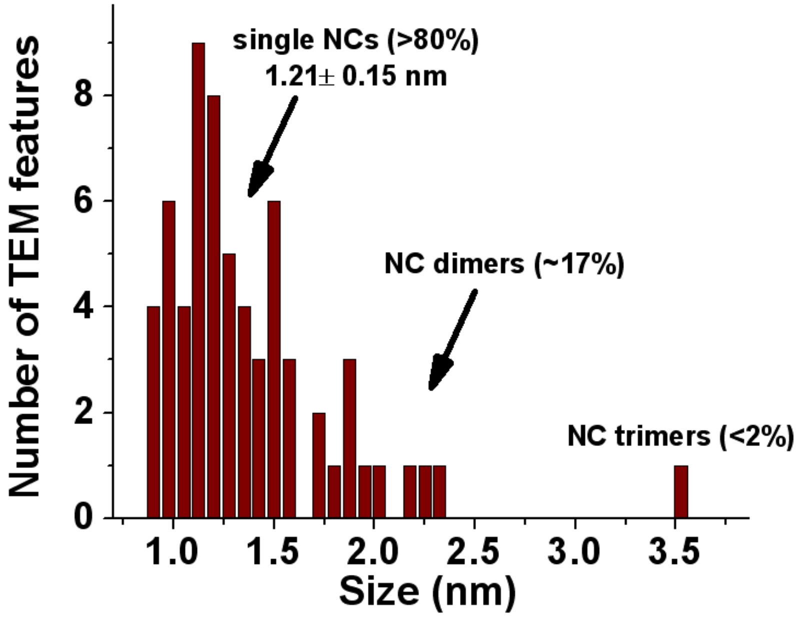

Figure 3-12: STEM analysis of $Au_{25}SG_{18}$ nanoclusters for 120 nM solution drop cast and air-dried on solid substrate

isolated single nanoclusters were observed with >80% abundance indicating that single nanoclusters are indeed isolated on the surface even if the conditions (concentration and drying duration) are highly favorable for aggregation. As depicted in figure 3-12, we were able to identify three different sizes for STEM imaging size distribution analysis. It is clear that only < 20% of nanoclusters were forming multimers (aggregates) and no features were present larger than ~3.6 nm. This clearly justifies the use of pH=7.2 for dissolution and disassembly of $Au_{25}SG_{18}$ nanoclusters into *isolated single nanoclusters* in solution. Also, it can be inferred that the aggregation have resulted from the inter-nanocluster encounters while the solvent was drying. Therefore, as shown in 3.9.2(a), we can calculate the number of inter-nanocluster collisions possible while the solvent is evaporating.

3.9.2 (a). Calculating the time between inter-nanocluster collisions and the number of inter-nanocluster encounters while the solvent drying

First, diffusion coefficient for the Au_{25} nanocluster motion in solution can be calculated as follows.

$$D \;=\; \frac{kT}{6\pi\eta r} \text{ ------- (5)}$$

D – Diffusion coefficient

k- Boltzmann constant ($1.38\text{x}\ 10^{-23}\ JK^{-1}$)

T – Absolute temperature (K)

η – Viscosity (1.0 cP= $1.0\text{x}10^{-3}$ Pa.s, for Water at 298 K)

r- radius of a Au_{25} nanocluster (~1.0 nm with the ligand)

By substituting the known values for equation 5,

$$D \;=\; \frac{1.38*10^{-23}*298}{6\pi*1.0*10^{-3}*1.0*10^{-9}} \text{ ------- (5)}$$

$D = 2.21 \text{ x } 10^{-10}\ m^2s^{-1}$ ($2.21 \text{ x } 10^{-6}\ cm^2s^{-1}$)

For a bi-molecular encounter, the Arrhenius constant (A_{diff}) for collisions,

$$\mathrm{A(diff)} = \frac{4\pi(r+r)(D+D)N}{1000} \text{ ------- (6)}$$

r-radius of a nanocluster

D –Diffusion coefficient (calculated from equation 5, 2.21 x 10^{-6} cm^2s^{-1})

N – Avogadro number (6.022 x 10^{23} mol^{-1})

By substituting for equation 6,

$$A(\text{diff}) = \frac{4\pi*(1.0+1.0)*10^{-7}*(2.21+2.21)*10^{-6}*6.022*10^{23}}{1000} \text{ ------- (6)}$$

A(diff) = 0.767 x 10^{10} $M^{-1}s^{-1}$

Since this is equal to the second order rate constant (due to zero activation barrier for *diffusion controlled motion* at 298 K) one can calculate the rate of collisional encounters for the given concentrations as a pseudo first order rate constant (k’) by multiplying with the Au_{25} concentration (C =120 nM).

Therefore, Rate = k’C

Rate = 0.767 x 10^{10} $M^{-1}s^{-1}$ x 120 x 10^{-9} M

Rate of inter-cluster collisions = 920 s^{-1}

Therefore, since the drying time is ~ 10 minutes (~ 600 s) the average number of collisions while the solvent is drying ~ 920 s^{-1} x 600 s ~ 552,000 ~ 0.55 million collisions.

3.9.2 (b). Calculating the high probability (>99.9%) of obtaining isolated single nanoclusters on the plasma cleaned glass substrates for 1.4 nM solutions

As determined in the previous section, the number of inter-nanocluster collisions while the solvent is evaporating ~ 0.55×10^6

Since the number of collisions is directly proportional to the nanocluster encounters and aggregation, we can state that the <20% aggregation observed for the 120 nM solution of $Au_{25}SG_{18}$ nanoclusters is proportional to the 0.55 million collisions that have taken place while the solvent was drying. However, for the preparation of TPEF NSOM samples we used *spin-coating* which causes the solvent to evaporate rapidly. Subsequently, a vacuum of 10 inHg is applied expediting the evaporation of any left-over solvent. At the same time, for TPEF NSOM we have used ~85-fold diluted $Au_{25}SG_{18}$ nanocluster solutions causing the collision frequency to be reduced ~85-fold (new collision frequency ~11 s^{-1}). Therefore, assuming that solvent evaporation is complete within the duration of spin-coating and application of vacuum (<200 s) the number of possible inter-nanocluster collisions are as follows.

Number of inter-nanocluster collisions ~ 11 s^{-1} x 200 s ~ 2200 collisions

Therefore, we can calculate the likelihood of aggregation for the 1.4 nM sample used for TPEF NSOM.

0.55×10^6 collisions α 20 % aggregation --- (1)

2200 collisions α x % aggregation --- (2)

Therefore, the likelihood of aggregation = $20 \times 2200 / 0.55 \times 10^6$

x = **0.08 %**

Therefore, it is clear that the ***likelihood of obtaining isolated single nanoclusters on the plasma cleaned glass substrate is >99.9%***.

3.9.2 (c). Calculating the average inter-nanocluster distances for the TPEF NSOM sample

From the analysis of figure 3-5(b) we were able to find that there were ~80 nanoclusters on the substrate within a ~70 nm x ~70 nm field of view (when all nanoclusters, i.e., single nanoclusters, dimers and trimers were taken in to account).

This gives us an average nanocluster density of, 80/(0.07 x 0.07) per μm^2

~ 16,300 nanoclusters/μm^2

We can approximate the nanocluster distribution on the substrate to a 2-D lattice with the average shortest inter-nanocluster distance to be "y (nm)" (as depicted in figure 3-13).

Therefore, the number of nanoclusters present (aligned) in one direction ~(1000/y)

Total number of nanoclusters on the 1000 nm x 1000 nm field of view ~ $(1000/y)^2$

Therefore, $(1000/y)^2 = 16,300$

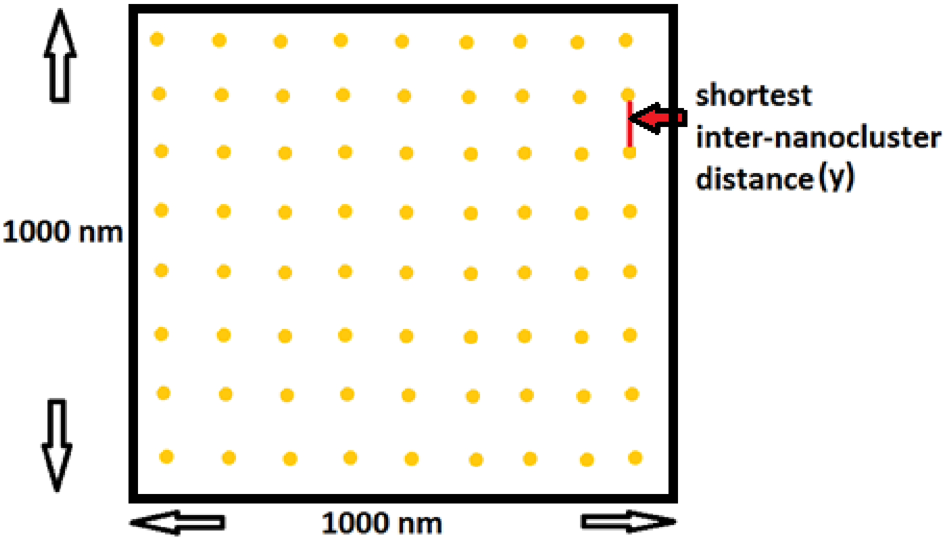

Figure 3-13: Schematic of a uniform nanocluster distribution on a substrate to determine the average inter-nanocluster distance

In other words, **y (inter-nanocluster distance for 120 nM sample drop-cast) ~ 7.8 nm**.

This agrees well with the observed STEM image shown in figure 3-5(b).

Since we are using an 85-fold diluted solution for the spin-coating of $Au_{25}SG_{18}$ nanoclusters on plasma cleaned glass substrate and by taking into account that 4 times were used for spin-coating, we can calculate the inter-nanocluster distance for the TPEF NSOM sample. The average number of nanoclusters dropped on to the solid (glass) substrate is reduced by ~21-fold (85/4). However, since the spin-coating procedure causes ~95% of the solution to be thrown away the actual number of nanoclusters left on the substrate is reduced by 420-fold (21x 20).

This indicates that the **nanocluster density for *TPEF NSOM samples*** should be,

~ 16,300/420 nanoclusters/μm^2 ~ 39 nanoclusters/μm^2

Also, one must note that since this density was due to *drop-casting* the value we obtain here is an overestimation since the nanoclusters are more or less concentrated in specific areas due to slow evaporation of the solvent.

Since, $(1000/y)^2 = 39$

y ~ 160 nm.

This clearly indicates that the ***single nanoclusters are isolated and separated by ~160 nm*** (on average) distances on the substrate. Also, the observed TPEF NSOM feature density of ~23 features/μm^2 agrees well with the expected density (~39 nanoclusters/μm^2) within a factor (and the overestimation of the density derived from STEM/TEM could be due to the congregation of nanoclusters since the solvent evaporates very slowly for the drop-cast technique. For example, with the STEM/TEM scans we were able to find areas on the Holey carbon copper grids where no nanoclusters were present.

Therefore, our *STEM/TEM analysis, inter-nanocluster collision calculations* and *inter-nanocluster distance calculations* all agree with the observed TPEF NSOM feature densities and they further prove that ***$Au_{25}SG_{18}$* single nanoclusters are indeed isolated and separated by sufficient distances (~160 nm) to be individually excited by a ~40 nm diameter NSOM probe**.

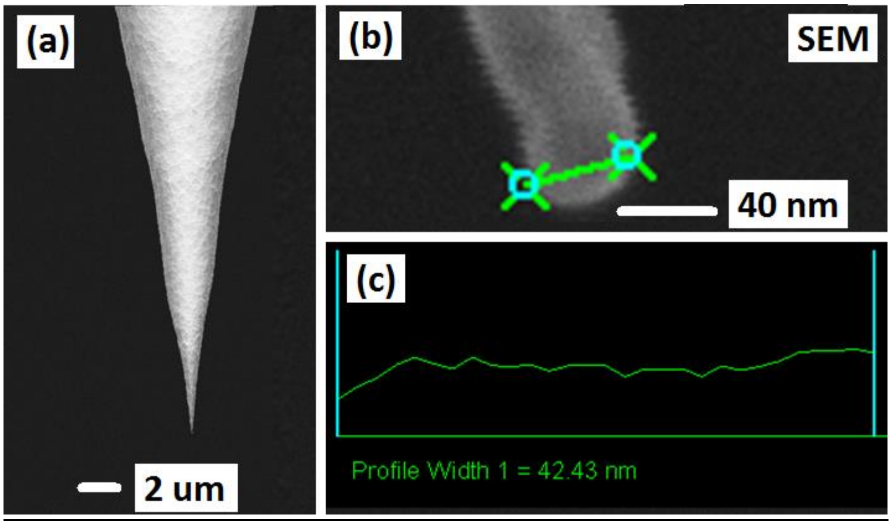

Figure 3-14: SEM image of a sample NSOM probe used with ~40 nm tip diameter (a) SEM image of ~10 um x ~18 um field of view (b) zoomed in SEM image of the NSOM tip (c) SEM profile

3.9.3 Calculation of two-photon absorption (TPA) cross section for single $Au_{25}SG_{18}$ nanoclusters

To calculate the two-photon absorption cross section for Au_{25} single clusters, single molecule TPEF NSOM counts for sub-monolayer Rhodamine B was measured (Rhodamine B photo-bleached in one scan). For similar background counts (and coupling powers) the TPEF counts for both Au_{25} single clusters and Rhodamine B single molecules were substituted for the following equation, [65]

$$< F(t) > = 0.5\ g\emptyset\eta_2\delta C\ \frac{8n<P(t)>^2}{\pi\lambda} \text{ ------- (1)}$$

Where, $< F(t) >$ = Average fluorescence rate,

$g = \frac{<I(t)^2>}{<I(t)>^2}$,

$\emptyset$ = Fluorescence collection efficiency of the optical set up (at the emission wavelength),

η_2 = Fluorescence quantum yield of the chromophore,

C = Concentration of the sample,

δ = Two photon absorption cross section,

n = Refractive index of the sample medium (assumed to be 1.0 for air),

$< P(t) >$ = Average excitation power,

λ = Wavelength of emission

For Rhodamine B single scan,

$$7555 = 0.5\, g * 0.99\emptyset * (0.70 * 260\ GM)C\ \frac{8*1.0*<0.000192>^2}{\pi*570} \text{ ---------- } (2)$$

$$26337 = 0.5\, g * 0.97\emptyset * (\eta_2 * \delta)C\ \frac{8*1.0*<0.000624>^2}{\pi*650} \text{ ----------- } (3)$$

Therefore, by dividing equation (2) from (3), for Au_{25} single cluster TPEF on solid phase the average Two-Photon Action Cross Section is (solid state emission wavelength for Au_{25} NCs was obtained from reference 66),

$(\eta_2 * \delta)$ = 69.9 GM

δ = 69.9 GM/ **1×10^{-4} =** 0.699×10^6 GM

$\delta_{solid} \sim 1.64 \times \delta_{solution\ ensemble}$

It is clear that the average TPA cross section of $Au_{25}SG_{18}$ single nanoclusters are **enhanced by 64%** compared to the previously reported solution-phase ensemble average value. This can be attributed to local electric field enhancement effects induced by the plasma cleaned glass substrate. Also, as can be observed in figure 3-6(a), it is clear that the distribution of δ_{solid} is not symmetrical which may hint at the possible heterogeneities of the local electric charge distributions on the substrate.

3.9.4: Accounting for the enhancement in two-photon absorption cross section

In order to further understand the enhancement observed, the two-photon absorption process with respect to a two-level approximation can be considered as depicted in the following equation. [67]

$$\delta\ (\nu_{10}) = \frac{4(1+2\ cos^2\alpha)}{5}\ \frac{\pi 10^3 \ln 10\ f^2}{hc^2\ N_A\ n}\ |\Delta\ \mu_{10}|^2\ \frac{\varepsilon(\nu_{10})}{\nu_{10}}$$

The terms of the equation can be defined as follows.

δ – two-photon absorption cross section

α – angle between transition dipole moment and $\Delta\mu_{10}$

f – local field factor = $(n^2+2)/3$

$\Delta\mu_{10}$ – difference between the permanent dipoles of the *ground* state and the *excited* state

ε - molar extinction coefficient

ν_{10} – frequency of the transition

Local field factor (f_{Hex}) for Hexane = $(1.37^2+2)/3 = 1.29$

Local field factor (f_{Air}) for air = $(1.00^2+2)/3 = 1.00$

Therefore, f^2/n for Hexane = $(1.29)^2/1.37 = 1.21$

By substituting for the above equation, 0.427×10^6 GM α $1.21 \times |\Delta\mu_{10}\,(\mathrm{Hex})|^2$ (for Hexane)

For air: 0.699×10^6 GM α $1.00 \times |\Delta\mu_{10}\,(\mathrm{On\ solid/Air})|^2$

By solving for the above relation (assuming the α remains unaltered)

$\Delta\mu_{10}$ (On solid/Air) = **1.33** x $\Delta\mu_{10}$ (Hex)

Therefore, the difference between permanent dipole moment is enhanced by *1.33* when moved on to the solid substrate. This enhancement can be attributed to an *electric-field-induced dipole moment change* due to a change in polarizability of the excited state with respect to the ground state. [68, 69]

3.9.5: Best TPEF NSOM point resolution observed was 30 nm

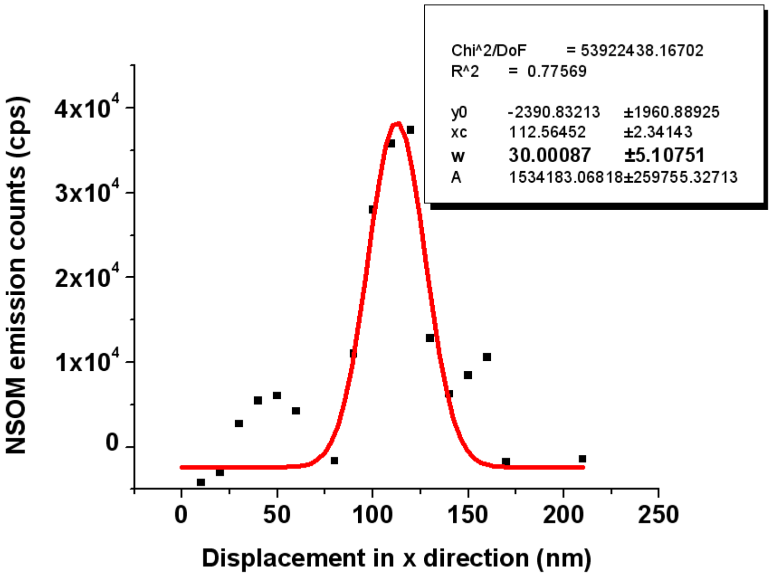

Figure 3-15: Gaussian fit for the raw data of a TPEF NSOM feature with S/N~7

3.9.6: Comparison of the steady state absorption spectra of $Au_{25}SG_{18}$ when moving from pH=5.0 to pH=7.0

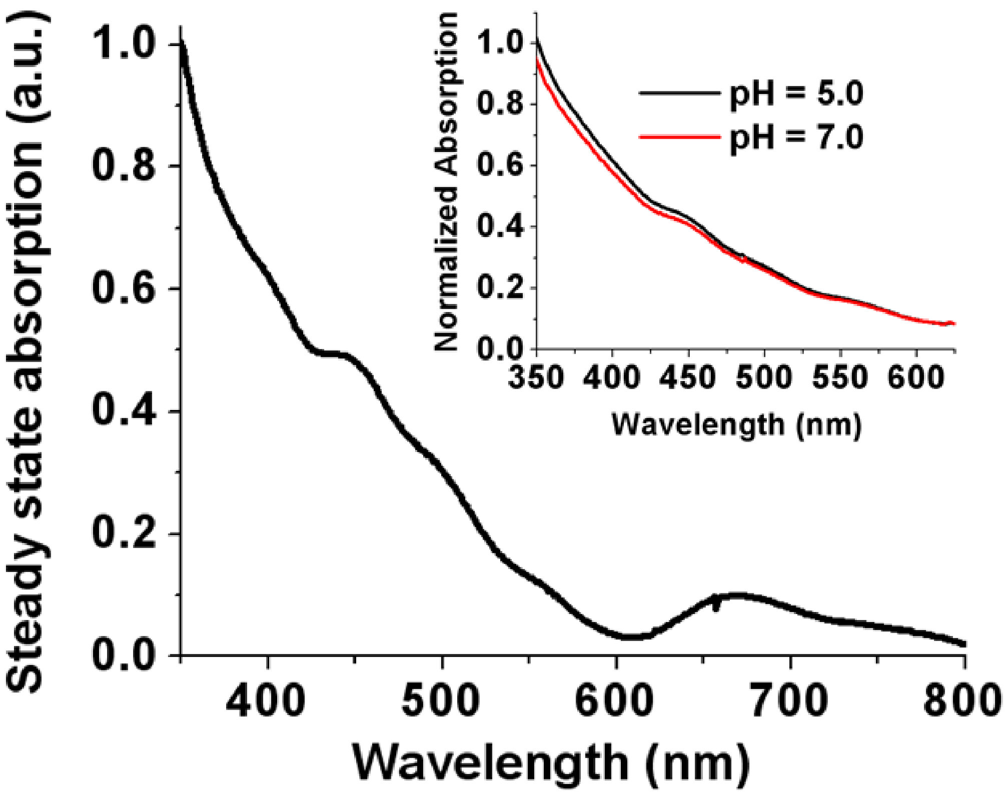

Figure 3-16: Comparison of the steady state absorption spectra of $Au_{25}SG_{18}$ when moving from pH=5.0 to pH=7.0

In the inset of the figure 3-15, the spectra were normalized at 625 nm (minimum point after the 400-500 nm absorption) which reveals only ~ 10 nm blue shift in absorption when the pH was increased from pH=5.0 to pH=7.0.

3.9.7: AFM images for different Au_{25} NC solution concentrations spin-coated on glass substrates in the *absence* of pH induced disassembly

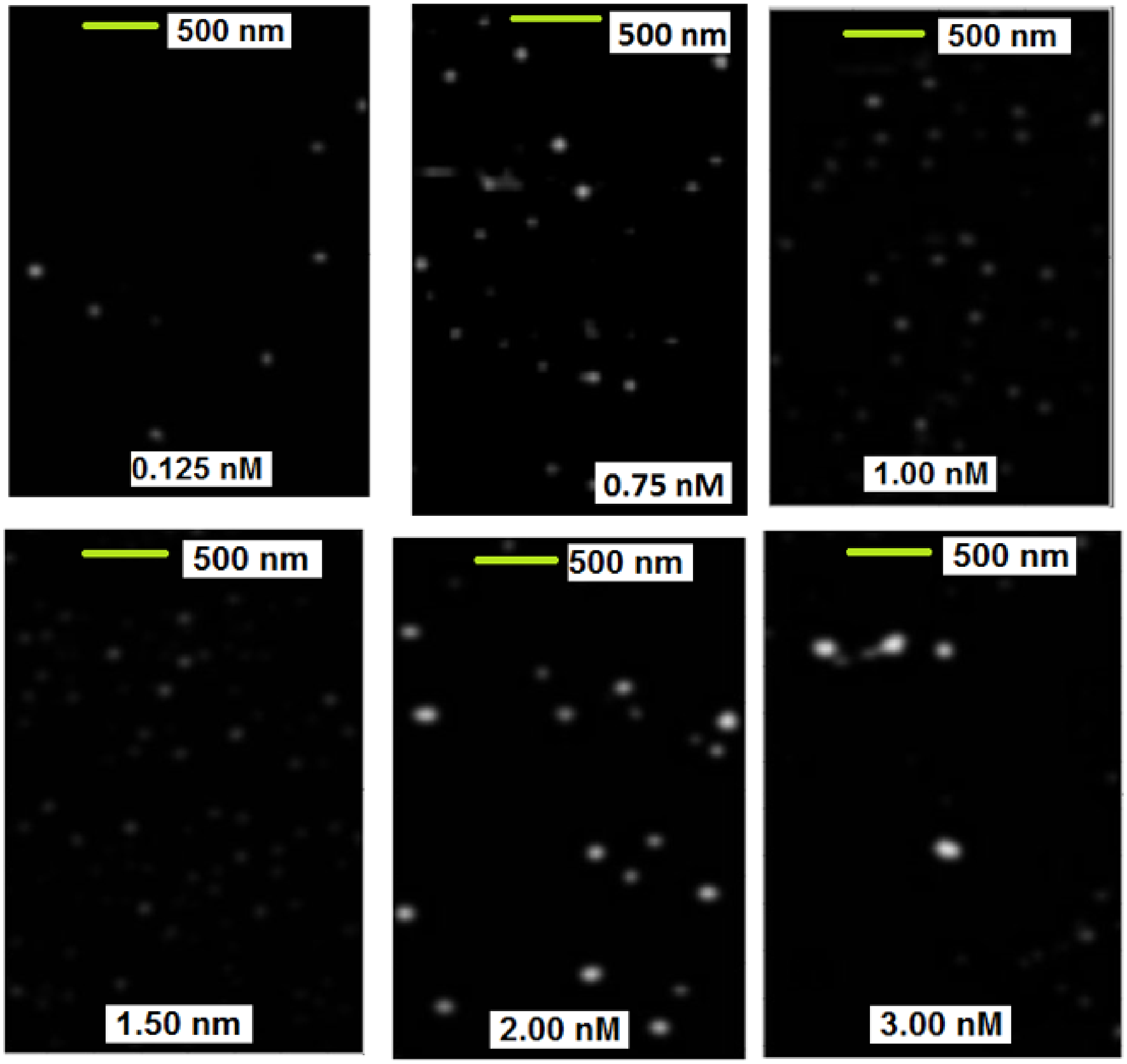

Figure 3-17: AFM images for different Au_{25} NC solution concentrations spin-coated on glass substrates in the *absence* of pH induced disassembly

3.9.8: Concentration dependent AFM feature density for Au_{25} NCs solutions spin coated on glass substrates in the absence of pH induced disassembly

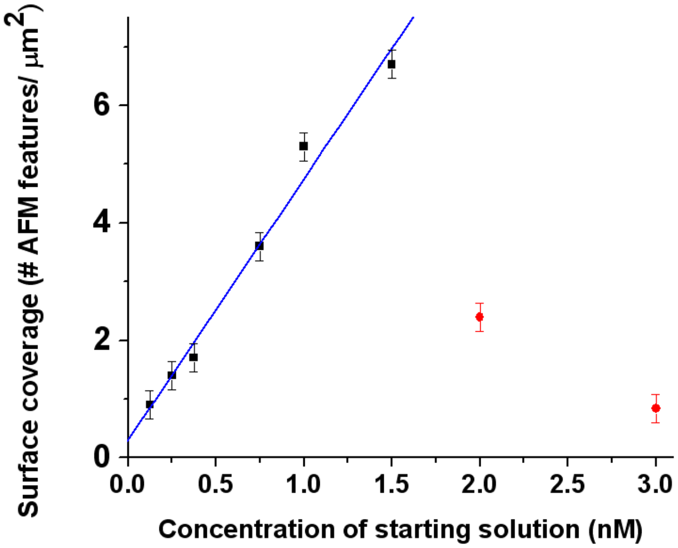

Figure 3-18: Concentration dependent AFM feature density for Au_{25} NCs solutions spin coated on glass substrates in the absence of pH induced disassembly

3.10 References

1. Jadzinsky, P. D. *et al*. Structure of a thiol monolayer-protected gold nanoparticle at 1.1 Å resolution. *Science* **318,** 430-433 (2007).
2. Li, Z. Y. *et al*. Three-dimensional atomic-scale structure of size-selected gold nanoclusters. *Nature*. **451,** 46-48 (2008).
3. Zhu, M. *et al*. Correlating the crystal structure of a thiol-protected Au_{25} cluster and optical properties. *J. Am. Chem. Soc.* **130,** 5883-5885 (2008).
4. Heaven, M. W. *et al*. Crystal structure of the gold nanoparticle $[N(C_8H_{17})_4][Au_{25}(SCH_2CH_2Ph)_{18}]$. *J. Am. Chem. Soc.* **130,** 3754-3755 (2008).
5. Desireddy, A. *et al*. Ultrastable silver nanoparticles. *Nature*. **501,** 399-402 (2013).
6. Yang, H. *et al*. All-thiol-stabilized Ag_{44} and $Au_{12}Ag_{32}$ nanoparticles with single crystal structures. *Nat. Commun.* **4,** 2422 (2013).
7. Azubel, M. *et al*. Electron microscopy of gold nanoparticles at atomic resolution. *Science* **345,** 909-912 (2014).

8. Lopez-Acevedo, O., Kacprzak, K. A., Akola, J. & Hakkinen, H., Quantum size effects in ambient CO oxidation catalyzed by ligand-protected gold clusters, *Nature Chem.* **2,** 329-334 (2010).
9. Chen, S. *et al*. Gold nanoelectrodes of varied size: Transition to molecule-like charging. *Science* **280,** 2098-2101 (1998).
10. Zhu, M. *et al*. Reversible switching of magnetism in thiolate-protected Au_{25} superatoms. *J. Am. Chem. Soc.* **131,** 2490-2492 (2009).
11. Yau, S. H., Varnavski, O. & Goodson III, T. An ultrafast look at Au nanoclusters. *Acc. Chem. Res.* **46,** 1506-1516 (2013).
12. Varnavski, O. *et al*. Critical size for the quantum confinement in optically excited gold clusters. *J. Am. Chem. Soc.* **132,** 16-17 (2010).
13. Yuan, X. *et al*. Highly luminescent silver nanoclusters with tunable emissions: cyclic reduction-decomposition synthesis and antimicrobial properties. *NPG Asia Materials* **5,** e39 (2013).
14. Yau, S. H., *et al*. Bright two-photon emission and ultrafast relaxation dynamics in a DNA-templated nanocluster investigated by ultrafast spectroscopy. *Nanoscale* **4,** 4247-4254 (2012).
15. Ramakrishna, G. *et al*. Quantum-sized gold nanoclusters as efficient two-photon absorbers. *J. Am. Chem. Soc.* **130,** 5032-5033 (2008).
16. Moerner, W. E. & Fromm, D. P. Methods of single molecule fluorescence spectroscopy and microscopy. *Review of Scientific Instruments* **74,** 3597-3619 (2003).
17. Scholl, J. A., Koh, A. L. & Dionne, J. A. Quantum plasmon resonances of individual metallic nanoparticles. *Nature* **483,** 421-428 (2012).
18. Bahena, D. *et al*. STEM electron diffraction and high resolution images used in the determination of the crystal structure of the $Au_{144}(SR)_{60}$ cluster. *J. Phys. Chem. Lett.* **4,** 975-981 (2013).
19. Jian, N. *et al.* Hybrid atomic structure of the Schmid cluster $Au_{55}(PPh_3)_{12}Cl_6$ resolved by aberration-corrected STEM. *Nanoscale* **7,** 885-888 (2015).
20. Rittweger, E., Han, K. Y., Irvine, S. E., Eggeling, C. & Hell, S. W. STED microscopy reveals crystal colour centres with nanometric resolution. *Nature Photon.* **3,** 144-147 (2009).
21. Hell, S. W. Toward fluorescence nanoscopy. *Nat. Biotechnol.* **21,** 1347-1355 (2003).
22. Hell, S. W. Far-field optical nanoscopy. *Science*. **316,** 1153-1158 (2007).

23. Westphal, V., Kastrup, L. & Hell, S. W. Lateral resolution of 28 nm (λ/25) in far-field fluorescence microscopy. *Appl. Phys. B* **77,** 377-380 (2003).
24. Betzig, E. & Chichester, R. J. Single molecules observed by near-field scanning optical microscopy. *Science*. **262,** 1422-1425. (1993).
25. Betzig, E. & Trautman, J. K. Near-field optics: Microscopy, spectroscopy, and surface modification beyond the diffraction limit. *Science*. **257,** 189-195 (1992).
26. Xie, X. S. & Dunn, R. C. Probing single molecule dynamics. *Science* **265,** 361-364 (1994).
27. Trautman, J. K., Macklin, J. J., Brus, L. E. & Betzig, E. Near-field spectroscopy of single molecules at room temperature. *Nature* **369,** 40-42. (1994).
28. Betzig, E., Trautman, J. K., Harris, T. D., Weiner, J. S. & Kostelak, R. L. Breaking the diffraction barrier: Optical microscopy on a nanometric scale. *Science* **251,** 1468-1470 (1991).
29. Betzig, E., Lewsi, A., Harootunian, A., Isaacson, M & Kratschmer, E. Near-field scanning optical microscopy (NSOM): Development and biophysical applications. *Biophys. J.* **49,** 269-279 (1986).
30. Sanchez, E. J., Novotny, L. & Xie, X. S. Near-field fluorescence microscopy based on two-photon excitation with metal tips. *Phys. Rev. Lett.* **82,** 4014-4017 (1999).
31. Grotjohann, T. *et al.* Diffraction-unlimited all-optical imaging and writing with a photochromic GFP. *Nature.* **478,** 204-208 (2011).
32. Denk, W., Strickler, J. H. & Webb, W. W. Two-photon laser scanning fluorescence microscopy. *Science* **248,** 73-76 (1990).
33. Jarret, J. W., Zhao, T., Johnson, J. S. & Knappenberger, Jr., K. L. Investigating plasmonic structure-dependent light amplification and electronic dynamics using advances in nonlinear optical microscopy. *J. Phys. Chem. C* **119,** 15779-15800 (2015).
34. Jarret, J. W. *et al.* Plasmon mediated two-photon photoluminescence-detected circular dichroism in gold nanosphere assemblies. *J. Phys. Chem. Lett.* **7,** 765-770 (2016).
35. Lewis, M. K., Wolanin, P., Gafni, A. & Steel, D. G. Near-field scanning optical microscopy of single molecules by femtosecond two-photon excitation. *Opt. Lett.* **23,** 1111-1113 (1998).
36. Ho Wu, R., Yau, S. H. & Goodson III, T. Linear and nonlinear optical properties of monolayer protected gold nanocluster films. *ACS Nano* **10,** 562-572 (2016).
37. Wu, Z. & Jin, R. On the ligand's role in the fluorescence of gold nanoclusters. *Nano Lett.* **10,** 2568-2573 (2010).

38. Dulkeith, E. *et al*. Plasmon emission in photoexcited gold nanoparticles. *Phys. Rev. B* **70,** 205424 (2004).
39. Goodson III, T., Varnavski, O. & Wang, Y. Optical properties and applications of dendrimer-metal nanocomposites. *Int. Rev. Phys. Chem.* **23,** 109-150 (2004).
40. Mooradian, A., Photoluminescence of metals. *Phys. Rev. Lett.* **22,** 185 (1969).
41. Wu, Z., Shuhan, J. & Jin, R. One-pot synthesis of atomically monodisperse, thiol-functionalized Au_{25} nanoclusters. *J. Mater. Chem.* **130,** 622-626 (2009).
42. Qian, H., Zhu, M., Wu, Z. & Jin, R. Quantum sized gold nanoclusters with atomic precision. *Acc. Chem. Res.* **45,** 1470-1479 (2012).
43. Zhu, M., Lanni, E., Garg, N., Bier, M. E. & Jin, R. Kinetically controlled, high-yield synthesis of Au_{25} clusters. *J. Am. Chem. Soc.* **130,** 1138-1139 (2008).
44. Negishi, Y. *et al*. Origin of magic stability of thiolated gold clusters: A case study on $Au_{25}(SC_6H_{13})_{18}$. *J. Am. Chem. Soc.* **129,** 11322-11323 (2008).
45. Kirchner, C. *et al*. Cytotoxicity of colloidal CdSe and CdSe/ZnS nanoparticles. *Nano Lett.* **5,** 331-338 (2005).
46. Negishi, Y., Nobusada, K. & Tsukuda, T. Glutathione-protected gold clusters revisited: Bridging the gap between gold (I)-thiolate complexes and thiolate-protected gold nanocrystals. *J. Am. Chem. Soc.* **127,** 5261-5270 (2005).
47. Yip, W-T., Hu, D., Yu, J., Bout, D. A. V. & Barbara, P. F. Classifying the photophysical dynamics of single- and multi-chromophoric molecules by single molecule spectroscopy. *J. Phys. Chem. A* **102,** 7564-7575 (1998).
48. Wang, Y. & Herron, N. Nanometer-sized semiconductor clusters: Materials synthesis, quantum size effects, and photophysical properties. *J. Phys. Chem.* **95,** 525-532 (1991).
49. Drobizhev, M., Makarov, N. S., Hughes, T. & Rebane, A. Resonance enhancement of two-photon absorption in fluorescent proteins. *J. Phys. Chem. B* **111,** 14501-14504 (2007).
50. Drobizhev, M., Makarov, N. S., Tillo, S. E., Hughes, T. & Rebane, A. Two-photon absorption properties of fluorescent proteins. *Nature Methods* **8,** 393-399 (2011).
51. Ponder, M. & Mathies, R. Excited-state polarizabilities and dipole moments of Diphenylpolyenes and Retinal. *J. Phys. Chem.* **87,** 5090-5098 (1983).
52. Drobizhev, M., Scott, J. N., Callis, P. R. & Rebane, A. All-optical sensing of the components of the internal local electric field in proteins. *IEEE Photonics J.* **4,** 1996-2001 (2012).

53. Kaplan, A. E. & Volkov, S. N. Nanoscale stratification of local optical fields in low dimensional atomic lattices. *Phys. Rev. Lett.* **101,** 133902 (2008).
54. Bedeaux, D. & Bloembergen, N. On the relation between macroscopic and microscopic nonlinearities. *Opt. J. Eur. Opt. Soc. Part B* **69,** 57-66 (1973).
55. Dolgaleva, K., Boyd, R. W. & Sipe, J. E. Cascaded nonlinearity caused by local field effects in the two-level atom. *Phys. Rev. A* **76,** 063806 (2007).
56. Baev, A., Autschbach, J., Boyd, R. W. Prasad, P. N. Microscopic cascading of second order molecular nonlinearity: new design principles for enhancing third order nonlinearity. *Opt. Express* **18,** 8713-8721 (2010).
57. Dolgaleva, K. & Boyd, R. W. Local field effects in nanostructured photonic materials. *Advances in Optics and Photonics* **4,** 1-77 (2012).
58. Cox, G. & Sheppard, C. J. R. Practical limits of resolution in confocal and nonlinear microscopy. *Microsc. Res. Tech.* **63,** 18-22 (2004).
59. Huang, X., Atwood, C. S., Moir, R. D., Hartshorn, M. A., Vonsattel, J.-P., Tanzi, R. E., & Bush, A. I. Zinc-induced Alzhemier's A-*beta*-140 Aggregation is Mediated by Conformational factors. *J. Biol. Chem.* **272,** 26464-26470 (1997).
60. Atwood, C. S., Moir, R. D., Huang, X., Scarpa, R. C., Bacarra, N. M., Romano, D. M., Hartshorn, M. A., J.-P., Tanzi, R. E., & Bush, A. I. Dramatic Aggregation of Alzheimer A-*beta* by Cu(II) is Induced by Conditions Representing Physiological Acidosis. *J. Biol. Chem.* **273,** 12817-12826 (1998).
61. Curtain, C. C., Ali, F., Volitakis, I., Cherny, R. A., Norton, R. S., Beyreuther, K., Barrow, C, J., Masters, C. L., Bush, A. I., & Barnham, K. J. Alzheimer's disease Amyloid-*beta* Binds Copper and Zinc to generate an Allosterically Ordered Membrane Penetrating Structure Containing Superoxide Dismutase-like Subunits. *J. Biol. Chem.* **276,** 20466-20473 (2001).
62. Using live cells, we have conducted cell-insertion studies of water soluble Au_{25} nanoclusters. Subsequently, we have excited the cells using increasing laser intensities which indicated a clear signature of cell insertion in live cells and retaining of the nanoclusters while the imaging was conducted. Also, accelerated cell damage was observed for nanocluster-inserted cells indicating the potential to conduct cancer cell therapy. No cell toxicity of the nanoclusters was observed throughout the study. This work will be submitted soon in a separate article.

63. Raymond, J. E. & Goodson, III, T. Single-particle two-photon absorption imaging and enhancement determination for organic nanoparticles. *J. Phys. Chem. Lett.* **2,** 329-333 (2011).
64. Yamaguchi, M., Nobusada, K., Kawazoe, T. & Takashi, Y. Two-photon absorption induced by electric field gradient of optical near-field and its application to photolithography. *Appl. Phys. Lett.* **106,** 191103 (2015).
65. Xu, C. & Webb, W. W. Measurement of two photon excitation cross sections of molecular fluorophores with data from 690 to 1050 nm. *J. Opt. Soc. Am. B* **13**, *481–491* (1996).
66. Shibu, E. S., Muhammed, M. A., Tsukuda, T. & Pradeep, T. Ligand exchange of $Au_{25}SG_{18}$ leading to functionalized gold clusters: spectroscopy, kinetics, and luminescence. *J. Phys. Chem. C* **112,** 12168-12176 (2008).
67. Drobizhev, M., Makarov, N. S., Hughes, T. & Rebane, A. Resonance enhancement of two-photon absorption in fluorescent proteins. *J. Phys. Chem. B* **111,** 14501-14504 (2007).
68. Drobizhev, M., Makarov, N. S., Tillo, S. E., Hughes, T. & Rebane, A. Two-photon absorption properties of fluorescent proteins. *Nature Methods* **8,** 393-399 (2011).
69. Ponder, M. & Mathies, R. Excited-state polarizabilities and dipole moments of Diphenylpolyenes and Retinal. *J. Phys. Chem.* **87,** 5090-5098 (1983).

Chapter 4

Interrogations of Quinoidal Bithiophene Reveal High Yield Ultrafast Intramolecular Singlet Exciton Fission: A New Hope in Organic Photovoltaics

4.1 Original Publication Information

This chapter primarily contains material that was originally published as the following document.

"High yield ultrafast intramolecular singlet fission in a quinoidal bithiophene"

Oleg Varnavski, Neranga Abeyasinghe, Juan Arago, Juan J. Serrano-Perez, Enrique Orti, Juan T. Lopez Navarette, Kazuo Takimiya, David Casanova, Juan Casado & Theodore Goodson III

The Journal of Physical Chemistry Letters **2015**, 6, 1375-1384.

The modifications to the original document is cosmetic and are used only to conform to the format of this dissertation or to provide uniformity of enumeration. I contributed to this work by conducting nonlinear transmission experiments that are used to determine intramolecular singlet fission efficiency, preparing samples for flash photolysis experiments, conducting solvent polarity dependent nonlinear transmission experiments and concentration dependent steady state absorption experiments, doing time-correlated single photon counting experiments and magnetic field dependent time-correlated single photon counting experiments etc. The calculations described in the text were carried out by our collaborators in Spain.

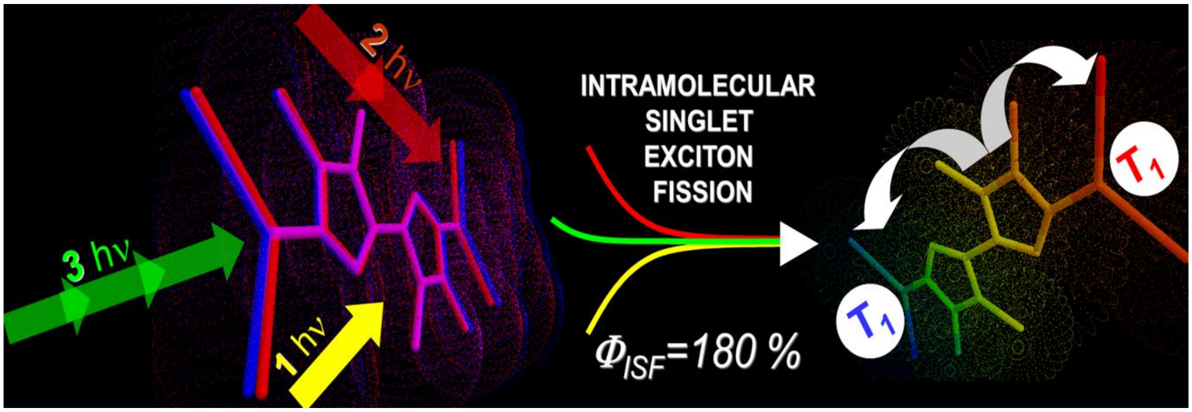

Figure 4-1 Table of contents image as published.

4.2 Abstract

We report the process of singlet exciton fission with high-yield upon photoexcitation of a quinoidal thiophene molecule. Efficient ultrafast triplet photogeneration and its yield are determined by photoinduced triplet−triplet absorption, flash photolysis triplet lifetime measurements, as well as by femtosecond time-resolved transient absorption and fluorescence methods. These experiments show that optically excited quinoidal bithiophene molecule undergoes ultrafast formation of the triplet-like state with the lifetime ~57 μs. CASPT2 and RAS-SF calculations have been performed to support the experimental findings. To date, high singlet fission rates have been reported for crystalline and polycrystalline materials, whereas for covalently linked dimers and small oligomers

it was found to be relatively small. In this contribution, we show an unprecedented quantum yield of intramolecular singlet exciton fission of ~180% for a quinoidal bithiophene system.

4.3 Introduction

Singlet exciton fission (SEF), discovered almost 50 years ago, has recently attracted renewed interest due to potential applications.[1-3] SEF, in which two triplet excited states are created from one singlet excited state, can potentially provide a pathway to increase the energy conversion efficiency in organic solar cells if each of the two generated triplet states is able to inject an electron.[2-7] SEF has been found in a number of selected systems, including large polyacenes,[8,9] polymers[10-12] carotenoids,[13-15] and in covalent dimers.[16-18] While the list of compounds that have been shown to undergo SEF continues to grow, a high-yield multi-electron generating system for real photovoltaic applications remains to be found.

SEF is a quantum-mechanically allowed process as opposed to the spin-forbidden singlet–triplet transition (intersystem crossing). Under favorable $E(S_1) > 2E(T_1)$ energetics, the fission process can be very fast due to its spin-allowed nature.[1,3,6,7] In most of the known SEF materials for photovoltaics, the correlated triplet pair state $^1(T_1T_1)$ is formed by sharing the initial singlet monomer exciton energy with a neighbouring molecule giving rise to an intermolecular excimer state in which each molecule embodies a triplet and the two triplets are electronically coupled to form a correlated triplet pair with singlet multiplicity $^1(T_1T_1)$. Even in the assumption of favorable energetics, the single-molecule excitation in these systems evolves to a bimolecular excimer, a process that might be a quite limiting step due to the intermolecular nature of $^1(T_1T_1)$ that requires suitable intermolecular electronic coupling (adequate pi contact and molecular orientation).[6,7]

Intramolecular SEF quantum yields reported until very recently[12] were small, typically well below 30% while for polycrystalline solids made from the same chromophores the intermolecular SEF yield could reach 200%.[6,16,18] The reason for this was not clearly understood and the potential of intramolecular fission has not been fully explored.[6,18] In an exciting new development high efficiency intramolecular SEF has been recently demonstrated in donor-acceptor polymers.[12] Intramolecular SEF is a very attractive route for multiple charge generation as it allows for accurate tuning of the geometry and intramolecular interactions through chemical synthesis. As a molecular property, SEF itself in this case may not require long molecular ordering or fine adjustment of intermolecular interaction in not-so-well controllable assembling process. Additionally, for intramolecular SEF molecules we can control the D-A interface parameters for charge separation much more precisely as compared to the microcrystalline contact, for example, by bonding the SEF molecule to a charge separation unit.

Besides covalent dimers, intramolecular SEF is known to occur in particular carotenoids bound to photosynthetic antenna light-harvesting proteins.[13,14] It has been also found in conjugated polymers.[10-12] The possibility of efficient localization of the resulting triplets in well separated polymer fragments within the maximal conjugation length plays an important role in generation of separated triplets. From this perspective a large molecular weight disordered polymer can be considered as multi-segment system showing some features of intermolecular process even in diluted solution (e.g. self-chain crossings due to disorder). From a mechanistic perspective, the polymer resorts to distance the two triplet excitations via extended conjugation length and delocalization of a parent singlet while the small molecule may mostly use a conformational gateway to accommodate them. In an attempt to better understand the SEF process in small molecules, dimers formed by two active molecules covalently connected by electronically inactive units have been studied.[16-18] These are certainly uni-molecular entities but they do not directly imply the concept described in carotenoids and conjugated polymers. In fact, these weakly coupled dimers show very low SEF quantum yields and, more importantly, slow, non-competitive triplet formation rate.[18] On the other hand conjugated polymers with strongly coupled charge-transfer character units demonstrated high SEF efficiency up to 170%.[12]

It is well known that absorption processes can efficiently promote the direct generation of multiple carriers in inorganic semiconductors and carbon nanotubes.[19] However, in organic molecules, these multi-exciton states can be strongly coupled and double electron injection capability is questionable. The molecular system should allow for two triplet excitations being more or less independent, but quantitatively, the extent of this anticipated independence with respect to efficient double electron injection remains unclear. For example, Chan et al. have demonstrated that the charge transfer rate from the correlated pair intermediate state of pentacene (ME/ME') to C_{60} is higher than that from separated triplets and, more importantly, that both electrons are transferred.[3] This observation indicates the importance of the intermediate state $^1(T_1T_1)$ for multiple charge extraction process and that the formation of perfectly independent triplet states may not be essential for efficient double charge injection.

While creation of the efficient photovoltaic cell utilizing SEF to exceed Shockley-Queisser limit goes beyond SEF suggesting the use of additional red-absorbing species to prevent the drop in open circuit voltage,[2] the discovery of new organic molecules possessing efficient intramolecular SEF in relatively small molecules and oligomers is an important step towards potentially controlling the SEF efficiency via chemical synthesis that will be pivotal for next generation photovoltaic applications. Efficient intramolecular SEF system in comparison with the intermolecular SEF counterpart can give the following important benefits: i) a higher efficiency (intermolecular steps preceding triplet-triplet formation are made unnecessary), ii) the SEF–active molecule can be potentially bound to the electron acceptor with a minimal travel distance for triplet exciton to reach the acceptor, thus ensuring more efficient electron injection competitive to detrimental triplet-triplet annihilation process, and iii) the system efficiency is expected to be less susceptible to the defects like those associated with the imperfections in microcrystalline structures.

Tetracyanomethylene quinoidal oligothiophenes (QOTn, Figure 3-2) have recently attracted substantial attention due to their unusual linear and nonlinear optical properties.[20-27] Long quinoidal oligothiophenes have been shown to possess a biradicaloid character in their ground state.[23-28] Biradicaloids are known to have low-lying triplet energy levels and therefore are promising structures to meet the requirement $E(S_1) \geq 2E(T_1)$.[6,7,29,30] The quinoidal structure of the thiophene rings results in a mostly planar ground state molecular configuration that undergoes distortions and twisting to stabilize their excited state.[24] Moreover, QOTn molecules are equipped with terminal –CN acceptor groups that may serve to facilitate the efficient formation of the correlated triplet pair state and subsequent separation into two individual triplets.[31, 32] The quinoidal features together with the great photostability of quinoidal thiophenes, make QOTn very promising candidates for a new generation of organic molecules for photovoltaics by virtue of the intramolecular SEF process.

In this paper we report on the generation of ~180% yield of triplet excitons via intramolecular SEF in a relatively small molecule tetracyanoquinodimethane bithiophene (QOT2,

Figure 4-2). QOT2 displays favorable energetic conditions for SEF imparted by its pro-biradicaloid character. We show that QOT2 undergoes ultrafast formation of a triplet-like species that lives for at least 57 μs using femtosecond and microsecond transient absorption measurements, ultrafast nonlinear transmission, time-correlated single photon counting, and femtosecond time-resolved fluorescence measurements. Moreover, our multiconfigurational CASSCF/CASPT2 and RAS Spin-Flip (SF) quantum chemical calculations on QOT2 confirm the possibility of intramolecular SEF by outlining the general energetic landscape during the formation of triplets. Using both experiment and theory we describe the pertinent mechanisms yielding the high population of the multi-exciton state under impulsive conditions, which efficiently produces triplet excitons via intramolecular SEF. We demonstrate that QOT2 has all ingredients necessary to be utilized in highly efficient organic photovoltaic devices operating via intramolecular SEF.

4.4 Results and Discussion

Investigations on QOTn have revealed that their steady-state absorption spectra extend much farther to the red as compared to the corresponding aromatic oligomers (Figure 4-2).[22,25,33] Moreover, these quinoidal structures have shown biradicaloid character of the ground state indicating the presence of low-lying triplet states that can help to meet the energetic requirement for singlet exciton fission [$2E(T_1) < E(S_1)$].[24,30] Experiments have been performed in QOT2 solutions having concentration in the range 2×10^{-6} M to 10^{-3}M (depending on the experiment) thus making the intermolecular processes very improbable on the time scales of the experiments.[34]

No concentration dependence of the steady-state spectra as well as the kinetics has been detected in this concentration range indicating negligible aggregate formation.

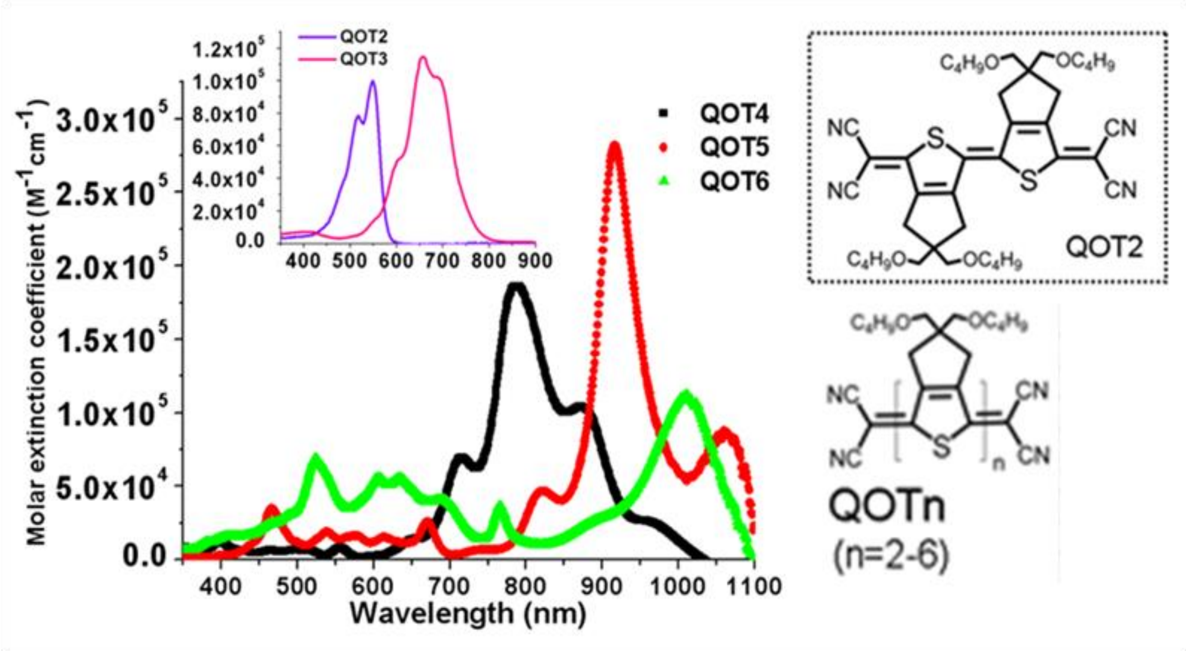

Figure 4-2 Steady-state absorption spectra for QOTn oligomers indicating their broader reach of the visible and near infrared wavelengths. The structure of quinoidal bithiophene QOT2 investigated in this work.

In order to establish the formation of triplet species, we have conducted transient absorption experiments on QOT2 excited at 445 nm using a flash photolysis apparatus as well as sensitization of the QOT2 triplets using tetracene. The excited state absorption (ESA) detected for the directly photo-generated species (Figure 4-3) displayed a peak at ~570 nm and had a lifetime of 57 ± 6 μs. This long lifetime taken together with the absence of systematic solvent polarity and viscosity dependence as well as the presence of magnetic field effects (see below) strongly suggest the formation of a triplet (or higher multiplicity) species upon photo-excitation of QOT2.

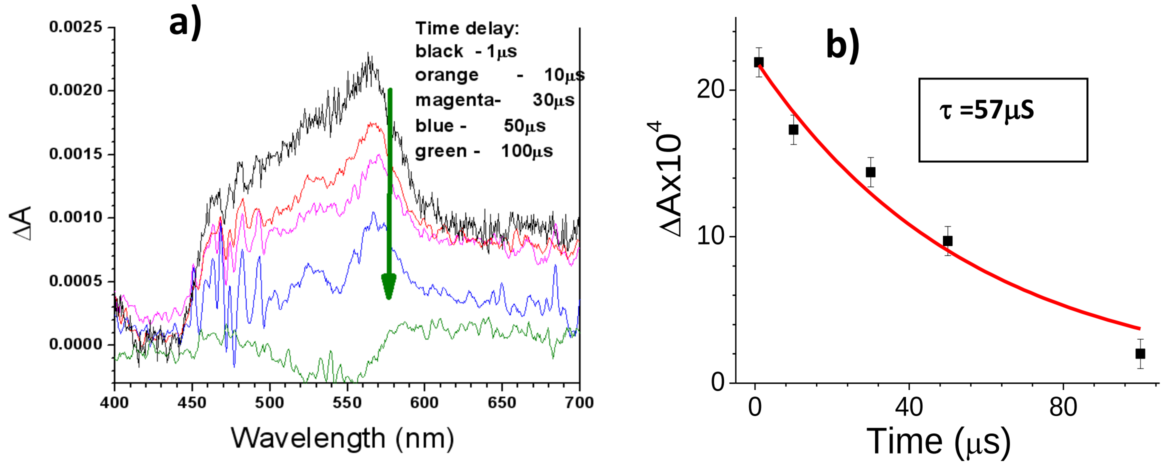

Figure 4-3 Efficient generation of long-lived species. (a) Transient absorption spectra (flash photolysis) of QOT2 at 445 nm excitation that yields 57 μs-lived transient species. (b) Fitting of the 570 nm excited state absorption to the exponential decay function.

Using the same set up we have also observed a tetracene-sensitized transient absorption feature associated with the triplet exciton energy transfer from the tetracene to QOT2 (Figures 4-4, 4-10, 4-11). Interestingly, in contrast to the direct excitation, sensitized QOT2 showed ESA shifted to the red (~ 600 nm) as compared to that for the direct excitation with a measured lifetime of 111 ± 19 μs (well beyond the tetracene triplet lifetime of 38 μs, Figures 4-4, 4-10). The shortening of the tetracene lifetime to 14.9 ± 0.1 μs clearly indicates the triplet sensitization of QOT2 by tetracene.

We can establish two possible long-lived transient species for photo-excited QOT2:

1. Single triplet species that lives for 111 μs – from sensitization experiment.
2. A long-lived species distinct from and that lives shorter than a single triplet exciton (57 μs) – from direct singlet excitation of the QOT2.

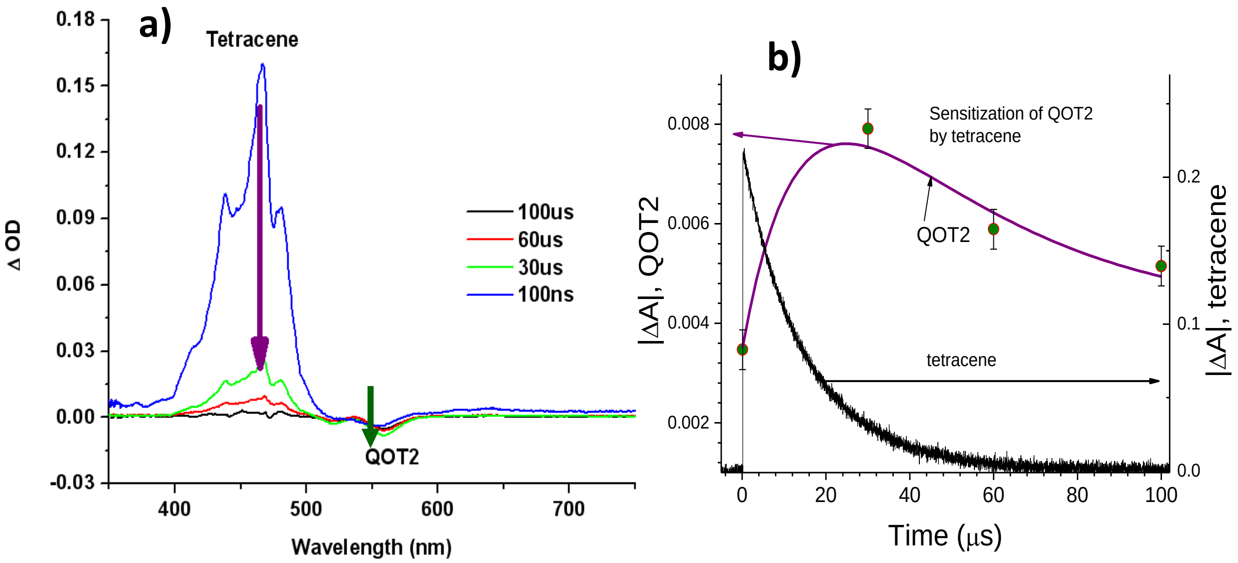

Figure 4-4 (a) Transient absorption spectra of tetracene and QOT2 sensitized with tetracene at excitation of 470 nm, (b) Triplet energy transfer kinetics from tetracene to QOT2 derived from transient absorption spectra. Tetracene quenching kinetics is also shown.

It is clear from these experiments that the direct excitation of QOT2 forms a species that has non-singlet character and that shows somewhat different excited state properties in comparison with the single triplet exciton produced by sensitization route. We assign this species to the triplet pair residing on one QOT2 molecule. The observation of the triplet pair on direct excitation with a lifetime shorter than that for a single triplet exciton may indicate an enhanced contribution of the triplet-triplet annihilation process if more than one triplet, i.e., a triplet pair, is formed in one molecule under direct excitation. It is also possible that the molecular conformation which stabilizes a triplet pair on one molecule is somewhat different from that stabilizing the single triplet which can result in different associated decay rates. Also, having an excited triplet pair distinguishable from the single triplet exciton (111 μs lifetime) is an indirect indication that the 57 µs-lived species has derived from a process other than intersystem crossing. This experiment has also located the triplet state energy of the QOT2 to be below triplet energy of tetracene i.e. 0.98 eV thus confirming the favourable energetics $E(S_1) > 2E(T_1)$ for SEF in QOT2 ($E(S) \cong 2.26$ eV).

We have examined the excited state absorption of QOT2 at 890 nm under excitation with a femtosecond pulse train at 445 nm. The 890 nm probe beam has been produced by the femtosecond laser system delivering 130 fs pulses at a repetition rate of 80 MHz while its second harmonic (445 nm, 2.79 eV) has been used as a pump. The 445 nm pump pulse train excites high-lying vibronic states of the one-photon-allowed transition (high energy side of the band spreading from 400 nm to 600 nm in Figure 4-2). In this experiment, a small fraction (<1 mW) of the fundamental beam (890 nm) probes the transmission of the sample in the wavelength range where the linear absorption of the sample is negligible. A surprisingly strong drop in transmission was observed at 890 nm (Figure 4-5).

Almost complete attenuation of the 890 nm probe beam under the moderate pump at 445nm (~14 mW) detected in this experiment is due to accumulation of a significant number density of excited state absorbing species. In order to better characterize this absorbing species, we performed this transmission experiment for QOT2 dissolved in a variety of solvents possessing different polarities and viscosities. Figure 4-6 shows the probe transmission profiles for QOT2 in solvents of different polarities ranging from nonpolar cyclohexane to highly polar acetonitrile. It is seen that the transient absorption induced by the 445 nm beam does not have systematic polarity dependence ruling out the formation of long-lived charge transfer products sensitive to the polar environment (such as radical anions and cations). The induced absorption profile also did not show

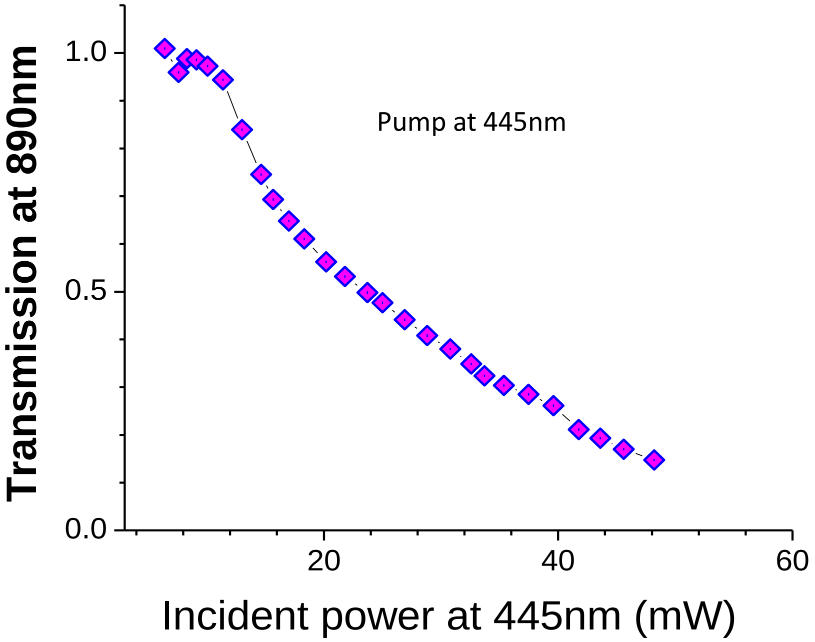

Figure 4-5: Transmission of QOT2 for the probe light at 890 nm as a function of the pump power at 445nm.

measurable dependence on the solvent viscosity (Figure 4-12) thus making the contribution of long–lived conformers or excited state species created in intermolecular processes controlled by diffusion (e.g. excimers) very improbable.

From the induced triplet absorption shown in Figure 4-5, one can estimate the number density of accumulated triplet excited states n_{TE} that is necessary to produce the observed beam attenuation of 48.5 % at 890 nm for the incident pump (445 nm) power of 14.5 mW. The molar extinction coefficient for triplet-triplet absorption was estimated to be 9.5×10^3 $M^{-1}cm^{-1}$: $n_{TE} = 3.65 \times 10^{16}$ triplets/cm^3. The number density of molecules in the singlet excited state n_S* created

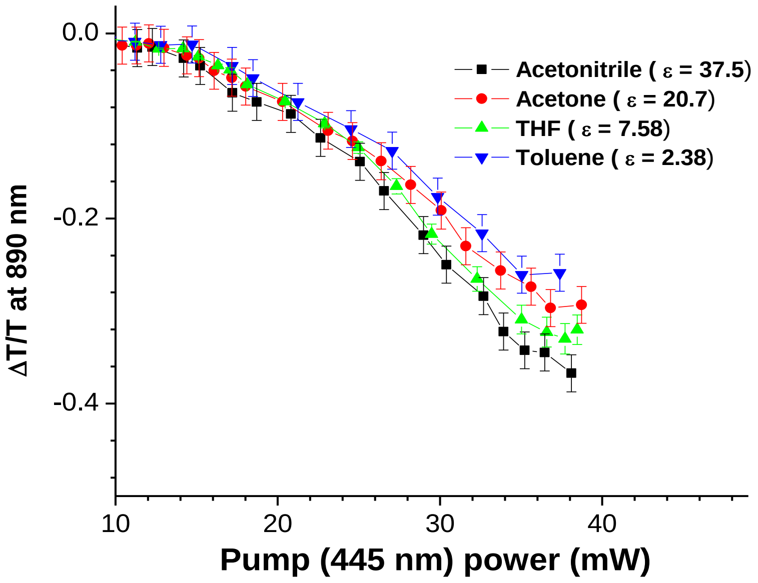

Figure 4-6 Transmission of QOT2 for the probe light at 890 nm as a function of the pump power at 445 nm in solvents of different polarity.

by the 445 nm laser pulse can be easily estimated from the optical density of the sample and pulse energy: $n_S* = 4.57 \times 10^{12}$ singlets/cm^3. Comparing the number of triplet states accumulated during the triplet lifetime with n_{TE}, the singlet-triplet conversion quantum efficiency α_{ST} can be calculated: α_{ST} =1.76 or 176% (see Supporting Information for details). In line with the unusually strong beam attenuation at 890 nm, the calculated singlet-triplet conversion efficiency above 100% indicates the presence of a very efficient SEF process in QOT2.

Previous studies on singlet exciton fission (tetracene, pentacene, carotenoids, etc) have reported the identification of an intermediate correlated triplet-pair state.[3,5,13,35] This intermediate state was found to emerge almost simultaneously (within the ~first picosecond) with the formation of a singlet excited state.[3,35] Moreover, it was found that this ultrafast formation is directly assisting

SEF to compete with other radiative and non-radiative relaxation processes to achieve highly efficient triplet generation.[6] In order to investigate possible ultrafast origins of the triplet-like excitons (triplet pair or correlated triplet pair), we have carried out femtosecond time-resolved two-color pump-probe experiments on QOT2 using a low-noise, cavity-dumped Ti-Sapphire femtosecond oscillator. The excitation occurred at 415 nm while the probe pulse wavelength was at 830 nm. The fast initial decay component (<1 ps) of the excited state absorption in Figure 4-7 is due to transient absorption contribution of a short-lived singlet excited state. This decay is followed by the excited state absorption by a long-lived species, which can be attributed to the absorption of the triplet-like species detected in the above experiments.

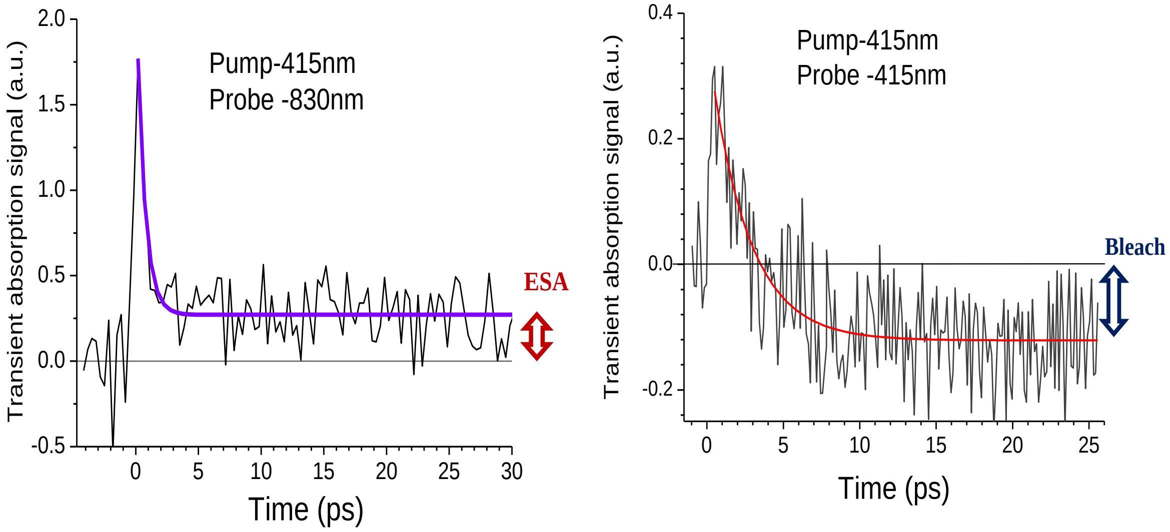

Figure 4-7 (a) Two-color pump-probe dynamics in the first 30 ps for QOT2 under 415 nm pump and 830 nm probe indicating the ultrafast formation (< 1 ps) of the long-lived species (b) Degenerate pump-probe dynamics showing formation of long-lived ground state bleach.

While the exact rise time of the long-lived transient absorption is obscured by the fast singlet state decay, it is clear that the long-lived absorption is fully established after 1ps. It can be inferred, then, that the same absorbing species is existent until 57 μs to give rise to the excited state absorption at 570 nm and at longer wavelengths (830 nm in this case). Moreover, a similar (~ 1 ps) decay profile was observed for our time-resolved fluorescence experiment (see below) at 600 nm emission substantiating the ultrafast decay (~1 ps) of the initial singlet excitation. This surprisingly short build up time for the triplet-like state in the sub-picosecond time range cannot be a result of the regular intersystem crossing induced by spin-orbit coupling mechanism as the latter is an orders-of-magnitude (10^{10} s^{-1} as opposed to $>10^{12}$ s^{-1}) slower process for systems without heavy atoms.

Out of the two interconverting singlet and triplet transient species generated on the picosecond time scale, the lowest singlet state population can be followed by the fluorescence dynamics. We have conducted femtosecond time-resolved fluorescence measurements to correlate the singlet state population dynamics with the triplet state population build up time. The time-resolved 600 nm (2.07 eV) - fluorescence profile measured with the fluorescence upconversion setup is shown in Figure 4-8a. It is clearly seen that the fluorescence (thus the singlet state population) decays within a few picoseconds. Best fit analysis of the short time-scale fluorescence dynamics (Figure 4-8a, inset) showed bi-exponential decay with time constants of 0.61±0.1ps and 2.0±0.3 ps, which are in excellent agreement with the transient absorption experiment monitoring mostly singlet excited states.[20, 21] This decay time also correlates well with the triplet-like population build up time estimated from the transient absorption experiment monitoring the triplet excited state absorption (Figure 4-7). These experiments showed that ultrafast singlet–triplet transformation plays a dominant role in the singlet population decay. The observed fast transformation of the singlet states into the triplet-like states (<1 ps) clearly indicates an intramolecular SEF process as the intersystem crossing rate is expected to be orders of magnitude slower.[6]

We have also performed time-correlated single-photon counting (TCSPC) measurements of the fluorescence decay at different wavelengths in order to better probe any possible long-lived emission components (e.g. delayed fluorescence). For the fluorescence at 580 nm (2.14 eV) reflecting the population of the lowest emissive singlet state, we found a decay on the nanosecond timescale (Figure 4-8b) as opposed to the fast decay at 470 nm (2.64 eV) mainly following the instrument response function profile.

The 470nm - fluorescence signal monitors the population dynamics of a higher-lying singlet state. As the excitation intensity in this photon counting experiment was extremely low (*less than one excitation per 10,000 molecules*) the singlet-singlet annihilation (and charge recombination) can be readily excluded. The 580 nm-fluorescence long tail is suggested to be due to the singlet excitations formed as a result of weak triplet-triplet exciton annihilation (delayed fluorescence). It decays well beyond the major excited singlet decay component of ~2 ps for QOT2[20,21] (shown in Figures 4-7 and 4-8a). The presence of a long-lived non-exponential emission component related to the delayed fluorescence was often used as a strong indication of the triplet state population.[36-38] It is also worth noting that due to the low concentration of molecules in solution used in this experiment ($<10^{-5}$ M), annihilation of two triplet excitations residing on

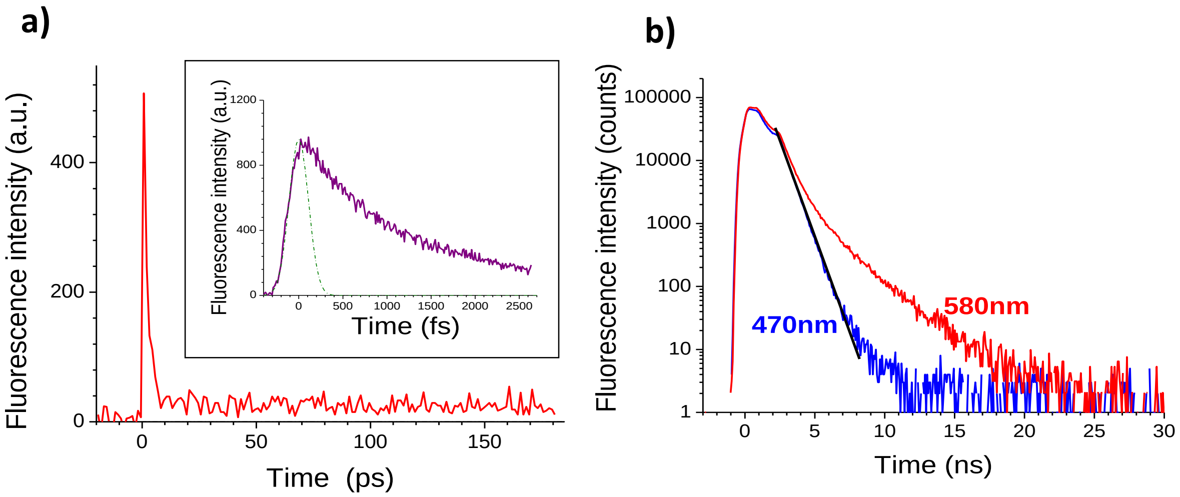

Figure 4-8 Time-resolved fluorescence dynamics. **(a)** Femtosecond time-resolved fluorescence decay at 600 nm. Inset: Short timescale fluorescence decay; instrument response function (FWHM = 0.25 ps) is indicated by dash-dot line. **(b)** Time-resolved fluorescence decay measured by time-correlated single photon counting (TCSPC) at 470 nm and 580 nm emission wavelengths.

different molecules can be neglected and the observed delayed fluorescence might be associated with the presence of two triplets residing on one molecule. The delayed fluorescence, as detected with this setup, lasts shorter than the triplet-related transient absorption features (Figure 4-3). It can be associated with low signal-to-noise ratio of the setup to detect extremely weak (in part due to relatively low annihilation rate) delayed fluorescence tail. Some conformational inhomogeneity can be also contributing to the enhanced delayed fluorescence at short times. It is also worth noting that the energy of the resultant singlet (following triplet-triplet annihilation) should be lower than 2.64 eV not to appear in the 470 nm emission. This distinction between the 470 nm and 580 nm emission may further indicate the excited-state energy relaxation of a correlated triplet-pair state (or an intermediate state) prior to their separation into two triplets. Additionally, we carried out magnetic field-dependent measurements to probe the triplet origin of the observed transients. We have carried out magnetic field measurements on the transmission drop and on the fluorescence. The excited state absorption at 890 nm increases by a value which is definitely beyond the noise uncertainty when an external magnetic field of ~100 Gauss is applied to the sample (Supporting Information, Figure 4-19). This observation indicates an increase in triplet-like population compared to the zero-field case. Since the observed excited state absorption corresponds to long time scales, it can be inferred that, by the point when ESA is significant, the triplet-like states have randomized their populations across the nine possible spin states[6,9] so that the pathways available for triplet-triplet annihilation are reduced. The magnetic field dependent fluorescence has been also observed. The data is shown in Supporting Information (Figures 4-20, 4-21 and 4-22). There is a clear change of the fluorescence intensity with and without the 100 Gauss magnetic field. While detailed mechanism of these effects is still under investigation, these experiments demonstrating a magnetic field dependence of the photogenerated absorbance and fluorescence in QOT2 provide additional support to its spin multiplet origin.

Multiconfigurational CASPT2 quantum-chemical calculations have been performed to explore the electronic structure and excited states of the strongly electron correlated QOT2 system (Figure 4-9). The CASPT2 protocol has been shown to provide accurate descriptions of photophysical/photochemical processes.[39, 40] Substituents at the β, β' positions of QOT2 have been omitted to simplify the model and reduce the computational cost. Calculations have been carried out using an active space of 10 electrons in 8 π molecular orbitals and the cc-pVDZ basis set (see

Supporting Information for full computational details). Molecular geometries of both the ground and the excited electronic states have been optimized at the CASPT2 level.

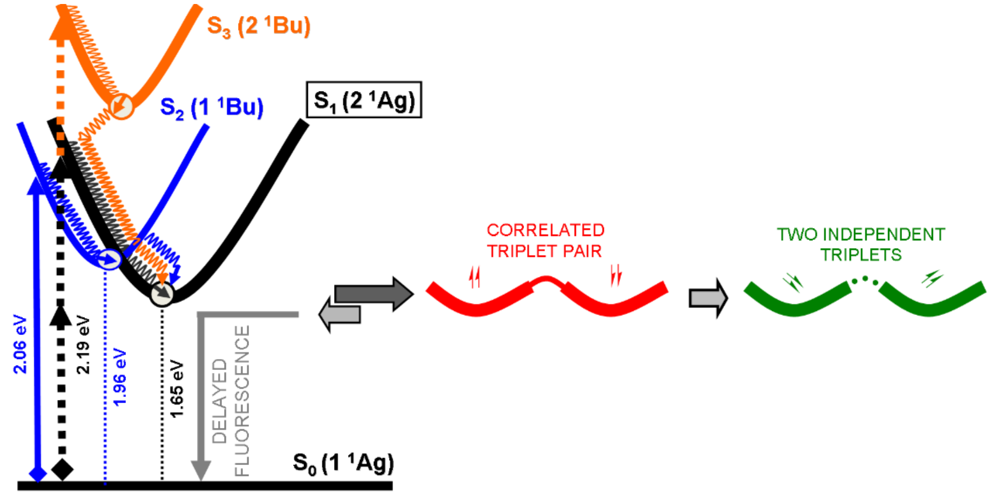

Figure 4-9 Schematic showing the computed CASPT2 energies (in eV) for the low-lying electronic states of QOT2. Possible relaxation paths are sketched by arrows.

CASPT2 calculations predict a strong one-photon-allowed vertical excitation to the 1^1B_u state at 2.06 eV, which correlates with the experimental band at 2.25 eV in the UV-Vis absorption spectrum. This $1^1A_g \rightarrow 1^1B_u$ excitation is mainly described as a one-electron promotion from the $7a_u$ HOMO to the $7b_g$ LUMO (Figure 4-13). In the Franck-Condon region, the next 2^1A_g excited singlet state lies at 2.19 eV (0.13 eV higher than the 1^1B_u). This dipole-forbidden $1^1A_g \rightarrow 2^1A_g$ excitation mainly results from a double electron promotion revealing the multi-exciton character of the 2^1A_g state.

We have also explored the minimum-energy regions for the two low-lying singlet excited states (1^1B_u and 2^1A_g). At the minimum of the 1^1B_u state, the 2^1A_g state lies 0.06 eV below and the energy difference increases to 0.36 eV at the optimized 2^1A_g geometry. These results clearly indicate that: i) the energy ordering of the two lowest-lying excited states (1^1B_u and 2^1A_g) is inverted when passing from the Franck-Condon region of the ground state [1^1A_g (S_0) < 1^1B_u (S_1) < 2^1A_g (S_2)] to the minimum of the 2^1A_g state [1^1A_g (S_0) < 2^1A_g (S_1) < 1^1B_u (S_2)], and ii) the energy difference for a possible $1^1B_u \rightarrow 2^1A_g$ internal conversion is small (0.06 eV at the minimum of 1^1B_u) conforming with the ultrafast internal conversion between the 1^1B_u and the 2^1A_g states experimentally detected by Kobayashi et al.[20] At the CASPT2 optimized geometry of 2^1A_g, the vertical energy difference between the 2^1A_g and 1^1A_g states is computed to be 1.65 eV.

The low-lying triplet excited states were also calculated at the fully-relaxed CASPT2 geometry of the 1^1A_g state (Figure 4-14). The first triplet excited state (1^3B_u) is predicted at 0.60 eV above the 1^1A_g ground state which is in qualitative agreement with the efficient QOT2 sensitisation by tetracene described above. Although the relevant triplet species detected in the intramolecular SEF mechanism are multi-excitations, the evaluation of single molecule triplet excitations, relative to the relevant singlets, can provide a qualitative estimation as for the overall energetics of the SEF process. In this sense the sum of the calculated energies of two isolated triplets residing on different molecules at the vertical states (i.e., $2\times T_1 = 1.20$ eV) is lower than 1.65 eV (2^1A_g) thus anticipating a clear exoergic energy balance for a hypothetical intermolecular SEF process to take place. Two triplets stabilized on one molecule may have different total energy due to their close proximity and different stabilizing nuclear arrangement in comparison to that of two single triplets on two different molecules. Direct excitation flash photolysis and tetracene sensitization experiments indicated differences in spectra and kinetics. Nonetheless, ultrafast and efficient intramolecular triplet formation clearly shows that energetics remains favorable for the intramolecular case too.

At the minimum of the 1^3B_u state (Figure 4-14), we have calculated the lowest-lying triplet excited states at CASPT2 and found that the lowest-energy 1^3B_u (T_1) → 1^3A_g (T_2) triplet-triplet excitation has an energy of 1.80 eV with a relatively weak oscillator strength (0.084) while the most intense triplet-triplet excitation is associated to the $1^3B_u(T_1) \rightarrow 3^3A_g(T_6)$ transition with an energy of 2.82 eV and an oscillator strength of 0.605.

In polyenes, the 2^1A_g multi-exciton singlet excited state (i.e., named covalent state) is described as a spin-wave state that consists of spin flip excitations.[41-42] For medium size polyenes, or carotenoids, the 2^1A_g is described as two intra-ethylene triplet excitations which are coupled into an overall singlet, or $^1(T_1T_1)$. The electronic structure computed for QOT2 shows a definitive resemblance with that of polyenes and its 2^1A_g excitation can be viewed as a double triplet excitation or with a strong $^1(T_1T_1)$ component (see next section for spin flip calculations). Described the 2^1A_g excited state of QOT2 as a $^1(T_1T_1)$ excitation, we notice that the fully-relaxed geometry of the 2^1A_g state features a significant elongation of the terminal carbon-carbon bonds by 0.096 Å (the central bond changes by 0.052 Å, see Table 1 and Figure 4-15) highlighting that the two coupled excitations are put apart towards the dicyanomethylene groups.

Restricted active space spin flip (RAS-SF) quantum chemical calculations reproduce with acceptable accuracy the relative energies of excited states of different multiplicity at a moderate computational cost.[43,44] RAS-SF calculations are thus very suitable to scan the energies of the excited states involved in SEF as it has been already described in a number of examples.[45-47] All calculations have been done with the double spin flip version of RAS-SF (RAS-2SF) using the lowest ROHF quintet determinant as the reference configuration, and the same active space (10, 8) and basis set (cc-pVDZ) as used in the CASPT2 case.

It is presumed by many authors that the intramolecular SEF might be assisted by a high spin quintet (Q_1) molecular state which should mediate the full separation of the initial excitation into two independent intramolecularly comprised triplets.[6] RAS-2SF/cc-pVDZ calculations predict the low lying Q_1 state in QOT2 (1^5A_g) at more than 4.5 eV above the 1^1A_g ground electronic state (Figure 3-16). Since intramolecular SEF in carotenenoid-like molecules is accompanied by stabilizing molecular distortions,[13, 14] we have scanned the energy evolution of the $2^1A_g/1^5A_g$ states by rotating from 0 to 90 º around the central CC bond (bond 1 in Table 4-1) resulting in an overall destabilization of both states (Figure 4-16), which is unfavourable for any photophysical process taking place at moderately low energies as those observed here.

Anticipated by the structure of the 2^1A_g state described at the CASPT2 level above, we have explored the energy evolution of the relevant low-energy lying excited states with respect to the simultaneous rotation around the bonds linking the dicyanomethylene groups and the thiophenes in Figure 3-17 (bonds 5 and equivalent in Table 4-1). Interestingly, the sole state that is stabilized with this distortion is the 1^5A_g state while the 2^1A_g gets destabilized being degenerate with the 1^5A_g at 90º conformation: this highlights the intrinsic multi-radical nature of the multi-exciton 2^1A_g of QOT2. We have calculated the tetra-radical character of the 2^1A_g wavefunction as a function of the discussed rotation and found that it progressively increases, having a 100% tetra-radical feature at 90º (Figure 4-18). One can argue that the biradical centers are spatially localized mainly at the terminal dicyanomethylene groups at this perpendicular disposition. This theoretical data reveals that a mechanism for intramolecular SEF in QOT2 assisted by a quintet state is rather unviable, as this requires high excitation energies to be activated. At the same time the fact that distortions in the peripheral dicyanomethylene groups stabilizing the multi-radical character alludes to a possible mechanistic pathway for intramolecular SEF with a twisted conformation of QOT2.

The theoretical description is in agreement with ultrafast spectroscopic results in QOT2. In our transmission experiments with the 445 nm (2.79 eV) laser excitation, QOT2 is directly excited to high-energy vibrational levels of the one-photon allowed 1^1B_u (S_2) state predicted at 2.06 eV, which might relax to its minimum undergoing ultrafast internal conversion to the 2^1A_g (S_1) state. The inversion of the energy ordering of the two lowest-lying excited states during the relaxation process can lead to the adiabatic relaxation pathway associated with the avoided crossing. This description is similar to that proposed for intermolecular SEF in tetracene films which describes an adiabatic pathway from 1^1B_u to an intermediate or "dull" state (could be the 2^1A_g in our case).[48] However in tetracene there is an intermolecular excimer state while in QOT2 this state is of intramolecular nature. In QOT2 the stabilization is provoked by a planarity distortion around the external CC bonds connecting the thiophenes and the dicyano groups. Two vibrational modes strongly coupled to the dark (S*) state of QOT2 reported in ref 49 (1466cm^{-1} due to stretching of the external C=C bonds and 446cm^{-1} due to the out-of-plane ring or interring deformation[49]) may support the adiabatic evolution along the avoided crossing from 1^1B_u (S_2) to the dark state. The small predicted energy difference near minimum of the 1^1B_u state ~ 0.06 eV may also suggest the existence of a conical intersection between the two potential energy hypersurfaces. Both mechanisms should warrant ultra-efficient/ultrafast internal conversion in accordance with the population within ~1 ps (see blue path in Figure 4-9) of the 2^1A_g lowest excited singlet.

In order for efficient intramolecular singlet exciton fission to occur, excited singlet state - $^1(T_1T_1)$ coupling has to be high enough. In light of recent findings by Busby [12] and co-workers and

Zhu and co-workers[31,32] the presence of electron withdrawing cyano groups as acceptors can facilitate strong coupling between singlet and triplet pair via charge-transfer state. Similarly, in QOT2 the presence of terminal –CN groups can render charge transfer character in its excited state which may be beneficial for the rapid formation of the triplet-pair and thus high intramolecular SEF efficiency in QOT2.

The triplet pair created from the 2^1A_g state might share structural characteristics with the 1^5A_g quintet (both are electronically decoupled triplet pairs, only differing in the sign and degree of the spin correlation). This analogy suggests that once this intermediate species is formed it could find a stabilization pathway by rotating around the inter-ring and dicyano-thiophene dihedral angles (such as in the quintet by RAS-2SF calculations, Figure 3-18), a relaxation route that increases its tetra-radical character (T_1T_1) favouring the full dissociation into two intramolecular independent triplets and enhancing the SEF efficiency up to values, 180%, close to complete singlet-triplet photo-conversion of 200%. This distortion gateway of the correlated triplet pair is similarly suggested in carotenoid-like systems as the way to accommodate the two triplets.[13, 14] These species are formed within picosecond time-scales and owing to its triplet character have a long lifetime of 57 μs in our case. The two intramolecular triplets or the intermediate correlated triplet pair $^1(T_1T_1)$ may follow the way back to the 2^1A_g singlet from which would weakly emit resulting in delayed fluorescence. Experimental observation of the delayed fluorescence at longer wavelengths (580 nm, 2.14 eV) rather than for the 470 nm (2.64 eV) indicates the upper level of the $^1(T_1T_1)$ energy which is in line with calculated energy of 1.65 eV.

Given the two-photon absorption character of the $1^1A_g \rightarrow 2^1A_g$ transition, the dark state can be directly populated by direct two-photon excitation (see black path in Figure 4-10). We have previously reported that $1^1A_g \rightarrow 2^1A_g$ two-photon activity for QOT2 lead to relevant three-photon absorption (two-photon mediated three photon absorption) allowing the population of even higher energy excited states that would also relax down to the 2^1A_g (see maroon path in Figure 8).[21] We have observed the nonlinear absorption build-up associated with triplet generation under multiphoton excitation at 800nm. Interestingly the number density of excited singlet states producing specific induced absorption in this experiment was estimated to be very close to that created with one-photon excitation described above ($ns^* = 4.57 \times 10^{12}$ singlets/cm^3). This result indicates the same mechanism and efficiency of triplet generation for both routes of singlet excitation.

Finally, the build-up of this strong triplet-like population is responsible for the drop in transmission for the 890 nm probe beam observed in the experiment. A different scenario is formed by sensitization with tetracene; that is the generation of a single triplet excitation. This triplet is characterized in the transient experiments with tetracene by an absorption feature at wavelengths longer than 600 nm, which is close to that predicted theoretically at 689 nm ($1^3B_u \rightarrow 1^3A_g$ (Figure 3-14). The triplet lifetime of 111 μs measured in the sensitization experiment is in agreement with its single triplet character in contrast to the shorter lifetime for the two-triplet species.

4.5 Conclusion

In conclusion, a quinoidal bithiophene, QOT2, has been shown to be a very promising system for intramolecular singlet exciton fission with an outstanding efficiency of ~180%. This SEF quantum yield is among the largest found for organic molecules featuring SEF and, to the best of our knowledge, by far the greatest one for intramolecular SEF. All critical parameters required for efficient SEF seems to coincide in QOT2: i) its electronic structure which provides the $^1(T_1T_1)$ character to the key multi-exciton 2^1A_g singlet electronic state; ii) essentially planar geometry of the ground state associated with quinoid structure acquires substantial distortions in more aromatic excited state that help to accommodate two triplets on one molecule iii) the biradicaloid character expressed in the relevant excited states which plays an important role in near optimal energy level arrangement for ultra-efficient SEF on a sub-picosecond time scale; and iv) the high photo-stability provided by the thiophene stabilization of the oligoene path. Ultrafast time-resolved and integrated triplet accumulation photo-induced absorption experiments as well as time-resolved singlet fluorescence experiments, supported by CASPT2 and RAS-2SF calculations, all confirmed the occurrence of an ultrafast and efficient *intramolecular* singlet fission process in QOT2. This study on QOT2 will surely stimulate the search for new organic dye materials with focus on the challenging and elusive intramolecular singlet fission in small molecules which up to now has been considered to be highly unlikely to exist.

4.6 Experimental methods

QOT synthesis has been reported previously.[22] For spectroscopic measurements on QOT2 solutions, the QOT2 was dissolved in THF unless otherwise noted. We have examined the transmission of the dimer (QOT2) solution in THF at 890 nm under constant illumination with the femtosecond pulse train beam at 445 nm. The 890 nm - light beam has been produced by tunable Mai Tai laser system (Spectra Physics) delivering 130 fs pulses at repetition rate of ~80 MHz. Second harmonic of this beam (445 nm, 2.79 eV) with the average power up to 80mW has been produced in BBO crystal and used for excitation of the sample while a small fraction of the fundamental beam (< 1 mW) has served to probe the transmission at 890 nm where the linear absorption of QOT2 is negligible. A variable density neutral filter has been used to adjust excitation power at the sample. The laser beam has been focused on the sample cell using the lens with 127 mm focal length. Pure THF sample has been used as a reference in all experiments. A calibrated photodiode was used to measure the incident power. The transmitted power has been measured with a wide aperture power meter to avoid any contribution of the thermal lensing effect. Flash photolysis experiments were performed using nanosecond excitation from the Vibrant LD 355 II Nd:YAG/OPO system (OPOTEK) operating at 10 Hz. The transient absorption data were collected with an LP920 laser flash photolysis system (Edinburgh Instruments). The samples were degassed by Argon prior to flash photolysis experiments. Femtosecond two-color pump-probe experiments on the dimer QOT2 were carried out using low noise, cavity –dumped Ti-Sapphire femtosecond oscillator. Excitation occurred at 415nm while the probe pulse wavelength was 830nm. Pump pulse energy did not exceed 0.5 nJ at repetition rate ~39 kHz. Instrument response function duration for the two-color pump-probe configuration was ~100 fs. The experimental setup has been described in detail elsewhere.[50, 51]

Time-correlated single photon counting (~1 ns resolution) was performed using the Ti:Sapphire cavity dumped laser described above as an excitation source. Pulse repetition rate was set at 755 kHz in these experiments. Average pulse energy was ~13 nJ. A BBO crystal converts the 840 nm pulsed light into 420 nm excitation pulses. The fluorescence from the sample was collected at a right angle of excitation. Time resolution was created by using a time to amplitude converter (TAC), a linear ramp generator in the TimeHarp 200 (PicoQuant) detection card. Femtosecond time –resolved fluorescence measurements were carried out using fluorescence upconversion system with excitation provided by a frequency-doubled light from a mode-locked Ti-sapphire laser (Tsunami, Spectra-Physics) at 800 nm. Fluorescence emitted from the sample was up-converted in a nonlinear crystal of β-barium borate using a pump beam at 800 nm, which first passed through a variable delay line. Instrument response function (IRF, ~250fs, FWHM) was measured using Raman scattering from water. Spectral resolution was achieved by using a monochromator and photomultiplier tube. More details of the upconversion setup are provided elsewhere.[51] The procedures and details of the theoretical studies are presented in the supporting information (section 4.7).

4.7 Supporting information

4.7.1 QOT2 sensitization with tetracene

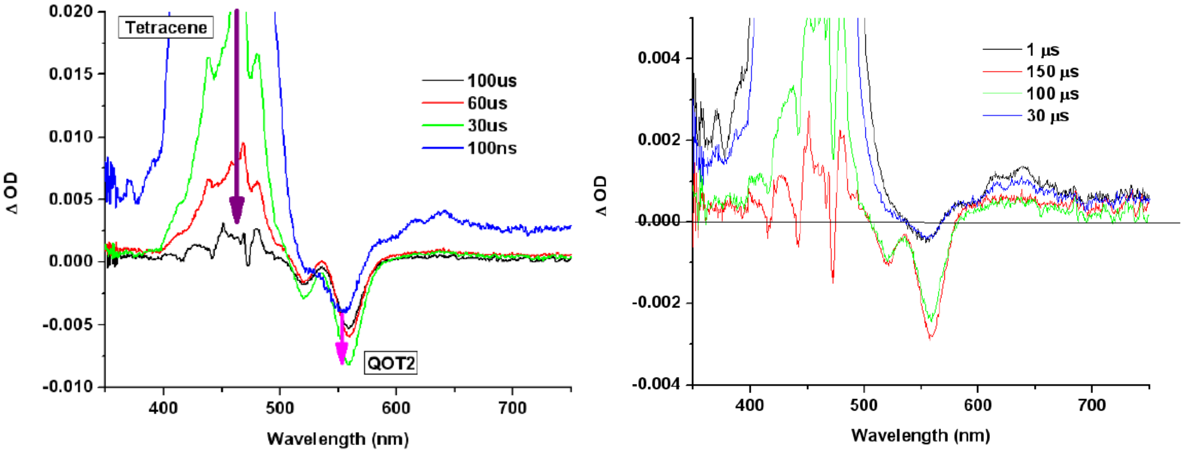

Figure 4-10. Left: transient absorption spectra for QOT2 sensitized with tetracene at excitation of 470 nm and up to 100 µs. Right: transient absorption spectra for QOT2 sensitized with tetracene at excitation of 470 nm and up to 150 µs.

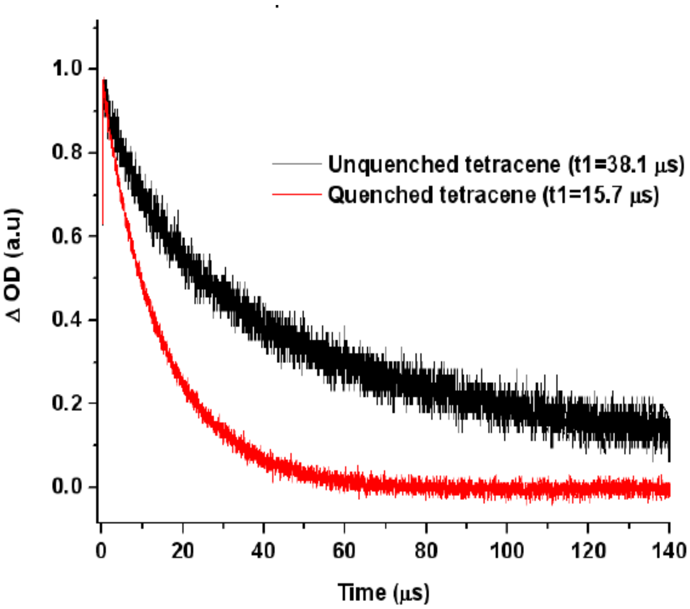

Figure 4-11 Comparison between the quenched (by QOT2) and unquenched tetracene kinetics.

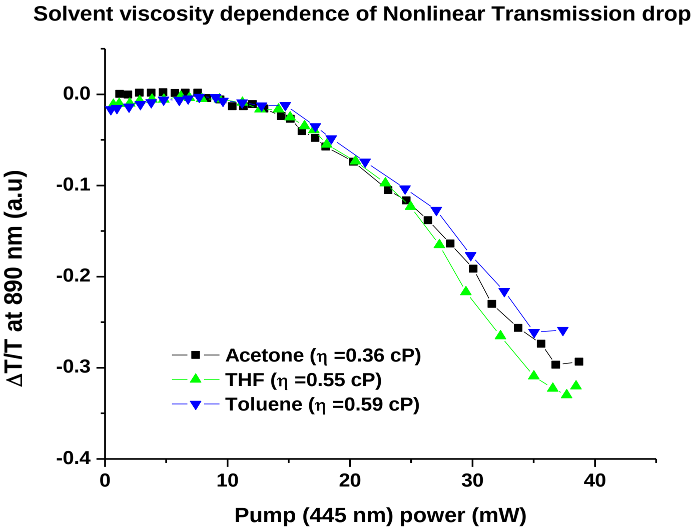

Figure 4-12 Induced transmission drop as a function of solvent viscosity

4.7.2 Singlet-triplet conversion efficiency revealed by two-color transient absorption experiment

Using the laser parameters, the 890nm - beam attenuation caused by 445nm pump to the singlet state one can estimate the singlet to triplet conversion efficiency in the QOT2 system. The presence of greater than unity singlet-triplet conversion efficiency supports the assertion that singlet exciton fission (SEF) should be at play during the femtosecond excitation process. Following information outlines the calculation of singlet-triplet conversion efficiency from experimental data.

1. Number of singlet excitations have been created by ultrashort 445nm laser pulse

a. Average laser power at 445 $nm = 14 mW$ (15.2mW –full power; 14.5 mW – pump (96%), 0.7 mW probe (4%), beam attenuation -0.364/0.186=2.06 or 48.5%)

b. Energy per pump pulse $= \frac{0.0145}{8\times10^{7}} = 0.18$ *nJ/pulse*

c. Pulse duration = 130 *fs* = 1.3×10^{-13} *s*

d. Laser beam divergence (full angle): $\leq 1\ mrad$ (Mai-Tai specs) = 10^{-3} *rad*

e. Focus of the focusing lens = 12.7 *cm*

Waist diameter of focal beam = 12.7×10^{-3} *cm* = 1.27×10^{-2} *cm* (127 *μm*)

Focal waist area = $\frac{\pi}{4} D^2 = 1.26 \times 10^{-4}$ cm^2

Excitation volume =$1.26*10^{-4}*0.5=0.63*10^{-4}$cm^3

f. Energy density for 445nm pump pulse $= \frac{0.18\times10^{-9}}{1.26\times10^{-4}} \approx 1.42 \times 10^{-6}$ *J/cm²*

Peak power density for 445nm pump pulse: $P = \frac{1.42 \times 10^{-6}}{1.3 \times 10^{-13}} = 1.1 \times 10^{7}$ *W/cm²*

Energy of a photon at 445 nm = 4.5×10^{-19} *J/photon*

Photon flux for 445nm pump pulse = $\frac{1.1 \text{ x } 10^{6}}{4.5 \text{ x } 10^{-19}} = 0.24 \text{ x } 10^{25}$ *photons/cm²*.*s*

Singlet excitations number density:

The number of absorbed photons at 445nm:

Optical density of the sample at 445nm =0.55

$I_{in}\text{-}I_{out}\text{=}I_{in}(1\text{-}10^{-0.55}) = I_{in}(1\text{-}0.28)\text{=}0.72{*}I_{in}$

$I_{in}\text{=}\frac{0.18\times10^{-9}}{4.5\times10^{-19}}\text{=}4\text{x}10^{8}$ phot/pulse

That is $0.72{*}4{*}10^{8} = 2.88{*}10^{8}$ photons have been absorbed per pulse.

The same number of molecules in the excited singlet state has been created in the excitation volume ($v\text{=}0.63{*}10^{-4}\text{cm}^{3}$)

$N_S{}^{*} = 2.88{*}10^{8}$ molecules

It corresponds to excited singlet number density:

$n_S{*}\text{=}4.57{*}10^{12}$ molecules/cm^{3}

Triplet excitation number density:

890nm - probe beam attenuation observed under pump of 14.5 mW is 48.5%

No focal mismatch is suggested in this version of calculations.

In order to create this attenuation for the matching part of the probe beam the concentration of the triplet states responsible for attenuation can be obtained:

$I_{out}/I_{in} = 0.515 = 10^{-\varepsilon l M t}$, (ε-extinction coefficient for triplet-triplet absorption, l – cell length, M_T - triplet states concentration) or

$-\varepsilon l M_T = \log(0.515) = -0.288$

$M_T = \dfrac{0.288}{0.5\times 9.1\times 10^3} = 0.606\times 10^{-4} M$ where $9.5*10^3$ $M^{-1}cm^{-1}$ is the molar extinction coefficient for triplet-triplet absorption estimated from the calculated oscillator strength 0.084 for 1.80eV $T_1 - T_2$ transition (linewidth - 1886 cm^{-1})

This molar concentration corresponds to the triplet population density n_{TE}:

$$n_{TE} = \frac{N_A}{1000} M_T = \frac{6.02\times 10^{23}}{10^3}\times 0.606\times 10^{-4} = 3.65\times 10^{16} \text{ triplets/cm}^3$$

Full number of triplet in the excitation volume v is

$N_{TT} = n_{TE}*v = 3.65*10^{16}*0.63*10^{-4} = 2.30*10^{12}$ molecules in the triplet state in the excitation volume,

Each pulse creates $N_S^* = 2.88*10^8$ molecules in the singlet state

The number of triplet states created by each pulse is:

$N_{TP} = \alpha*2.88*10^8$ molecules in the triplet state in the excitation volume.

Now the triplet state accumulation at relatively high pulse repetition rate should be taken into account:

$N_{Taccum}=N_{TP}*\tau_T*8*10^7$; where τ_T is triplet state lifetime (~57μs), $8*10^7$ Hz - laser pulse repetition rate

$N_{Taccum}=2.88*10^8*\alpha*4.56*10^3$:

In order to create the experimentally observed absorption

$N_{Taccum} = N_{TT}$

This equation results in singlet-triplet conversion efficiency α:

$$\alpha=\frac{N_{TT}}{2.88\times10^{8}\times4.56\times10^{3}}=\frac{2.30\times10^{12}}{1.31\times10^{12}}=1.76$$

or 176%

4.7.3 Computational Details

For the sake of completeness of the story the details of the theoretical calculations, that were carried out by our collaborators, are described below. The present calculations were carried out using the CASSCF (Complete Active Space Self-Consistent Field) multi-configurational wave functions as reference, the second-order perturbation theory through the CASPT2 (Complete Active Space Perturbation Theory to second order) was employed in the calculation of the energy of the electronic states. At the CASSCF level, a multi-configurational wave function, which includes all configurations generated by a set of active orbitals and active electrons that fulfills spatial and spin symmetry requirements, is constructed. In this manner, the non-dynamic correlation effects owing to configurations which are very close in energy are included. In a subsequent step, the so-called dynamic correlation, due to short-range electronic interactions, is taken into account at the CASPT2 level. The CASPT2 method calculates the first-order wave function and the energy up to second order and has repeatedly proved its accuracy.[52, 53] The imaginary level-shift technique was employed in order to prevent the effect of intruder states.[54] A shift parameter of 0.2 a.u. was selected. In addition, Cholesky decomposition of the electron repulsion integral matrix was used to alleviate the computational cost.[55, 56]

The standard cc-pVDZ basis set was employed for all the calculations[56]. The active space was selected according to natural orbital populations from state-average (SA)-RASSCF (Restricted Active Space Self-Consistent Field) calculations for the lowest-energy electronic states of the ^1A_g and ^1B_u symmetries. In these RASSCF calculations, the whole π space was distributed among the RAS1 (occupied MOs) and RAS3 (virtual MOs) subspaces, and up to triple excitations were considered. Occupied (virtual) molecular orbitals with natural orbital populations below (above) 1.90 (0.10) were included in the CASSCF active space: 10 electrons in 8 molecular orbitals. Within the irreducible representations (a_g,b_g,a_u,b_u) of the C_{2h} point group this active space can be labeled as (0,4,4,0). In all the single-point calculations, CASSCF wave functions were generated as SA-CASSCF roots of a given symmetry (the number of selected SA-CASSCF roots were 4, 3, and 4 for ^1A_g, ^1B_u and ^3B_u symmetries, respectively).

All calculations were carried out on a simplified model of QOT2 where the bis(butoxymethyl)cyclopentane groups fused to the thiophene rings have been removed. Geometry optimizations were obtained by computing numerical gradients at the CASPT2 level of calculation for the ground and the lowest-lying excited states. The need to include dynamic correlation in the optimization process was considered to be crucial in this case. The molecular symmetry was constrained to C_{2h} point group. Finally, the CAS state interaction (CASSI) method was used to compute the oscillator strengths with CASPT2 excitation energies. All CASSCF/CASPT2 calculations were done with the MOLCAS 7.6 program package.[57]

Restricted active space spin-flip calculations were performed using the lowest high-spin restricted Hartree-Fock quintet (1^5Ag) as the reference configuration. The ground and low-lying excited states were obtained by considering all possible double spin-flip excitations within the 10 electrons in 8 orbitals of Figure S5 (RAS2), all possible configurations with up to one hole in RAS1 and all determinants with one electron in RAS3. The RAS1 (RAS3) subspace was taken as the entire set of fully occupied (virtual) molecular orbitals outside of RAS2. All RAS-2SF calculations were done with the Q-Chem program package.[58]

Table 4-1. Selected CASPT2(10,8)/cc-pVDZ-optimized bond lengths (Å) for QOT2.

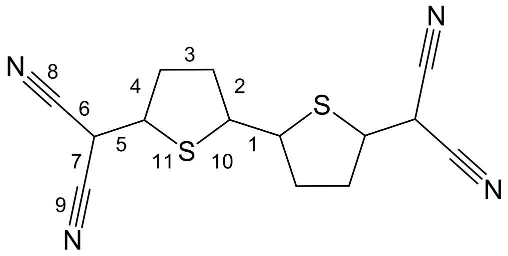

Bond	1^1A_g	1^1B_u	2^1A_g	1^3B_u
1	1.392	1.411	1.439	1.462
2	1.439	1.434	1.413	1.404
3	1.377	1.393	1.400	1.410
4	1.447	1.432	1.425	1.418
5	1.386	1.409	1.452	1.425
6	1.435	1.426	1.416	1.424
7	1.434	1.427	1.412	1.421
8	1.190	1.195	1.198	1.195
9	1.191	1.195	1.200	1.196
10	1.773	1.748	1.757	1.736
11	1.760	1.763	1.743	1.748

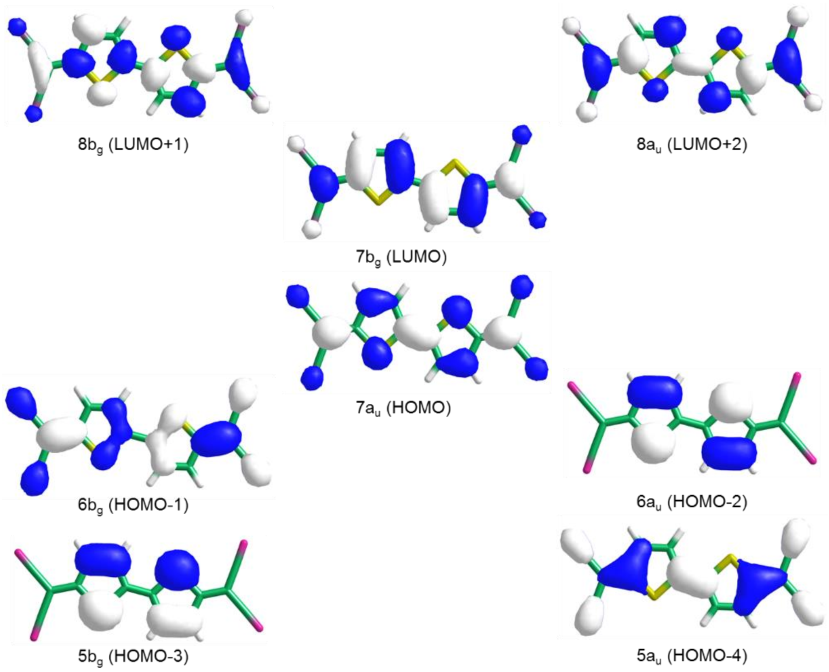

$8b_g$ (LUMO+1)

$8a_u$ (LUMO+2)

$7b_g$ (LUMO)

$7a_u$ (HOMO)

$6b_g$ (HOMO-1)

$6a_u$ (HOMO-2)

$5b_g$ (HOMO-3)

$5a_u$ (HOMO-4)

Figure 4-13. Electronic density isocontours (0.03 e bohr^{-3}) calculated at the CASSCF(10,8) level for the molecular orbitals included in the active space of QOT2.

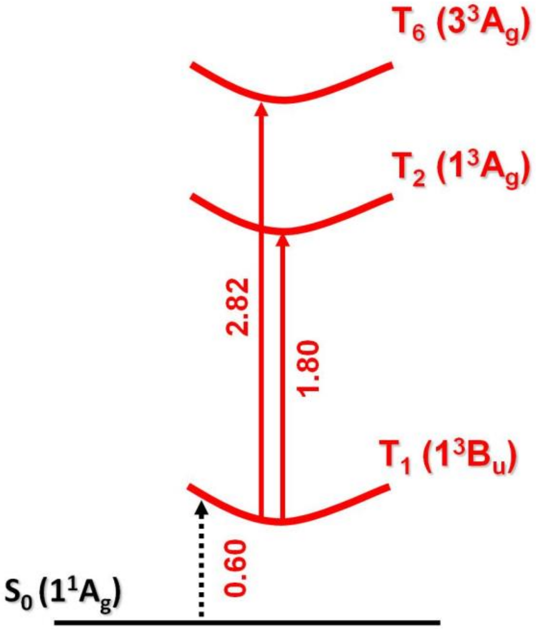

Figure 4-14 Scheme showing the computed CASPT2 energies (in eV) for the low-lying triplet electronic states of QOT2.

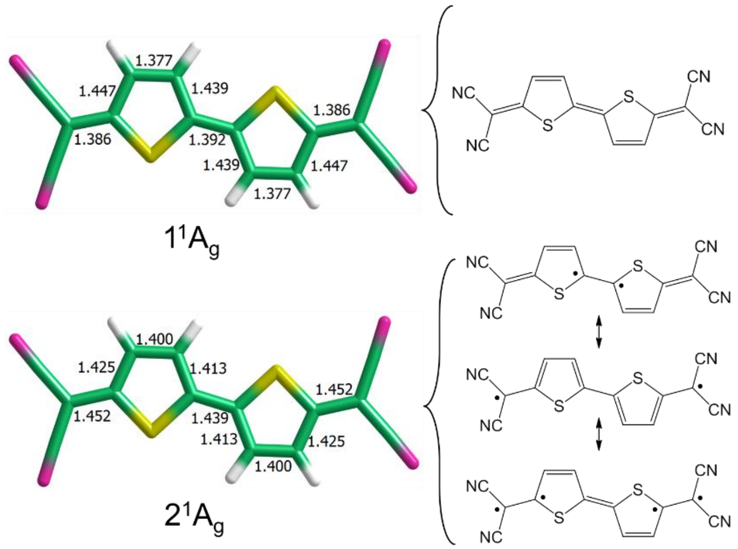

Figure 4-15 Selected CASPT2-optimized bond lengths for the 1^1A_g and 2^1A_g states as well as a scheme of the possible resonance structures that contribute to the description of these ^1A_g states.

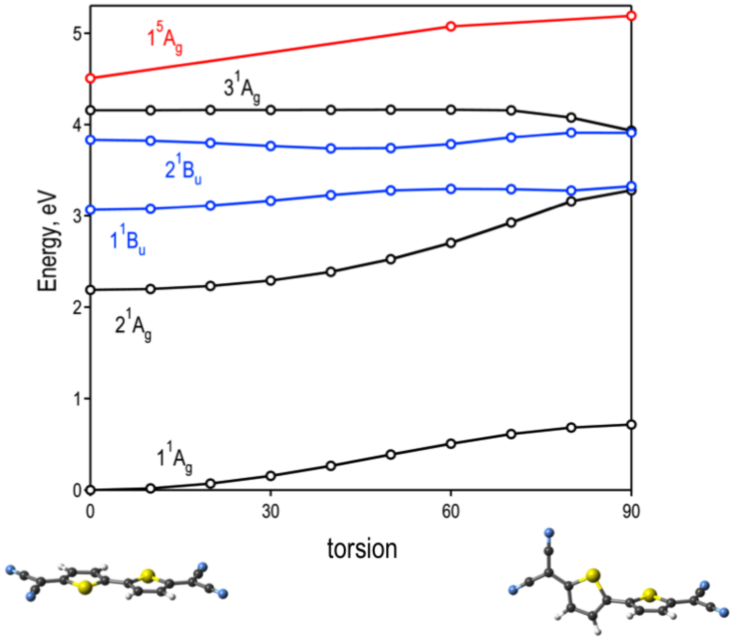

Figure 4-16. RAS-2SF energy profiles of the low lying singlets and the lowest quintet states along the rotation of the central C-C bond of QOT2 (see Table 4-1).

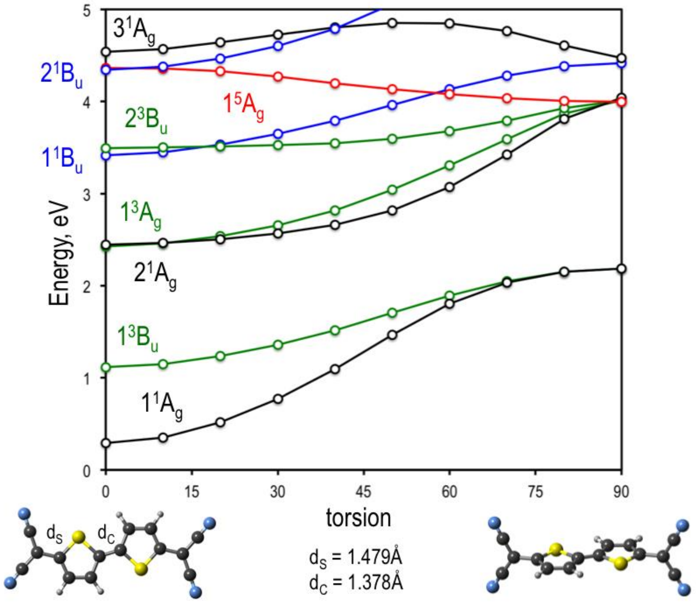

Figure 4-17 RAS-2SF energy profiles of the low-lying states along the simultaneous rotation of the side C-C bonds of QOT2 (see Table 4-1). Energies are given with respect to the ground state optimized geometry.

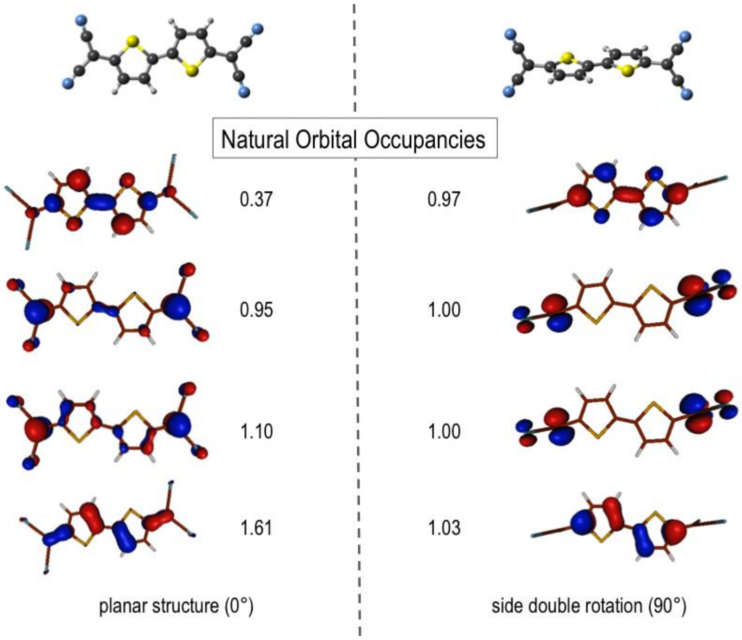

Figure 4-18 RAS-2SF calculation of the tetraradical character of QOT2 (2^1A_g). Frontier natural orbitals and their occupancies of the 2^1A_g state for initial (left) and final (right) according to the simultaneous rotation around bond 1 and equivalent see (Table 4-1).

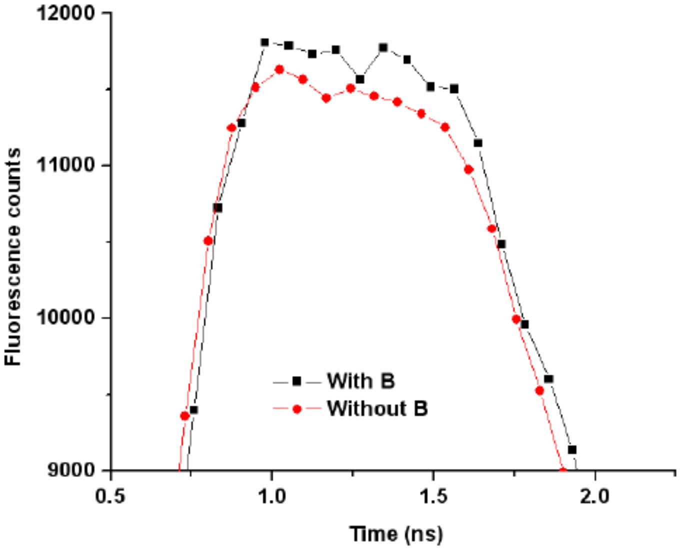

Figure 4-19 Magnetic field dependent for QOT2 emission using TCSPC within the first few nanoseconds upon excitation at 420 nm and detection at 580 nm

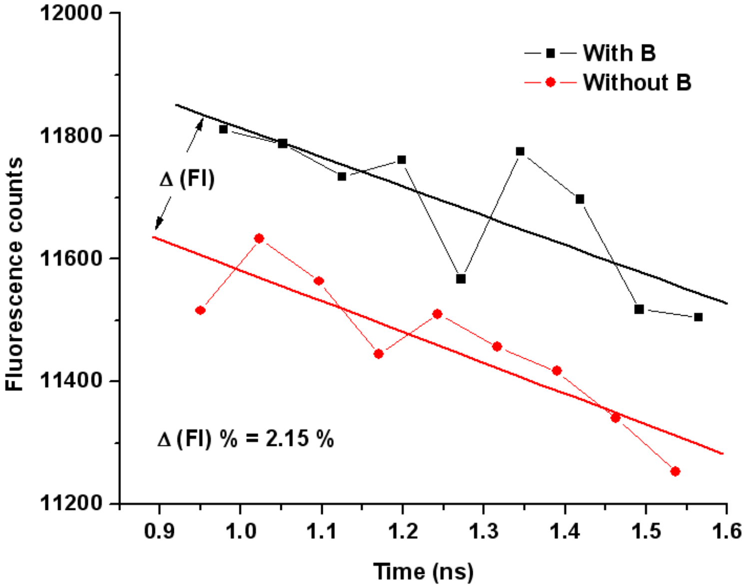

Figure 4-20 Magnified plot of magnetic field dependence for QOT2 emission within the first few nanoseconds upon excitation at 420 nm and detection at 580 nm

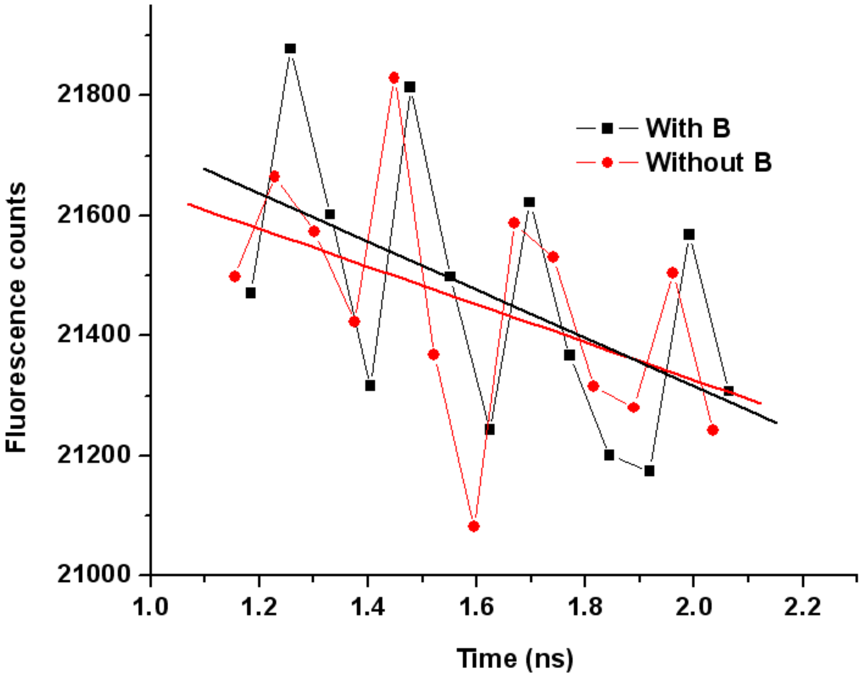

Figure 4-21 Magnetic field dependence for reference Coumarin 153 dye within the first few nanoseconds exciting at 420 nm.

4.8 References

1 Singh, S., Jones, W.J., Siebrand, W., Stoicheff, B.P., Schnider, W.G. Laser Generation of Excitons and Fluorescence in Anthracene Crystals. *J. Chem. Phys.* **1965,** *42*, 330- 343.

2 Congreve, D.N. et al External Quantum Efficiency Above 100% in a Singlet-Exciton-Fission-Based Organic Photovoltaic Cell *Science,* **2013,** *340*, 334-337.

3 Chan, W.-L. *et al.* Observing the Multiexciton State in Singlet fission and Ensuing Ultrafast Multielectron Transfer. *Science,* **2011,** *334*, 1541-1545.

4 Ehrler, B. *et al In situ* Measurement of Exciton Energy in Hybrid Singlet-Fission Solar Cells *Nature Communs* **2012,** *3*, 1019.

5 Zimmerman, P.M., Zhang, Z., Musgrave, C.B. Singlet Fission in Pentacene through Multi-exciton Quantum States *Nature Chem.* **2010,** *2*, 648-652.

6 Smith, M.B., Michl, J. Siglet Fission. *Chem. Rev.* **2010,** *110*, 6891-6936.

7 Paci, I. *et al*. Singlet Fission for Dye-Sensitized Solar Cells: Can a Suitable Sensitizer Be Found? *J. Am. Chem. Soc.* **2006,** *128*,16546-16553.

8 Geacintov, N., Pope, M., Fogel, F. Effect of Magnetic Field on the Fluorescence of Tetracene Crystals: Exciton Fission. *Phys. Rev. Lett.* **1969,** *22*, 593-596.

9 Burdett, J.J., Bardeen, C.J. Quantum Beats in Crystalline Tetracene Delayed Fluorescence Due to Triplet Pair Coherences Produced by Direct Singlet Fission. *J. Am. Chem. Soc.* **2012,** *134*, 8597-8607.

10 Lanzani, G. *et al.* Triplet-Exciton Generation Mechanism in a New Soluble (Red-Phase) Polydiacetylene. *Phys. Rev. Lett.* **2001,** *87*, 187402.

11 Huynh, U.; Basel, T.; Xu, T.; Lu, L.; Zheng, T.; Yu, L.; Vardeny, V. Optical Properties of Low Bandgap Copolymer PTB7 for Organic Photovoltaic Applications. *Proc. SPIE,* **2014,** *vol. 9165,* 91650Z.

12 Busby, E.; Xia, J.; Wu, Q.; Low, J.Z.; Song, R.; Miller, J.R.; Zhu, X-Y.; Campos, L.M.; Sfeir, M.Y. A Design Strategy for Intramolecular Singlet Fission Mediated by Charge-transfer States in Donor-Acceptor Organic Materials. *Nat. Mater.* **2015,** doi:10.1038/nmat4175.

13 Gradinaru, C.C. *et al.* An Unusual Pathway of Excitation Energy Deactivation in Carotenoids: Singlet-to-Triplet Conversion on an Ultrafast Timescale in a Photosynthetic Antenna. *Proc. Natl. Acad. Sci. U.S.A.* **2001,** *98***,** 2364-2369.

14 Polivka, T. et al Femtosecond Carotenoid to Retinal Energy Transfer in Xanthorhodopsin *Biophys. J.* **2009,** *96***,** 2268-2277.

15 Wang, C., Tauber, M.J. High-Yield Singlet Fission in a Zeaxanthin Aggregate Observed by Picosecond Resonance Raman Spectroscopy. *J. Am. Chem. Soc.* **2010,** *132***,** 13988-13991.

16 Müller, A.M.; Avlasevich, Y.S.; Müllen, K.; Bardeen, C.J. Evidence for Exciton Fission and Fusion in a Covalently Linked Tetracene dimer. *Chem. Phys. Lett.* **2006,** *421***,** 518-522.

17 Michl, J. *et al.* Toward Singlet Fission for Excitonic Solar Cells. *Proc. SPIE,* **2007,** *6656***,** 66560E.

18 Johnson, J.C. et al Toward Designed Singlet Fission: Solution Photophysics of Two Indirectly Coupled Covalent Dimers of 1,3-Diphenylisobenzofuran *J. Phys. Chem. B* **2013,** *117***,** 4680-4695.

19 Nozik, A. Nanoscience and Nanostructures for Photovoltaics and Solar Fuels. *Nano Lett.* **2010,** *10***,** 2735-2741.

20 Wang, Z., Kobayashi, T. Electronic Relaxation and Vibrational Dynamics in a Thiophene Oligomer Studied Under the Same Experimental Condition with Sub-5fs Laser *New J. Phys.* **2008,** *10,* 123021.

21 Raymond, J.E., Casado, J., Lopez Navarrete, J.T., Takimiya, K., Goodson, III, T. Two-Photon Mediated Three-Photon Fluorescence: Lessons from a Quinoidal Oligothiophene Dimer. *J. Phys. Chem. Lett*. **2011,** *2***,** 2179-2183.

22 Takahashi, T., Matsuoka, K., Takimiya, K., Otsubo, T., Aso, Y. Extensive Quinoidal Oligothiophenes with Dicyanomethylene Groups at Terminal Positions as Highly Amphoteric Redox Molecules. *J. Am. Chem. Soc.* **2005,** *127***,** 8928-8929.

23 Casado, J., Lopez Navarrete, J.T. The Longest Quinoidal Oligothiophene: A Raman Story. *Chem. Rec.* **2011,** *11***,** 45-53.

24 Ortiz, R.P. *et al.* Quinoidal Oligothiophenes: Towards Biradical Ground-State Species. *Chem. Eur. J.* **2010,** *16***,** 470-484.

25 Ortiz, R.P. *et al.* On the Biradicaloid Nature of Long Quinoidal Oligothiophenes: Experimental Evidence Guided by Theoretical Studies. *Angew. Chem. Int. Ed. Engl.* **2007,** *46***,** 9057-9061.

26 Casado, J., Ponce Ortiz, R., López Navarrete, J.T. Quinoidal Oligothiophenes: New Properties behind an Unconventional Electronic Structure. *Chem. Soc. Rev.* **2012,** *41***,** 5672-5686.

27 Gonzalez, S.R., Ie, Y., Aso, Y., Lopez Navarrete, J.T., Casado, J. The Frontiers of Quinoidal Stability in Long Oligothiophenes: Raman Spectra of Dicationic Polaron Pairs. *J. Am. Chem. Soc.* **2011,** *133***,** 16350-16353.

28 Di Motta, S., Negri, F., Fazzi, D., Castiglioni, C., Canesi, E.V. The Biradicaloid and Polyenic character of Quinoidal Oligothiophenes Revealed by the Presence a Low Lying Double-exciton State. *J. Phys. Chem. Lett.* **2011,** *1***,** 3334-3339.

29 Bonaicic-Koutecky, V.; Koutecky, J.; Michl, J. A Neutral and Charged Biradicals, Zwitterions, Funnels in S_1 and Proton Translocation :Their Role in Photochemistry, Photophysics, and Vision *Angew. Chem. Int. Ed.* **1987,** *26,* 170-189.

30 Minami, T., Nakano, T. Diradical Character View of Singlet Fission. *J. Phys. Chem. Lett.* **2011,** *3***,** 145-150.

31 Trinh, M.T., Zhong, Y., Chen, Q., Schiros, T., Jockusch, S., Sfeir, M.Y., Steigerwald, M., Nuckolls, C., Zhu, X. Intra- to Intermolecular Singlet Fission. *J. Phys. Chem. C* **2014,** *119,* 1312-1319.

32 Monahan, N., & Zhu, X.-Y. Charge-Transfer-Mediated Singlet Fission *Annu. Rev. Phys. Chem.* **2015**, *66*, 601-618.

33 Izumi, T., Kobashi, S., Takimiya, K., Aso, Y., Otsubo, T. Synthesis and Spectroscopic Properties of a Series of α-Blocked Long Oligothiophenes up to the 96-mer: Revaluation of Effective Conjugation Length. *J. Am. Chem. Soc.* **2003,** *125***,** 5286-5287.

34 Walker, B.J.; Musser, A.J.; Beljonne, D.; Friend, R.H. Singlet Exciton Fission in Solution *Nat. Chem.* **2013,** *5***,** 1019-1024.

35 Chan, W.-L. *et al* The Quantum Coherent Mechanism for Singlet Fission: Experiment and Theory *Acc. Chem. Res.* **2013,** *46***,** 1321-1329.

36 Ryasnyanskiy, A., Biaggio, I. Triplet Exciton Dynamics in Rubrene Single Crystals *Phys.Rev. B*, **2011,** *84*,193203.

37 Roberts, S.T. *et al.* Efficient Singlet Fission Discovered in a Disordered Acene Film *J. Am. Chem. Soc.* **2012,** *134***,** 6388−6400.

38 Müller, A.M., Avlasevich, Y.S., Schoeller, W.W., Müllen, K., Bardeen, C.G. Exciton Fission and Fussion in Bis(tetracene) Molecules with Different Covalent Linker Structures *J. Am. Chem. Soc.* **2007,** *129***,** 14240-14250.

39 Serrano-Andres, L. Merchan, M. Quantum Chemistry of the Excited State: 2005 overview *J. Mol.Struc. (Theochem)* **2005,** *729,* 99-108.

40 Serrano-Andrés, L. Serrano-Pérez, J. J. in Handbook of Computational Chemistry (Ed. Jerzy Leszczynski) Ch. 14, 483-560 (Springer Netherlands, **2012**).

41 Shulten, K., Karplus, M. On the Origin of a Low-Lying Forbidden Transition in Polyenes and Related Molecules. *Chem. Phys. Lett.* **1972**, *14,* 305-309.

42 Tavan, P., Schulten, K. Electronic Excitations in Finite and Infinite Polyenes *Phys. Rev. B* **1987,** *36*, 4337-4358.

43 Casanova, D., Head-Gordon, M. Restricted Active Space Spin-flip Configuration Interaction Approach: Theory, Implementation and Examples *Phys. Chem. Chem. Phys.* **2009,** *11*, 9779-9790.

44 Casanova, D. Efficient Implementation of Restricted Active Space Configuration Interaction with the Hole and Particle Approximation *J. Comp. Chem*. **2013,** *34*, 720-730.

45 Bell, F., Casanova, D., Head-Gordon, M. Theoretical Study of Substituted PBPB Dimers: Structural Analysis, Tetraradical Character, and Excited States *J. Am. Chem. Soc*. **2010,** *132*, 11314-11322.

46 Zimmerman, P.M., Bell, F., Casanova, D., Head-Gordon, M. Mechanism for Singlet Fission in Pentacene and Tetracene: From Single Exciton to Two Triplets *J. Am. Chem. Soc*. **2011,** *133*, 19944-19952.

47 Zimmerman, P.M., Musgrave, C.B., Head-Gordon, M. A Correlated Electron View of Singlet Fission *Acc. Chem. Res*. **2013,** *46*, 1339-1347.

48 Tayebjee, M.J.Y.; Clady, R.G.C.R.; Schmidt, T.W. The Exciton Dynamics in Tetracene Thin Film *Phys. Chem. Chem. Phys.* **2013,** *15,* 14797-14805.

49 Wang, Z.; Otsubo, T.; Kobayashi, T. Chirped Modulation of Molecular Vibration in Quinoidal Thiophene after Sub-5 fs Excitation *Chem. Phys. Lett.* **2006,** *430,* 45–50.

50 Donehue, J.E., Varnavski, O.P., Cemborski, R., Iyoda, M., Goodson III, T. Probing Coherence in Synthetic Cyclic Light-Harvesting Pigments. *J. Am. Chem. Soc.* **2011,** *133*, 4819-4828.

51 Varnavski, O., Yan, X., Mongin, O., Blanchard-Desce, M., Goodson III, T. Strongly Interacting Organic Conjugated Dendrimers with Enhanced Two-photon aAbsorption. *J. Phys. Chem. C.* **2007,** *111*, 149-162.

52 Serrano-Andres, L. & Merchan, M. Quantum chemistry of the excited state: 2005 overview. J. Mol.Struc.(Theochem) **729,** 99-108 (2005).

53 Serrano-Andrés, L. & Serrano-Pérez, J. J. in Handbook of Computational Chemistry (ed Jerzy Leszczynski) Ch. 14, 483-560 (Springer Netherlands, 2012).

54 Roos, B. O. et al. Applications of level shift corrected perturbation theory in electronic spectroscopy. J. Mol. Struc.(Theochem) **388,** 257-276 (1996).

55 Aquilante, F., Lindh, R. & Pedersen, T. B. Unbiased auxiliary basis sets for accurate two-electron integral approximations. J. Chem. Phys. **127,** 114107 (2007).

56 Aquilante, F., Todorova, T. K., Gagliardi, L., Pedersen, T. B. & Roos, B. O. Systematic truncation of the virtual space in multiconfigurational perturbation theory. J. Chem. Phys. **131,** 034113 (2009).

57 Aquilante, F. et al. Software News and Update MOLCAS 7: The Next Generation. J. Comput. Chem. **31,** 224-247 (2010).

58 Shao, Y., Molnar, L. F., Jung, Y., Kussmann, J., Ochsenfeld, C., Brown, S. T., Gilbert, A. T. B., Slipchenko, L. V., Levchenko, S. V., O'Neill, D. P., DiStasio Jr, R. A., Lochan, R. C., Wang, T., Beran, G. J. O., Besley, N. A., Herbert, J. M., Lin, C. Y., Voorhis, T. V., Chien, S. H., Sodt, A., Steele, R. P., Rassolov, V. A., Maslen, P. E., Korambath, P. P., Adamson, R. D., Austin, B., Baker, J., Byrd, E. F. C., Dachsel, H., Doerksen, R. J., Dreuw, A., Dunietz, B. D., Dutoi, A. D., Furlani, T. R., Gwaltney, S. R., Heyden, A., Hirata, S., Hsu, C.-P., Kedziora, G., Khalliulin, R.

Z., Klunzinger, P., Lee, A. M., Lee, M. S., Liang, W., Lotan, I., Nair, N., Peters, B., Proynov, E. I., Pieniazek, P. A., Rhee, Y. M., Ritchie, J., Rosta, E., Sherrill, C. D., Simmonett, A. C., Subotnik, J. E., Iii, H. L. W., Zhang, W., Bell, A. T., Chakraborty, A. K. Phys. Chem. Chem. Phys. **8**, 3172 (2006).

Chapter 5

Summary, Future Directions and Methods

5.1 Summary

The summary will be divided into two segments to include the insights gained from the nanocluster investigations and the investigations of quinoidal bithiophene for intramolecular singlet exciton fission.

5.1.1 Summary of the investigations of monolayer protected quantum confined nanoclusters

Previous linear and nonlinear optical investigations on quantum confined monolayer protected gold nanoclusters in solution phase ensembles were able to demonstrate the optical effects of quantum confinement present in condensed phase nanoclusters in great detail. [1-12] Also, such investigations revealed the clear difference between the gold nanoparticles and quantum confined gold nanoclusters. All of the observations made on Au nanoclusters in the solution ensembles presented one common theme. That is, the ability of elemental gold nanoclusters to form molecule-like "super atoms" in the condensed phase allowing researchers to delve deeper in to the science of nanoclusters. [13- 30] The idea of building up molecule like super atoms from elemental atoms had started to receive increased attention over the last two decades due to their enormous potential in a variety of applications such as bioimaging, sensing, molecular electronics and molecular logic applications. [31- 42] However, until now optical investigations on monolayer protected nanoclusters have not been reported on how the effects of quantum confinement will manifest when the nanoclusters are removed from ensemble solutions and placed on solid substrates. Moreover, quantum confined nanocluster investigations were never reported on what effects occur when one isolates nanoclusters from an aggregate.

In my dissertation work, I have been able to interrogate highly stable isolated Au_{25} nanoclusters on solid substrate when they are removed from solution phase ensemble and from solid state aggregates. The crystal structure of Au_{25} was well known for nearly a decade[24, 25] and their atomically precise synthesis [43, 44] as well as their chemical stability [45] allowed researchers to investigate them in the solution phase ensembles in an extensive manner revealing many details of the realm of quantum confinement. The utilization of the TPEF NSOM for these investigations allowed me to carry out these investigations at an unprecedented 30 nm point resolution. This allowed me to avoid excitation of more than a single nanocluster (at a time) on solid state with two-photon excitation. Interestingly, when the quantum confined nanoclusters were isolated from the solution ensembles, the two-photon cross section increased, indicating the presence of local field enhanced nonlinear optical effects for isolated clusters. Also, the presence of nanoclusters in close proximity tend to reduce the two-photon absorption cross section due to inter-nanocluster interactions. These interactions could vary from dipole coupling, energy transfer or local field enhancement/reductions due to magic number arrangements of nanoclusters resulting from packing and inter-nanocluster distances. These observations indicate that ensemble investigations can, to a certain extent, veil the native quantum confinement effects present in nanoclusters. Also, our current investigations further support the super atom concept where gold serves as an element to build up some stable quantum confined nanoclusters that possess properties that are uniquely different from their elemental atoms, molecules, nanoparticles and bulk metal. Based on the understanding we gathered, nanocluster community should be able to generate many new ideas to obtain a deeper physical understating of these quantum confined systems and elemental quantum clusters in general.

Also, the investigations carried out on DNA-templated Ag nanoclusters indicated that the physical and electronic states and their excited state dynamics in Ag NCs were similar to the solution phase Au nanoclusters. The fact that dsDNA-Ag NCs behave more like a typical quantum confined Au nanocluster as opposed to the ssDNA-Ag NCs implies the importance of the ligand protection in retaining the symmetry of a quantum confined system there by possessing the required energy levels to act similar to a gold nanocluster. Overall, steady state absorption, emission, time resolved dynamics and two-photon absorption imply that the DNA-templated Ag NCs are indeed quantum confined in their stabilized state. Also, the unusually large two-photon absorption cross section of dsDNA-Ag NCs indicate their potential use in near IR biological imaging.

Overall, my work on the aforementioned quantum confined systems in *ensemble*, *aggregate* and as *isolated nanoclusters* on solid substrate indicates the importance of the fundamental physical investigations of this interesting new material form. While the field of elemental nanoclusters is still burgeoning, it can be easily surmised as to the many type of materials possible with these “super atom” or “magic cluster” systems. As I had indicated at the beginning of this dissertation, adding a new degree of freedom to material science is no longer a pipe dream. As we speak, there are many new metal nanocluster materials that are synthesized and that possess interesting and useful material properties. Therefore, adding a new dimension to the periodic table to form certain stable super atom compositions from single elemental atoms will not only be possible but it will also be able to give rise to properties that were hitherto unheard of.

5.1.2 Summary for quinoidal oligothiophene investigations

For single junction solar cells, singlet exciton fission could increase their power conversion efficiency (PCE) from 33% to ~45%. The ability to overcome this Shockley-Queisser limit may eliminate a barrier in the power conversion efficiency of organic photovoltaics (OPV). [46 - 56] Typically, singlet exciton fission was reported to occur in systems where there are molecules arranged in close proximity to one another facilitating intermolecular coupling to facilitate singlet exciton fission (SEF). This intermolecular requirement causes the molecules to be arranged in a specific spatial geometry that limits the full utilization of the singlet exciton fission process. On the contrary, *intramolecular* SEF do not depend on the arrangement/geometry between chromphores for efficient singlet fission. [47- 63] However, until our work, efficiencies exceeding 100% for intramolecular SEF was not reported for small organic molecules. [64] If singlet-to-triplet conversion efficiencies approaching 200% can be found from small organic molecules, researchers can use such molecular/electronic structures to tune the efficiencies by modifying molecular properties through simple synthetic procedures. This will help us to improve the PCE of OPVs to obtain high efficiencies that can be a cheap and environmentally benign energy solution. In the work discussed in this dissertation, we report ~180% ultrafast intramolecular SEF for a quinoidal bitiopehene molecule. Also, in a subsequent theoretical work in collaboration with Zimmerman group we were able to find the conical intersection that may be responsible for the ultrafast singlet to triplet conversion. However, the theoretical calculations were not reported for longer than 1 picosecond time scales. Since there are many photophysical events taking place until the excited triplet exciton decay after 57 microseconds our current theoretical understading of this intramolecular SEF process in far from complete. Therefore, there is plenty of room for the mechanistic investigation of the *intramolecular* singlet exciton fission process of this small organic material. Also, the physics required to utilize this process is something the community is actively working on.

My work in the investigations of quinoidal bithiophenes for ultrafast intramolecular SEF resulted in several important observations. The flash photolysis experiments that were carried out indicated a lifetime of 57 microseconds for the triplet exciton. Also, the triplet sensitization experiments carried out using tetracene revealed a 111 microsecond triplet excited state for a single triplet exciton. This indicates that the shorter lived (57 microsecond) exciton cannot be a single triplet exciton. Also, from my two-color transmission experiment studies, we were able to determine the singlet-to-triplet conversion efficiency to be ~180%. My solvent polarity dependent nonlinear transmission studies indicated the absence of charged polaronic excited states in these excited quinoidal thiophene molecules. Finally, the magnetic field dependent time-correlated fluoresce signal for the first few ns of emission also supported the hypothesis of the singlet exciton fission process that was also observed in many singlet fission materials previously. [65-69] In addition to that our work on ultrafast fluorescence up conversion and transient absorption experiments revealed the conversion of a singlet exciton to a long lived excited state that goes beyond our measurement time window. This excited state at 580 nm was found to give a delayed fluorescence signal that is also consistent with the triplet-triplet annihilation to form more singlet excitons over long times. Also, the concentration dependent absorption studies I have conducted indicated no shift in steady state absorption on increasing of the concentrations (up to ~60 x 10^{-6} M) indicating no aggregation of QOT2 in the solution. Therefore, the experimental observations we have made are all consistent with the initial formation of intramolecular SEF for QOT2.

Subsequent observations of intramolecular SEF with high efficiencies were reported for covalently linked pentacene dimers. [70] Since the intramolecular SEF with high efficiency was shown with several small molecules [64, 70] and polymeric [57] materials, the field of organic photovoltaics would require ways to understand this quantum mechanical process in greater detail. The fundamental photophysics such as energy level spacing, presence of conical intersections and possible formation of charge transfer intermediate states may not necessarily be the only parameters required in these highly efficient molecular events. Future directions section for this research will be dedicated to discussing these possible avenues the community may explore via experimental and theoretical means.

5.2 Future directions

The field of quantum confined nanoclusters and the field of intramolecular singlet fission materials are growing rapidly. In this section I try to discuss the possible future directions to pursue in order to deepen our current understanding of these exciting materials.

5.2.1 Quantum confined nanoclusters

The field of monolayer protected nanoclusters had grown to an area of its own right. Due to the ability to synthesize atomically precise structures, cluster science was able to enjoy a phenomenal growth in terms of the number of materials available to investigate and deeper insights gained of this quantum cluster realm. Previous investigations by our group on Au nanoclusters were able to experimentally pinpoint exactly the size range the nanoparticle to quantum nanocluster transition occur. [1-10] This size range is consistent with the metal-to-insulator transition theoretically predicted using Kubo criterion (see Chapter 1 for details). However, due to the presence of many valence electrons available in these Au nanoclusters, it is still not straight forward as to whether these quantum sized nanoclusters would behave similar to molecules.

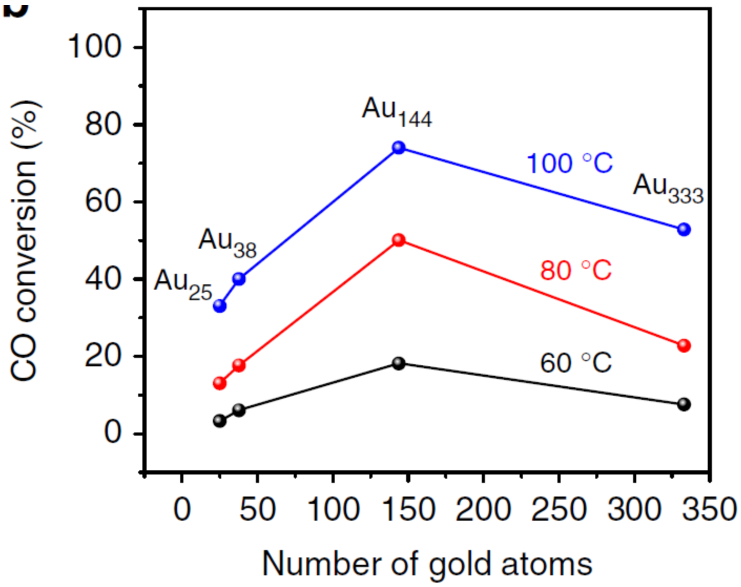

Figure 5-1 Catalytic CO oxidation efficiency with the number of gold atoms. [71]

Recent work by Jin and coworkers reported an interesting generalization. [71] That is, based on the optical, electronic and catalytic behavior of various sizes of Au monolayer protected particles (clusters and nanoparticles), the transition from metal-to-nonmetal is not abrupt. As can be seen in figure 5-1, the catalytic oxidation efficiency for CO oxidation reached a peak for Au_{144} while the Au_{333} (with a diameter > 2.0 nm) showed a significant drop in CO conversion efficiency. Also, the oxidation current density on Au nanoclusters/nanoparticles followed a similar trend where the current density was a maximum for Au_{144}. Their observations lead to a conclusion of the size range where the metallic to non-metallic transition is occurring (Figure 5-2). However, it is still not clear whether nanoclusters possessing Au_{144} or even Au_{25} (red areas in figure 5-2) should be called molecules. The presence of large number of valence electrons that can be excited, and the availability of electronic states with different types of symmetries within the same energy range, the possibility of relativistic effects in Au, and the possibility to relax the typical quantum mechanical selection rules of optical excitation via spin-orbit coupling and electronic correlation

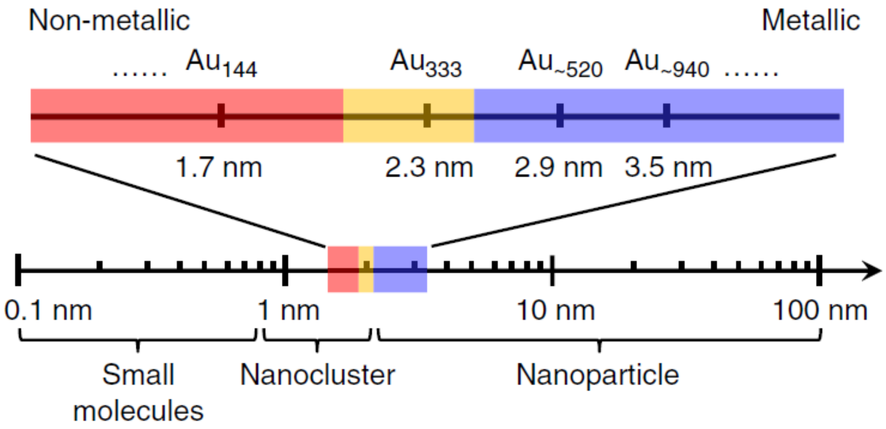

Figure 5-2 Evolution from metallic to non-metallic regime in gold nanoparticles. [71]

effects can all play roles to make them significantly different from typical molecules. For example, one cannot exclude the possibility of quantum confined nanoclusters to undergo multiple electronic excitations to form multiple excitons. While investigations into aforementioned possibilities are encouraged, it can be argued that quantum confined nanoclusters made out of elemental atoms (e.g. Au) should be placed in a position in the realm of materials that cannot be deemed atomic, molecular, semiconductor, bulk or nanoparticle. Therefore, due to the unique size dependent optical, electronic, catalytic properties of nanoclusters and due to their electronic structures, elemental nanoclusters should be placed in its own class as a different form of matter.

Also, the fact that Ag nanoclusters demonstrate high quantum yields and the ability of dsDNA-templated Ag NCs to show bright two photon emission with unprecedented two-photon action cross sections indicate their potential to be used in bio-imaging applications. Also, it is clear that such DNA-templated Ag NCs would be an interesting system to study using TPEF NSOM to see how their two-photon absorption cross section varies when they are removed from solution ensembles. Few questions we will be able to answer through such investigations are as follows. Is the two-photon absorption cross section going to be enhanced for Ag NCs similar to what I observed in Au_{25} nanoclusters? How would their two-photon response vary with respect to the dsDNA-Ag NC aggregates? One practical road-block one may have to encounter in those studies is the identity of the Ag NC. Can we make sure that the number of atoms per Ag nanocluster is fixed? I think the Ag NC synthetic techniques have recently been receiving an increased attention due to their potential use in biological and sensing applications. For example, recent reports of Ag_{44} crystal structures hint at the direction the community is taking to optimize the Ag NC synthetic procedures. [26, 27]

As indicated in Chapter 3, the ability of magic number systems to show local field induced microscopic cascading (LFIMC) indicates the potential use of nanoclusters in molecular computing. If nanocluster arrays can be synthesized where they are connected by covalent linker ligands, and if the ideal inter-nanocluster distances can be found, I think large enhancements (> order of magnitude) in two-photon absorption cross section can potentially be obtained. The reason for such enhancements can be understood as an enhancement of the nanocluster local fields via constructive interferences of individual local field upon excitation by an oscillating field (i.e. electromagnetic field). Therefore, I think that TPEF NSOM would be a great tool to study such nanocluster *arrays*, *networks* or *lattices* with ideal "magic number" configurations to obtain unusually enhanced two-photon excited emission to use them in molecular computing and molecular logic applications at the nanoscale.

5.2.2 Future directions in Quionoidal oligithiophenes and singlet exciton fission

Recent experimental and theoretical investigations carried out on *intermolecular* SEF have shed more light on how this quantum mechanically interesting process is occurring at ultrafast time scales. [72- 79] While the understanding of some key parameters essential for singlet fission process are understood, there are still few major questions that requires further work. For example, when a singlet exciton fission process occurs is it essential to go through a conical intersection? Or is it possible to form a charge transfer intermediate that are relatively higher in energy compared to the excited state to form the final triplet pair? What is the nature of the correlated triplet pair exciton? Is it an excitation wave-packet that is changing its multiplicity and energy over time?

What molecular parameters are essential to facilitate the conversion of the correlated triplet pair into two separate spin wave-functions? How is it quantum mechanically possible to form an exciton in a neighboring molecule that is not excited by light (if it is not an energy transfer process)? Answers to questions such as above may expand our understanding of this interesting photochemical process which in turn help the scientific community identify certain parameters that can be used in tuning molecular structures to make highly efficient organic photovoltaic materials.

On the other hand, highly efficient *intramolecular* singlet efficient process needs a significant degree of further theoretical and experimental investigations to understand the mechanistic details of the process. In our recent work with the Zimmerman group, we were able to identify a conical intersection that govern the initial transition of the singlet exciton to the correlated triplet exciton ^{1}(TT) that has A_g symmetry. [80] Since the dynamical simulations were not carried out beyond the picosecond timescales after the excitation, it is still not clear the exact evolution of that correlated triplet pair state. Therefore, experimental and theoretical work in the field of *intramolecular* singlet exciton fission would help us to answer the following questions. Are the torsional states required to stabilize the two triplet excitons formed in the same molecule? Or is it essential to have a completely separated two triplet wavefunctions? Can the correlated triple pair state exist as a long lived excitons and be extracted from the photoexcited quinoidal bithiophene? Due to the presence of proper energy level arrangement and quinoidal electronic structures, can the quinoidal trithiopehene or tetrathiophene show intramolecular singlet exciton fission?

In order to answer some of these questions our group is working on solution phase extraction of triplet excitons through an intermolecular electron/energy transfer process by using a suitable acceptor molecule. If the triplet excitons can be extracted via this approach it is possible to do molecular level control of intramolecular singlet exciton fission solar cells for high PCE organic photovoltaic applications. This is work is currently in progress.

Also, recent reports by Guldi and coworkers [70] on the efficient *intramolecular* SEF in regioisomeric pentacene dimer molecules showed an important point that may require further theoretical and experimental investigations. In their work, the highest *intramolecular* SEF efficiency was reported for a dimer molecule where the two pentacene molecules are substituted to a bezene ring's meta position. This creates an angle between the two pentacene molecules close to 120 degrees. This specific geometry was showing more efficient *intramolecular* SEF than the meta and para substituted molecules indicating an optimum angle for possible wavefucntion overlap and subsequent separation of the excitons in to two separate triplets in the two pentacene monomer molecules. Since the initial electronic coupling of the conjugation may be as important as the subsequent separation of excitons via (possible) torsional distortions, a critical angle may exist that maximizes the singlet to triplet conversion efficiency. Further investigations in the mechanism of *intramolecular* SEF in these pentacene dimers will reveal more details of these parameters. Also, an interesting observation one may make in their study is the change in singlet fission efficiency upon changing of solvent. When the solvent was made a bit polar (from Toluene to Benzonitrile), the SEF efficiency increased. A question that may arise is: Could this enhancement in SEF efficiency be due to a possible charge transfer intermediate that may be involved in this intramolecular SEF process? Hopefully, future investigations on these dimer molecules may be able to answer this question.

As can be understood, intramolecular singlet exciton fission is a burgeoning field in the organic photovoltaic community. The independence on the intermolecular arrangement/geometry for high SEF efficiencies indicate that this process in small organic molecules could be utilized for tuning of SEF efficiencies using simple synthetic tools that are already available for organic chemists. The fundamental physical chemical understanding we may gain through such studies will reveal the physical chemistry rules that govern the electronic structure, geometry and other parameters of potential intramolecular SEF materials. Therefore, future investigations of these small organic molecules for highly efficiency *intramolecular* SEF will help the community to make environmentally benign, cheap photovoltaic devices.

5.3 Experimental Techniques

5.3.1 Overview

In this section of the dissertation, I will be discussing the microscopic and spectroscopic techniques used for the aforementioned investigations and the synthesis of atomically precise monolayer protected synthesis utilized to obtain Au_{25} monolayer protected nanoclusters. The techniques used for nanocluster isolation in solution phase and then their subsequent preparation as isolated nanoclusters on the substrate will also be discussed. The operating principles of the instruments used will also be included in this chapter so that the reader can refer to it if they require a detailed understanding of the physics, chemistry and engineering involved in each experiment.

5.3.2 Steady state absorption and emission

Steady state absorption and emission processes allows one to characterize a sample to find its optically allowed transitions. They serve as a guide to determine the optical band gap of a material and one-photon transitions involved in the absorption and emission processes. Optical absorption is measured using the optical density (OD) which gives a quantitative description of probability of various transitions. Absorption experiments are carried out with an Agilent Model 8341 spectrophotometer. The spectrometer has two set of lamps to generate UV and visible radiation. Deuterium and tungsten lamps are used to provide a spectrum ranging from 200 nm - 1100 nm. The samples are contained in a Quartz or SOG cuvette manufactured by Starna. The cuvette (or cell) has a path length of 0.4 cm. To ensure that absorption data is free from contaminations from the environment, a blank spectrum is taken with the same cell containing either solvent or air. The collected blank spectrum was subtracted from the final spectra. OD is measured as the $-\log_{10}$ T, where T stands for the transmittance of the sample under study. The ratio between the transmitted intensity and the incident intensity of light is measured as Transmittance (equation 5-1).

Equation 5-1 $$\boldsymbol{T = \frac{I_{trans}}{I_{incident}}}$$

OD is related to the concentration of the sample used (c, M), the path length the light beam travels across the sample (l, cm) during the absorption process and the extinction coefficient (ε, $M^{-1}cm^{-1}$) of a material via Beer-Lambert Law (equation 5-2).

Equation 5-2 $$\boldsymbol{A(OD) = \varepsilon c l}$$

Extinction coefficient is unique to the material under study and can be used to estimate the linear (one-photon) absorption cross section of a material (assuming scattering is negligible for materials that are much smaller than the wavelength of light). For example, for a material having an extinction coefficient of 10^5 $M^{-1}cm^{-1}$ would mean its absorption cross section is 1.66 x 10^{-16} cm^2/molecule. The absorption cross section of a material is directly proportional to the transition dipole moment and thus the oscillator strength of the transition.

In steady state emission, one measures the time-averaged emission of the material under a specific excitation wavelength. The energy that is absorbed by the material can lose some of its energy due to the vibrational and rotational friction with their environment. The rest of the excitation energy will be lost by emission of radiation. Therefore, the emission will be from a lower energy state than the excitation (which is referred to as Stokes-shifted). The fraction of absorbed light that is emitted is known as the emission quantum yield (Φ_{sample}) of the material. Typically, the quantum yield measurements can be carried out with respect to a reference dye material with a known quantum yield. First, a reference material that absorbs at the same wavelength as the sample and that can emit within the same range of wavelengths as the sample is chosen. Then, a set of known concentrations of the reference material and the sample are prepared. The OD of each sample and reference with different concentrations are measured followed by the measurement of emission spectra for each and every sample under consideration. Then a plot as of absorbance (OD) vs integrated fluorescence is made as shown in the Figure 5-3.

Equation 5-3

$$\boldsymbol{\Phi_{sample} = \Phi_{reference}\left(\frac{Grad_{sample}}{Grad_{reference}}\right)\left(\frac{n_{sample}}{n_{reference}}\right)^{2}}$$

The gradients of the plots, the quantum yield of the reference material and the refractive indices of the solvents used for each solution can be used for the quantum yield calculation. As shown in equation 5-3, the emission quantum yield can be calculated. Here, n_{sample} is the refractive index of the solvent in which the sample dissolves. $Grad_{sample}$ and $Grad_{reference}$ are the corresponding gradients of the plot shown in Figure 5-3.

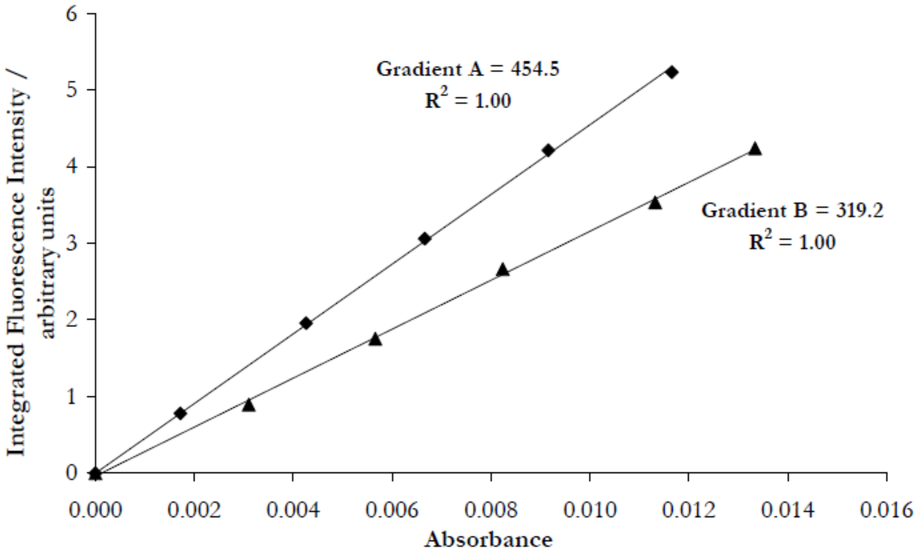

Figure 5-3 Plot of absorbance vs integrated emission

The steady state emission spectra were measured using a SPEX Fluoromax-2 fluorimeter. A Xenon lamp is used as the main excitation source and a diffraction grating is used for wavelength selection. The SPEX fluorimeter has a resolution of ~1 nm for both excitation and emission wavelengths and the slit widths for collection and excitation can be controlled. The emission spectrum is collected with a photomultiplier tube and has excellent sensitivity from 300 nm to about ~800 nm. The sample cell used in absorption can be used as it is for emission measurement. The emission spectrum is collected perpendicular to the excitation beam.

Another important property that I have discussed in chapter 3, chapter 4, section 5.1 and 5.2, is the ability to detect the effects of aggregation using steady state absorption and emission. Typically, the absorption spectrum and the emission spectrum may change their maximum wavelength of absorption or emission upon aggregation of nanoclusters or molecules. This was clearly observed in the case of Au_{25} nanoclusters, where the emission became narrower as the nanoclusters were disassembled in solution. This narrowing results due to the reduction of emission densities of states (DOS) upon removal of the coupling of the emissive states. Also, it was interesting to note that shift in absorption for Au_{25} nanoclusters were negligible indicating the near independence of absorption maximum upon aggregation.

For organic molecules, the emission typically occurs from its lowest excited energy level for a given spin multiplicity (referred to as Kasha’s rule). [81] However, as the reader may have noticed, nanoclusters as well as certain organic molecules tend to break this rule and emit at more than one possible wavelength depending on the electronic structure, density of states and excited state dynamics involved. Regardless of whether a molecule/nanocluster obeys the Kasha’s rule or not, in order to gain a more detailed understanding of the excited state emission dynamics of a chromophore, one may carry out the time resolved experiments. [82]

5.3.3 Time-resolved fluorescence up conversion

In order to understand the excited state chemical dynamics, one technique I used was the fluorescence up conversion. Here, the excitation dynamics immediately following the excitation of the chromophore can be measured starting at the first 100 femtoseconds (1 fs = 10^{-15} s; i.e. millionth of a billionth of a second). As depicted in the diagram of the figure 5-4, the fluorescence emitted by a chromophore (S) is sum-frequency mixed by a gate pulse (~800 nm from the Tsunami) to produce the up converted signal (at the NC2; beta Barium Borate Crystal). Since the temporal overlap between the emission and the gate pulse is critical for up conversion, we can use the time delay between the gate pulse and the emission pulse as a measure of the time difference between the excitation and emission. For the excitation of the sample (S), frequency doubled 400 nm pulses (NC1) are used. For the generation of the fundamental beam a mode-locked Ti:Sapphire oscillator (Tsunami) is used. The up converted signal is collected by a photomultiplier tube (PMT

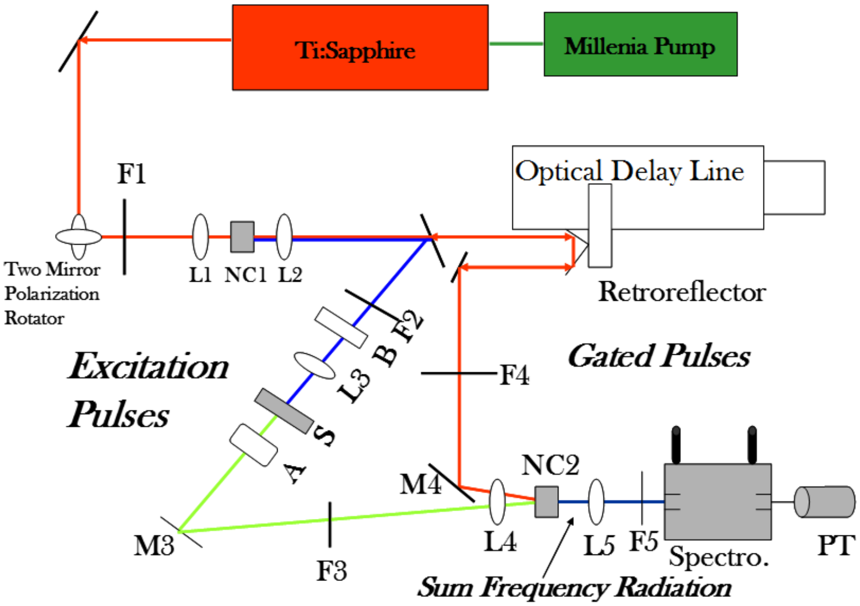

Figure 5-4 Optical diagram of the time resolved fluorescence up conversion set up.

or PT). The signal from the computer is sent to the computer and the Lumex software controls the delay stage motors. The step size of the delay line is ~6.75 fs which. Fluorescence emission from the first 100 fs to 1 ns can be measured using this set up.

The sample of the fluorescence up conversion experiment is kept in a rotating cell with 1 mm path length. The rotation of the sample tries to minimize the photo-damage due to the prolonged exposure to light. Since the laser has a pulse duration of 110 fs, the instrument response function (IRF) which has a Gaussian profile. Therefore, the dynamics occurring at the first 110 fs will be hidden inside this IRF response which will be recorded by the set up. Once can consider the IRF as the beginning of the signal and measure the emission of the subsequent events. We use Origin and MATLAB programs to determine the decay rates from the time-resolved fluorescence data.

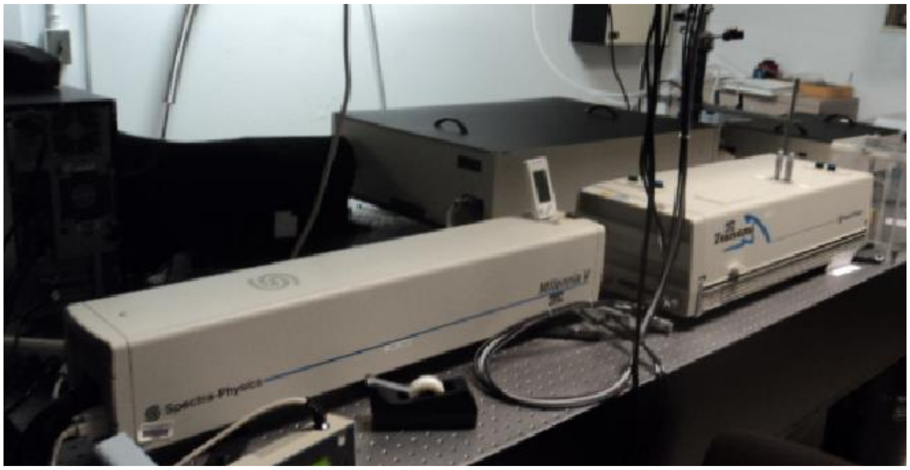

Figure 5-5 Image of the time resolved fluorescence up conversion set up.

From the fluorescence dynamics of a molecule one may be able to obtain information such as emission linewidths and transition dipole moments. If we assume the emission dipole is isolated in vaccuum, we can represent the spontaneous decay rate (i.e. emission rate) according to the following equation. [83]

Equation 5-4
$$\gamma_0 = \frac{\omega_0^3|\mu|^2}{3\pi\varepsilon\hbar c^3}$$

Here, the γ_0 is the decay rate of the emission dipole in a vacuum, ω_0 is the frequency of the transition, μ is the transition dipole moment extracted from the transition dipole matrix element $<g|\ \mu\ |e>$, ε is the permittivity of the vacuum, c is the speed of light. While the transition dipole moments associated with the molecules in condensed phase may require corrections or approximations for the above equation, it is clear that the time-resolved fluorescence up conversion decay rate can be used to determine the transition dipole moments involved in an emissive transition.

5.3.4 Ultrafast transient absorption

Ultrafast transient absorption measures the difference in absorption of the ground state and the excited state. A delay stage that delays the probe pulse investigates the absorption of the sample at different time delays. Briefly, the sample is being excited by ~ 10 μJ pulses generated from the Optical Parametric Amplifier (OPA) system. These pump pulses serve as the excitation light source of the sample (In order to obtain high energy pulses required for the OPA, a regenerative amplifier [Spitfire by Spectra Physics] is used). Then, a white light continuum (450 nm to 750 nm) pulse with a known delay is sent to probe the excited state absorption and bleach dynamics. A charged coupled device (CCD; Ocean Optics 2000) is used to measure the signal from the white light continuum and the change in transmission is converted to ΔA units. In this approach we can measure the excited state absorption decay dynamics as well as bleach recovery dynamics. Excited state energy delocalization and energy transfer processes of molecules can be measured using this technique. For a detailed description of this set up used in Goodson group the reader is referred to the reference 84 and 85.

Figure 5-6 Transient absorption set up in the Goodson Lab.

5.3.5 Two-photon absorption (TPA) and two-photon excited fluorescence (TPEF)

Two-photon absorption was first predicted by Maria Goeppert-Mayer in her doctoral dissertation.[86] It is a third order nonlinear optical process where two-photons are absorbed simultaneously by a chromophore. One very important aspect of two-photon process is, the probability of TPA increase as the *square of the excitation intensity*. This will be discussed in detail when discussing two-photon excited fluorescence. In order to understand the two-photon absorption process better, one may consider the two-level approximation (Figure 5-7) for two-photon absorption (TPA). [87] The electronic transition from ground state (0) to the first excited state (1) occurs via simultaneous absorption of two-photons each possessing half of the energy of the energy gap being excited. As can be seen in Figure 5-7, there is no real energy level present for the first photon to be excited. Therefore, we consider that as a virtual state through which the second excitation occurs. In order for this process to be quantum mechanically allowed, the time gap between the first and second photon being absorbed should typically be on the order of femtoseconds. Therefore, two photon absorption requires high intensities of excitation radiation. Since the advent of pulsed lasers, two-photon absorption experiments became straightforward as the *instantaneous intensity* necessary can be provided by femtosecond pulses. According to the Figure 5-7, the permanent dipole moment (labeled **μ_0, μ_1**) of the chromophore can change when it is excited from ground state to the excited state. Also, the two photon transition involves a two-photon transition dipole moment (**μ_{10}**) which is the matrix element responsible for excitation by both photons under the dipole moment operator ~<*1*|*μ*|*i*><*i*| *μ* |*0*>.

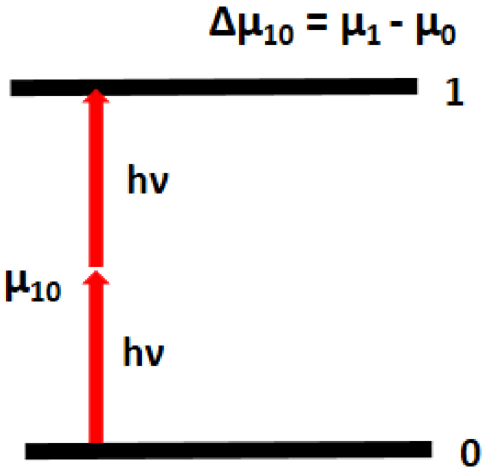

Figure 5-7 Two-photon absorption according to a two-level approximation.

The equation 5-5 shows the relationship between the two photon absorption cross section (δ), the change in permanent dipoles upon two-photon excitation ($\Delta\, \boldsymbol{\mu}_{10}=\boldsymbol{\mu}_1 - \boldsymbol{\mu}_0$) and the angle ($\alpha$) between the transition dipole moment ($\boldsymbol{\mu}_{10}$) and the $\Delta\, \boldsymbol{\mu}_{10}$. [87]

Equation 5-5 $$\delta\,(\nu_{10}) = \frac{4(1+2\cos^2\alpha)}{5}\,\frac{\pi 10^3 \ln 10\, f^2}{hc^2\, N_A\, n}\,|\Delta\, \mu_{10}|^2\,\frac{\varepsilon(\nu_{10})}{\nu_{10}}$$

The terms of the equation can be defined as follows.

δ – two-photon absorption cross section

α – angle between transition dipole moment and $\Delta\mu_{10}$

f – local field factor = $(n^2+2)/3$

$\Delta\mu_{10}$ – difference between the permanent dipoles of the *ground* state and the *excited* state

ε - molar extinction coefficient

ν_{10} – frequency of the transition

Figure 5-8, can be used as a schematic to understand the relationship between the difference in the dipole moments ($\Delta\, \boldsymbol{\mu}_{10}=\boldsymbol{\mu}_1 - \boldsymbol{\mu}_0$) and the transition moment ($\boldsymbol{\mu}_{10}$). Interestingly, if the $\Delta\, \boldsymbol{\mu}_{10}$ can be increased the two photon absorption may be increased resulting higher two photon absorption cross sections. This implies that the two-photon absorption process is more sensitive to ultrafast excited state electron delocalization, charge transfer events and local field enhancement. Previous work on electric field sensitive two-photon chromophores have been shown to create an induced dipole in the presence of electric fields causing the δ to increase. [88- 90] In the next part of this section, I will discuss how I used two-photon excited fluorescence to calculate the two-photon absorption cross section (δ).

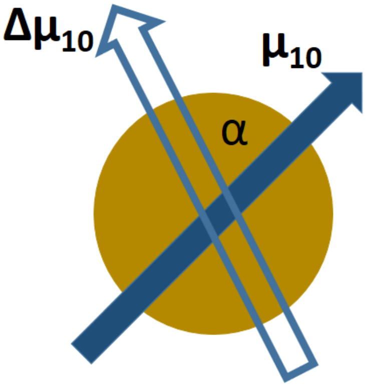

Figure 5-8 Schematic of the relationship between the change in permanent dipole moments and the transition dipole moments

Once the molecule is excited, it undergoes the typical energy relaxation resulting in the subsequent emission of a photon. This is known as the two-photon excited fluorescence (TPEF) and was utilized in my experiments involving the isolated Au_{25} nanocluster microscopy, Au_{25} aggregate microscopy and DNA-templated Ag NC spectroscopy. Similar to TPA, the TPEF signal is proportional to the square of the intensity of radiation. This quadratic intensity dependence can be utilized as a measure to distinguish the TPEF process from any linear scattering or emission processes. Also, since two-photon absorption requires longer wavelengths to excite specific transitions, and the fact that the quadratic intensity dependence allows the 3-dimensional excitation and better contrast of the images, [91] TPEF is a better candidate to do biological imaging compared to its one-photon counterpart. I will discuss the TPEF imaging in detail in the context of TPEF NSOM.

In my experiments of TPEF, I used a Mai Tai or Kapteyn-Murnane lasers working at ~80 MHz repetition rates with ~110 fs pulse durations. For the solution phase studies reported the following procedure is followed. The two-photon excitation beam is focused on to the sample cell and the TPEF signal that is perpendicular to the excitation beam is directed towards a

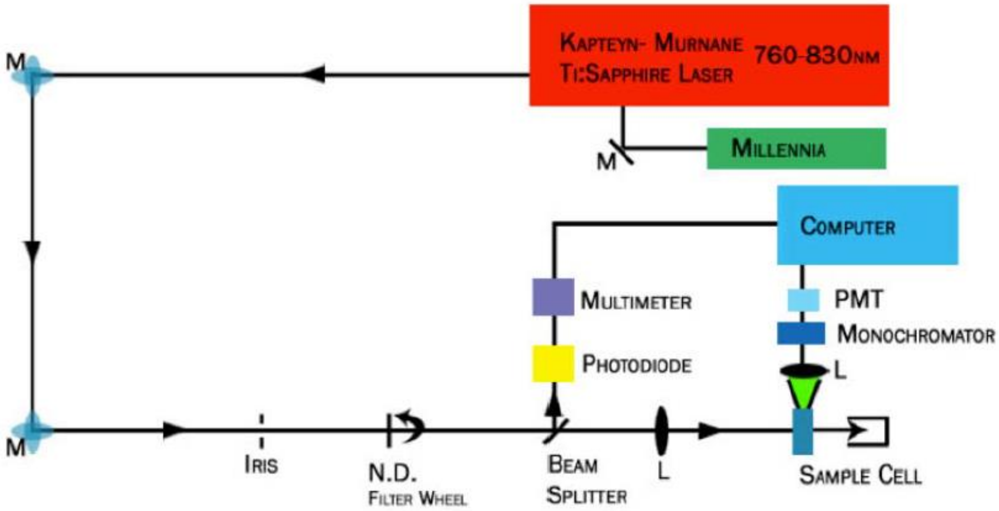

Figure 5-9 Optical diagram of the TPEF set up.

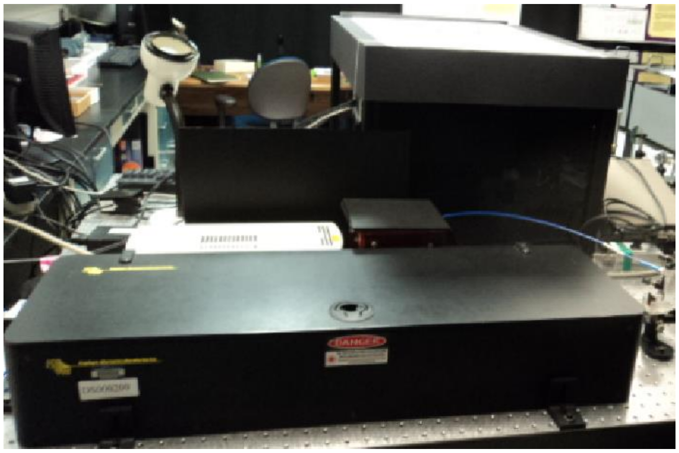

Figure 5-10 A TPEF set up in the Goodson Lab.

photomultiplier tube (PMT). The signal from the PMT is sent to the computer and recorded using a Labview program. A neutral density (ND) filter is used to adjust the excitation intensity incident on the sample and the corresponding TPEF signal is recorded. Then, a log-log plot of the incident intensity vs fluorescence counts is made. For TPEF chromophore, the slope of this plot should be ~2.0 which is the signature of the two-photon absorption process. In order to calculate the two-photon absorption cross section (δ) of a chromophore one can use a reference TPEF material that has a known reported δ value. Then, using the following equation for both the known and the unknown, one can easily calculate the two-photon absorption cross section of the unknown. [92]

Equation 5-6 $$< \mathbf{F(t)} > = \mathbf{0.5\ g\emptyset\eta_2\delta C\ \frac{8n<P(t)>^2}{\pi\lambda}}$$

Where, $< F(t) >$ = Average fluorescence rate,

$g = \frac{<I(t)^2>}{<I(t)>^2}$,

$\emptyset$ = Fluorescence collection efficiency of the optical set up (at the emission wavelength),

η_2 = Fluorescence quantum yield of the chromophore,

C = Concentration of the sample,

δ = Two photon absorption cross section,

n = Refractive index of the sample medium (assumed to be 1.0 for air),

$< P(t) >$ = Average excitation power,

λ = Wavelength of emission

As can be seen in equation 5-6, the TPEF intensity *F(t)*, depends quadratically on the excitation intensity. Even in the TPEF NSOM experiments, this nonlinear dependence of fluorescence on excitation intensity was used as a signature of the TPEF NSOM process.

Another interesting aspect of the TPA process is that the quantum mechanical selection rules governing two-photon excitation is different from that of the one-photon counterpart. Most importantly, the symmetry selection rules are clearly different. For example, if we excite an organic molecule possessing an A_g ground state and B_u and A_g excited states, the one-photon excitation should cause an electronic excitation to the B_u excited state whereas the TPA would result in an A_g excited state. Therefore, it is possible that two-photon active crystalline structures may prefer certain two-photon transitions over the others (depending on their symmetry) which can be utilized in solid state TPEF spectroscopy of molecular symmetry.[93-95] However, in the case of quantum confined gold nanocluster systems (metal NC systems) these selection rules may be somewhat relaxed. This is due to the presence of many valence electrons that can be excited and the multiple energy levels aligning nearby possessing different symmetries.

5.3.6 Two-photon excited fluorescence (TPEF) near-field scanning optical microscopy (NSOM)

5.3.6.1 A brief history of TPEF microscopy below the diffraction limit

Many advances in optical imaging and spectroscopy of nanoscale objects were reported during the past few decades.[96-111] Until the end of the 20th century, Abbe's limit of diffraction had apparently set a theoretical limit on the resolution an optical microscope can have. At the beginning of the 20th century, obtaining point resolutions below the diffraction limit (~λ/2; >200 nm for optical microscopy) was deemed unlikely by many microscopists. Optical imaging below the diffraction barrier during the last few decades was considered major progress. [96- 111] These advancements allowed closely-spaced nano-sized objects to be probed when they are separated by tens of nanometers apart. As depicted in Figure 5-11, if resolution of an imaging system is significantly larger in size than the inter-chromophore separation, the two chromophores will be imaged as one object hiding the individual information unique to the chromophore. Point resolution of a microscope can be defined as the full width at half maximum (FWHM) of the representative point spread function (PSF) obtained from a single point-like object. For far-field optical microscopy, improvement of *point resolution* below 200 nm required the modification of the excitation or detection mechanism.[96-99] It was generally considered that if a molecule has a nonlinear optical response, diffraction-unlimited point resolutions can be attained readily. [97] Nonetheless, with far-field two-photon excited fluorescence imaging (due to the use of longer

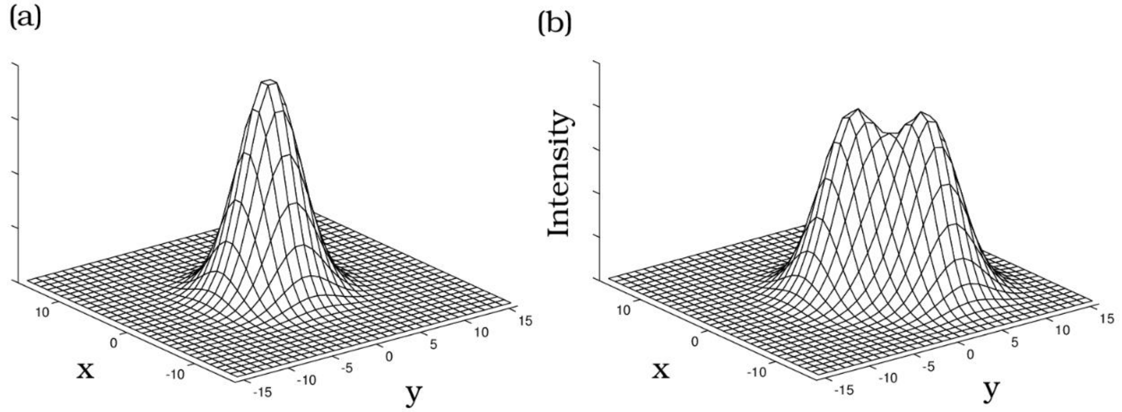

Figure 5-11 (a) Point spread function (PSF) and the (b) Overlapping of two PSFs. Full-width at half maximum is referred to as the point resolution.

wavelengths), the excitation spot in the x-y plane (lateral) will be twice as large compared to its

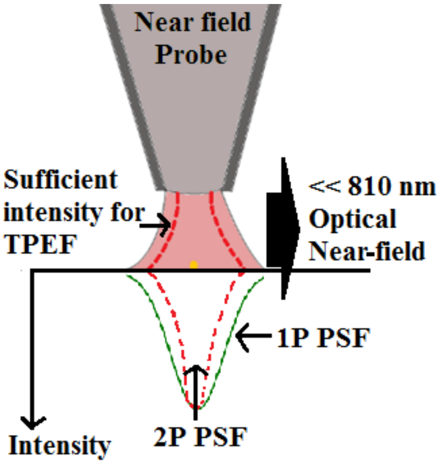

Figure 5-12 Comparison between the expected PSFs for one-photon and two-photon fluorescence under aperture-based NSOM excitation. Intensity dependence of the TPEF allows better confinement of the effective excitation field.

one-photon counterpart. [97] Consequently, typical *far-field* multiphoton fluorescence microscopy [98] has not been able to enhance the lateral point resolution below 200 nm. However, it must be noted that due to the use of longer wavelengths for excitation, multiphoton fluorescence microscopy has the advantages of lower background fluorescence; and due to quadratic dependence of fluorescence on excitation intensity, improved contrast of the optical image is observed.[106]

Contrary to far-field techniques, near-field optical imaging eliminates the diffraction barrier altogether by using evanescent fields near (<<λ) a sharp metal tip or an aperture (by reducing the effective excitation volume).[100] [-106] Betzig *et al*[100] have demonstrated room-temperature one-photon excited fluorescence (1PEF) NSOM with point resolutions below 100 nm. Compared to 1PEF NSOM, multi-photon fluorescence (e.g. TPEF) NSOM is also able to realize an enhanced point resolution due to its independence of diffraction by lateral confinement of light and strong intensity dependence inherent to two-photon excitation. In other words, TPEF NSOM carries all of the advantages of typical TPEF microscopy *and* the ability to (unlike far-field TPEF) obtain sub-diffraction *point resolutions*. Along these lines, TPEF NSOM of Rhodamine B single molecules were reported by Steel and coworkers[113]. However, point resolutions better than ~175 nm were not materialized for aperture based TPEF NSOM. It was inferred that with smaller diameters of the apertures, insufficient intensities of the electric field component at the optical near-field may have caused this difficulty. [113] Also, rapid photo-damage of *typical* organic TPEF chromophores under high TPEF excitation intensities clearly limits the success of this approach. However, since noble-metal nanoclusters have demonstrated unusually large TPA cross sections [114] and high stability under optical excitation, interrogating of Au_{25} single nanoclusters using TPEF NSOM appeared as a viable idea. In the next sections, I will discuss the TPEF NSOM set up I used

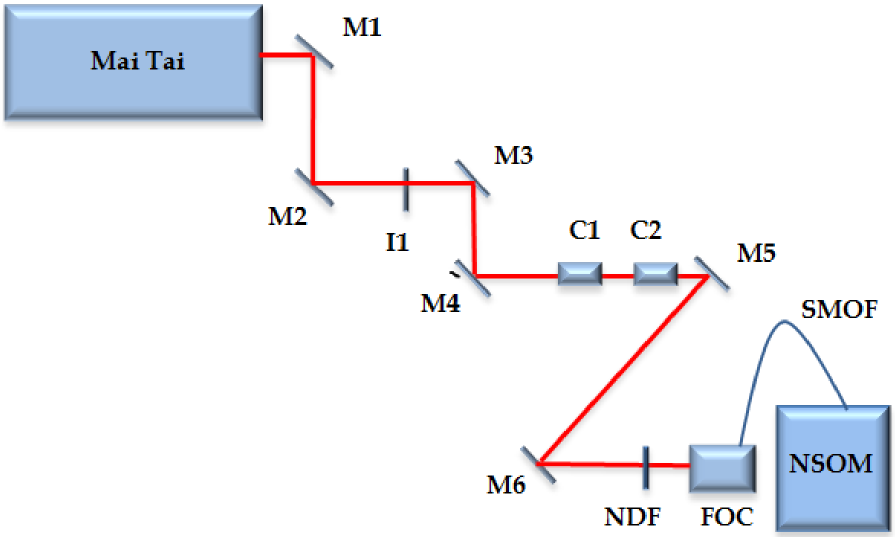

Figure 5-13 Optical diagram of the TPEF NSOM set up.

for the isolated single nanocluster investigations and the road blocks that were needed to overcome to accomplish isolated single nanocluster imaging using TPEF NSOM.

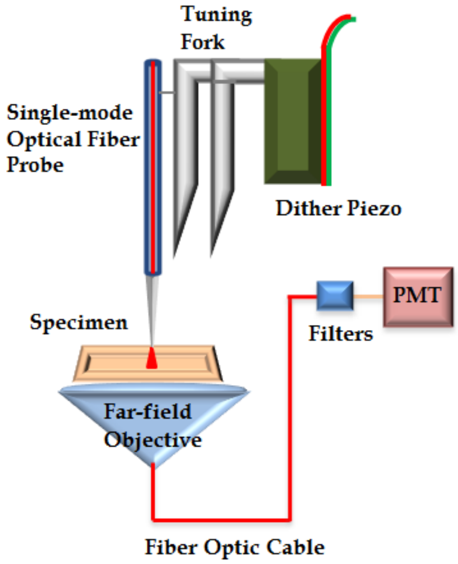

Figure 5-14 Diagram of NSOM microscope after coupling and the near-filed illumination geometry inside the NSOM (tip-sample distance <<<λ).

5.3.6.2 Experimental set up used for TPEF NSOM

The TPEF NSOM set up utilized for isolated single Au_{25} nanocluster investigations can be described as follows. A Mai Tai femtosecond laser source with a repetition rate of 80 MHz was used for the excitation (Figure 5-13). Pulses of ~110 fs (FWHM) at 810 nm were coupled to a single mode optical fiber (maximum throughput at ~ 780 nm) and the tapered end of the optical fiber serves as the local excitation source for the NSOM set-up. Near-field illumination of the sample generates the two-photon excited fluorescence (TPEF) from single gold nanoclusters. Raster scanning of the 1 um x 1 um areas with 10 nm pixels at 36 milliseconds bin times generated TPEF NSOM images. The fluorescence emission of the single gold nanoclusters and transmitted

810 nm photons were collected using a far-field inverted objective and transferred through a fiber optic cable to a photomultiplier tube (PMT).

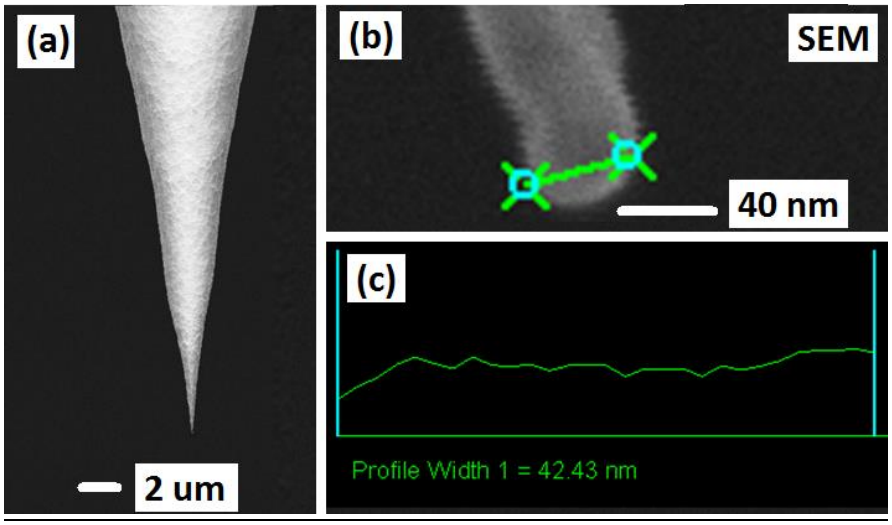

Figure 5-15 SEM image of a sample NSOM probe used with ~40 nm tip diameter (a) SEM image of ~10 um x ~18 um field of view (b) zoomed in SEM image of the NSOM tip (c) SEM profile. [115]

As shown in Figure 5-14, the transmitted 810 nm light is sent through a filter housing and attenuated using a two 808 nm notch filters and a short-pass filter. Thus, the anti-stokes shifted TPEF can be detected (in the visible region) with sufficient intensities for single molecule imaging. The TPEF NSOM intensities were analyzed using FemtoScan Online software and the Gaussian fits for TPEF NSOM point resolution were obtained using Origin 7 fitting software. The final TPEF NSOM scans were displayed using ImageJ software. The probe tip diameter used was ~ 40 nm.

5.3.6.3 Obtaining high NSOM coupling efficiencies for TPEF NSOM

Investigating single nanoclusters with a 40 nm diameter NSOM probe tip using TPEF requires large near-field intensities. If the near-field coupling efficiency of an NSOM probe is not large enough, one has to increase the actual laser power incident on the fiber for coupling.

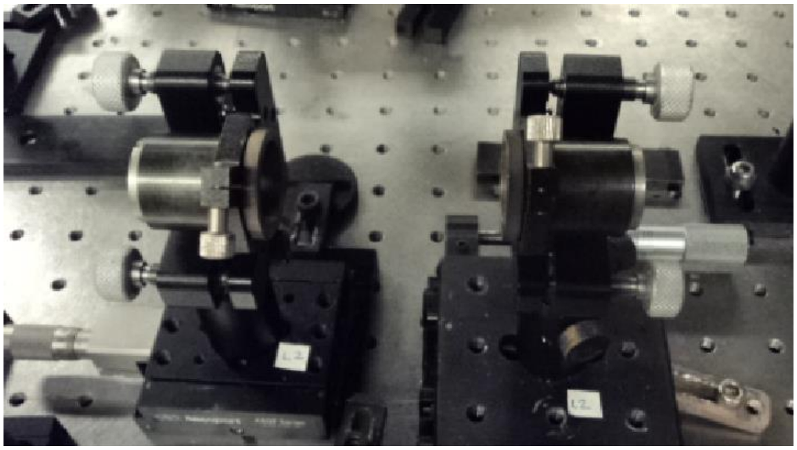

Figure 5-16 Image of the collimator used at the NSOM coupling

However, there is a limit to increasing the laser power at the coupling end of the optical fiber, because due to the taper of the near-field tip, the rest of the light that is not propagating trough the core of the single mode optical fiber (SMOF) could cause heating and burning of the near-field probe tip. Also, heating of the probe tip at high powers increases the noise of the NSOM tip vibrations causing the near-field noise to increase. Therefore, increasing the coupling efficiency of a near-field probe is key to doing measurements that requires high sensitivity. To this end the spatial profile/quality of the beam that is being coupled to the SMOF, the parallel nature of the beam to the fiber and the presence of a perpendicular cut at the coupling end of the SMOF are some parameters that must be optimized. While collimating of the beam is carried out before the coupling (C1 and C2 in Figure 5-13 and Figure 5-16), beam profile and quality emanating from the Mai Tai laser can be made better. In order to obtain a better quality beam profile, I used a spatial filter before the collimators. A spatial filter manages to filter out the imperfect, low quality portions of a beam. In the spatial filter I used, the beam is focused by a convex lens with 25 cm focus and sent through a pin hole ~300 μm in diameter. Then, the beam is made parallel by another convex lens with 25 cm focus. While this cuts off a significant portion of the light transmitted

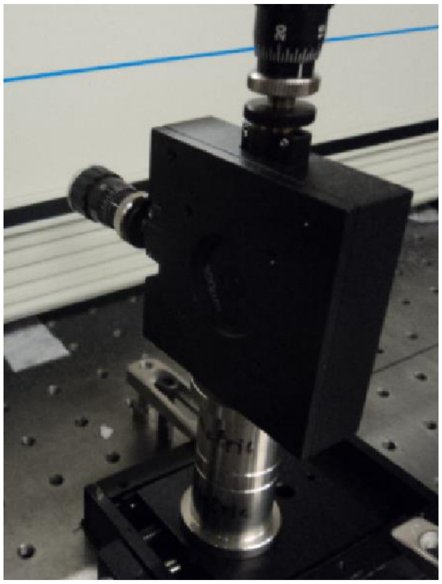

Figure 5-17 Pin hole of the spatial filter.

through the pinhole, it generates an airy disk profile (a bright spot with concentric rings) as in Figure 5-18. This is the two-dimensional Fourier transform of the initial beam's *transverse*

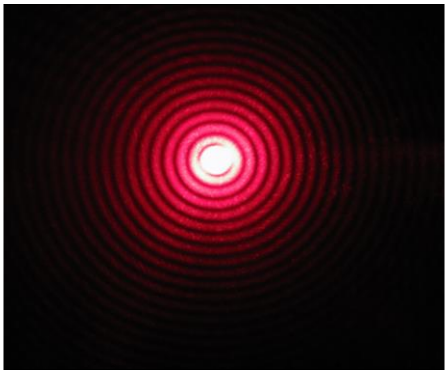

Figure 5-18 Airy disk beam profile after spatial filtering.

intensity distribution. That implies that the central spot in the airy disk correspond to the perfect part of the beam while the concentric rings are the filtered out imperfect parts of the beam. Once the spatial filtering is done, the coupling efficiency of the central spot of the airy disk to the SMOF would ensure generating a larger fraction of the propagating mode in the SMOF that is important for high near field coupling efficiency.

Figure 5-19 Image of the Jeweller's lens used.

Once the spatial mode is made better making the beam parallel requires alignment of the beam using several mirrors before the coupling end of the SMOF. Then, obtaining a perfectly perpendicular cut of the single mode optical fiber usually requires several cuts of the SMOF coupling end using a sharp axo blade and examination of it under jeweller's lens (Figure 5-19). Once the SMOF coupling end has a perfectly perpendicular cut, I move to coupling the laser to the SMOF, optimizing and measuring the coupling efficiency.

For initial coupling of the laser beam, I use a 50 mW of 810 nm laser power (80 MHz). The coupling is done by adjusting the x, y, and z positions of the fiber coupler and the mirrors right before the SMOF coupling end. In order to measure the coupling efficiency, I use the following procedure. First a pinhole smaller than 200 μm is placed on the microscope sample holder area. Then, a power meter is placed below that pinhole. Using the feedback mechanism of the NSOM microscope, I lower the NSOM probe using the uScope software so that the probe tip is centered in the pinhole. Then, the coupling is optimized and the power transmitted through the pin hole is measured. The ratio between the transmitted power and the coupled power gives the coupling efficiency (CE). Since measuring the CE in this approach is tedious and prone to damage the NSOM tip, I use the output form the collection optics (fiber bundle) and send that coupled light to a photodiode. The photodiode (PD) gives a mV signal which is calibrated with respect to an

Figure 5-20 Image of the MoScan NSOM microscope enclosure (left), the optical and inverted microscope (right) for NSOM collection.

actual CE measurement using the procedure described above. Once the PD is calibrated, I can safely measure the CE frequently and when necessary. Once the high CEs were obtained using this procedure, I moved to conduct TPEF NSOM investigations of single nanoclusters.

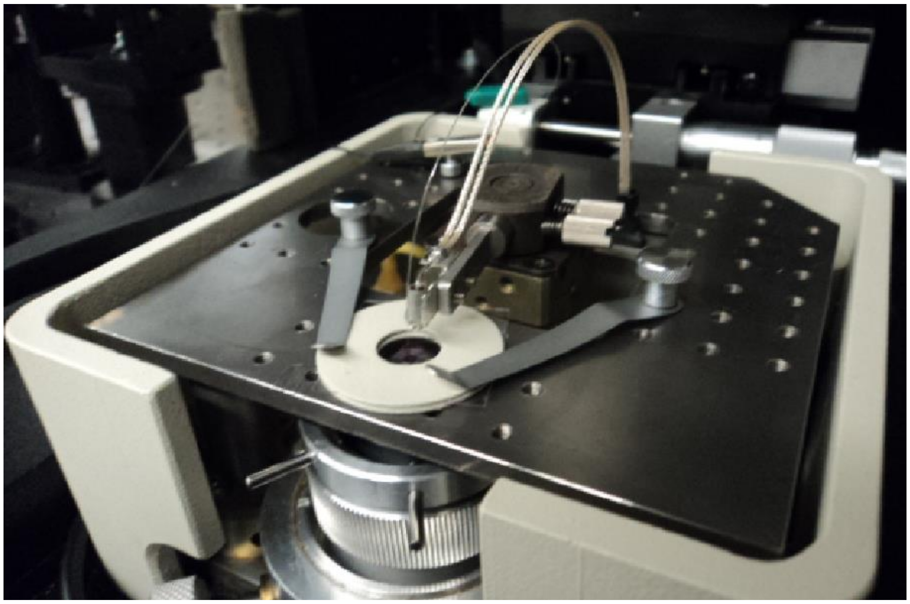

Figure 5-21 NSOM instrument with the sample in place. Below the sample stage is the inverted microscope the collects the transmitted light and sends through an fiber bundle to the PMT

5.3.6.4 Conducting TPEF NSOM on $Au_{25}(PET)_{18}$ nanoclusters

Initially (before using $Au_{25}[GSH]_{18}$), I used 0.75 nM concentrations of $Au_{25}(PET)_{18}$ solutions to deposit nanoclusters on glass cover slides. Since PET (phenylethylthiol) is an organo-soluble ligand, I used toluene as the solvent. After many attempts of NSOM experiments involving different concentrations, I arrived at 0.75 nM concentrations (used for spin coating) to obtain single NC TPEF NSOM where the aggregation as the spin coating proceeds was not a likely. The TPEF

NSOM (Figure 5-22) with a log-log plot having a slope of ~1.7 was observed. Also, when the two photon cross section was calculated for the TPEF features observed, a cross section of 1.31 x 10^6

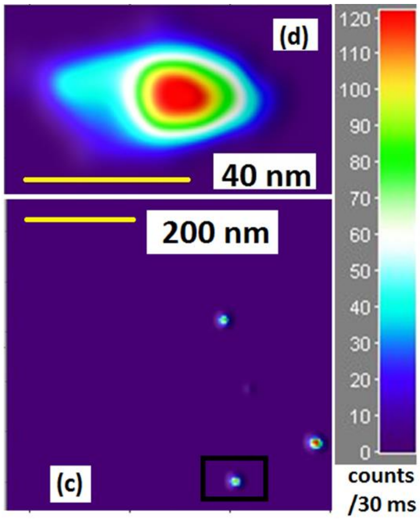

Figure 5-22 TPEF NSOM of $Au_{25}(PET)_{18}$ nanoclusters.

GM was observed. While this value is about 3-fold enhanced compared to the solution phase counterpart that was reported previously, the actual number of nanoclusters investigated was not clear. Because, even if one obtains an arbitrarily and infinitely small concertation of $Au_{25}(PET)_{18}$ solution, the possibility of solution phase aggregation of nanoclusters is not excluded. Therefore, I decided to solve the aforementioned problem in the following steps. First and foremost, find a method to definitively isolate single nanoclusters *in solution*. Then, deposit them as single nanoclusters and confirm they can indeed be isolated on the substrate. Finally, run the TPEF NSOM experiments on these isolated single nanoclusters.

To make sure that I can isolate single Au_{25} nanoclusters in solution, I have decided to use glutathione (GS) protected Au_{25} NCs. The advantage of using glutathione (GS) is that by increasing the pH glutathiolate ligand attached to the Au, can be ionized due to the presence of dangling carboxylate groups facing the solution. Due to inter ligand repulsion, Au_{25} disassemble

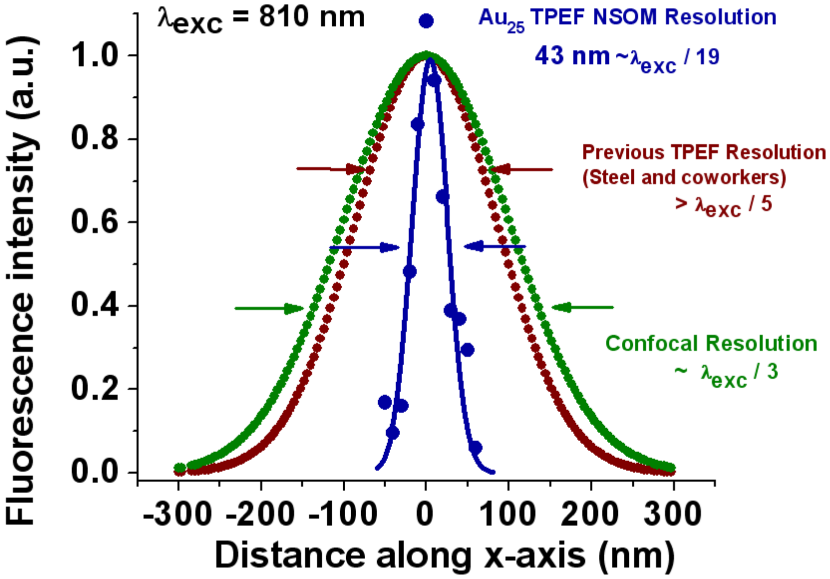

Figure 5-23 Comparison between the point resolutions for confocal, previous best TPEF NSOM and current aperture based TPEF NSOM point resolution. [115]

even in the solution phase. As discussed in detail in Chapter 3, I synthesized $Au_{25}(SG)_{18}$ nanoclusters using a well-established procedure to synthesize atomically precise Au_{25} NCs. [32, 33] Then, the pH=7.2 solutions were used to isolate Au_{25} NCs in solution. Subsequently, the Au_{25} NCs were confirmed to be isolated (using STEM) on solid substrate even when the conditions (concentrations) were highly favorable for aggregation. The reader is referred to Chapter 3 for more details. Once the isolated single nanoclusters were deposited on plasma cleaned glass substrates, TPEF NSOM were conducted that allowed me to compare many interesting differences in the TPEF response between the isolated Au_{25} NCs, Au_{25} NC aggregates and solution phase Au_{25} NCs.

5.3.6.5 Unprecedented point resolution of TPEF NSOM of Au_{25} NCs

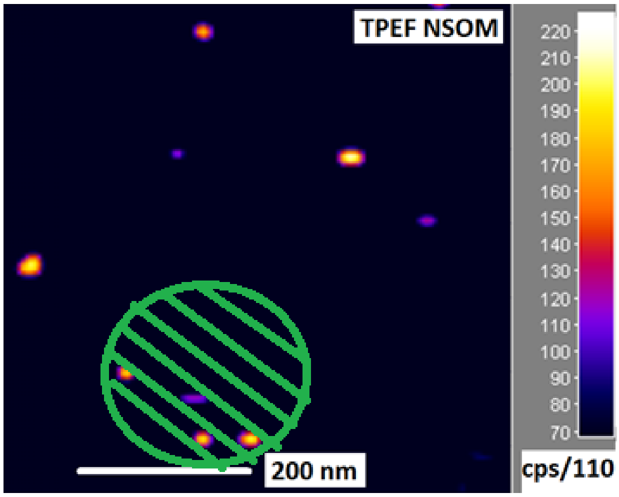

Figure 5-24 Confocal excitation may excite more than one isolated nanocluster.

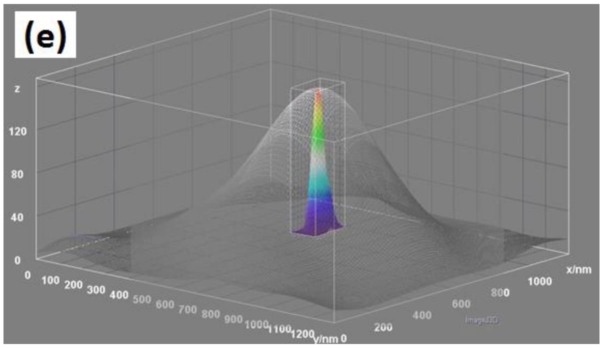

Figure 5-25 Comparison between TIRF (mesh) and TPEF NSOM (pseudocolor) images.

As discussed in chapter 3, I was able to obtain a point resolution of 30 nm for aperture based TPEF NSOM when investigating isolated single Au_{25} NCs. As depicted in the figure 5-23, the confocal resolution is about ~ 200 nm, [118] and the previous aperture based TPEF NSOM resolution was ~ 175 nm. [113] Interestingly, the point resolution observed by us implies that when the nanoclusters are about 50 nm apart, they can still be investigated separately. As depicted in the figure 5-24, this is not possible in confocal microscopy. The entire area covered by the green striped circle would be excited by confocal microscopy giving rise to a single image spot whereas TPEF NSOM was able to identify separate nanoclusters as separate TPEF NSOM features. This remarkably better resolution was evident even when the total internal reflection (TIRF) images were obtained for Au_{25} nanoclusters. As the comparison in the figure 5-25 reveals, the TIRF and TPEF NSOM point resolutions were compared that demonstrates the same point mentioned above.

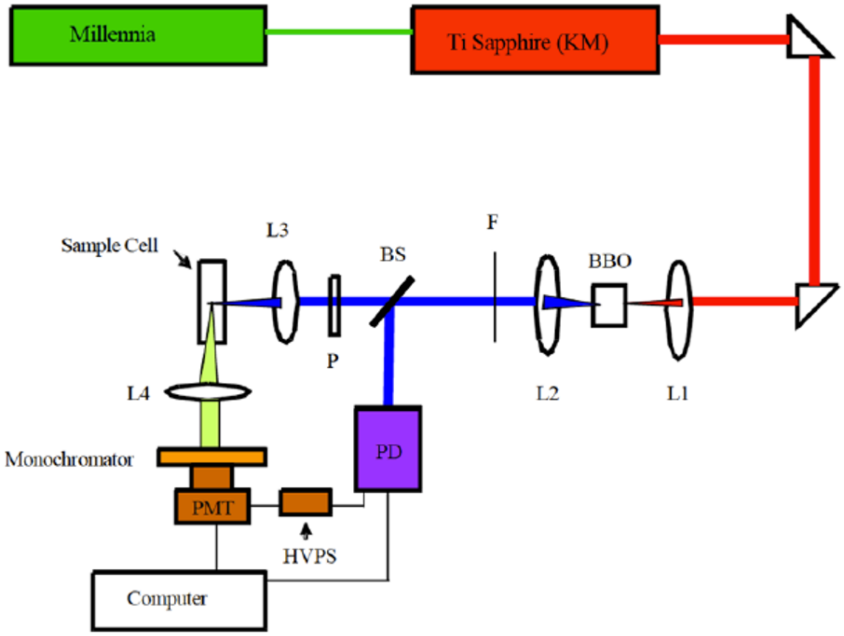

Figure 5-26 Optical diagram for the time-correlated single photon counting set up.

5.3.7 Time-correlated singlet photon counting

Time-correlated single photon counting (TCSPC, ~1 ns resolution) was performed using a Ti:Sapphire cavity dumped laser. The cavity dumped laser set up that was described in reference

119 and 120 was used as an excitation source. Pulse repetition rate was set at 755 kHz in the experiments conducted on QOT2 delayed fluorescence and magnetic field dependent delayed fluorescence experiments. Average pulse energy was ~13 nJ. A BBO crystal converts the 840 nm pulsed light into 420 nm excitation pulses. The fluorescence from the sample was collected at a right angle for the excitation beam. Time resolution was created by using a time to amplitude converter (TAC), a linear ramp generator in the TimeHarp 200 (PicoQuant) detection card. Using time-correlated single photon counting the emission after the first 1 ns could be measured. QOT2 molecules dissolved in THF, was able to give a non-exponential decay at 580 nm emission but a clear exponential decay at 470 nm emission. This delayed fluorescence at a lower emissive energy indicated the reverse process of the singlet exciton fission, namely the triplet-triplet annihilation. When a magnetic field about ~200 Gauss (using Neodymium ring magnets) was applied on the sample, I saw an increase in fluorescence counts for the peak of the TCSPC signal in its first few ns of emission. Singlet-to-triplet conversion process was known to be sensitive to magnetic fields.

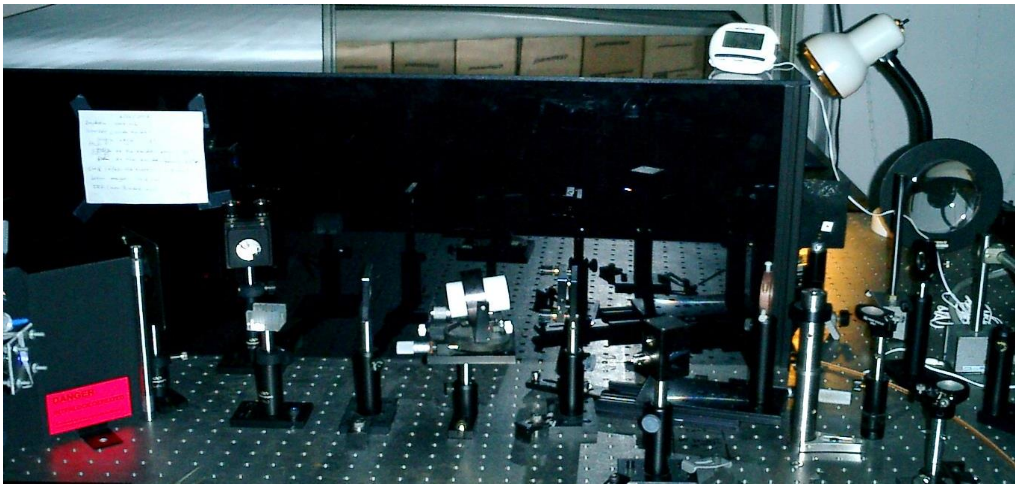

Figure 5-27 Image of the time-correlated single photon counting set up.

Therefore, I concluded that this was due to the reduction of the singlet-to-triplet conversion efficiency in the singlet fission process of QOT2 resulting in higher population of singlet excitons for emission. This was consistent with the observations made by Bardeen and coworkers. [121- 124]

5.3.8 $Au_{25}(SG)_{18}$ nanocluster synthesis

As described previously in the chapter 3, and section 5.3.6, I synthesized atomically precise monolayer protected Au_{25} nanoclusters using a well-optimized kinetically controlled synthetic procedure. [116, 117] Briefly, a 0.1698 g of $HAuCl_4$ was dissolved in 100 ml of Methanol and stirred at 0 °C (ice bath) for 15 minutes. Following the dissolution (and cooling) step, 0.614 g of GSH (glutathione) was added to the mixture and the reaction was left to proceed (while stirring) for another 30 minutes. . In this step, the main reaction that is taking place is the initial reaction of Au(III) to form thiolate bound Au(I).

Figure 5-28 The reaction mixture when the $HAuCl_4$ is reacting with glutathione ligands.

In order to finish the redcution of Au(I) to mostly Au(0) (i.e. for core Au of the nanoclusters), another step of reduction is required. Therefore, 0.1891 g $NaBH_4$ was dissolved in 25 ml water and added drop wise in to the reaction mixture. The reaction was further run for another 1 hr. All of the aforementioned steps were condcuted in a 0 °C ice bath. After the reaction with $NaBH_4$ was complete (i.e. after 1 hr), the resulting reaction mixture was centrifuged and the precipitate was washed 3 times with Methanol (vortex, sonicate and then centrifuge) followed by drying in the vacuum at room temperature. While this completes the reaction, it produces Au_nSG_m clusters. The optimization of reaction conditions using kineticl control requires another step which is referred to as size focusing. [116, 117]

In this step, which we refer to as the etching step, precise temperature and stirring conditions were maintained in the presence of excess thiolated ligand. The resulting Au_nSG_m clusters (82 mg) were dissolved in 7 ml water and heated in a water bath at 55 °C followed by the addition of a 132 mg portion of GSH. (Water bath was set at least an hour prior to the beginning of the experiment

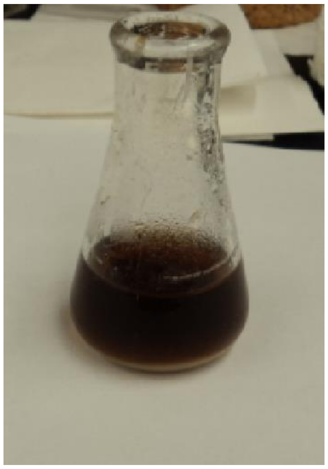

Figure 5-29 The reaction mixture after the etching step.

and the temperature was set at 55 °C which was maintained throughout the experiment). The reaction was stirred slowly (~300-400 rpm; not faster than that) for 4 hr. Then the reaction mixture was centrifuged followed by discarding of the precipitate. The resulting supernatant was transferred to a new centrifuge tube followed by the addition of 2-3 ml of Ethanol to precipitate $Au_{25}SG_{18}$ nanoclusters. This preciptate was further purified 3 times by dissolution (by water) and precipitation (by Ethanol) cycles to obtain monodisperse $Au_{25}SG_{18}$ nanoclusters. Then the solid nanocluster sample was dried in vacuum at room temperature which was subsequently stored in the freezer. I used milipore grade water for all of our synthesis and purification steps. Also all of the solvents used were of spectroscopic grade (or better). All of our glassware must be very clean in order for this reaction to occur as described. Therefore, cleaning of glassware by a base bath and subsequent drying is done at least a day prior to the synthesis begins.

Then STEM characterization was carried out by depositing the filtered pH=7.2 solutions as described in chapter 3 which confirmed the formation of single Au_{25} nanoclusters. [115]

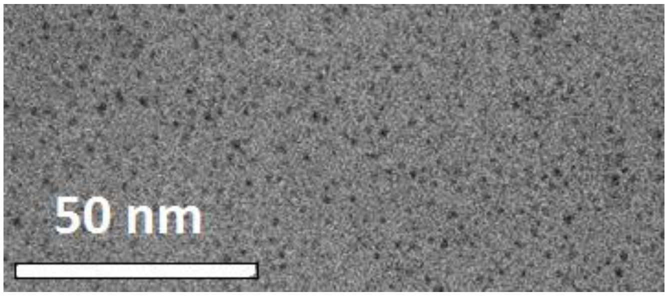

Figure 5-30 STEM image of a Au_{25} nanocluster sample dissolved in pH=7.2, deposited on a holey-carbon copper grid.

5.4 References

1. Yau, S. H., Varnavski, O. & Goodson III, T. An ultrafast look at Au nanoclusters. *Acc. Chem. Res.* **46,** 1506-1516 (2013).
2. Varnavski, O. *et al*. Critical size for the quantum confinement in optically excited gold clusters. *J. Am. Chem. Soc.* **132,** 16-17 (2010).
3. Ramakrishna, G. *et al*. Quantum-sized gold nanoclusters as efficient two-photon absorbers. *J. Am. Chem. Soc.* **130,** 5032-5033 (2008).
4. Varnavski, O., Ispasoiu, R. G., Balogh, L., Tomalia, D. and Goodson, T. Ultrafast time resolved photoluminescence from novel metal–dendrimer nanocomposites. *J. Chem. Phys.* **114,** 1962 (2001).
5. Ispasoiu, R. G., Balogh, L., Varnavski, O. P., Tomalia, D. A. and Goodson, T. Large optical limiting from novel metal-dendrimer nanocomposite materials. *J. Am.Chem. Soc* **122,** 11005–11006 (2000).
6. Goodson III, T., Varnavski, O. & Wang, Y. Optical properties and applications of dendrimer-metal nanocomposites. *Int. Rev. Phys. Chem.* **23,** 109-150 (2004).
7. Ramakrishna, G., Dai, Q., Zou, J., Huo, Q. and Goodson III, T. Interparticle electromagnetic coupling in assembled gold-necklace nanoparticles. *J. Am.Chem. Soc* **129,** 1848–1849 (2007).
8. Varnavski, O., Ramakrishna, G., Kim, J., Lee, D. and Goodson, T. Optically excited acoustic vibrations in quantum-sized monolayer-protected gold clusters. *ACS Nano* **4,** 3406–3412 (2010).
9. Devadas, M. S., Kim, J., Sinn, E., Lee, D., Goodson, T. and Ramakrishna, G. Unique Ultrafast Visible Luminescence in Monolayer-Protected Au_{25} Clusters. *J. Phys. Chem. C* **114,** 22417–22423 (2010).
10. Yau, S. H., Varnavski, O., Gilbertson, J. D., Chandler, B., Ramakrishna, G. and Goodson, T. Ultrafast Optical Study of Small Gold Monolayer Protected Clusters: A Closer Look at Emission. *J. Phys. Chem. C* **114,** 15979–15985 (2010).
11. Ho Wu, R., Yau, S. H. & Goodson III, T. Linear and nonlinear optical properties of monolayer protected gold nanocluster films. *ACS Nano* **10,** 562-572 (2016).

12. Wu, Z. and Jin, R. On the ligand's role in the fluorescence of gold nanoclusters. *Nano Lett.* **10,** 2568-2573 (2010).
13. Frohlich, H. The specific heat of the electrons of small metal particles at low temperatures. *Physica IV.* **5,** 406-412 (1937).
14. Kubo, R. Electronic properties of metallic fine particles. *J. Phys. Soc. Japan* **17,** 975-986 (1962).
15. Rao, C. N. R., Kulkarni, G. U, Thomas, P. J. and Edwards, P. P. Size-dependent chemistry: Properties of nanocrystals. *Chem. Eur. J.* **8,** 28-35 (2002).
16. De Heer, W. A., Knight, W. D., Chou, M. Y. and Cohen, M. L. Electronic shell structure and metal clusters. *Solid State Physics* **40,** 93-181 (1987).
17. Ekardt, W. Collective multipole excitations in small metal particles: Critical angular momentum l^{cr} for the existences of collective surface modes. *Phys. Rev. B* **32,**1961-1970 (1985).
18. Beck, D. E. Self-consistent calculations of eigenfrequencies for the electronic excitations in small jellium spheres. *Phys. Rev. B* **35,**7325-7333 (1987).
19. Bonacic-Koutecky, V., Fantucci, J. P. and Koutecky, J. Quantum chemistry of small clusters of elements of group Ia, Ib, and IIa: Fundamental concepts, predictions, and interpretation of experiments. *Chem. Rev. B* **91,**1035-1108 (1991).
20. Knight, W. D. *et al* Electronic shell structure and abundances of sodium clusters. *Phys. Rev. Lett.* **52,** 2141-2143 (1984).
21. Walter, M., Akola, J., Lopez-Acevedo, O., Jadzinsky, P. D., Calero, G., Ackerson, C. J., Whetten, R. L., Gronbeck, H. and Hakkinen, H. A Unified View of ligand-protected gold clusters as superatom complexes. *Proc. Natl. Acad. Sci.* **105,** 9157-9162 (2008).
22. Jadzinsky, P. D. *et al*. Structure of a thiol monolayer-protected gold nanoparticle at 1.1 Å resolution. *Science* **318,** 430-433 (2007).
23. Li, Z. Y. *et al*. Three-dimensional atomic-scale structure of size-selected gold nanoclusters. *Nature.* **451,** 46-48 (2008).
24. Zhu, M. *et al*. Correlating the crystal structure of a thiol-protected Au_{25} cluster and optical properties. *J. Am. Chem. Soc.* **130,** 5883-5885 (2008).

25. Heaven, M. W. *et al*. Crystal structure of the gold nanoparticle $N(C_8H_{17})_4][Au_{25}(SCH_2CH_2Ph)_{18}]$. *J. Am. Chem. Soc.* **130,** 3754-3755 (2008).
26. Desireddy, A. *et al*. Ultrastable silver nanoparticles. *Nature.* **501,** 399-402 (2013).
27. Yang, H. *et al*. All-thiol-stabilized Ag_{44} and $Au_{12}Ag_{32}$ nanoparticles with single crystal structures. *Nat. Commun.* **4,** 2422 (2013).
28. Azubel, M. *et al*. Electron microscopy of gold nanoparticles at atomic resolution. *Science* **345,** 909-912 (2014).
29. Khanna, S. N. and Castleman, A. W., Jr. Clusters, superatoms, and building blocks of new materials. *J. Phys. Chem. C* **113,** 2664-2675 (2009).
30. Kreibig, U. and Vollmer, M. Optical Properties of metal clusters. ir
31. Roy, X., *et al* Nanoscale atoms in solid-state chemistry. *Science* **341,** 157-160 (2013).
32. Drobizhev, M., Makarov, N. S., Hughes, T. & Rebane, A. Resonance enhancement of two-photon absorption in fluorescent proteins. *J. Phys. Chem. B* **111,** 14501-14504 (2007).
33. Drobizhev, M., Makarov, N. S., Tillo, S. E., Hughes, T. & Rebane, A. Two-photon absorption properties of fluorescent proteins. *Nature Methods* **8,** 393-399 (2011).
34. Ponder, M. & Mathies, R. Excited-state polarizabilities and dipole moments of Diphenylpolyenes and Retinal. *J. Phys. Chem.* **87,** 5090-5098 (1983).
35. Drobizhev, M., Scott, J. N., Callis, P. R. & Rebane, A. All-optical sensing of the components of the internal local electric field in proteins. *IEEE Photonics J.* **4,** 1996-2001 (2012).
36. Zhu, M. *et al*. Reversible switching of magnetism in thiolate-protected Au_{25} superatoms. *J. Am. Chem. Soc.* **131,** 2490-2492 (2009).
37. Chen, S. *et al*. Gold nanoelectrodes of varied size: Transition to molecule-like charging. *Science* **280,** 2098-2101 (1998).
38. Kaplan, A. E. & Volkov, S. N. Nanoscale stratification of local optical fields in low dimensional atomic lattices. *Phys. Rev. Lett.* **101,** 133902 (2008).
39. Bedeaux, D. & Bloembergen, N. On the relation between macroscopic and microscopic nonlinearities. *Opt. J. Eur. Opt. Soc. Part B* **69,** 57-66 (1973).

40. Dolgaleva, K., Boyd, R. W. & Sipe, J. E. Cascaded nonlinearity caused by local field effects in the two-level atom. *Phys. Rev. A* **76,** 063806 (2007).

41. Baev, A., Autschbach, J., Boyd, R. W. Prasad, P. N. Microscopic cascading of second order molecular nonlinearity: new design principles for enhancing third order nonlinearity. *Opt. Express* **18,** 8713-8721 (2010).

42. Dolgaleva, K. & Boyd, R. W. Local field effects in nanostructured photonic materials. *Advances in Optics and Photonics* **4,** 1-77 (2012).

43. Qian, H., Zhu, M., Wu, Z. & Jin, R. Quantum sized gold nanoclusters with atomic precision. *Acc. Chem. Res.* **45,** 1470-1479 (2012).

44. Zhu, M., Lanni, E., Garg, N., Bier, M. E. & Jin, R. Kinetically controlled, high-yield synthesis of Au_{25} clusters. *J. Am. Chem. Soc.* **130,** 1138-1139 (2008).

45. Negishi, Y. *et al*. Origin of magic stability of thiolated gold clusters: A case study on $Au_{25}(SC_6H_{13})_{18}$. *J. Am. Chem. Soc.* **129,** 11322-11323 (2008).

46. Singh, S., Jones, W.J., Siebrand, W., Stoicheff, B.P., Schnider, W.G. Laser Generation of Excitons and Fluorescence in Anthracene Crystals. *J. Chem. Phys.* **1965,** *42*, 330- 343.

47. Congreve, D.N. et al External Quantum Efficiency Above 100% in a Singlet-Exciton-Fission-Based Organic Photovoltaic Cell *Science,* **2013,** *340*, 334-337.

48. Chan, W.-L. *et al.* Observing the Multiexciton State in Singlet fission and Ensuing Ultrafast Multielectron Transfer. *Science,* **2011,** *334*, 1541-1545.

49. Ehrler, B. *et al In situ* Measurement of Exciton Energy in Hybrid Singlet-Fission Solar Cells *Nature Communs* **2012,** *3*, 1019.

50. Zimmerman, P.M., Zhang, Z., Musgrave, C.B. Singlet Fission in Pentacene through Multi-exciton Quantum States *Nature Chem.* **2010,** *2*, 648-652.

51. Smith, M.B., Michl, J. Siglet Fission. *Chem. Rev.* **2010,** *110*, 6891-6936.

52. Paci, I. *et al*. Singlet Fission for Dye-Sensitized Solar Cells: Can a Suitable Sensitizer Be Found? *J. Am. Chem. Soc.* **2006,** *128*,16546-16553.

53. Geacintov, N., Pope, M., Fogel, F. Effect of Magnetic Field on the Fluorescence of Tetracene Crystals: Exciton Fission. *Phys. Rev. Lett.* **1969,** *22*, 593-596.

54. Burdett, J.J., Bardeen, C.J. Quantum Beats in Crystalline Tetracene Delayed Fluorescence Due to Triplet Pair Coherences Produced by Direct Singlet Fission. *J. Am. Chem. Soc.* **2012,** *134***,** 8597-8607.

55. Lanzani, G. *et al.* Triplet-Exciton Generation Mechanism in a New Soluble (Red-Phase) Polydiacetylene. *Phys. Rev. Lett.* **2001,** *87***,** 187402.

56. Huynh, U.; Basel, T.; Xu, T.; Lu, L.; Zheng, T.; Yu, L.; Vardeny, V. Optical Properties of Low Bandgap Copolymer PTB7 for Organic Photovoltaic Applications. *Proc. SPIE,* **2014,** *vol. 9165,* 91650Z.

57. Busby, E.; Xia, J.; Wu, Q.; Low, J.Z.; Song, R.; Miller, J.R.; Zhu, X-Y.; Campos, L.M.; Sfeir, M.Y. A Design Strategy for Intramolecular Singlet Fission Mediated by Charge-transfer States in Donor-Acceptor Organic Materials. *Nat. Mater*. **2015,** doi:10.1038/nmat4175.

58. Gradinaru, C.C. *et al.* An Unusual Pathway of Excitation Energy Deactivation in Carotenoids: Singlet-to-Triplet Conversion on an Ultrafast Timescale in a Photosynthetic Antenna. *Proc. Natl. Acad. Sci. U.S.A.* **2001,** *98***,** 2364-2369.

59. Polivka, T. et al Femtosecond Carotenoid to Retinal Energy Transfer in Xanthorhodopsin *Biophys. J.* **2009,** *96***,** 2268-2277.

60. Wang, C., Tauber, M.J. High-Yield Singlet Fission in a Zeaxanthin Aggregate Observed by Picosecond Resonance Raman Spectroscopy. *J. Am. Chem. Soc.* **2010,** *132***,** 13988-13991.

61. Müller, A.M.; Avlasevich, Y.S.; Müllen, K.; Bardeen, C.J. Evidence for Exciton Fission and Fusion in a Covalently Linked Tetracene dimer. *Chem. Phys. Lett.* **2006,** *421***,** 518-522.

62. Michl, J. *et al.* Toward Singlet Fission for Excitonic Solar Cells. *Proc. SPIE,* **2007,** *6656***,** 66560E.

63. Johnson, J.C. et al Toward Designed Singlet Fission: Solution Photophysics of Two Indirectly Coupled Covalent Dimers of 1,3-Diphenylisobenzofuran *J. Phys. Chem. B* **2013,** *117***,** 4680-4695.

64. Oleg Varnavski, Neranga Abeyasinghe, Juan Arago, Juan J. Serrano-Perez, Enrique Orti, Juan T. Lopez Navarette, Kazuo Takimiya, David Casanova, Juan Casado and Theodore

Goodson III High yield ultrafast intramolecular singlet exciton fission *J. Phys. Chem. Lett.* **6,** 1375-1384 (2015).

65. Burdett, J. J., Piland, G. B., Bardeen, C. J. Magnetic field effects and the role of spin states in singlet fission. *Chem. Phys. Lett.* **585,** 1-10 (2013).

66. R. P. Groff, Avakian, P. and Merrifield. Coexistence of exciton fission and fusion in tetracene crystals. *Phys. Rev. B* **1,** 815-817 (1970).

67. Burdett, J.J., Bardeen, C.J. Quantum Beats in Crystalline Tetracene Delayed Fluorescence Due to Triplet Pair Coherences Produced by Direct Singlet Fission. *J. Am. Chem. Soc.* **2012,** *134***,** 8597-8607.

68. Müller, A.M.; Avlasevich, Y.S.; Müllen, K.; Bardeen, C.J. Evidence for Exciton Fission and Fusion in a Covalently Linked Tetracene dimer. *Chem. Phys. Lett.* **2006,** *421***,** 518-522.

69. Müller, A.M., Avlasevich, Y.S., Schoeller, W.W., Müllen, K., Bardeen, C.G. Exciton Fission and Fussion in Bis(tetracene) Molecules with Different Covalent Linker Structures *J. Am. Chem. Soc.* **2007,** *129,* 14240-14250.

70. Zirzlmeiera, J. *et al.* Singlet fission in pentacene dimers. *Proc. Natl. Acad. Sci.* **112,** 5325-5330 (2015).

71. Zhou, M. *et al.* Evolution from the plasmon to exciton state in ligand-protected atomically precise gold nanoparticles. *Nature. Commun.* **7,** 1340 (201).

72. Yost, S. R. *et al.* A transferable model for singlet fission kinetics. *Nat. Chem.* **5,** 492-497 (2014).

73. Musser, A. J. *et al.* Evidence for singlet exciton fission dynamics mediating ultrafast singlet exciton fission. *Nat. Phys.* **11,** 352-357 (2015).

74. Walker, B.J., Musser, A.J., Beljonne, D., Friend, R.H. Singlet Exciton Fission in Solution *Nat. Chem.* **5,** 1019-1024 (2013).

75. Chan, W.-L. *et al* The Quantum Coherent Mechanism for Singlet Fission: Experiment and Theory *Acc. Chem. Res.* **46,** 1321-1329 (2013).

76. Monahan, N., & Zhu, X.-Y. Charge-Transfer-Mediated Singlet Fission *Annu. Rev. Phys. Chem.* **66,** 601-618 (2015).

77. Zimmerman, P.M., Zhang, Z., Musgrave, C.B. Singlet Fission in Pentacene through Multi-exciton Quantum States *Nature Chem.* **2,** 648-652 (2010).

78. Zimmerman, P.M., Bell, F., Casanova, D., Head-Gordon, M. Mechanism for Singlet Fission in Pentacene and Tetracene: From Single Exciton to Two Triplets *J. Am. Chem. Soc*. **133,** 19944-19952 (2011).

79. Zimmerman, P.M., Musgrave, C.B., Head-Gordon, M. A Correlated Electron View of Singlet Fission. *Acc. Chem. Res*. **46,** 1339-1347 (2013).

80. Chien, A. D. *et al.* Structure and dynamics of the ^{1}(TT) state in a quinoidal bithiophene: Characterizing a promising intramolecular singlet fission candidate. *J. Phys. Chem. C* **119,** 28258-28268 (2015).

81. Kasha, M. Characterization of electronic transitions in complex molecules. *Discuss. Faraday. Soc.* **9,** 14-19 (1950).

82. Lakowicz, J. R. Principles of fluorescence spectroscopy. Kluwer Academic/Plenum Press, New York, 2nd Ed. (1999).

83. Novotny, L. and Hecht, B. Principles of nano-optics. Cambridge University Press, Cambridge, 1st Ed. (2006).

84. Yau, S. H., Varnavski, O. & Goodson III, T. An ultrafast look at Au nanoclusters. *Acc. Chem. Res.* **46,** 1506-1516 (2013).

85. Yau, S. H.; Varnavski, O.; Gilbertson, J. D.; Chandler, B.; Ramakrishna, G.; Goodson, T. Ultrafast Optical Study of Small Gold Monolayer Protected Clusters: A Closer Look at Emission. *J. Phys. Chem. C* **114,** 15979–15985 (2010).

86. Goeppert-Mayer, M. Elementary processes with two quantum transitions. *Ann. Phys. (Berlin)* **9,** 273-294 (1931).

87. Drobizhev, M., Makarov, N. S., Hughes, T. & Rebane, A. Resonance enhancement of two-photon absorption in fluorescent proteins. *J. Phys. Chem. B* **111,** 14501-14504 (2007).

88. Drobizhev, M., Makarov, N. S., Tillo, S. E., Hughes, T. & Rebane, A. Two-photon absorption properties of fluorescent proteins. *Nature Methods* **8,** 393-399 (2011).

89. Ponder, M. & Mathies, R. Excited-state polarizabilities and dipole moments of Diphenylpolyenes and Retinal. *J. Phys. Chem.* **87,** 5090-5098 (1983).

90. Drobizhev, M., Scott, J. N., Callis, P. R. & Rebane, A. All-optical sensing of the components of the internal local electric field in proteins. *IEEE Photonics J.* **4,** 1996-2001 (2012).

91. Sanchez, E. J., Novotny, L. & Xie, X. S. Near-field fluorescence microscopy based on two-photon excitation with metal tips. *Phys. Rev. Lett.* **82,** 4014-4017 (1999).

92. Xu, C. & Webb, W. W. Measurement of two photon excitation cross sections of molecular fluorophores with data from 690 to 1050 nm. *J. Opt. Soc. Am. B* **13**, *481–491* (1996).

93. Mahan, G. D. Theory of two-photon spectroscopy in solids. *Phys. Rev.* **170,** 825-838 (1978).

94. Bonin, K. D. and McIlrath, T. J. Two-photon electric dipole selection rules. *J. Opt. Soc. Am. B* **1,** 52-55 (1984).

95. Wang, C-K., Mecak, Y. L. and Agren, H. Effects of pi centers and symmetry on two-photon absorption cross sections of organic chromophores. *J. Chem. Phys.* **114,** 9813-9820 (2001).

96. Rittweger, E., Han, K. Y., Irvine, S. E., Eggeling, C. & Hell, S. W. STED microscopy reveals crystal colour centres with nanometric resolution. *Nature Photon.* **3,** 144-147 (2009).

97. Hell, S. W. Toward fluorescence nanoscopy. *Nat. Biotechnol.* **21,** 1347-1355 (2003).

98. Hell, S. W. Far-field optical nanoscopy. *Science*. **316,** 1153-1158 (2007).

99. Westphal, V., Kastrup, L. & Hell, S. W. Lateral resolution of 28 nm (λ/25) in far-field fluorescence microscopy. *Appl. Phys. B* **77,** 377-380 (2003).

100. Betzig, E. & Chichester, R. J. Single molecules observed by near-field scanning optical microscopy. *Science*. **262,** 1422-1425. (1993).

101. Betzig, E. & Trautman, J. K. Near-field optics: Microscopy, spectroscopy, and surface modification beyond the diffraction limit. *Science*. **257,** 189-195 (1992).

102. Xie, X. S. & Dunn, R. C. Probing single molecule dynamics. *Science* **265,** 361-364 (1994).

103. Trautman, J. K., Macklin, J. J., Brus, L. E. & Betzig, E. Near-field spectroscopy of single molecules at room temperature. *Nature* **369,** 40-42. (1994).

104. Betzig, E., Trautman, J. K., Harris, T. D., Weiner, J. S. & Kostelak, R. L. Breaking the diffraction barrier: Optical microscopy on a nanometric scale. *Science* **251,** 1468-1470 (1991).

105. Betzig, E., Lewsi, A., Harootunian, A., Isaacson, M & Kratschmer, E. Near-field scanning optical microscopy (NSOM): Development and biophysical applications. *Biophys. J.* **49,** 269-279 (1986).

106. Sanchez, E. J., Novotny, L. & Xie, X. S. Near-field fluorescence microscopy based on two-photon excitation with metal tips. *Phys. Rev. Lett.* **82,** 4014-4017 (1999).

107. Grotjohann, T. *et al.* Diffraction-unlimited all-optical imaging and writing with a photochromic GFP. *Nature.* **478,** 204-208 (2011).

108. Birnbaum, D., Kook, S. K. and Kopelman, R. Near-field scanning optical spectroscopy: Spatially resolved spectra of micro-crystals and nano-aggregates in doped polymers. *J. Phys. Chem.* **97,** 3091-3094 (1993).

109. Lewis, A. and Kopelman, R. Light microscopy beyond the limits of diffraction and to the limits of single molecule resolution. *SPIE* **1205,** Bioimaging and two-dimensional spectroscopy, 60-62 (1990).

110. Kopelman, R. Exciton microscopy and reaction kinetics in restricted spaces. *Physical and Chemical Mechanisms in Molecular Radiation Biology*, edited by W. A. Glass and M. Varma, Plenum Press, New York, Basic Life Sciences **58**, 475-502 (1991).

111. Kopelman, R. and Tan, W. Near-field optical microscopy, spectroscopy and chemical sensors. *Spectroscopic and Microscopic Imaging of the Chemical State*, edited by M. D. Morris, Marcel Dekker, Inc. 227-254 (1993).

112. Denk, W., Strickler, J. H. & Webb, W. W. Two-photon laser scanning fluorescence microscopy. *Science* **248,** 73-76 (1990).

113. Lewis, M. K., Wolanin, P., Gafni, A. & Steel, D. G. Near-field scanning optical microscopy of single molecules by femtosecond two-photon excitation. *Opt. Lett.* **23,** 1111-1113 (1998).

114. Ramakrishna, G. *et al*. Quantum-sized gold nanoclusters as efficient two-photon absorbers. *J. Am. Chem. Soc.* **130,** 5032-5033 (2008).

115. Neranga Abeyasinghe, Santosh Kumar, Kai Sun, John F. Mansfield, Rongchao Jin and Theodore Goodson III. *J. Am. Chem. Soc.* (2016). **DOI: 10.1021/jacs.6b07737**.

116. Wu, Z., Shuhan, J. & Jin, R. One-pot synthesis of atomically monodisperse, thiol-functionalized Au_{25} nanoclusters. *J. Mater. Chem.* **130,** 622-626 (2009).

117. Qian, H., Zhu, M., Wu, Z. & Jin, R. Quantum sized gold nanoclusters with atomic precision. *Acc. Chem. Res.* **45,** 1470-1479 (2012).

118. Cox, G. and Sheppard, C. J. R. Practical limits of resolution in confocal and nonlinear microscopy. *Microsc. Res. Tech.* **63,** 18-22 (2004).

119. Donehue, J.E., Varnavski, O.P., Cemborski, R., Iyoda, M., Goodson III, T. Probing Coherence in Synthetic Cyclic Light-Harvesting Pigments. *J. Am. Chem. Soc.* **2011,** *133*, 4819-4828.

120. Varnavski, O., Yan, X., Mongin, O., Blanchard-Desce, M., Goodson III, T. Strongly Interacting Organic Conjugated Dendrimers with Enhanced Two-photon aAbsorption. *J. Phys. Chem. C.* **2007,** *111*, 149-162.

121. Burdett, J. J., Piland, G. B., Bardeen, C. J. Magnetic field effects and the role of spin states in singlet fission. *Chem. Phys. Lett.* **585,** 1-10 (2013).

122. Burdett, J.J., Bardeen, C.J. Quantum Beats in Crystalline Tetracene Delayed Fluorescence Due to Triplet Pair Coherences Produced by Direct Singlet Fission. *J. Am. Chem. Soc.* **2012,** *134***,** 8597-8607.

123. Müller, A.M.; Avlasevich, Y.S.; Müllen, K.; Bardeen, C.J. Evidence for Exciton Fission and Fusion in a Covalently Linked Tetracene dimer. *Chem. Phys. Lett.* **2006,** *421***,** 518-522.

124. Müller, A.M., Avlasevich, Y.S., Schoeller, W.W., Müllen, K., Bardeen, C.G. Exciton Fission and Fussion in Bis(tetracene) Molecules with Different Covalent Linker Structures *J. Am. Chem. Soc.* **2007,** *129***,** 14240-14250.